MASSEY UNIVERSITY
TE KUNENGA KI PŪREHUROA
UNIVERSITY OF NEW ZEALAND

Effects of Multiphase Turbulence on the Flow and Hazard Behavior of Dilute Pyroclastic Density Currents

A thesis submitted in partial fulfilment for the degree of

Doctor of Philosophy
in Earth Science

At Massey University, Palmerston North, New Zealand

Daniel Holger Uhle

2024

This thesis is dedicated to my mother, Beate, and brother, Martin.

Abstract

Pyroclastic surges (also dilute pyroclastic density currents or dilute PDCs) are amongst the most hazardous volcanic phenomena associated with explosive volcanic eruptions and hydrothermal explosions. These fast-moving, turbulent, polydisperse multiphase flows of hot volcanic particles and gas occur frequently and have severe impacts on life and infrastructure. This is attributed to a compounding of hazard effects: large flow-internal dynamic pressures of tens to hundreds of kilopascals destroy reinforced buildings and forests; temperatures of up to several hundreds of degrees Celsius pose severe burn hazards; and readily respirable hot fine ash particles suspended inside dilute PDCs cause rapid asphyxiation. Direct measurements inside pyroclastic density currents are largely absent, and previous research has used a combination of detailed field studies on PDC deposits, laboratory experiments on analog density currents, numerical modeling, and theoretical work to interrogate the internal flow structure, gas-particle transport, sedimentation and destructiveness of dilute PDCs. Despite major scientific advances over the last two decades, significant fundamental gaps in understanding the turbulent multiphase flow behavior of dilute PDCs endure, preventing the development of robust volcanic hazard models that can be deployed confidently. Critical unknowns remain regarding: (i) how turbulence is generated in dilute PDCs; (ii) how multiphase processes modify the flow and turbulence structure of dilute PDCs; and (iii) if and how turbulent gas-particle feedback mechanisms affect their destructiveness. To address these gaps in understanding, this PhD research involved high-resolution measurements of velocity, dynamic pressure, particle concentration, and temperature inside large-scale experimental dilute PDCs.

It is shown that dilute PDCs are characterized by a wide turbulence spectrum of damage-causing dynamic pressure. This spectrum is strongly skewed towards large dynamic pressures with peak pressures that exceed bulk flow values, routinely used for hazard assessments, by one order of magnitude. To prevent severe underestimation of the damage potential of dilute PDCs, the experimentally determined ratio of turbulence-enforced pressure maxima and routinely estimated bulk pressures should be used as a safety factor in hazard assessments. High-resolution measurements of dynamic pressure and Eulerian-Lagrangian multiphase simulations reveal that these pressure maxima are attributed to the clustering of particles with critical particle Stokes numbers ($St = \mathcal{O}(1)$) at the margins of coherent turbulence structures. The characteristic length scale and frequency of coherent structures modified in this way are controlled by the availability of the largest particles with critical Stokes number. Through this, spatiotemporal variations in peak pressures are governed by the mass loading and subsequent sedimentation of these clustered particles. In addition to the 'continuum phase' loading pressure, the measurements also revealed that the direct impact of clustered margins and high Stokes number particles decoupling from margins with structures generate instantaneous impacts. These piercing-like impact pressures exceed bulk pressure values by two orders of magnitude. Particle impact pressures can cause severe injuries and damage structures. They can be identified as pockmarks on buildings and trees after eruptions. This new type of PDC hazard and the magnitude of pressure impacts need to be accounted for in hazard assessments.

Systematic measurements of the evolving experimental pyroclastic surges along the flow runout demonstrate that time-averaged vertical profiles of all flow velocity components and flow density obey self-similar distributions. Variations of the roughness of the lower flow boundary, geometrically scaling ash- to boulder-sized natural substrates, showed the self-

similar distributions are independent of the roughness. Mathematical relationships developed from the self-similar velocity and density distribution reveal the self-similar vertical distribution of mean dynamic pressure. This empirical model can inform multi-layer PDC models and estimate the height and values of peak time-averaged dynamic pressure for dilute PDCs of arbitrary scale.

Turbulence fluctuations around the mean were investigated through Reynolds decomposition. The large-scale turbulence structure and the dominant source of turbulence generation are shown to be controlled by free shear with the outer flow boundary, while strong density gradients at the basal high-shear flow boundary dampen turbulence generation. The large-scale, shear-induced coherent turbulence structures can be tracked along the runout and were found to be superimposed by smaller turbulence structures. In Fourier spectra of dynamic pressure, flow velocity, and temperature, these sub-structures are observed as discrete frequency bands that correspond to the coarse modes of the spatiotemporally evolving flow grain-size distributions. This can be associated with the preferential clustering of particles at the peripheries of the sub-structures. Following the decoupling of particle clusters, the rapid sedimentation of particle clusters occurs periodically at the characteristic frequency of the turbulence sub-structures. This mechanism of preferential clustering, decoupling and rapid sedimentation of particles with critical particle Stokes numbers is an important mechanism of turbulent sedimentation to explain the spatiotemporally evolving flow grain-size distribution of pyroclastic surges.

Acknowledgments

Firstly, I would like to thank my primary supervisor, Gert Lube, who provided me with the chance to pursue my PhD in beautiful Aotearoa (New Zealand). Through his expertise and valuable input through his experience, valuable discussions, and consistent support throughout this PhD. I would also like to express my sincere gratitude to co-supervisor Jim Jones, who greatly contributed to this PhD through insightful discussions and great advice. Also, Luke Fullard is thanked for his great supervision and interesting discussions on mathematics, data processing, and longboards.

I want to thank my collaborators Eric C. P. Breard (University of Edinburgh), Joe Dufek (University of Oregon), Susanna Jenkins (Earth Observatory Singapore), and Eckart Meiburg (University of California), with whom it was a pleasure to work during my PhD and who I hope to also collaborate with in future projects. Experiments conducted in PELE are always a team effort, and I would like to thank everyone involved with the experimental preparation and execution. I want to thank Ermanno Brosch for his help with the experimental runs that would not have been possible without his experience. Also, special thanks go out to James Ardo for his collaboration in the experimental series and his help with the data processing. Many thanks also go out to Lucas Corna, Kevin Kreutz, and David Feek for their help in the PELE setup and everyone who came and helped during the experimental runs. Also, Kate Arentsen is thanked for her administrative help.

I also want to thank Matthias Hort (University of Hamburg) and Lea Scharff (University of Hamburg) for their guidance and support that started during my undergraduate degree and

helped me to find my path toward a PhD in New Zealand. Also, thank you to my friend, past tutor, and now collaborator, Michel Bänsch, for his help throughout my B.Sc., M.Sc., and PhD.

I want to thank Martin Yakas for hosting me and igniting my passion for the outdoors and the ocean during my high school year in New Zealand. Without my friends in New Zealand, the time of my PhD would have been less enjoyable, and I am grateful to have met so many great people from all corners of the world. I want to especially thank Kevin Kreutz, Rupsa Chakraborty, Paul Brett, Shannen Mills, Sarah Tapscott, Charline Lormand, Nathan and Vela Laurie, Martin and Megan Yakas, Sandeep Kumar, Nessa D'Mello, Carlos Corella Santa Cruz, Michael Morgan, Nicholas Kan, and Hanze Fu for their friendship and support through this PhD. But not only new friends in New Zealand but also old friends continued to play a big role in the past years. I want to thank especially Eugen Blohm for his friendship and all the amazing memories we share. Further, I want to thank Daniel Fröbel and Lasse Ohlsen for being great friends.

I want to also thank my father, Holger, who has always been there for me with advice and support and who is dearly missed. Most importantly, I want to thank my mother, Beate, and brother, Martin, for always being there, even if from afar, this thesis is dedicated to them. Danke für alles Beate und Martin diese Arbeit ist euch gewidmet!

This PhD was financially supported through a MARSDEN grant from the Royal Society of New Zealand (MAU1902).

Table of Contents

List of Figures

List of Supplementary Figures

List of Tables

1 Introduction

This chapter motivates the conducted research and summarizes the relevant research. The introduction includes the definition of research objectives and research questions and a selective summary of previous research focusing primarily on the internal dynamics of dilute pyroclastic density currents, the vertical structure of concentrations and velocities, and the turbulent gas-particle interactions in general turbulence and pyroclastic density currents.

1.1 Motivation

Globally, more than half a billion people live close to volcanoes (Dunkley and Norton, 2002), and are affected by the various threats caused by volcanoes. The main threats include ashfall (Baxter and Horwell, 2015), lava flows (Peterson and Tilling, 2000), and pyroclastic density currents (PDC) (Nakada, 2000, Valentine and Fisher, 2000, Baxter *et al.*, 2008). PDCs are considered the most lethal volcanic phenomenon of those hazards, accounting for at least one-third of fatalities caused by volcanic activity (Auker *et al.*, 2013). Excluding the five largest disasters, Auker *et al.* (2013) find PDCs responsible for 46% of volcanic fatalities.

Pyroclastic density currents can be generated during eruptions of all magnitudes (Dufek, 2016) and are triggered by various processes. These processes include eruption column collapse (Clarke *et al.*, 2002, Scharff *et al.*, 2019, Trolese *et al.*, 2019), caldera collapse (Self and Rampino, 1981), phreatomagmatic explosions (Fisher and Waters, 1970, Glicken and Nakamura, 1988, Yamamoto *et al.*, 1999, Breard *et al.*, 2015), and directed blasts (Christiansen and Peterson, 1981, Belousov *et al.*, 2007, Sutawidjaja, 2013), to name a few.

Despite the significant research efforts on pyroclastic density currents (PDCs) over the past decades, understanding these ground-hugging gravity currents of hot particles and gas is still limited. Advancing this understanding is a central objective in volcanology (Lube *et al.*, 2020) and is necessary to improve risk management and mitigation for populations that life in the vicinity of volcanoes (Cashman and Sparks, 2013).

PDCs are highly polydisperse and strongly vertically density-stratifies multiphase flows of hot particles and gas. The term pyroclastic density current encompasses a spectrum of gas-particle transport mechanisms from non-turbulent, dry granular flow, over gas pore-pressure modified granular flow to fully dilute, fully turbulent suspensions. Based on the characteristics of their deposits, PDCs have been traditionally subdivided into two types or end-members: pyroclastic flows and pyroclastic surges (Sparks, 1976). In pyroclastic flows, the majority of the flow mass is envisaged to be transported in a basal flow region as a gas pore-pressure modified granular flow, which has originally been envisaged to behave akin to a fluidized granular bed (Wilson, 1980) and which is overlain by a dilute turbulent ash-cloud surge. In pyroclastic surges (Valentine, 1987), most of the flow mass is transported as a dilute, fully turbulent suspension, and dense granular flow processes are restricted to a thin basal bedload region. The term pyroclastic density current encompasses the full spectrum of transport processes from dense granular flow to dilute turbulent suspensions. This PhD research is centered on the effects of turbulence on the multiphase flow and hazard behaviors of dilute pyroclastic density currents. Therefore, this research introduction will be focused on the dilute turbulent endmember of PDC transport (hereafter dilute PDCs or dPDCs).

Previous research has highlighted that the destructiveness of dilute PDCs, and PDCs in general, results from a combination of effects: high flow velocities and densities result in damage-causing dynamic pressures of tens to hundreds of kilopascals that can destroy forests and buildings (Valentine, 1998, Spence *et al.*, 2004a, Baxter *et al.*, 2005, Jenkins *et al.*, 2013,

Lerner *et al.*, 2022); flow temperatures of several hundreds of degrees Celsius constitute severe burn hazards (Lacroix, 1904, Baxter, 1990, Jenkins *et al.*, 2013, Baxter *et al.*, 2017); while high concentrations of readily respirable fine ash particles create a high risk for asphyxiation (Baxter, 1990). However, there is a fundamental lack of measurements to detail the spatial distributions of velocity, particle concentration, temperature, and particle grain-size inside flows and how these distributions evolve in space and time during flow propagation. This limits predictions of how exactly hazard effects are generated inside PDCs, and how they perpetuate and vary during flow evolution. Therefore, further research is needed to understand how destructiveness develops inside PDCs to implement appropriate hazard forecasting and risk mitigation strategies (Cashman and Sparks, 2013, Lube *et al.*, 2020). To assess the potential hazard impacts of PDCs, volcanologists try to estimate bulk flow properties, such as integral averages of flow velocity, flow density (or particle volume concentration), flow temperature, and flow particle size (e.g., Dellino *et al.*, 2008, Roche *et al.*, 2013, Dioguardi and Dellino, 2014, Dufek *et al.*, 2015, Dioguardi and Mele, 2018). Brosch *et al.* (2021) have shown turbulence fluctuations in velocity and density to be the main destruction-driving mechanism in PDCs, generating dynamic pressures 3-5 times higher than their average values. They explained this characteristic through the focusing of energy in large turbulence structures and internal gravity waves.

The destructiveness and unpredictability of PDCs occurrences limit detailed direct measurement campaigns into PDCs, and only two direct measurements into natural PDCs exist (Scharff *et al.*, 2019, Brosch *et al.*, 2021). Most of the understanding of dilute PDCs stems from the interpretation of deposits, numerical simulations, and analog experiments (Dufek, 2016, Lube *et al.*, 2020). Previous experimental studies on dilute PDCs used the analog of aqueous compositional and particle-laden gravity currents (e.g., Burgisser *et al.*,

2005, Lube *et al.*, 2015, Brosch *et al.*, 2022). Recently, it has been highlighted that the complex multiphase flow processes of PDCs cannot be downscaled to benchtop-scale experiments and that aqueous gravity currents do not fully scale to the dynamics and complexity of particle-gas transport in PDCs (Burgisser *et al.*, 2005, Lube *et al.*, 2015). Therefore, sufficiently large-scale experimental studies of fully turbulent gas-particle flow are needed to investigate the internal flow dynamics of PDCs (Esposti Ongaro *et al.*, 2020a, Cerminara M., 2021, Shimizu *et al.*, 2021) and to validate computational models (Esposti Ongaro *et al.*, 2020a, Cerminara M., 2021, Shimizu *et al.*, 2021). Over the past decades, different large-scale facilities have been developed to generate the dilute end member of pyroclastic density currents. These setups are located in Italy (Dellino *et al.*, 2007), in the USA (Andrews and Manga, 2011), and in Aotearoa/New Zealand (Dellino *et al.*, 2007, Andrews and Manga, 2011, Lube *et al.*, 2015).

Large-scale turbulence has been shown to majorly affect the hazard potential of dilute PDCs (Brosch *et al.*, 2021). How turbulence affects the particle distributions and particle coupling in PDCs has been described through theoretical models (Burgisser and Bergantz, 2002, Burgisser *et al.*, 2005, Breard *et al.*, 2016, Lube *et al.*, 2020). To date, the energy transfer from large to small turbulence structures inside PDCs and how these affect the hazard potential of PDCs, the flow-internal particle coupling, and grain-size distributions have not been studied systematically. Even in homogenous turbulence, it is not well understood how the presence of particles modulates the energy cascades of turbulent suspensions (Brandt and Coletti, 2022), though most studies suggest increased energy transfer to smaller structures under the presence of particles (Yang and Shy, 2005, Bosse *et al.*, 2006, Poelma and Ooms, 2006).

Motivated by these gaps in knowledge, this thesis is focused on the effects of turbulence on PDC transport and hazard behavior. An experimental series in the Pyroclastic flow Eruption Large-scale Experiment (PELE) (Lube *et al.*, 2015) was conducted to investigate these. Different roughness elements varying from dynamically smooth to roughness in length scales of the viscous sublayer were installed in the experimental setup to investigate the role of the substrate on the PDC propagation. High-resolution Piezoelectric pressure sensors expanded the measurement system in PELE, and existing thermocouple temperature sensors were replaced with faster sensors to get more valuable insights into the turbulence of the generated flows. The experimental series is aimed to advance the understanding of the internal velocity and density distributions in PDCs, and to investigate how turbulence affects the particle clustering and the hazard potential of dilute PDCs. This research builds on the PhD theses of Eric C. P. Breard (Breard, 2016) and Ermanno Brosch (Brosch, 2020).

1.2 Research Aims and Objectives

The following three research questions (summarized in Table 1-1) motivated and guided this PhD project:

I. ***What are the processes behind the destruction-causing dynamic pressure in pyroclastic density currents, and how do these processes relate to hazard impacts?***

   Recent experimental results and coincidental measurements into natural PDCs revealed the dynamic pressure to be focused in large turbulence structures and to span a wider spectrum than previously expected (Brosch *et al.*, 2021). The mechanisms causing these broad dynamic pressure spectra remain enigmatic, necessitating more detailed experimental work.

Objective 1: Perform direct high-resolution measurements of dynamic pressure to quantify its turbulence spectrum.

Objective 2: Understand how turbulence fluctuations in dynamic pressure are generated and how these relate to hazard.

II. ***How can the internal flow and turbulence structure of PDCs be characterized, and how does it evolve during flow runout?*** To date, the ferocity and unpredictability of PDCs prohibited most efforts to obtain direct measurements inside flows, limiting the ability to validate flow models of PDCs. This motivates continued experimental efforts to characterize the internal structure of PDCs and to understand the hazard potential of PDCs better.

Objective 3: Describing the vertical structure of velocity and concentration in dilute PDCs.

Objective 4: Describing the turbulence structure inside dilute PDCs and track the evolution of turbulence structures during flow propagation.

Objective 5: Generate data to benchmark and inform numerical models.

III. ***What are the effects of turbulent gas-particle feedback mechanisms on the behavior of PDCs, and how do these feedback mechanisms modify the flow and turbulence structure of PDCs?*** Theoretical models about the gas particle interactions in pyroclastic density currents have been suggested (Burgisser and Bergantz, 2002, Breard and Lube, 2017), but comprehensive understanding on the interplay between particles and turbulence has not been developed yet, also for other turbulence settings this is not fully understood (Brandt and Coletti, 2022).

Objective 6: Recording and investigating the turbulent energy cascades inside experimental dilute PDCs.

Objective 7: Determining how the turbulence and gas particle interactions affect the flow propagation.

Objective 8: Determining how the turbulence characteristics of dilute PDCs is presented in different characteristic flow variables (e.g., velocity, pressure, and temperature).

Table 1-1 Objectives, methods, and goals. The table summarizes the suggested research's objectives, methods, and goals.

Objective	Method	Goal
What are the processes behind the destruction-causing dynamic pressure in pyroclastic density currents, and how do these processes relate to hazard impacts?	Experimental Approach: • Deployment of high-resolution pressure sensors • Updating temperature sensors with faster sensors • Systematic series of large-scale experiments Data Analysis: • Develop new algorithms to investigate dynamic pressure and other measurements obtained in PELE. • Investigation of Fourier spectra to quantify the frequency content of the measured signals.	Perform direct high-resolution measurements of dynamic pressure to quantify its turbulence spectrum. Understand how turbulence fluctuations in dynamic pressure are generated and how these relate to hazard.
How can the internal flow and turbulence structure of PDCs be characterized, and how does it evolve during flow runout?	Experimental Approach: • Measuring time-varying flow parameters (e.g., velocity, temperature, dynamic pressure) in highly turbulent experimental dilute PDCs • Perform measurements at different runout distances to investigate how dilute PDCs evolve during flow propagation. Data Analysis: • Development of new analysis algorithms to investigate the recorded data-sets and their turbulence	Describing the vertical structure of velocity and concentration in dilute PDCs. Describing the turbulence structure inside dilute PDCs and track the evolution of turbulence structures during flow propagation. Generate data to benchmark and inform numerical models.

What are the effects of turbulent gas-particle feedback mechanisms on the behavior of PDCs, how do these feedback mechanisms modify the flow and turbulence structure of PDCs?	Experimental Approach: • Measuring spatially and temporally variant flow parameters (e.g., velocity, temperature, dynamic pressure) in experimental dilute PDCs Data Analysis: • Development of new analysis algorithms to investigate the recorded data-sets and their turbulence • Investigation of Fourier spectra to quantify the frequency content of the measured signals.	Recording and investigating the turbulent energy cascades inside experimental dilute PDCs. Determining how the turbulence and gas particle interactions affect the flow propagation. Determining how the turbulence characteristics of dilute PDCs is presented in different characteristic flow variables (e.g., velocity, pressure, and temperature).

1.3 Thesis Outline and Structure

The presented thesis is subdivided into six chapters, followed by an appendix.

Chapter 1: Introduction

The introduction chapter motivates the conducted research and summarizes selected previous research in the field. The introduction encompasses the definition of research questions and objectives. The outlined previous work primarily focuses on the internal dynamics of PDCs, the vertical structure of concentrations and velocities, and the turbulent gas-particle interactions in general turbulence and PDCs.

Chapter 2: Methods

The methods chapter summarizes and explains the existing PELE setup and expansions made as part of this research. The proposed experimental series is described, and the design of new sensors and analysis algorithms is explained.

Chapter 3: Deadly coupling – hazard impacts of pyroclastic density currents exacerbated by mesoscale particle clusters

The first research chapter focuses on Research Question 1, the turbulent gas-particle interactions, and how these exacerbate the destructive potential of dilute PDCs. High-resolution measurements of dynamic pressure are used to investigate the multiphase physics

inside PDCs. Multiphase numerical modeling, field observations, and non-dimensional analysis support the results. It is shown that particle clustering in the peripheries of coherent turbulence structures generates a focusing of energies and leads to dynamic pressures that are up to 13 times the mean pressure values. Further, it is demonstrated that the clustering of particles does not only generate strong turbulence fluctuations in dynamic loading pressure but, through direct impact of particle clusters with structures, they are responsible for the generation of large discrete pressure excursions. It is highlighted how these processes of gas-particle feedback relate to hazard impacts that need to be considered in future risk management.

The manuscript is prepared and structured for submission to Nature Communications Earth and Environment. Therefore, the methods section is included in the Supplementary Material.

Both the PhD candidate as well as co-authors contributed:

Chapter 4: Characterizing the Flow and Turbulence Structure of Dilute Pyroclastic Density Currents Through Large-Scale Experiments

Chapter 4 focuses on Research Question 2, how the internal flow and turbulence structure of dilute PDCs can be characterized, and how it evolves along flow propagation. An experimental series with variable bed roughness, simulating the conditions of ash- to boulder-dominated surfaces of volcanic landscapes, was conducted to investigate this problem. It is shown that the time-averaged velocity and particle concentration (and flow density) structure of dilute PDCs obey distinct self-similar distributions that are largely unmodified during flow runout. In combination, these distributions yield a self-similar distribution of dynamic pressure and allow vertical profiles of destruction-causing dynamic pressure in dilute PDCs to be estimated for arbitrary ranges in bulk flow velocity and concentration (or flow density). Furthermore, it is shown that, for the range in roughness conditions tested, the substrate roughness does not modify the self-similar flow structure.

Following the recognition of a self-similar time-integrated flow structure of dilute PDCs, Chapter 4 demonstrates how Savitzky-Golay filters can be used to decompose the flow fields of highly unsteady multiphase flows into their mean and turbulent components. This technique is applied to the experimental measurements to visualize the spatiotemporally variable distribution of turbulence fluctuation, turbulence intensity, and turbulent kinetic energy inside dilute PDCs. The results from this analysis highlight the importance of moderate shear at the outer free-shear boundaries of PDCs for turbulence generation, while the strong density gradients dampen turbulence generation at the basal high-shear boundaries.

The manuscript is prepared to be submitted as a full-length research article.

Both the PhD candidate as well as co-authors contributed:

Chapter 5: Turbulence Structures in Dilute Pyroclastic Density Currents and their Implications on Turbulent Gas Particle Coupling

Chapter 5 addresses research question three. This research interrogates how flow-internal measurements of flow velocity, temperature, and dynamic pressure relate to the turbulence structure of dilute PDCs and polydisperse turbulent multiphase flow in general. It is demonstrated that velocity data and high-speed video imagery can be used to track the spatial evolution of large coherent turbulence structures and mesoscale turbulence. Furthermore, this research shows that spatiotemporal changes in the flow grain-size distribution relate to characteristics of the turbulent energy cascades and focusing of energies in measurements of flow velocity, dynamic pressure, and temperature. It is suggested that it is the clustering of particles with high particle Stokes numbers at the peripheries of coherent turbulence structures that generates the focusing of energies and modulations of turbulent energy cascades. The subsequent decoupling of particle clusters from coherent turbulence structures

leads to the selective sedimentation of particle sizes and generates polymodalities in the flow grain-size distributions.

The manuscript is in preparation for submission to Earth and Planetary Science Letters.

Both the PhD candidate as well as co-authors contributed:

Chapter 6: Discussion and Synthesis

The final chapter of this thesis summarizes the main results, links them, and puts them in the scientific context. Future perspectives are suggested, and preliminary results are shown to suggest future research.

1.4 Dilute Pyroclastic Density Currents - a Type of Particle Laden Gravity Current

PDCs are vertically density stratified particle-laden gravity currents, with the dense bedload at the base, the body composed of the wall and jet region above that, and the wake at the top of the PDC (see Figure 1-1). The frontal part of the flow is referred to as the head and is envisaged to contain a frontal head vortex. The head is followed by the flow body region (Figure 1-1).

PDCs have been traditionally divided into two end-members: pyroclastic flows (also dense PDCs) and pyroclastic surges (also dilute PDCs) (Sparks, 1976). Both end-members are characterized by strong vertical stratification in particle solid concentration (Burgisser and Bergantz, 2002). In dense PDCs, conceptual models envisage a non-turbulent concentrated granular-fluid underflow with particle concentration of several tens of volume percent that carries most of the flow's mass, dominates flow behavior and is overlain by a dilute turbulent ash cloud surge with bulk concentration of less than 1 vol.% (Wilson, 1980). Dilute PDCs are considered to have bulk flow concentrations of less than one volume percent. These fully

turbulent currents are envisaged to have a more continuous vertical density stratification than pyroclastic flows (Valentine, 1987). This research focuses on dilute pyroclastic density currents, particularly the characteristics of turbulent multiphase flow and hazard behaviors of these currents.

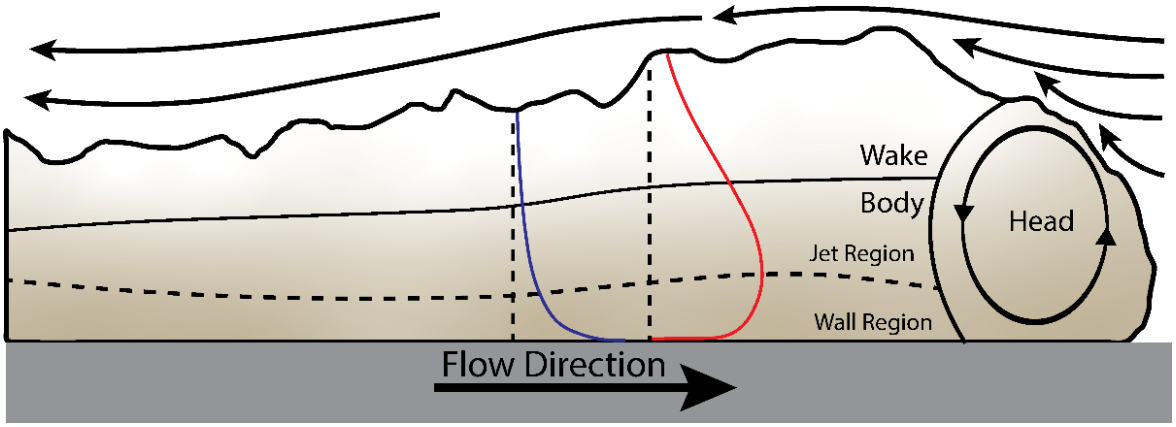

Figure 1-1 Conceptual structure of dilute pyroclastic density currents, redrawn from PELE experiments. *The frontal part of the PDC is composed of the shear-induced head vortex followed by the main flow body. The main flow body is vertically stratified and envisaged to be layered. The layers are the wall region, jet region, and wake. At the lowermost boundary, a dense bedload can form. The conceptual concentration (blue) and velocity (red) distribution are marked.*

1.5 Physical Parameters in Pyroclastic Currents

The lack of direct measurements inside dilute PDCs necessitated the use of bulk flow properties to study the dynamics of pyroclastic currents (Dufek, 2016). Average flow properties have been inferred from deposit characteristics (Dioguardi and Dellino, 2014, Mele *et al.*, 2015), estimated from field observations (Baxter *et al.*, 2005, Jenkins *et al.*, 2013), and from numerical simulations (Esposti Ongaro *et al.*, 2011b). The destructiveness and lethality of PDCs are largely controlled by the dynamic pressure (Valentine, 1998,

Clarke and Voight, 2000, Sparks *et al.*, 2002), the flow temperature (Baxter *et al.*, 2005, Jenkins *et al.*, 2013), and the ash load (Baxter, 1990, Baxter *et al.*, 2017).

Velocity: Pyroclastic currents travel down the volcano's flanks with a wide spectrum of possible velocities, ranging from a few tens of meters per second to over $300\ \mathrm{m \cdot s^{-1}}$ (Dufek, 2016). The 1980 Mount St. Helens blast involved dilute PDCs that traveled at an average flow front velocity close to $100\ \mathrm{m \cdot s^{-1}}$ while initial overpressure-driven velocities exceeded $200\ \mathrm{m \cdot s^{-1}}$ (Moore and Rice, 1984b, Brand *et al.*, 2023). Breard and Lube (2017) and Brosch *et al.* (2022) have observed that the flow internal velocity in experimental PDCs exceeds the flow front velocity. Brosch *et al.* (2021) have shown pulsing of velocity and dynamic pressure in PDCs. Direct numerical simulations by Sweeney and Valentine (2017) have shown that under poorly coupled particles, the gas phase beneath an impinging subsonic jet is displaced, increasing the acceleration of the gas phase. Further analysis of this numerical model by Valentine and Sweeney (2018) reports a decompression and recompression to occur due to the displacement of gas by poorly coupled particles. This decompression/recompression leads to the formation of Mach disks that are stationary in space. Brosch *et al.* (2021) and Brosch *et al.* (2022) generated experimental PDCs through the gravitational collapse of hot volcanic material. Sweeney and Valentine (2017) and Valentine and Sweeney (2018) numerically simulated PDCs generated through the gravitational collapse of an ash column. The studies performed by Brosch *et al.* (2021) and Brosch *et al.* (2022) are experimental and do not investigate the impact zone but rather characterize the spatiotemporal propagation of the generated PDCs. Valentine and Sweeney (2018) focus on only one timestep and the formation of the Mach disks. The results of Brosch *et al.* (2022) confirm the results of Sweeney and Valentine (2017) and their comparison to

Breard *et al.* (2016), just this time for dilute pyroclastic surges. The pulses seen by Brosch *et al.* (2021) cannot be linked to the Mach disk shown by Valentine and Sweeney (2018).

Density stratification: PDCs are characterized by a strong vertical density stratification (Sparks *et al.*, 1978, Fisher, 1979, Valentine, 1987, Wohletz, 2001, Branney and Kokelaar, 2002, Burgisser and Bergantz, 2002, Dellino *et al.*, 2008, Breard *et al.*, 2016, Brosch, 2020, Brosch and Lube, 2020). The density stratification is attributed to the settling of particles with different terminal fall velocities (Dellino *et al.*, 2005, Dioguardi and Mele, 2018), turbulent sedimentation (Burgisser and Bergantz, 2002), sedimentation through mesoscale clusters (Agrawal *et al.*, 2001, Breard *et al.*, 2016, Breard and Lube, 2017, Weit *et al.*, 2019, Brosch, 2020), and entrainment of air at the free boundary (Sparks *et al.*, 1993) or particles at the base. Due to the lack of observations of the density stratification in dilute PDCs, current models of the vertical distribution of flow density originate from research on turbidity currents (Altinakar *et al.*, 1996). The main assumption is that the density gradient develops a Rouseian profile (Graf, 1984). The Rouseian profile originates from the assumption that turbulent flows suspend finer particles better than coarser particles, expressed by the Rouse number. This leads to coarse particles accumulating at the base of the current, creating a high-concentration layer at the base of the PDCs. Recently, Brosch and coauthors (Brosch and Lube, 2020, Brosch *et al.*, 2021) measured vertical profiles of flow density in large-scale experimental dilute pyroclastic currents. They identified mesoscale clusters that affect the settling and the density stratification in PDCs majorly.

Dynamic Pressure: Most commonly, the velocity and the dynamic pressure are associated with the destructiveness of PDCs (Valentine, 1998, Clarke and Voight, 2000, Jenkins *et al.*, 2013, Brosch *et al.*, 2021), where the dynamic pressure ($P_{dyn} = \frac{1}{2}\rho v^2$) depends on the velocity v and flow density ρ and equates to the kinetic energy per unit volume. In the

aftermath of volcanic eruptions, the dynamic pressure is often estimated as the minimum dynamic pressure that was needed to cause this destruction on manmade infrastructure (e.g., Valentine, 1998, Clarke and Voight, 2000, Spence *et al.*, 2004b, Baxter *et al.*, 2005, Jenkins *et al.*, 2013) Also, vegetation can be destroyed and used to analyze the force of PDCs after the 1980 Mount St. Helens eruption flattening large areas of forest (Druitt, 1992, Clarke and Voight, 2000, Brand *et al.*, 2023). Tables and values in which dynamic pressures can cause destruction patterns, inferred from nuclear tests, can be found in Valentine (1998). Further research expanded on this research by systematic data collection on the aftermath of volcanoes (e.g., Baxter *et al.*, 2005, Jenkins *et al.*, 2013, Lerner *et al.*, 2022). Dellino *et al.* (2008) applied theoretical models of turbulent boundary layers and principles of hydraulic sediment transport to relate grain-size characteristics of PDC deposits to estimates of local time-integrated dynamic pressure. Based on the work of Dellino *et al.* (2008) computer programs where developed to calculate the dynamic pressure of dilute PDCs based on deposit characteristics (e.g., grainsize distribution and deposit thickness) (Dioguardi and Dellino, 2014, Dioguardi and Mele, 2018). For the velocity distribution, a so-called "law of the wall" (Prandtl, 1905, Batchelor and Proudman, 1956) profile is used. Recent research on PDCs has shown a Power Gaussian form to describe the velocity distribution (Brosch *et al.*, 2021, Cerminara *et al.*, 2021), contradicting assumptions made by Dellino *et al.* (2008). Even though the model was validated experimentally (Dellino *et al.*, 2010a) and through field data (Dioguardi and Dellino, 2014, Mele *et al.*, 2015), direct internal observations, as in Brosch and Lube (2020), were not available to link the internal fluid dynamics with sedimentary processes. Recent experimental work by Brosch *et al.* (2021) revealed strong pulsing in dynamic pressures, exceeding the previously used mean values by a factor of 3-5. The process behind this is not understood yet. In the 1982 eruption of El Chichón (Mexico) pyroclasts caused impact craters on a basketball pole, which require far higher velocities

than those caused by gravitational acceleration (Scolamacchia and Schouwenaars, 2009). This observation makes the presence of shockwaves as caused by volcanic eruptions plausible (Scolamacchia and Schouwenaars, 2009, Sweeney and Valentine, 2017, Valentine and Sweeney, 2018). The exceeded mean values and the particle impact craters highlight two gaps in knowledge. What causes the fluctuation in dynamic pressure in PDCs, and how important are single particle collisions in PC hazards?

Temperature: The temperature in PDCs varies between ambient temperatures up to hundreds of degrees (Moore, 1967, Waters and Fisher, 1971, Sigurdsson *et al.*, 1987), such as during the 1997 Soufriere hills eruption reaching 400 °C (Loughlin *et al.*, 2002) and the Mount St. Helens 1980 eruption temperatures up to 250 °C (Banks and Hoblitt, 1981). Cooling of pyroclastic density currents is controlled by the entrainment of the substrate and ambient air, leading to the dilute PDC further propagating as a gravity current (Valentine, 1987). Temperatures of natural flows are often inferred from the aftermath, such as the analysis of thermal damages and charring of vegetation (e.g., Rosi *et al.*, 1993, Baxter *et al.*, 2005, Jenkins *et al.*, 2013, Lerner *et al.*, 2022). First in situ temperature measurements in synthetic pyroclastic currents were performed by Brosch *et al.* (2022).

1.6 Field measurements of PDCs

To date, I am only aware of two direct geophysical measurements inside PDCs (Scharff *et al.*, 2019, Brosch *et al.*, 2021). The first in situ measurement was performed by Scharff *et al.* (2019), who achieved flow internal measurements using a frequency modulated continuous wave (FMCW) Doppler radar installed at Vulcan de Colima (Scharff, 2012), as they are used for volcano monitoring (Hort and Seyfried, 1998, Voege *et al.*, 2005, Hort and Scharff, 2016). FMCW radar measure spectra of the radial velocity for multiple

measurement volumes along the radar beam. The amplitude associated with each velocity depends on the amount of material traveling with this velocity toward the radar. Scharff *et al.* (2019) suggest their data lend itself to validate and benchmark numerical models. This potentially understates the importance of the radar data, which might hold unique information on the turbulence and turbulent energy cascade inside real-world PDCs, at different observer locations. In combination with other data, such as large-scale experiments, the data could inform on scale dependence of processes.

The second data set of measurements of PDCs was recorded during the eruption of Whakaari (White Island) on 9 December 2019, creating a dilute PDC. At Whakaari, a seismic-acoustic network measured in situ pressure data of the dilute PDC. This data has so far only been analyzed for their frequency contents and the number of pressure pulses (Brosch *et al.*, 2021).

The measurements with the radar at Vulcan de Colima (Scharff *et al.*, 2019) and of pressures inside the PDC at Whakaari (Brosch *et al.*, 2021) reported here are not plannable. This is mostly due to the unpredictability and destructiveness of PDCs destroying most sensors and making installations very dangerous.

In addition to these rare in situ measurements, satellite-based sensors can be used to observe PDCs. A satellite-based infrared sensor measured the propagation of the 1980 Mount St. Helens (USA) lateral blast (Moore and Rice, 1984a). The sparse satellite coverage limits satellite-based measurements of PDCs (Lube *et al.*, 2020). Also, the seismic-acoustic signal generated by PDCs can be used to locate PDCs and estimate flow velocities (Yamamoto *et al.*, 1993, Ripepe *et al.*, 2009, Watson *et al.*, 2023).

1.7 Synthesizing Pyroclastic Density Currents

Over the past decade, large-scale experiments have gained importance in the investigations of the complex dynamics of PDCs. Large-scale experiments aim to perform measurements that otherwise could not be performed due to the violence of PDCs. As in every fluid dynamic experiment, dynamic similarity needs to be achieved to get meaningful results. This cannot be achieved easily with benchtop (small-scale) experiments. Large-scale experimental facilities synthesizing dilute PDCs are outlined briefly below.

The first large-scale experimental setup is located at the University of Bari (Italy) (Dellino *et al.*, 2007). The apparatus creating the PDCs is composed of a conduit (a 2.2 m high and 60 cm wide barrel) and gas-supply. The conduit is filled with pyroclastic material, and the pressurized gas accelerates the pyroclastic material vertically upwards. A gas-particle column is generated, which then collapses and creates a PDC (see Figure 1-2). This experimental setup achieves runout distances of up to 10 m. By adjusting the conduit length, mass of pyroclastic material, and gas pressure, different eruption scenarios can be simulated (Dellino *et al.*, 2014). With this setup, radially spreading PDCs are created. Experimental work at this facility provided the first direct internal pressure measurements (Dellino *et al.*, 2010a) these results further got used to calculate vertical distributions of dynamic pressure (Dellino *et al.*, 2008, Sulpizio *et al.*, 2014), informed on entrainment rates (Dellino *et al.*, 2019). Through its ability to generate a range of eruption scenarios this setup also helped to link the source conditions to resulting flow regimes (Dellino *et al.*, 2010b, Sulpizio *et al.*, 2014). Numerical models were utilized to obtain internal flow parameters (Doronzo *et al.*, 2011).

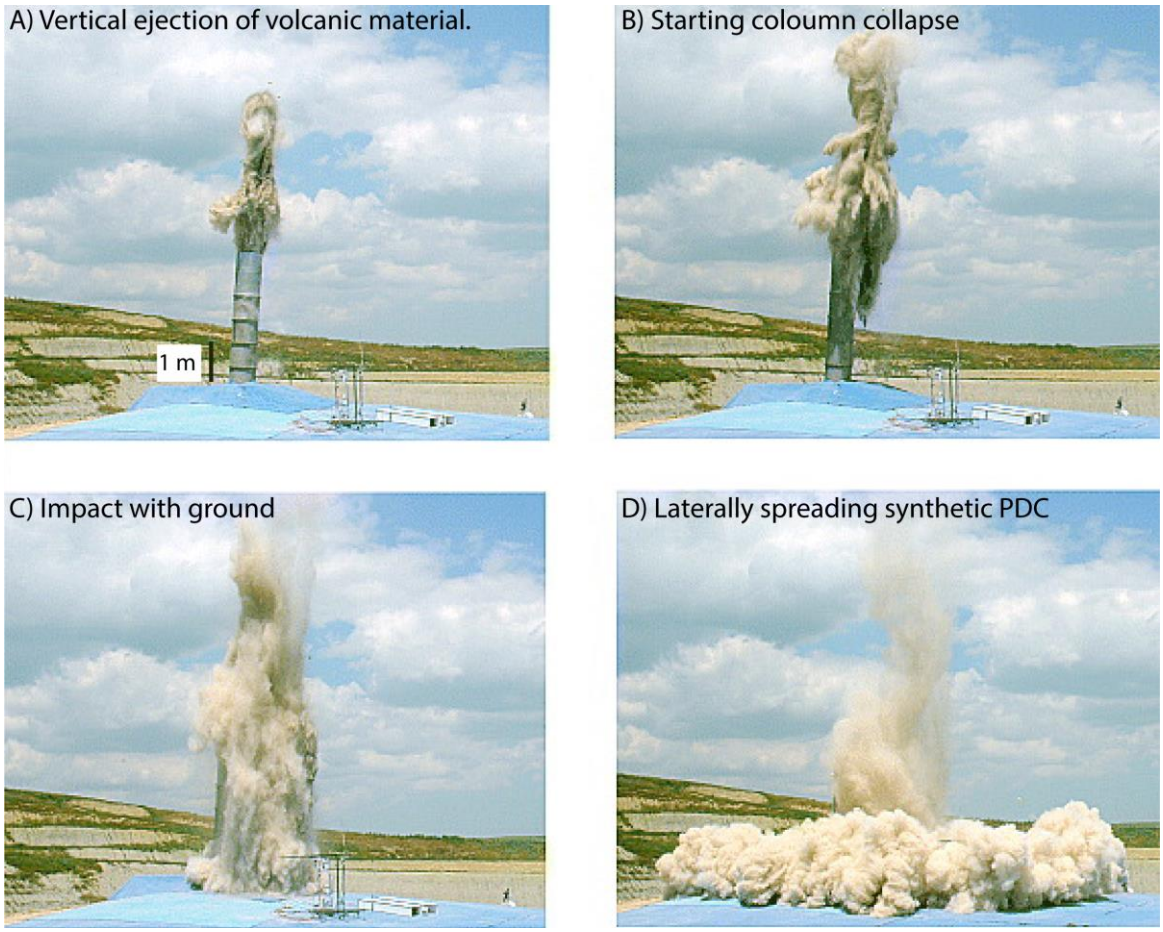

Figure 1-2 Image sequence from a column collapse generated by Dellino et al. (2010b). *A) Volcanic material is vertically ejected from. B) The volcanic material starts to fall. C) The volcanic material collapses on the ground and generates a PDC. C) The generated PDC spreads laterally. Modified from Dellino et al. (2010b).*

The second large-scale experiment is located at the Smithsonian Institution (Washington DC, USA) and was first introduced by Andrews and Manga (2011). The authors create gas-particle gravity currents inside an acrylic tank (6.5 m x 1.8 m x 0.6 m). In an experimental run, talcum powder is heated to 30 – 100 °C and fed into the tank at a known mass discharge rate. This generates dilute, fully turbulent particle-laden gravity currents (see Figure 1-3). The data logging consists of four high-definition video cameras. Topographic obstacles can be placed at different locations inside the tank (see Figure 1-3). The facility was later updated, and experiments were conducted at a larger scale (8.5 m x 6 m x 2.5 m). Deploying three differently colored sheet lasers allowed the authors to obtain three-dimensional

velocity measurements (Andrews, 2014). Experiments in this facility showed the ability of dilute PDCs to surmount topographic obstacles (Andrews and Manga, 2011), investigated entrainment of ambient air (Andrews, 2014), and showed that flows at low or ambient temperatures spread more than hot flows (Andrews, 2014).

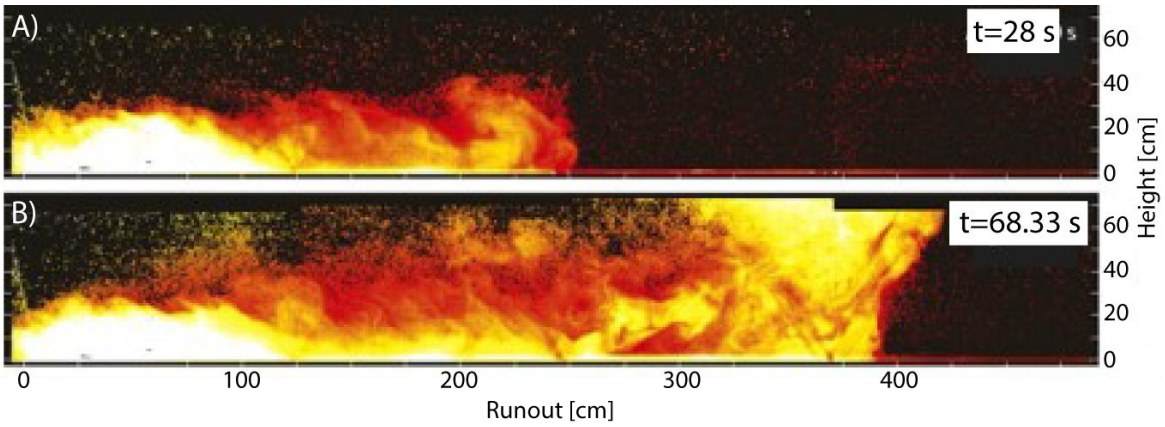

Figure 1-3 Imaged of an experiment conducted by Andrews and Manga (2011). *A synthetic gravity current created from talcum powder travels along a smooth bed. A) shows the propagating current at 28 s. B) shows the propagating current at 68.33 s where the current buoyantly lifts off. Modified from Andrews and Manga (2011).*

The third large-scale experimental setup is located at Massey University (Palmerston North, New Zealand). It was introduced by Lube *et al.* (2015) and is currently the largest experimental setup synthesizing PDCs. Experimental PDCs generated at the PELE facility have been demonstrated to scale well to natural PDCs and to encompass a wide spectrum of PDC flow behavior, including dense pyroclastic flow and turbulent dilute pyroclastic surge endmembers. Previous studies investigated the spatiotemporal variations of flow conditions for dilute, intermediate, and dense flow regimes (Lube *et al.*, 2015, Breard *et al.*, 2016, Breard and Lube, 2017, Breard *et al.*, 2018, Lube *et al.*, 2019, Brosch, 2020, Brosch and Lube, 2020, Brosch *et al.*, 2021, Brosch *et al.*, 2022). More detailed summaries and descriptions of the setup can be found in Lube *et al.* (2015) and Chapter 3 (Methods).

1.8 Numerical Modeling of dilute Pyroclastic Density Currents

Numerical modelling of PDCs is an important approach to study and advance the understanding of the complex multiphase physics inside PDCs (Dufek, 2016). Numerical models have been used to reconstruct and study past eruptions (Doronzo *et al.*, 2011, Esposti Ongaro *et al.*, 2020b), and to investigate physical processes of PDCs (Dufek, 2016, Lube *et al.*, 2020). Further, numerical models are able to produce data that cannot be easily measured in experiments (Doronzo and Dellino, 2011). To investigate PDCs, different classes of numerical models are used including 1D integral models, 2D and 3D depth averaged models, and 2D and 3D multiphase simulations.

1D Integral Models: In order to describe the kinematic of the flow front of dilute non-entraining PDCs, Dade and Huppert (1995) used a box model assuming conservation of mass and volume. This model was later applied to interpret the characteristics of the PDCs that emplaced the Taupo ignimbrite (Dade and Huppert, 1996). Bursik and Woods (1996) included entrainment of ambient air and the conservation of thermal energy, to describe the propagation of flows before buoyant lift-off. Fauria *et al.* (2016) introduced a integral PDC model that allows for entrainment of ambient air, as well as sedimentation and sediment loss of variable particle size classes to describe spatiotemporal variation in flow density and flow velocity.

Depth Averaged Models: Current depth averaged models are used to achieve computationally inexpensive models of the propagation of dilute PDCs and are designed to describe stratified flows (Doyle *et al.*, 2010, Kelfoun, 2017, Shimizu *et al.*, 2019). These models subdivide the currents in two layers based on their stratification, an upper layer and a lower layer (Shimizu *et al.*, 2021) and include assumptions of the flow geometry (e.g. $thickness \ll length$). The upper layer mainly focuses on the influence of particle settling,

entrainment, thermal expansion and outer drag, while the lower layer mainly focuses on deposition and basal friction (Shimizu *et al.*, 2021). These layers are then linked through mass and momentum exchanges.

Eulerian Continuum Approach: The Eulerian approach is most often used and approximates the suspended solid particles as a continuum fluid (Gidaspow, 1994, Goldhirsch, 2008, Armanini, 2013). These models are accepted to appropriately describe the transport regimes in dilute PDCs (Dufek, 2016), and have been widely applied to study the dynamic of dilute PDCs (e.g., Dobran *et al.*, 1993, Neri *et al.*, 2003, Dufek and Bergantz, 2007b, Sweeney and Valentine, 2017, Valentine and Sweeney, 2018).

Eulerian Lagrangian Approach: The Lagrangian approach numerically solves the Newton's equations for interacting particles. Computationally, Lagrangian models are too expensive for the application to pyroclastic density currents and are therefore not widely used (Esposti Ongaro *et al.*, 2020a). Combining the Eularian and Lagrangian approach shows to be an effective solution. In this approach multiple particle classes are considered (Dufek and Bergantz, 2007a, Breard *et al.*, 2018).

Eulerian Eulerian Lagrangian Approach: The Eulerian Eulerian Lagrangian approach uses multiple continua to describe gas as well as solid phases. This approach allows different particle and gas phases to have independent conservations of mass, momentum, and energy and further allows drag coupling between these different phases (Dufek and Bergantz, 2007b). One example of the application of the Eulerian Eulerian Lagrangian approach is the open-source Multiphase Flow with Interphase eXchanges (MFIX) solver, developed by the National Energy Technology Laboratory (NETL) within the US Department of Energy (Musser *et al.*, 2021).

Complex multiphase physics (Dufek, 2016, Lube *et al.*, 2020), as well as restrictions on the spatial and temporal resolution (Esposti Ongaro *et al.*, 2011a, Cerminara *et al.*, 2016), make numerical modeling of PDCs challenging. Further, volcanic eruptions, by nature, are stochastic with significant uncertainties in their initial and boundary conditions of PDCs (Sparks and Aspinall, 2004).

1.9 Vertical Distribution of Velocity and Concentration

In the past, different models have been suggested to describe the vertical distribution of velocity and concentration inside dilute gravity currents. Altinakar *et al.* (1996) suggest models for the concentration and velocity distributions based on an experimental series with aqueous gravity currents (turbidity currents). In their experiment, they discharged three different mixtures into water, two mixtures with water and sediments and one mixture with water and salt. The authors state no distinction can be made in the velocity and concentration distributions of their particle-laden and saline gravity currents.

Their gravity currents are divided into a wall and a jet region. Those two regions are separated at the height (h_m) where the maximum velocity (U_m) occurs. Following this distinction, they describe the wall and jet region with different mathematical functions for the velocity and concentration distribution (Altinakar *et al.*, 1996).

The velocity in the wall region ($z < h_m$) is given by two different functions in the paper by Altinakar *et al.* (1996).

The first is a law of the wall description

$$\frac{u(z)}{u_*} = \kappa^{-1} \ln(z) + Ct \qquad \textit{EQN. 1-1}$$

And the second is an empirical power law with the fit parameter $n = 1/6$

$$\frac{u(z)}{U_m} = \left(\frac{z}{h_m}\right)^n \qquad \textit{EQN. 1-2}$$

For the jet region ($z > h_m$) the velocity is given as

$$\frac{u(z)}{U_m} = \exp\left[-\alpha_c \left(\frac{z - h_m}{h - h_m}\right)^m \right]. \qquad \textit{EQN. 1-3}$$

In this near-Gaussian expression of the mean velocity distribution (Hug, 1975) α_c and m are fit parameters.

The concentration in the wall region is fitted by

$$\frac{c_s(z) - C_m}{c_b - C_m} = \frac{h_m - z}{h_m}. \qquad \textit{EQN. 1-4}$$

With c_b being a reference concentration and C_m the concentration at $z = h_m$.

This description is a linear simplification of a Rouseian relation (Graf, 1984)

$$\frac{c_s(z)}{c_b} = \left(\frac{(h_m - z)}{z}\frac{b}{(h_m - b)}\right)^{\eta}. \qquad \textit{EQN. 1-5}$$

With $c_b$being a reference concentration at the height b. The exponent η is a function of the Karman constant κ , the particle fall velocity, and bed-shear velocity u_{*b} ($\eta = v_s/\kappa u_{*b}$). Altinakar *et al.* (1996) used the simplified function due to difficulties in obtaining reliable concentration data in the wall region.

For the jet region, Altinakar *et al.* (1996) also propose a near-Gaussian relation similar to their description of the velocity in this region:

$$\frac{c_s(z)}{C_m} = exp\left[-\beta_c \left(\frac{z - h_m}{h - h_m}\right)^{\lambda_c}\right] \qquad \textit{EQN. 1-6}$$

This function is fit using β_c and λ_c as fit parameters, where λ_c can be kept constant. Concentration measurement in their experiment scatters significantly which the authors use to explain the large variation in their fit parameter β_c.

Cantero-Chinchilla *et al.* (2015) give another set of equations approximating the vertical velocity and concentration profiles for turbidity and salinity currents. The main difference between Cantero-Chinchilla *et al.* (2015) and previous studies (e.g. (Altinakar *et al.*, 1996)) is the definition of a single velocity distribution for the whole flow instead of separating the flow into wall and jet regions:

$$\hat{u}(\eta) = \sigma\eta^{\xi}(1-\eta)^{\chi}\,. \qquad \textit{EQN. 1-7}$$

Here $\hat{u} = u/U_m$ is the non-dimensional velocity, and $\eta = z/h_f$ (h_f is the turbidity current's depth) the non-dimensional height, σ is a coefficient, and ξ and χ are exponents fitted using experimental data. The authors show σ to be a function of ξ and χ meaning a reduction in free parameters. The authors further compare their model to the model of Altinakar *et al.* (1996) and state their model overpredicts most experimental velocity data.

Cantero-Chinchilla *et al.* (2015) also suggest a single concentration distribution, which contains a typical boundary layer approximation for the wall region and an asymptotically vanishing distribution for the jet region. This takes the form:

$$\hat{c}(\eta) = \exp\left[-\phi(\eta^{\zeta} - \eta_w^{\zeta})\right] \qquad \textit{EQN. 1-8}$$

Where $\hat{c} = c/C_m$ and C_m is the reference concentration at the boundary between the wall and jet region, η_w the dimensionless position of the wall-jet boundary. The parameters ζ and ϕ are empirically determined.

Earlier works focusing on the vertical distribution of velocities in dilute PDCs by Dellino *et al.* (2008) assume a Roussian profile for the concentrations and a law of the wall (Prandtl, 1905, Batchelor and Proudman, 1956) for the velocity distribution. The law of the wall profile assumed by Dellino *et al.* (2008) implies a free slip at the upper flow boundary. At the basal boundary, the law of the wall does not define a boundary condition due to its mathematical form.

Based on experimental data of dilute PDCs, Brosch *et al.* (2021) and Cerminara *et al.* (2021), recently suggested a Power-Gaussian distribution for the horizontal velocity component:

$$u(\eta,t) = U_m(t)\eta(t)^{\xi(t)} exp\left[-\left(\frac{\eta(t)-1}{\chi(t)}\right)^2 - \xi(t)(\eta(t)-1)\right]. \quad \text{EQN. 1-9}$$

In this equation $\eta(t) = z/h_m(t)$ is the dimensionless height and $h_m(t)$ the height of the wall region where $U_m(t)$ occurs. The terms $\xi(t)$ and $\chi(t)$ are time-dependent functions that are fit to experimental data. $\xi(t)$ is the inner layer exponent, and $\chi(t)$ the outer layer exponent. The parameters are fit over time to fit the passage of a PDC at a static vertical profile. Polynomials are used for those parameters to avoid overfitting and to get physical logic results (Cerminara *et al.*, 2021). The degree of those polynomials has to be kept as low as possible.

The Power-Gaussian function describes the wall region, as a boundary layer flow, with a no-slip condition at the base and the jet region as a free-surface turbulent layer (Cerminara *et al.*, 2021).

Brosch *et al.* (2021) and Cerminara *et al.* (2021) also show concentration data and fitted the function proposed by Cantero-Chinchilla *et al.* (2015). In Brosch *et al.* (2021) the authors find empirical concentration distributions (Altinakar *et al.*, 1996, Cantero-Chinchilla *et al.*, 2015) to deviate from their experimental data due to mesoscale clustering occurring in PDCs (Breard and Lube, 2017, Brosch, 2020, Lube *et al.*, 2020).

The density stratification of PDCs (Valentine, 1987, Branney and Kokelaar, 2002, Burgisser and Bergantz, 2002, Breard *et al.*, 2016) also guided the development of two-layered depth-averaged models for the estimation of PDC runout distances, with low computational cost (Doyle *et al.*, 2008, Doyle *et al.*, 2010, Kelfoun, 2017, Shimizu *et al.*, 2019).

The influence of the bed roughness on the flow propagation has not yet been tested for dilute PDCs. For turbidity currents, Kashefipour *et al.* (2017) investigated the influence of bed roughness on the velocity profiles in sedimentary water particle gravity currents. They found the wall region height to increase with increasing roughness while the maximum velocity decreases. Kashefipour *et al.* (2017) deployed roughness elements that scale to the wall region thickness. Corna (2023) investigated the influence of topographic obstacles with similar size to the roughness deployed by Kashefipour *et al.* (2017), on the propagation of dilute PDCs. The experiments by Corna (2023) shows remobilization of suspended material leading to modulation of the velocity profile.

1.10 Particle Settling

The most basic form to approach particle settling in multiphase physics is to consider particles settling in a static gas medium. In such a case, the terminal fall velocity of single particles can be obtained from a force balance of body forces (e.g., gravity) and surface forces (e.g., drag) acting on the particle. The terminal fall velocity calculates to be (Crowe *et al.*, 2012)

$$v_T = \frac{g\tau_V}{f}\left(1 - \frac{\rho_c}{\rho_d}\right). \qquad \textit{EQN. 1-10}$$

Here, g is the gravitational acceleration, τ_V the particle velocity response time, f the drag factor, ρ_c the fluid density, and ρ_d the particle density. The incorporation of different Reynolds numbers can be found in Eqn. 4.67 of Crowe *et al.* (2012).

Using experimental data, Dellino *et al.* (2005) analyze the terminal fall velocity for pyroclastic material. The authors derive a model to account for the density and shape of volcanic ash particles. This work applied to investigate dilute PDC deposits (Dioguardi and Dellino, 2014). And expanded upon by the development of an empirical one-equation drag

model for irregularly shaped volcanic particles, through an experimental series including a wide range of particle densities, shapes and different fluid viscosities and densities (Dioguardi *et al.*, 2018).

With those estimates, one has to consider that the terminal fall velocity of a single particle is the lower boundary for the settling velocities in gas-particle suspensions. The terminal fall velocity in those gas-particle suspensions increases with the particle concentration (Del Bello *et al.*, 2017).

Weit *et al.* (2018) generated a vertical turbulent flow with Reynolds numbers of 10^4-10^6 inside a vertical cylinder. They found that exceeding a critical particle concentration where all particles were in suspension, particles added to the mixture build clusters and settle downward to build a dense bedload. They find maximum concentrations of 0.3-2.8 vol. % in dilute mixtures. This might also apply to particle solid concentrations in dilute parts of pyroclastic density currents and other geophysical multiphase flows. Mesoscale clusters have already been shown to occur in PDCs and to increase the terminal fall velocity manifolds (Breard *et al.*, 2016, Brosch, 2020). Further studies have shown the maximum supported concentration to grow with the particle Reynolds number ($C_{max} = 0.78 \cdot Re_p{}^{0.17}$), and infer that geophysical turbulent gas-particle flows (Reynolds numbers from 10^2 to 10^5) to have solid concentrations of about 2-5 vol. % (Weit *et al.*, 2019).

The concept of a flow stratification occurring in every PDC was first introduced by Valentine (1987) who links particle transport with the Rouse number, Brunt Väisälä frequency, and other flow properties through a theoretical study that was not verified by experimental data. Since then, the way particle concentrations evolve inside PDCs has mostly been studied through analog experiments or depositional features of ignimbrites. For this purpose, Woods and Bursik (1994) conducted benchtop experiments to first investigate how entrainment generates buoyancy through an experimental series generating gravity currents using

mixtures of methanol, ethylene glycol, and water. In a second experimental series, Woods and Bursik (1994) generate water particle currents to investigate the influence of sedimentation. Those two experimental series enabled them to separate the influences of entrainment and sedimentation on the bulk concentration of the flow. Further studies by Choux and Druitt (2002) and Choux *et al.* (2004) using water particle currents focused on the depositional features, not the internal flow stratification.

In Burgisser and Bergantz (2002) five different transport and segregation regimes are described, which were also observed in the dilute part of experimental dense PDCs (Breard and Lube, 2017). A deeper understanding of those processes in PDCs must be established to understand the settling behaviour of particles. This is one of the objectives of this PhD. Once a fundamental understanding is established, particle concentration profiles can be calculated. Current vertical velocity and concentration distributions are summarized in the following section.

1.11 Multiphase Physics of Dilute Pyroclastic Density Currents

The motion and particle-gas transport of dilute PDCs is governed by a range of coexisting fluid dynamic processes. These include particle–particle interactions, fluid–particle interactions, fluid shear, turbulence fluctuations, entrainment of ambient air, and mixing of ambient air. The characteristic length- and timescales of each of these processes are broad; they span several orders of magnitude and are strongly overlapping (see Figure 1 b in Lube *et al.* (2020b) for a mapping of the characteristic length and timescales in PDCs). This leads to a broad range of co-existing flow regimes and explains why dilute PDCs are one of the most complex types of natural multiphase processes in nature.

1.11.1 Turbulent Energy Cascade

One of the most intuitive descriptions of the energy cascade was given by Lewis F. Richardson in the book Weather Prediction by Numerical Processes (Richardson, 1922) in the form of the rhyme:

"Big whirls have little whirls that feed on their velocity,

and little whirls have lesser whirls and so on to viscosity."

This rhyme incorporates the most important concept of the energy cascade, which is the presence of the largest eddies containing most of the energy. Large eddies transfer their energy to smaller eddies. The smaller eddies do the same until the energy is dissipated into heat through viscous effects (Pope, 2000).

Kolmogorov (1941) added complexity to this by answering the main questions that arose from the theory of Richardson with three hypotheses (Pope, 2000):

1. Local isotropy: The small-scale turbulent motion is locally isotropic for sufficiently high Reynolds numbers.
2. First similarity hypothesis: At high Reynolds numbers, the form of the small-scale motion is universally uniquely defined by the kinematic viscosity ν and the dissipation rate ε. Which defines the Kolmogorov scales for length ($\eta = \sqrt[4]{\nu^3/\varepsilon}$), velocity ($u_\eta = \sqrt[4]{\nu\varepsilon}$), and time ($u_\eta = \sqrt{\nu/\varepsilon}$), characterizing the smallest dissipative eddies.
3. Second similarity hypothesis: The second similarity hypothesis is like the first one, just for even smaller turbulence scales, which are not of interest for this thesis.

From the second of Kolmogorov's hypotheses, the Kolmogorov $-\frac{5}{3}$ spectrum follows (Pope, 2000):

$$E(k) = C\varepsilon^{2/3}k^{-5/3} \qquad \textit{EQN. 1-11}$$

C is a constant, ε is the dissipation rate describing the energy transfer from large to small eddies in the inertial subrange, and k is the wave number ($k = 2\pi/l$), with l the eddy size. From this, it follows that the energy cascade has a slope of -5/3 in the inertial sub-range. The calculations and theoretical work behind this are based on single-phase turbulence. The reader is referred to (Pope, 2000) for a detailed derivation. The -5/3 slope in the logarithmic energy cascade is found in the spectra of velocity, compressible velocity, density, pressure, temperature, and entropy for the inertial subrange (Wang *et al.*, 2019). In pressure spectra of turbulent free shear flows, the energy cascade has a slope of $-7/3$ for the inertial subrange and for the turbulence-mean shear contribution a slope of $-11/3$ (George *et al.*, 1984). Initially, it was assumed that the presence of particles smaller than the Kolmogorov scale ($d < \eta$) lead to an attenuation of turbulence (Brandt and Coletti, 2022). This has been contradicted by other studies that investigated the effect of dispersed particles on the turbulence of the carrier fluid, indicating an enhanced energy transfer from larger to smaller structures (Yang and Shy, 2005, Bosse *et al.*, 2006, Poelma and Ooms, 2006). This highlights that energy cascades can be investigated in a variety of measurements and that there is no clear consensus on whether the energy transfer is enhanced or decreased due to the presence of particles. Especially highly polydisperse flows with particles of different densities and geometry are little investigated, necessitating a detailed analysis for the case of dilute PDCs.

1.11.2 Turbulence Generation

At the beginning of the energy cascade is the so call energy-containing range, where the production/generation of turbulence takes place (Pope, 2000). The mechanisms for turbulence generation in PDCs constitute shear, buoyancy, particles, and the sedimentation of mesoscale particle clusters (Brosch, 2020, Lube *et al.*, 2020, Brosch *et al.*, 2021). Close to the no-slip boundary, the turbulence strength is assumed to approach zero, and a laminar/viscous sublayer forms (Cebeci, 2013). Assuming a turbulent open channel flow creating a "law of the wall" logarithmic velocity profile as used by Dellino *et al.* (2008a), mechanisms of shear-induced turbulence generation can be highlighted. Large-scale experimental results suggest that the vertical velocity distributions in pyroclastic density currents are similar to turbidity currents' velocity distributions (Brosch *et al.*, 2021, Cerminara *et al.*, 2021). For turbidity currents, an upper free shear boundary and a lower solid shear is assumed (Graf, 1984, Altinakar *et al.*, 1996, Cantero-Chinchilla *et al.*, 2015). Brosch *et al.* (2022) Cerminara *et al.* (2021)show the presence of large coherent turbulence structures and a separation of turbulence structures at the wall jet boundary, where shear is minimal. Studies by Salinas *et al.* (2021) also showed the separation at the wall jet boundary for submarine water particle flows.

Other turbulence generation mechanisms are buoyancy in the form of plumes rising and creating vortices, particles with high stokes numbers generating turbulent wakes, and mesoscale clusters (Brosch, 2020).

1.11.3 Particle-Gas Coupling

In gas-particle systems, three different flow regimes are defined by concentrations, the dilute regime (concentrations under 10^{-2}), the dense regime (concentrations over 0.3-0.4), and in-between those two the intermediate regime (Lube *et al.*, 2020) (shown in Figure 1.4).

One-way coupling assumes that particle motion is affected by the fluid motion the particle motion does not affect the fluid motion. In dilute regimes where one-way coupling is dominant, particles have a negligible influence on the turbulence due to very low particle volume fraction (Elghobashi, 1994).

During one-way coupling, the momentum of one particle $\vec{p}_P$ is only modified by gravitational $\vec{F}_G$ and viscous forces $\vec{F}_v$:

$$\frac{d\vec{p}_P}{dt} = \vec{F}_G + \vec{F}_v \,. \qquad \textit{EQN. 1-12}$$

Increasing the particle concentration, the regime of two-way coupling starts where the particle motion is modulated by the turbulence, and the turbulence is modulated by the presence of particles. Rarely, particle collisions act as another force ($\vec{F}_P$) on the particle momentum $\vec{p}_P$

$$\frac{d\vec{p}_P}{dt} = \vec{F}_G + \vec{F}_v + \vec{F}_P. \qquad \text{EQN. 1-13}$$

In dilute gas-particle flows, the dynamics are still dominated by viscous forces, as particle collisions rarely occur (Dufek, 2016).

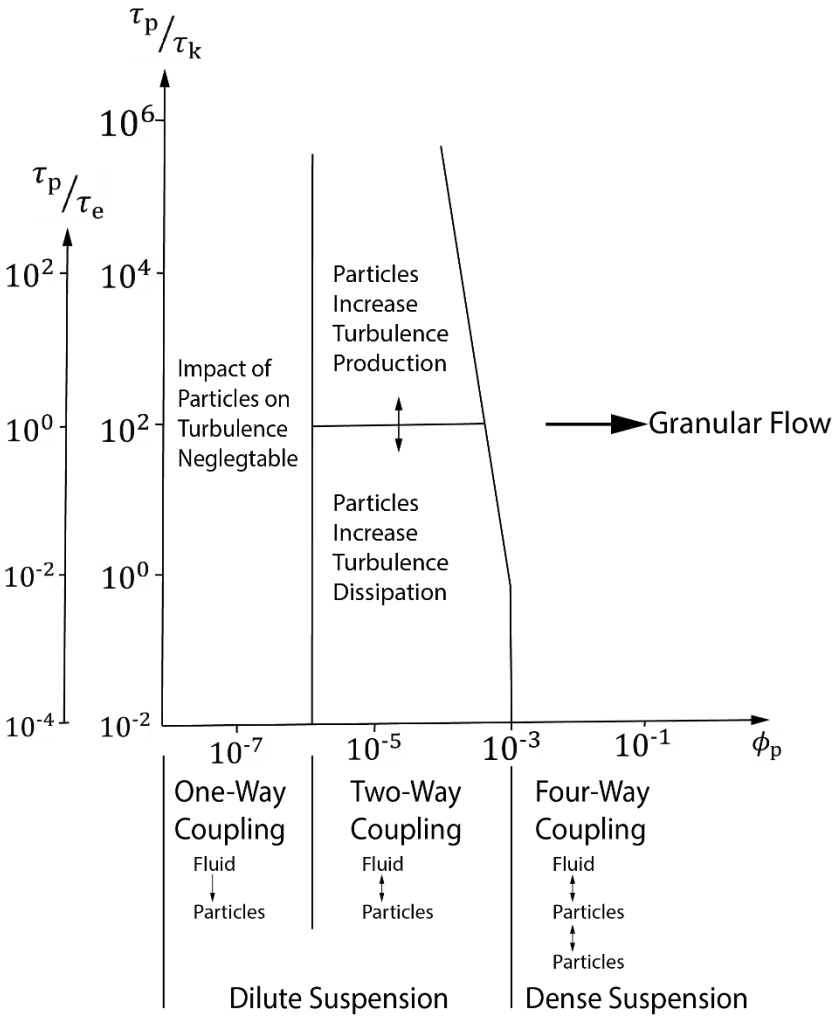

Figure 1-4 Different particle coupling regimes. ϕ_p ***is the particle volume fraction,*** τ_p ***paricle response time,*** τ_k ***Kolmogorow time scale, and*** τ_e ***the turnover time of the largest eddies.*** *Redrawn and modified from Elghobashi (1994).*

Depending on the particle properties, the influence of the particle on the turbulence changes if the particle response time τ_p is changed. Increasing τ_p the particle Reynolds number increases until it reaches a critical point where particles enhance the turbulence production by shedding vortexes in their wake (Figure 1-5). Lowering τ_p on the other side, increases the dissipation rate ε of turbulence energy (Elghobashi, 1994). All those models hold for monodisperse particle suspensions. The dependence of the particle volume fraction does not always hold. Balachandar (2009) gives a different model, where particle response times

separate one-way and two-way coupling. In highly polydisperse gas-particle suspensions with wide ranges of particle sizes from micrometer scales to centimeter scales, a wide range of particle Stokes numbers are present. This leads to different behaviors of different particles in the fluid flow. Therefore, even at low particle solid concentrations, two-way and four-way coupling can occur when considering polydisperse suspensions with varying particle densities (Brandt and Coletti, 2022).

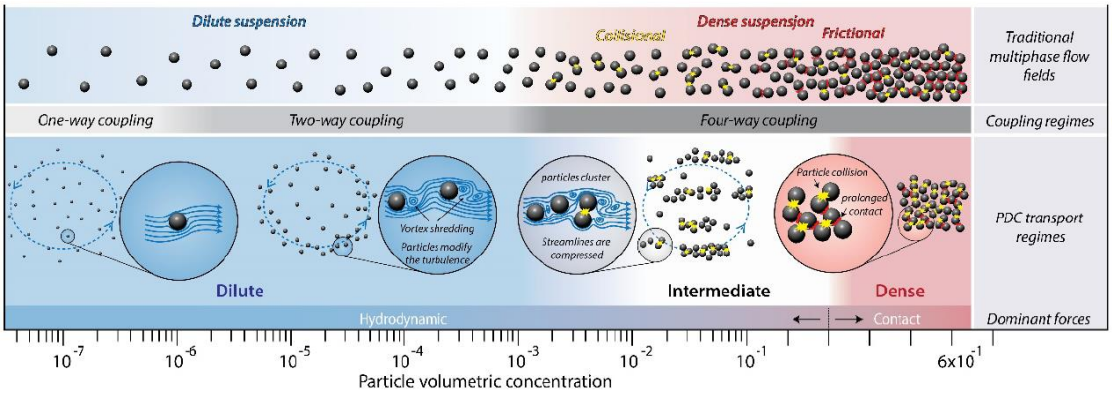

Figure 1-5 Different particle feedback regimes in PDCs. *The transition from dilute to dense particle interactions is shown. Figure modified from Lube et al. (2020).*

Even in isotropic turbulence, the particles are not homogeneously distributed (Maxey, 1987, Elghobashi and Truesdell, 1993, Balachandar and Eaton, 2010), but statistical properties of the flow are homogeneous in the whole flow. The behavior of particles in a turbulent carrier fluid can be described by the particle Stokes number comparing particle response times (τ_P) with characteristic time scales of the fluid motion, such as eddy turnover times (τ_E) (Burgisser and Bergantz, 2002)

$$St = \frac{\tau_P}{\tau_E} = f^{-1}\frac{\Delta\rho d^2 \Delta U}{18\mu\delta}. \qquad \textit{EQN. 1-14}$$

With f being the Stokes drag factor, $\Delta\rho$ the density difference between solid and gas phase, d the particle diameter, ΔU the eddy's rotational velocity, μ the dynamic viscosity, and δ the eddies diameter. The Stokes number quantitatively measures how well a particle is coupled to the ambient fluid, comparing the particle response times with fluid time scales. Particles with $St \ll 1$ couple well with the ambient fluid, for $St \sim 1$ particles start to decouple and move towards outer regions of eddies, for high particle Stokes numbers $St \gg 1$ particles decouple from the fluid motion. With the Froude number F_R (inertial forces divided by gravitational forces), the stability number is defined as the ratio of the Stokes and Froude numbers (Burgisser and Bergantz, 2002)

$$\Sigma_T = \frac{St}{{F_R}^2} = \frac{U_T}{\Delta U}. \qquad \textit{EQN. 1-15}$$

With U_T the particle settling velocity.

Using particle Stokes number and stability number, five gas-particle transport zones have been defined (Burgisser and Bergantz, 2002):

- The Fall ($\Sigma_T \gg 1$ and $St > 1$): Particles sediment ("fall") from eddies.
- The Unroll Zone ($\Sigma_T \sim 1$ and $St > 1$): Particles disconnect towards the margins of eddies.
- The Margins Zone ($\Sigma_T < 1$ and $St \sim 1$): Particles accumulate at the eddy's margins.
- The Turbulent Sedimentation Zone ($\Sigma_T \sim 1$ and $St < 1$): Turbulent structures impact the sedimentation of particles.
- The Homogenous Transport Zone ($\Sigma_T \ll 1$ and $St \ll 1$): Particles follow the fluid flow.

Large-scale experiments showed all those transport regimes to coexist in the same current (Breard and Lube, 2017, Brosch, 2020). This indicates that strong polydispersity and resulting wide ranges of transport regimes significantly impact the density stratification of dilute PDCs.

The intermediate flow regime has just recently moved into the focus of PDC research. It occurs at solids volumetric concentrations between 10^{-2} and 0.3, and one of its main characteristics is particle clustering, leading to heterogeneous particle distributions (Agrawal *et al.*, 2001, Fullmer and Hrenya, 2017). In large-scale PDC experiments, particle clustering occurred already at concentrations of $3 \cdot 10^{-3}$ (Lube *et al.*, 2020). The occurrence of particle clustering was shown through experimental work (Breard *et al.*, 2016, Weit *et al.*, 2019).

Thus far, three different processes have been proposed to cause this particle clustering in PDCs (Lube *et al.*, 2020):

- Collisions-Induced Clustering: Granular temperature is dissipated by friction, and inelastic collisions between particles occur (Goldhirsch and Zanetti, 1993, Garzó, 2005). (Agrawal *et al.*, 2001)
- Drag-Induced Clustering: The drag induced by a fluid medium decreases the particle's relative velocities leading to a clustering effect (Wylie and Koch, 2000).
- Wake-Induced Clustering: Particles cluster in the low-pressure zone behind a bigger particle (wake) (Kajishima and Takiguchi, 2002, Uhlmann and Doychev, 2014).

Clustering, often referred to as mesoscale clustering, has a strong influence on the particle settling in intermediate flow regimes (Agrawal *et al.*, 2001, Breard *et al.*, 2016, Breard and Lube, 2017, Weit *et al.*, 2019, Brosch, 2020). Breard *et al.* (2016) and Brosch (2020) observed settling velocities up to five times the expected terminal fall velocity in large-scale PDC experiments, creating regularly occurring sedimenting particle streaks.

Clusters also have been observed to create fluid turbulence (Capecelatro *et al.*, 2014). This observation is contrary to the assumption that turbulence is hindered by particles in more concentrated gas-particle suspensions (Lube *et al.*, 2020).

In general, the intermediate regime is poorly understood but highly important to the overall dynamics of PDCs, linking the dilute and the dense regime and majorly influencing the concentration distribution in the entire flow.

If the concentration increases further past solids volume fractions of 0.3-0.4, the dynamics of the gas-particle suspension becomes dominated by interparticle friction and collisions (Elghobashi, 1994, Chen, 2016, Breard and Lube, 2017). In the dense regime, a granular flow is created. As the dense bedload is very thin, most particles are suspended in the dilute part of dilute PDCs, as considered in this thesis. The dense regime is important only in terms of boundary conditions. The dense flow contrast dilute PDCs (Brosch *et al.*, 2021, Cerminara *et al.*, 2021) and basal slip boundary conditions are observed (Breard and Lube, 2017).

1.12 Pulsing in Gravity Currents

Brosch *et al.* (2021) showed strong pulsing in PDCs velocities (Figure 1-6) and densities to increase peak dynamic pressures by a factor of 3-5. The exact generation mechanism of these pulses is not yet understood, and two causes are currently discussed in the PDC community. 1) Large eddies focusing kinetic energy and 2) internal gravity waves traveling through the current.

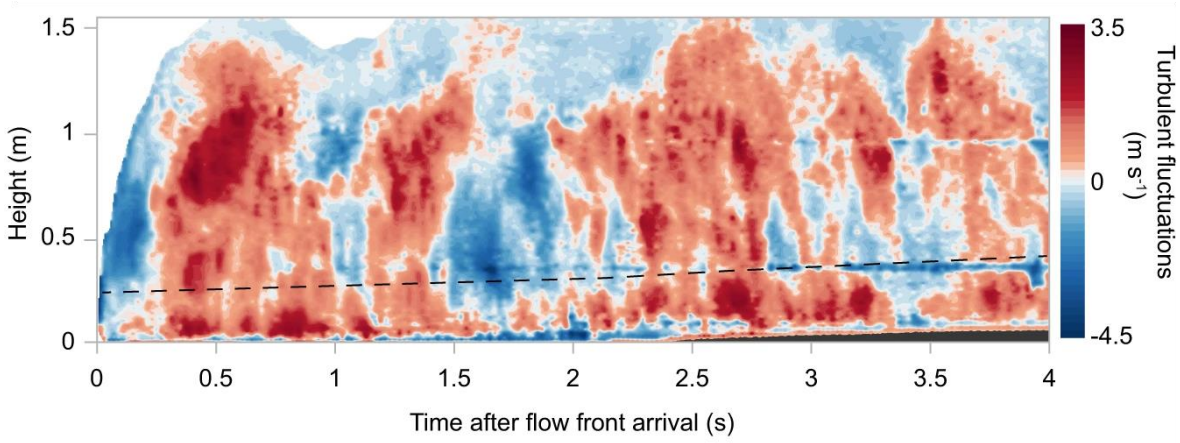

Figure 1-6 Turbulence fluctuations of the downstream velocity component u' measured in the PELE setup (Brosch et al., 2021). *Contour colors show strong velocity pulsing, the dashed line marks the wall jet boundary, and the grey surface shows the thickening deposit. Modified from Brosch et al. (2021).*

Velocity and concentration pulsing is also observed in continuous gravity/turbidity currents like rivers feeding into lakes (Best *et al.*, 2005, Kostaschuk *et al.*, 2018). This necessitates the pulses to be self-induced and no artifact of the feeding mechanism. Combining field measurements, laboratory experiments, and numerical models, Kostaschuk *et al.* (2018) link the occurrence of pulsing with Rayleigh-Taylor instabilities and Kelvin-Helmholtz instabilities leading to interfacial waves. A similar setting has been used by Marshall *et al.* (2021), the authors create a continuous gravity current, where they are able to analyze the dynamics of the pseudo steady body. A dynamic mode decomposition of their velocity data isolates "wave like structures" (Marshall *et al.*, 2021) within the body of the gravity current. Marshall *et al.* (2021) suggest these structures to be internal gravity waves after comparing them with the Brunt-Väisälä frequency. Matching the conclusions of Kostaschuk *et al.* (2018), Marshall *et al.* (2021) observe the waves also with a smooth substrate at the base of the gravity current. They interpret those must be instabilities in the upper interface, such as Kelvin-Helmholtz instabilities.

Having a strong indication that self-induced gravity waves are generated in continuous and constantly feed gravity currents, is the first indication, that the pulsing observed by Brosch *et al.* (2021) is caused by internal gravity waves. Stancanelli *et al.* (2018) and Musumeci Rosaria *et al.* (2017) generated gravity currents through a full-depth lock exchange while they mechanically induced surface waves on the side of the denser fluid. Through this approach, they can investigate the influence of waves on gravity current dynamics. They observe a velocity pulsing in the gravity current body region that corresponds to wave-induced orbital movement amplitudes. The same pulsation takes place in the flow front velocity. Both forms of pulsing are also observable in large-scale experiments in large-scale PDC experiments (Brosch *et al.*, 2021).

A different approach to lock exchange experiments by Ho *et al.* (2018) created gravity currents with multiple pulses by generating subsequent gravity currents with lock exchange experiments. The propagation of the second gravity current through the first one shows great similarity to the observations of Brosch *et al.* (2021). The second pulse travels at a higher velocity than the flow front, is marked by a strong color contrast in the shape of a flow front, and the flow front is accelerated when the pulse catches up to the front. In Brosch *et al.* (2021), the pulses traveling at higher velocities have the optical footprint of density discontinuities, and when the pulses catch up, the flow front shows a pulsing behavior. Walker *et al.* (1995) hypothesized that pyroclastic currents travel as a transient wave in line with all discussed causes for pulsing in gravity currents.

1.13 Research Opportunities

Dilute PDCs are perhaps one of the most complex types of natural multiphase flow. Despite strong advances in understanding through a combination of field, experimental, numerical,

and theoretical modeling approaches, important aspects of dilute PDC behavior remain enigmatic. The following outline of research opportunities is by no means comprehensive but informs the main objectives of the PhD research. Measurements of the vertical structure of velocity and concentration of experimental dilute PDCs are sparse and have only been performed at one observer location and for one substrate roughness (Brosch *et al.*, 2021). Previous studies have not focused on the vertical velocity component that must be strongly linked with particle settling, the vertical momentum transfer, and the generation of density stratification. Further investigations of the vertical structure of PDCs are needed to inform depth-averaged multilayered models (e.g., Doyle *et al.*, 2010, Kelfoun, 2017, Shimizu *et al.*, 2019). Derivation of an empirical function for the vertical velocity will help guide potential reevaluation of the definition of depth-averaged layers, which are currently split into the dense bedload and the suspended load (Shimizu *et al.*, 2017). Recent discoveries suggest that the definition of three layers, the dense bed load, the wall region, and the jet region, might be beneficial and able to increase the quality of depth-averaged models. Ultimately, this would lead to increased accuracy of flow models with a low computational cost that could be deployed for risk assessment globally. The vertical velocity component needs to be studied to achieve this. Also, the evolution of the vertical structure of dilute PDCs has to be tracked along the flow runout.

The effect of the basal roughness on the propagation of dilute gas-particle gravity currents has not been investigated yet. For sediment-laden gravity currents, I am aware of only one study by Kashefipour *et al.* (2017) investigating water particle currents. Systematic studies investigating the influence of naturally scaled roughness are needed.

The least investigated and least understood is the multiphase turbulence inside dilute PDCs. Dilute PDCs show high complexity due to a wide range of particle sizes, densities, and

resulting coupling regimes. These complexities are not approached by scientific communities looking at the coupling mechanisms and fluid dynamics of turbulent suspensions. Which usually look at idealized systems with very fine particles rather than gas-particle suspensions from air and highly polydisperse and irregularly shaped volcanic material. Though the PDC community has recognized the importance of turbulence and work by Burgisser and Bergantz (2002) already suggested models for turbulent gas-particle interactions. Models like this are not tested in situ experimentally or in the real world.

To date, the turbulent energy cascades in PDCs have not been systematically investigated, and it is mostly unknown how turbulent energy is transferred from large to small structures in PDCs. Also, focusing of energy has been previously shown by Brosch *et al.* (2021), but the exact mechanisms are not known. The energy transfer and focusing of energies is also an active field of research for more idealized systems, and so far, no clear consensus has been established (Brandt and Coletti, 2022). Successful measurements inside real-world or experimental PDCs have the potential to inform the wider scientific community working on PDCs, volcanic plumes, and general multiphase physics of turbulent suspensions. Therefore, developing measurement systems for experimental setups and real-world flows should be a key objective of volcanology.

This thesis presents a dataset derived from three large-scale experiments conducted over a variation of bed roughness from dynamically smooth to scales of the viscous sublayer. For this purpose, new and improved measurement setups expanded the PELE experimental setup, allowing to capture the spatial-temporal evolution and multiphase turbulence of dilute PDCs.

1.14 References

Agrawal, K., Loezos, P.N., Syamlal, M. & Sundaresan, S., 2001. The role of meso-scale structures in rapid gas–solid flows. *Journal of Fluid Mechanics,* 445**,** 151-185.

Altinakar, M.S., Graf, W.H. & Hopfinger, E.J., 1996. Flow structure in turbidity currents. *Journal of Hydraulic Research,* 34**,** 713-718.

Andrews, B.J., 2014. Dispersal and air entrainment in unconfined dilute pyroclastic density currents. *Bulletin of Volcanology,* 76**,** 852.

Andrews, B.J. & Manga, M., 2011. Effects of topography on pyroclastic density current runout and formation of coignimbrites. *Geology,* 39**,** 1099-1102.

Armanini, A., 2013. Granular flows driven by gravity. *Journal of Hydraulic Research,* 51**,** 111-120.

Auker, M.R., Sparks, R.S.J., Siebert, L., Crosweller, H.S. & Ewert, J., 2013. A statistical analysis of the global historical volcanic fatalities record. *Journal of Applied Volcanology,* 2**,** 2.

Balachandar, S., 2009. A scaling analysis for point–particle approaches to turbulent multiphase flows. *International Journal of Multiphase Flow,* 35**,** 801-810.

Balachandar, S. & Eaton, J.K., 2010. Turbulent Dispersed Multiphase Flow. *Annual Review of Fluid Mechanics,* 42**,** 111-133.

Banks, N.G. & Hoblitt, R.P., 1981. Summary Of Temperature Studies Of 1980 Deposits. *In* P.W. Lipman & D.R. Mullineaux (eds.) *The 1980 eruptions of Mount St. Helens, Washington.* Washington University Press: US Geological Survey Professional Paper, 1250, 295-313.

Batchelor, G.K. & Proudman, I., 1956. The large-scale structure of homogenous turbulence. *Philosophical Transactions of the Royal Society of London. Series A, Mathematical and Physical Sciences,* 248**,** 369-405.

Baxter, P.J., 1990. Medical effects of volcanic eruptions. *Bulletin of Volcanology*, 52**,** 532-544.

Baxter, P.J., Aspinall, W.P., Neri, A., Zuccaro, G., Spence, R.J.S., Cioni, R. & Woo, G., 2008. Emergency planning and mitigation at Vesuvius: A new evidence-based approach. *Journal of Volcanology and Geothermal Research,* 178**,** 454-473.

Baxter, P.J., Boyle, R., Cole, P., Neri, A., Spence, R. & Zuccaro, G., 2005. The impacts of pyroclastic surges on buildings at the eruption of the Soufriere Hills volcano, Montserrat. *Bulletin of Volcanology,* 67**,** 292-313.

Baxter, P.J. & Horwell, C.J., 2015. Chapter 60 - Impacts of Eruptions on Human Health. *In* H. Sigurdsson (ed.) *The Encyclopedia of Volcanoes (Second Edition).* Amsterdam: Academic Press, 1035-1047.

Baxter, P.J., Jenkins, S., Seswandhana, R., Komorowski, J.C., Dunn, K., Purser, D., Voight, B. & Shelley, I., 2017. Human survival in volcanic eruptions: Thermal injuries in pyroclastic surges, their causes, prognosis and emergency management. *Burns,* 43**,** 1051-1069.

Belousov, A., Voight, B. & Belousova, M., 2007. Directed blasts and blast-generated pyroclastic density currents: a comparison of the Bezymianny 1956, Mount St Helens 1980, and Soufrière Hills, Montserrat 1997 eruptions and deposits. *Bulletin of Volcanology,* 69**,** 701-740.

Best, J.L., Kostaschuk, R.A., Peakall, J., Villard, P.V. & Franklin, M., 2005. Whole flow field dynamics and velocity pulsing within natural sediment-laden underflows. *Geology,* 33**,** 765-768.

Bosse, T., Kleiser, L. & Meiburg, E., 2006. Small particles in homogeneous turbulence: Settling velocity enhancement by two-way coupling. *Physics of Fluids,* 18.

Brand, B.D., Pollock, N., Vallance, J.W., Ongaro, T.E., Roche, O., Trolese, M., Giordano, G., Marshall, A.A. & Criswell, C.W., 2023. Advances in our understanding of pyroclastic current behavior from the 1980 eruption sequence of Mount St. Helens volcano (Washington), USA. *Bulletin of Volcanology,* 85**,** 24.

Brandt, L. & Coletti, F., 2022. Particle-Laden Turbulence: Progress and Perspectives. *Annual Review of Fluid Mechanics,* 54**,** 159-189.

Branney, M.J. & Kokelaar, B.P., 2002. *Pyroclastic Density Currents and the Sedimentation of Ignimbrites*: Geological Society.

Breard, E.C.P., 2016. Dynamics of pyroclastic density currents. Massey University.

Breard, E.C.P., Dufek, J. & Lube, G., 2018. Enhanced Mobility in Concentrated Pyroclastic Density Currents: An Examination of a Self-Fluidization Mechanism. *Geophysical Research Letters,* 45**,** 654-664.

Breard, E.C.P. & Lube, G., 2017. Inside pyroclastic density currents – uncovering the enigmatic flow structure and transport behaviour in large-scale experiments. *Earth and Planetary Science Letters,* 458**,** 22-36.

Breard, E.C.P., Lube, G., Cronin, S.J. & Valentine, G.A., 2015. Transport and deposition processes of the hydrothermal blast of the 6 August 2012 Te Maari eruption, Mt. Tongariro. *Bulletin of Volcanology,* 77**,** 1-18.

Breard, E.C.P., Lube, G., Jones, J.R., Dufek, J., Cronin, S.J., Valentine, G.A. & Moebis, A., 2016. Coupling of turbulent and non-turbulent flow regimes within pyroclastic density currents. *Nature Geoscience,* 9**,** 767-771.

Brosch, E., 2020. Inside pyroclastic surges – a characterisation of the flow behaviour, hazard impact mechanisms and sedimentation processes through large-scale experiments: a thesis presented in partial fulfilment of the requirements for the

degree of Doctor of Philosophy in Earth Sciences at Massey University, Manawatū, Palmerston North, New Zealand. Doctoral. Massey University.

Brosch, E. & Lube, G., 2020. Spatiotemporal sediment transport and deposition processes in experimental dilute pyroclastic density currents. *Journal of Volcanology and Geothermal Research,* 401**,** 106946.

Brosch, E., Lube, G., Cerminara, M., Esposti-Ongaro, T., Breard, E.C.P., Dufek, J., Sovilla, B. & Fullard, L., 2021. Destructiveness of pyroclastic surges controlled by turbulent fluctuations. *Nature Communications,* 12**,** 7306.

Brosch, E., Lube, G., Esposti-Ongaro, T., Cerminara, M., Breard, E.C.P. & Meiburg, E., 2022. Characteristics and controls of the runout behaviour of non-Boussinesq particle-laden gravity currents – A large-scale experimental investigation of dilute pyroclastic density currents. *Journal of Volcanology and Geothermal Research,* 432**,** 107697.

Burgisser, A. & Bergantz, G.W., 2002. Reconciling pyroclastic flow and surge: the multiphase physics of pyroclastic density currents. *Earth and Planetary Science Letters,* 202**,** 405-418.

Burgisser, A., Bergantz, G.W. & Breidenthal, R.E., 2005. Addressing complexity in laboratory experiments: the scaling of dilute multiphase flows in magmatic systems. *Journal of Volcanology and Geothermal Research,* 141**,** 245-265.

Bursik, M.I. & Woods, A.W., 1996. The dynamics and thermodynamics of large ash flows. *Bulletin of Volcanology,* 58**,** 175-193.

Cantero-Chinchilla, F.N., Dey, S., Castro-Orgaz, O. & Ali, S.Z., 2015. Hydrodynamic analysis of fully developed turbidity currents over plane beds based on self-preserving velocity and concentration distributions. *Journal of Geophysical Research-Earth Surface,* 120**,** 2176-2199.

Capecelatro, J., Desjardins, O. & Fox, Rodney o., 2014. Numerical study of collisional particle dynamics in cluster-induced turbulence. *Journal of Fluid Mechanics,* 747**,** R2.

Cashman, K.V. & Sparks, R.S.J., 2013. How volcanoes work: A 25 year perspective. *GSA Bulletin,* 125**,** 664-690.

Cebeci, T., 2013. Chapter 4 - General Behavior of Turbulent Boundary Layers. *In* T. Cebeci (ed.) *Analysis of Turbulent Flows with Computer Programs (Third Edition).* Oxford: Butterworth-Heinemann, 89-153.

Cerminara, M., Brosch, E. & Lube, G., 2021. A theoretical framework and the experimental dataset for benchmarking numerical models of dilute pyroclastic density currents. *arXiv preprint arXiv:2106.14057.*

Cerminara, M., Esposti ongaro, T. & Berselli, L.C., 2016. ASHEE-1.0: a compressible, equilibrium–Eulerian model for volcanic ash plumes. *Geosci. Model Dev.,* 9**,** 697-730.

Cerminara M., B.E., Lube G., 2021. A theoretical framework and the experimental dataset for benchmarking numerical models of dilute pyroclastic density currents.

Chen, C., 2016. *Investigations on Mesoscale Structure in Gas–Solid Fluidization and Heterogeneous Drag Model*: Springer.

Choux, C., Druitt, T. & Thomas, N., 2004. Stratification and particle segregation in flowing polydisperse suspensions, with applications to the transport and sedimentation of pyroclastic density currents. *Journal of Volcanology and Geothermal Research,* 138**,** 223-241.

Choux, C.M. & Druitt, T.H., 2002. Analogue study of particle segregation in pyroclastic density currents, with implications for the emplacement mechanisms of large ignimbrites. *Sedimentology,* 49**,** 907-928.

Christiansen, R.L. & Peterson, D.W., 1981. Chronology of the 1980 eruptive activity. *US Geol. Surv. Prof. Pap,* 1250**,** 17-30.

Clarke, A.B. & Voight, B., 2000. Pyroclastic current dynamic pressure from aerodynamics of tree or pole blow-down. *Journal of Volcanology and Geothermal Research,* 100**,** 395-412.

Clarke, A.B., Voight, B., Neri, A. & Macedonio, G., 2002. Transient dynamics of vulcanian explosions and column collapse. *Nature,* 415**,** 897-901.

Corna, L., 2023. The interactions of pyroclastic density currents with obstacles : a large-scale experimental study : a thesis presented in partial fulfilment of the requirements for the degree of Doctor of Philosophy in Earth Sciences at Massey University, Manawatū, Palmerston North, New Zealand. Doctoral. Massey University.

Crowe, C., Schwarzkopf, J., Sommerfeld, M. & Tsuji, Y., 2012. *Multiphase Flows with Droplets and Particles* Boca Raton: CRC Press.

Dade, W.B. & Huppert, H.E., 1995. A Box Model for Non-Entraining, Suspension-Driven Gravity Surges on Horizontal Surfaces. *Sedimentology,* 42**,** 453-471.

Dade, W.B. & Huppert, H.E., 1996. Emplacement of the Taupo ignimbrite by a dilute turbulent flow. *Nature,* 381**,** 509-512.

Del Bello, E., Taddeucci, J., De' Michieli Vitturi, M., Scarlato, P., Andronico, D., Scollo, S., Kueppers, U. & Ricci, T., 2017. Effect of particle volume fraction on the settling velocity of volcanic ash particles: insights from joint experimental and numerical simulations. *Sci Rep,* 7**,** 39620.

Dellino, P., Buttner, R., Dioguardi, F., Doronzo, D.M., La Volpe, L., Mele, D., Sonder, I., Sulpizio, R. & Zimanowski, B., 2010a. Experimental evidence links volcanic

particle characteristics to pyroclastic flow hazard. *Earth and Planetary Science Letters,* 295**,** 314-320.

Dellino, P., Dioguardi, F., Doronzo, D.M. & Mele, D., 2019. The Entrainment Rate of Non-Boussinesq Hazardous Geophysical Gas-Particle Flows: An Experimental Model With Application to Pyroclastic Density Currents. *Geophysical Research Letters,* 46**,** 12851-12861.

Dellino, P., Dioguardi, F., Mele, D., D'addabbo, M., Zimanowski, B., Büttner, R., Doronzo, D.M., Sonder, I., Sulpizio, R., Dürig, T. & La Volpe, L., 2014. Volcanic jets, plumes, and collapsing fountains: evidence from large-scale experiments, with particular emphasis on the entrainment rate. *Bulletin of Volcanology,* 76**,** 834.

Dellino, P., Dioguardi, F., Zimanowski, B., Buttner, R., Mele, D., La Volpe, L., Sulpizio, R., Doronzo, D.M., Sonder, I., Bonasia, R., Calvari, S. & Marotta, E., 2010b. Conduit flow experiments help constraining the regime of explosive eruptions. *Journal of Geophysical Research-Solid Earth,* 115**,** B04204.

Dellino, P., Mele, D., Bonasia, R., Braia, G., La Volpe, L. & Sulpizio, R., 2005. The analysis of the influence of pumice shape on its terminal velocity. *Geophysical Research Letters,* 32**,** L21306.

Dellino, P., Mele, D., Sulpizio, R., La Volpe, L. & Braia, G., 2008a. A method for the calculation of the impact parameters of dilute pyroclastic density currents based on deposit particle characteristics. *Journal of Geophysical Research-Solid Earth,* 113**,** B07206.

Dellino, P., Zimanowski, B., Buttner, R., La Volpe, L., Mele, D. & Sulpizio, R., 2007. Large-scale experiments on the mechanics of pyroclastic flows: Design, engineering, and first results. *Journal of Geophysical Research-Solid Earth,* 112**,** B04202.

Dioguardi, F. & Dellino, P., 2014. PYFLOW: A computer code for the calculation of the impact parameters of Dilute Pyroclastic Density Currents (DPDC) based on field data. *Computers & Geosciences,* 66**,** 200-210.

Dioguardi, F. & Mele, D., 2018. PYFLOW_2.0: a computer program for calculating flow properties and impact parameters of past dilute pyroclastic density currents based on field data. *Bulletin of Volcanology,* 80**,** 28.

Dioguardi, F., Mele, D. & Dellino, P., 2018. A New One-Equation Model of Fluid Drag for Irregularly Shaped Particles Valid Over a Wide Range of Reynolds Number. *Journal of Geophysical Research: Solid Earth,* 123**,** 144-156.

Dobran, F., Neri, A. & Macedonio, G., 1993. Numerical-Simulation of Collapsing Volcanic Columns. *Journal of Geophysical Research-Solid Earth,* 98**,** 4231-4259.

Doronzo, D.M., De Tullio, M.D., Dellino, P. & Pascazio, G., 2011. Numerical simulation of pyroclastic density currents using locally refined Cartesian grids. *Computers & Fluids,* 44**,** 56-67.

Doronzo, D.M. & Dellino, P., 2011. Interaction between pyroclastic density currents and buildings: Numerical simulation and first experiments. *Earth and Planetary Science Letters,* 310**,** 286-292.

Doyle, E.E., Hogg, A.J., Mader, H.M. & Sparks, R.S.J., 2008. Modeling dense pyroclastic basal flows from collapsing columns. *Geophysical Research Letters,* 35.

Doyle, E.E., Hogg, A.J., Mader, H.M. & Sparks, R.S.J., 2010. A two-layer model for the evolution and propagation of dense and dilute regions of pyroclastic currents. *Journal of Volcanology and Geothermal Research,* 190**,** 365-378.

Druitt, T.H., 1992. Emplacement of the 18 May 1980 Lateral Blast Deposit ENE of Mount St-Helens, Washington. *Bulletin of Volcanology,* 54**,** 554-572.

Dufek, J., 2016. The Fluid Mechanics of Pyroclastic Density Currents. *Annual Review of Fluid Mechanics, Vol 48,* 48**,** 459-485.

Dufek, J. & Bergantz, G.W., 2007a. Dynamics and deposits generated by the Kos Plateau Tuff eruption: Controls of basal particle loss on pyroclastic flow transport. *Geochemistry Geophysics Geosystems,* 8.

Dufek, J. & Bergantz, G.W., 2007b. Suspended load and bed-load transport of particle-laden gravity currents: the role of particle–bed interaction. *Theoretical and Computational Fluid Dynamics,* 21**,** 119-145.

Dufek, J., Esposti Ongaro, T. & Roche, O., 2015. Pyroclastic Density Currents: Processes and Models. *In* H. Sigurdsson (ed.) *The Encyclopedia of Volcanoes.* Amsterdam: Academic Press, 617-629.

Dunkley, P.N. & Norton, G.E., 2002. *Mitigation of volcanic risk: prevention, preparedness, and emergency response planning*.

Elghobashi, S., 1994. On predicting particle-laden turbulent flows. *Applied Scientific Research,* 52**,** 309-329.

Elghobashi, S. & Truesdell, G.C., 1993. On the two-way interaction between homogeneous turbulence and dispersed solid particles. I: Turbulence modification. *Physics of Fluids A: Fluid Dynamics,* 5**,** 1790-1801.

Esposti Ongaro, T., Barsotti, S., Neri, A. & Salvetti, M.V., 2011a. Large-eddy simulation of pyroclastic density currents. *In* M.V. Salvetti, B. Geurts, J. Meyers & P. Sagaut (eds.) *Quality and Reliability of Large-Eddy Simulations II.* Dordrecht: Springer Netherlands, 161-170.

Esposti Ongaro, T., Cerminara, M., Charbonnier, S.J., Lube, G. & Valentine, G.A., 2020a. A framework for validation and benchmarking of pyroclastic current models. *Bulletin of Volcanology,* 82**,** 51.

Esposti Ongaro, T., Cerminara, M., Charbonnier, S.J., Lube, G. & Valentine, G.A., 2020b. A framework for validation and benchmarking of pyroclastic current models. *Bulletin of Volcanology*.

Esposti Ongaro, T., Widiwijayanti, C., Clarke, A.B., Voight, B. & Neri, A., 2011b. Multiphase-flow numerical modeling of the 18 May 1980 lateral blast at Mount St. Helens, USA. *Geology,* 39**,** 535-538.

Fauria, K.E., Manga, M. & Chamberlain, M., 2016. Effect of particle entrainment on the runout of pyroclastic density currents. *Journal of Geophysical Research-Solid Earth,* 121**,** 6445-6461.

Fisher, R.V., 1979. Models for Pyroclastic Surges and Pyroclastic Flows. *Journal of Volcanology and Geothermal Research,* 6**,** 305-318.

Fisher, R.V. & Waters, A.C., 1970. Base surge bed forms in maar volcanoes. *American Journal of Science,* 268**,** 157-180.

Fullmer, W.D. & Hrenya, C.M., 2017. The Clustering Instability in Rapid Granular and Gas-Solid Flows. *Annual Review of Fluid Mechanics,* 49**,** 485-510.

Garzó, V., 2005. Instabilities in a free granular fluid described by the Enskog equation. *Physical Review E,* 72**,** 021106.

George, W.K., Beuther, P.D. & Arndt, R.E., 1984. Pressure spectra in turbulent free shear flows. *Journal of Fluid Mechanics,* 148**,** 155-191.

Gidaspow, D., 1994. *Multiphase flow and fluidization: continuum and kinetic theory descriptions*: Academic press.

Glicken, H. & Nakamura, Y., Year. Restudy of the 1888 eruption of Bandai volcano, Japaned.^eds. *Proc Kagoshima Int Conf Volcanoes, Japan*, 392-395.

Goldhirsch, I., 2008. Introduction to granular temperature. *Powder Technology,* 182**,** 130-136.

Goldhirsch, I. & Zanetti, G., 1993. Clustering instability in dissipative gases. *Physical review letters,* 70**,** 1619.

Graf, W.H., 1984. *Hydraulics of sediment transport*: Water Resources Publication.

Ho, V.L., Dorrell, R.M., Keevil, G.M., Burns, A.D. & Mccaffrey, W.D., 2018. Pulse propagation in turbidity currents. *Sedimentology,* 65**,** 620-637.

Hort, M. & Scharff, L., 2016. Chapter 8 - Detection of Airborne Volcanic Ash Using Radar. *In* S. Mackie, K. Cashman, H. Ricketts, A. Rust & M. Watson (eds.) *Volcanic Ash.* Elsevier, 131-160.

Hort, M. & Seyfried, R., 1998. Volcanic eruption velocities measured with a micro radar. *Geophysical Research Letters,* 25**,** 113-116.

Hug, M., 1975. Mécanique des fluïdes appliquée. *Editions Eyrolles, Paris, F.*

Jenkins, S., Komorowski, J.C., Baxter, P.J., Spence, R., Picquout, A., Lavigne, F. & Surono, 2013. The Merapi 2010 eruption: An interdisciplinary impact assessment methodology for studying pyroclastic density current dynamics. *Journal of Volcanology and Geothermal Research,* 261**,** 316-329.

Kajishima, T. & Takiguchi, S., 2002. Interaction between particle clusters and particle-induced turbulence. *International Journal of Heat and Fluid Flow,* 23**,** 639-646.

Kashefipour, S.M., Daryaee, M. & Ghomeshi, M., 2017. Effect of bed roughness on velocity profile and water entrainment in a sedimentary density current. *Canadian Journal of Civil Engineering,* 45**,** 9-17.

Kelfoun, K., 2017. A two-layer depth-averaged model for both the dilute and the concentrated parts of pyroclastic currents. *Journal of Geophysical Research: Solid Earth,* 122**,** 4293-4311.

Kolmogorov, A.N., 1941. The local structure of turbulence in incompressible viscous fluid for very large Reynolds numbers. *Doklady Akademiia Nauk SSSR,* 30**,** 301-305.

Kostaschuk, R., Nasr-Azadani, M.M., Meiburg, E., Wei, T., Chen, Z., Negretti, M.E., Best, J., Peakall, J. & Parsons, D.R., 2018. On the Causes of Pulsing in Continuous Turbidity Currents. *Journal of Geophysical Research: Earth Surface,* 123**,** 2827-2843.

Lacroix, A., 1904. *La Montagne Pelée et ses éruptions* Paris: Masson.

Lerner, G.A., Jenkins, S.F., Charbonnier, S.J., Komorowski, J.-C. & Baxter, P.J., 2022. The hazards of unconfined pyroclastic density currents: A new synthesis and classification according to their deposits, dynamics, and thermal and impact characteristics. *Journal of Volcanology and Geothermal Research,* 421**,** 107429.

Loughlin, S.C., Calder, E.S., Clarke, A., Cole, P.D., Luckett, R., Mangan, M.T., Pyle, D.M., Sparks, R.S.J., Voight, B. & Watts, R.B., 2002. Pyroclastic flows and surges generated by the 25 June 1997 dome collapse, Soufrière Hills Volcano, Montserrat. *Geological Society, London, Memoirs,* 21**,** 191-209.

Lube, G., Breard, E.C.P., Cronin, S.J. & Jones, J., 2015. Synthesizing large-scale pyroclastic flows: Experimental design, scaling, and first results from PELE. *Journal of Geophysical Research-Solid Earth,* 120**,** 1487-1502.

Lube, G., Breard, E.C.P., Esposti-Ongaro, T., Dufek, J. & Brand, B., 2020. Multiphase flow behaviour and hazard prediction of pyroclastic density currents. *Nature Reviews Earth & Environment,* 1**,** 348-365.

Lube, G., Breard, E.C.P., Jones, J., Fullard, L., Dufek, J., Cronin, S.J. & Wang, T., 2019. Generation of air lubrication within pyroclastic density currents. *Nature Geoscience,* 12**,** 381-386.

Marshall, C.R., Dorrell, R.M., Keevil, G.M., Peakall, J. & Tobias, S.M., 2021. Observations of large-scale coherent structures in gravity currents: implications for flow dynamics. *Experiments in Fluids,* 62**,** 120.

Maxey, M.R., 1987. The gravitational settling of aerosol particles in homogeneous turbulence and random flow fields. *Journal of Fluid Mechanics,* 174**,** 441-465.

Mele, D., Dioguardi, F., Dellino, P., Isaia, R., Sulpizio, R. & Braia, G., 2015. Hazard of pyroclastic density currents at the Campi Flegrei Caldera (Southern Italy) as deduced from the combined use of facies architecture, physical modeling and statistics of the impact parameters. *Journal of Volcanology and Geothermal Research,* 299**,** 35-53.

Moore, J.G., 1967. Base surge in recent volcanic eruptions. *Bulletin Volcanologique,* 30**,** 337-363.

Moore, J.G. & Rice, C.J., 1984a. Chronology and character of the May 18, 1980, explosive eruptions of Mount St Helens. *explosive volcanism: inception, evolution, and hazards. National Academy, Washington***,** 133-142.

Moore, J.G. & Rice, C.J., 1984b. Chronology and character of the May 18, 1980, explosive eruptions of Mount St. Helens. *Explosive volcanism: inception, evolution, and hazards,* 10**,** 133-157.

Musser, J., Vaidheeswaran, A. & Clarke, M.A., 2021. MFIX Documentation Volume 3: Verification and Validation Manual; 3rd ed. NETL-PUB-22050; NETL Technical Report Series; U.S. Department of Energy, National Energy Technology Laboratory: Morgantown, WV.

Musumeci Rosaria, E., Viviano, A. & Foti, E., 2017. Influence of Regular Surface Waves on the Propagation of Gravity Currents: Experimental and Numerical Modeling. *Journal of Hydraulic Engineering,* 143**,** 04017022.

Nakada, S., 2000. Hazards from pyroclastic flows and surges. *Encyclopedia of Volcanoes***,** 945-956.

Neri, A., Ongaro, T.E., Macedonio, G. & Gidaspow, D., 2003. Multiparticle simulation of collapsing volcanic columns and pyroclastic flow. *Journal of Geophysical Research-Solid Earth,* 108**,** n/a-n/a.

Peterson, D.W. & Tilling, R.I., 2000. Lava Flow Hazards. *In* H. Sigurdsson (ed.) *The Encyclopedia of Volcanoes.* Amsterdam: Academic Press, 957-971.

Poelma, C. & Ooms, G., 2006. Particle-Turbulence Interaction in a Homogeneous, Isotropic Turbulent Suspension. *Applied Mechanics Reviews,* 59**,** 78-90.

Pope, S.B., 2000. *Turbulent Flows* Cambridge: Cambridge University Press.

Prandtl, L., 1905. Uber Flussigkeitsbewegung bei sehr kleiner Reibung. *Verhandl. 3rd Int. Math. Kongr. Heidelberg (1904), Leipzig*.

Richardson, L.F., 1922. Weather prediction by numerical process. *Quarterly Journal of the Royal Meteorological Society,* 48**,** 282-284.

Ripepe, M., De Angelis, S., Lacanna, G., Poggi, P., Williams, C., Marchetti, E., Donne, D.D. & Ulivieri, G., 2009. Tracking Pyroclastic Flows at Soufrière Hills Volcano. *Eos, Transactions American Geophysical Union,* 90**,** 229-230.

Roche, O., Phillips, J.C., Kelfoun, K., Fagents, S.A., Gregg, T.K.P. & Lopes, R.M.C., 2013. Pyroclastic density currents. *In* R.M.C. Lopes, S.A. Fagents & T.K.P. Gregg (eds.) *Modeling Volcanic Processes.* Cambridge: Cambridge University Press, 203-229.

Rosi, M., Principe, C. & Vecci, R., 1993. The 1631 Vesuvius eruption. A reconstruction based on historical and stratigraphical data. *Journal of Volcanology and Geothermal Research,* 58**,** 151-182.

Salinas, J.S., Balachandar, S., Shringarpure, M., Fedele, J., Hoyal, D., Zuñiga, S. & Cantero, M.I., 2021. Anatomy of subcritical submarine flows with a lutocline and an intermediate destruction layer. *Nature Communications,* 12**,** 1649.

Scharff, L., 2012. Eruption Dynamics of Vulcanian and Sub-Plinian Volcanoes: From the Generation of Pulses to the Formation of Clouds. Staats-und Universitätsbibliothek Hamburg Carl von Ossietzky.

Scharff, L., Hort, M. & Varley, N.R., 2019. First in-situ observation of a moving natural pyroclastic density current using Doppler radar. *Scientific Reports,* 9**,** 7386.

Scolamacchia, T. & Schouwenaars, R., 2009. High-speed impacts by ash particles in the 1982 eruption of El Chichón, Mexico. *Journal of Geophysical Research: Solid Earth,* 114.

Self, S. & Rampino, M.R., 1981. The 1883 eruption of Krakatau. *Nature,* 294**,** 699-704.

Shimizu, H.A., Koyaguchi, T. & Suzuki, Y.J., 2017. A numerical shallow-water model for gravity currents for a wide range of density differences. *Progress in Earth and Planetary Science,* 4**,** 8.

Shimizu, H.A., Koyaguchi, T. & Suzuki, Y.J., 2019. The run-out distance of large-scale pyroclastic density currents: A two-layer depth-averaged model. *Journal of Volcanology and Geothermal Research*.

Shimizu, H.A., Koyaguchi, T., Suzuki, Y.J., Brosch, E., Lube, G. & Cerminara, M., 2021. Validation of a two-layer depth-averaged model by comparison with an experimental dilute stratified pyroclastic density current. *Bulletin of Volcanology,* 83**,** 73.

Sigurdsson, H., Carey, S.N. & Fisher, R.V., 1987. The 1982 eruptions of El Chichon volcano, Mexico (3): Physical properties of pyroclastic surges. *Bulletin of Volcanology,* 49**,** 467-488.

Sparks, R.S.J., 1976. Grain size variations in ignimbrites and implications for the transport of pyroclastic flows. *Sedimentology,* 23**,** 147-188.

Sparks, R.S.J. & Aspinall, W.P., 2004. Volcanic Activity: Frontiers and Challenges in Forecasting, Prediction and Risk Assessment. *The State of the Planet: Frontiers and Challenges in Geophysics***,** 359-373.

Sparks, R.S.J., Barclay, J., Calder, E.S., Herd, R.A., Komorowski, J.-C., Luckett, R., Norton, G.E., Ritchie, L.J., Voight, B. & Woods, A.W., 2002. Generation of a debris avalanche and violent pyroclastic density current on 26 December (Boxing Day) 1997 at Soufrière Hills Volcano, Montserrat. *Geological Society, London, Memoirs,* 21**,** 409-434.

Sparks, R.S.J., Bonnecaze, R.T., Huppert, H.E., Lister, J.R., Hallworth, M.A., Mader, H. & Phillips, J., 1993. Sediment-Laden Gravity Currents with Reversing Buoyancy. *Earth and Planetary Science Letters,* 114**,** 243-257.

Sparks, R.S.J., Wilson, L. & Hulme, G., 1978. Theoretical modeling of the generation, movement, and emplacement of pyroclastic flows by column collapse. *Journal of Geophysical Research: Solid Earth,* 83**,** 1727-1739.

Spence, R.J.S., Baxter, P.J. & Zuccaro, G., 2004a. Building vulnerability and human casualty estimation for a pyroclastic flow: a model and its application to Vesuvius. *Journal of Volcanology and Geothermal Research,* 133**,** 321-343.

Spence, R.J.S., Zuccaro, G., Petrazzuoli, S. & Baxter, P.J., 2004b. Resistance of Buildings to Pyroclastic Flows: Analytical and Experimental Studies and Their Application to Vesuvius. *Natural Hazards Review,* 5**,** 48-59.

Stancanelli, L.M., Musumeci, R.E. & Foti, E., 2018. Dynamics of Gravity Currents in the Presence of Surface Waves. *Journal of Geophysical Research: Oceans,* 123**,** 2254-2273.

Sulpizio, R., Dellino, P., Doronzo , D.M. & Sarocchi, D., 2014. Pyroclastic density currents: state of the art and perspectives. *Journal of Volcanology and Geothermal Research,* 283**,** 36-65.

Sutawidjaja, I.S., 2013. Directed Volcanic Blast as a Tragedy of October 26th, 2010 at Merapi Volcano, Central Java. *Indonesian Journal on Geoscience,* 8**,** 135-141.

Sweeney, M.R. & Valentine, G.A., 2017. Impact zone dynamics of dilute mono- and polydisperse jets and their implications for the initial conditions of pyroclastic density currents. *Physics of Fluids,* 29**,** 093304.

Trolese, M., Cerminara, M., Esposti Ongaro, T. & Giordano, G., 2019. The footprint of column collapse regimes on pyroclastic flow temperatures and plume heights. *Nature Communications,* 10**,** 2476.

Uhlmann, M. & Doychev, T., 2014. Sedimentation of a dilute suspension of rigid spheres at intermediate Galileo numbers: the effect of clustering upon the particle motion. *Journal of fluid mechanics,* 752**,** 310-348.

Valentine, G. & Fisher, R., 2000. Pyroclastic surges and blasts. *Encyclopedia of Volcanoes***,** 571-580.

Valentine, G.A., 1987. Stratified flow in pyroclastic surges. *Bulletin of Volcanology,* 49**,** 616-630.

Valentine, G.A., 1998. Damage to structures by pyroclastic flows and surges, inferred from nuclear weapons effects. *Journal of Volcanology and Geothermal Research,* 87**,** 117-140.

Valentine, G.A. & Sweeney, M.R., 2018. Compressible Flow Phenomena at Inception of Lateral Density Currents Fed by Collapsing Gas-Particle Mixtures. *Journal of Geophysical Research: Solid Earth,* 123**,** 1286-1302.

Voege, M., Hort, M. & Seyfried, R., 2005. Monitoring volcano eruptions and lava domes with Doppler radar. *Eos, Transactions American Geophysical Union,* 86**,** 537-541.

Walker, G.P.L., Hayashi, J.N. & Self, S., 1995. Travel of Pyroclastic Flows as Transient Waves - Implications for the Energy Line Concept and Particle-Concentration Assessment. *Journal of Volcanology and Geothermal Research,* 66**,** 265-282.

Wang, J., Wan, M., Chen, S., Xie, C., Wang, L.-P. & Chen, S., 2019. Cascades of temperature and entropy fluctuations in compressible turbulence. *Journal of Fluid Mechanics,* 867**,** 195-215.

Waters, A.C. & Fisher, R.V., 1971. Base Surges and Their Deposits: Capelinhos and Taal Volcanoes. *Journal of Geophysical Research,* 76**,** 5596-5614.

Watson, L.M., Cannata, A. & Andronico, D., 2023. Tracking a Pyroclastic Density Current With Seismic Signals at Mt. Etna (Italy). *Journal of Geophysical Research: Solid Earth,* 128**,** e2022JB026114.

Weit, A., Roche, O., Dubois, T. & Manga, M., 2018. Experimental Measurement of the Solid Particle Concentration in Geophysical Turbulent Gas-Particle Mixtures. *Journal of Geophysical Research-Solid Earth,* 123**,** 3747-3761.

Weit, A., Roche, O., Dubois, T. & Manga, M., 2019. Maximum Solid Phase Concentration in Geophysical Turbulent Gas-Particle Flows: Insights From Laboratory Experiments. *Geophysical Research Letters,* 46**,** 6388-6396.

Wilson, C.J.N., 1980. The role of fluidization in the emplacement of pyroclastic flows: An experimental approach. *Journal of Volcanology and Geothermal Research,* 8**,** 231-249.

Wohletz, K., 2001. Pyroclastic surges and compressible two-phase flow. *From magma to tephra*.

Woods, A.W. & Bursik, M.I., 1994. A Laboratory Study of Ash Flows. *Journal of Geophysical Research-Solid Earth,* 99**,** 4375-4394.

Wylie, J.J. & Koch, D.L., 2000. Particle clustering due to hydrodynamic interactions. *Physics of Fluids,* 12**,** 964-970.

Yamamoto, T., Nakamura, Y. & Glicken, H., 1999. Pyroclastic density current from the 1888 phreatic eruption of Bandai volcano, NE Japan. *Journal of Volcanology and Geothermal Research,* 90**,** 191-207.

Yamamoto, T., Takarada, S. & Suto, S., 1993. Pyroclastic flows from the 1991 eruption of Unzen volcano, Japan. *Bulletin of Volcanology,* 55**,** 166-175.

Yang, T.S. & Shy, S.S., 2005. Two-way interaction between solid particles and homogeneous air turbulence: particle settling rate and turbulence modification measurements. *Journal of Fluid Mechanics,* 526**,** 171-216.

2 Methods

This chapter introduces the PELE setup, describes expansions made as part of this PhD project, and the experimental series conducted. Further existing and new algorithms for the analysis of data are explained.

2.1 Large-Scale Experiments

Pyroclastic density currents (PDCs) are too dangerous, destructive, and unpredictable in their occurrence to be systematically studied in the real world. Only a few unplanned measurements of real-world pyroclastic density currents exist (Brosch et al., 2021; Scharff et al., 2019). These incidental measurements hold valuable information about real-world PDCs but are insufficient for a detailed analysis of the complex internal dynamics. Therefore, large-scale experiments are the strongest tool for obtaining in-situ measurements inside pyroclastic density currents. The Pyroclastic flow Eruption Large-scale Experiment "PELE" (Lube et al., 2015) used in this study is located in an old boiler house (length 25 m, width 18 m, height 16 m) Massey University situated on the Manawatu campus is the largest of these large scale PDC experiments.

The construction of PELE began in 2013 and was initially only designed to investigate dense pyroclastic flows. Later, PELE was expanded to generate all PDC endmembers, from dense granular pyroclastic flows to fully dilute, fully turbulent pyroclastic surges (Brosch, 2020). This enables PELE to produce PDCs with up to 4 t of natural volcanic material that can be heated to temperatures up to 400°C. The generated flows reach velocities up to $30\ \mathrm{m \cdot s^{-1}}$, with flow heights of $2 - 4.5$ m. The runout distance is limited to 33.5 m by a natural cliff.

In the presented research, only dilute pyroclastic density currents were synthesized. The specifics of setup components exclusively used to synthesize dense PDCs are left out in the further description of the setup but can be found in Lube et al. (2015) and Breard (2016).

The channeled experimental setup and the ability to look and measure inside synthetic pyroclastic density currents distinguished PELE from other large-scale experiments using natural volcanic material to create column collapse PDCs in Italy by Dellino et al. (2007).

The conditions of PELE provide a controlled environment to systematically synthesize and investigate pyroclastic density currents with changing conditions (e.g., flow density, temperature, and terrain). Therefore, PELE is a strong tool to drive the understanding of the internal workings of PDCs. Firstly, this includes the characterization of transport and sedimentation processes inside pyroclastic density currents, providing knowledge on how to interpret natural deposits. Secondly, PELE provides Benchmark datasets to test and improve numerical and hazard models (Cerminara et al., 2021; Esposti Ongaro et al., 2020). Thirdly, the dynamics of highly polydisperse multiphase flows and associated gas-particle interactions and coupling and how variations of the flow's initial conditions (e.g., the surface roughness, the used volcanic material, the flow temperature, and discharge rates) affect the flow behavior of generated PDCs.

2.2 The PELE Setup

PELE's working principle is to discharge volcanic material from the hopper into an instrumented channel, which, on impact creates PDCs. PELE experimental setup can be divided into five main structural and functional components (see Figure 2.1):

1. **Tower:** A 13m high metal tower with a 3x3 m base, capable of holding two different hopper sizes with different mass discharge rates. A lifting system allows for both vertical and horizontal positioning of the hoppers.
2. **Hopper:** The small hopper with a total volume of approximately 0.7 m^3 to accommodate and heat the ash mixture and synthesize dilute pyroclastic density currents is used in the presented experiments. The hopper includes a heating system composed of three u-shaped 800 W heating elements to heat the mixture to the desired temperature with a total power of 24 kW. Further, the hopper is insulated with rock wool to achieve minimal heat loss and ensuring an evenly heated ash mixture. Nine metal bars at the outlet of the hopper control the discharge, ensuring realistic conditions. The hopper weight and discharge of material are monitored using four loadcells during experimental runs.
3. **Shrouding:** A column built by a shroud made from heat and fire-resistant tarpaulin channels the hot ash mixture into the channel.
4. **Channel:** The channel is an approximately 14.6 m long and 50 cm wide ramp underneath the hopper opening. For all analysis, 0 m is defined as the position where the planar runout begins after the initially curved slope underneath the hopper. The channel is confined by two side walls, one steel wall and a glass wall enabling a view inside the generated PDCs. The steel side accommodates various sensors to obtain in-situ measurements inside PDCs. Vertical arrays of Piezoelectric pressure sensors (PCB PIEZOTRONICS 106B51) are installed in wing-shaped structures in the center of the channel. Those side walls' height is initially 180 cm (between 0 m and 6.4 m). Between 6.4 and 10.6 m, the side walls have a height of 120 cm. In this interval (from 0 m to 10.6 m), the channel is inclined by 6°. From 10.6 up to 11.7 m, the channel is not inclined, and the height of the side walls decreases further to 60 cm.

5. **Runout:** After the last section of the channel (11.7 m from impact), the horizontal runout begins. The initial runout is confined by 60 cm high glass walls, which end at a runout distance of 14.6 m. Here the generated pyroclastic current can spread laterally during propagation over a concrete surface. The unconfined runout holds Piezoelectric pressure sensors, temperature sensors, and vertical arrays of passive sediment samplers. The unconfined runout ends at 33.5 m m from impact at a several meters high cliff.

For details on the initial setup and updated setup, the reader is referred to Lube et al. (2015), Breard (2016), and Brosch (2020).

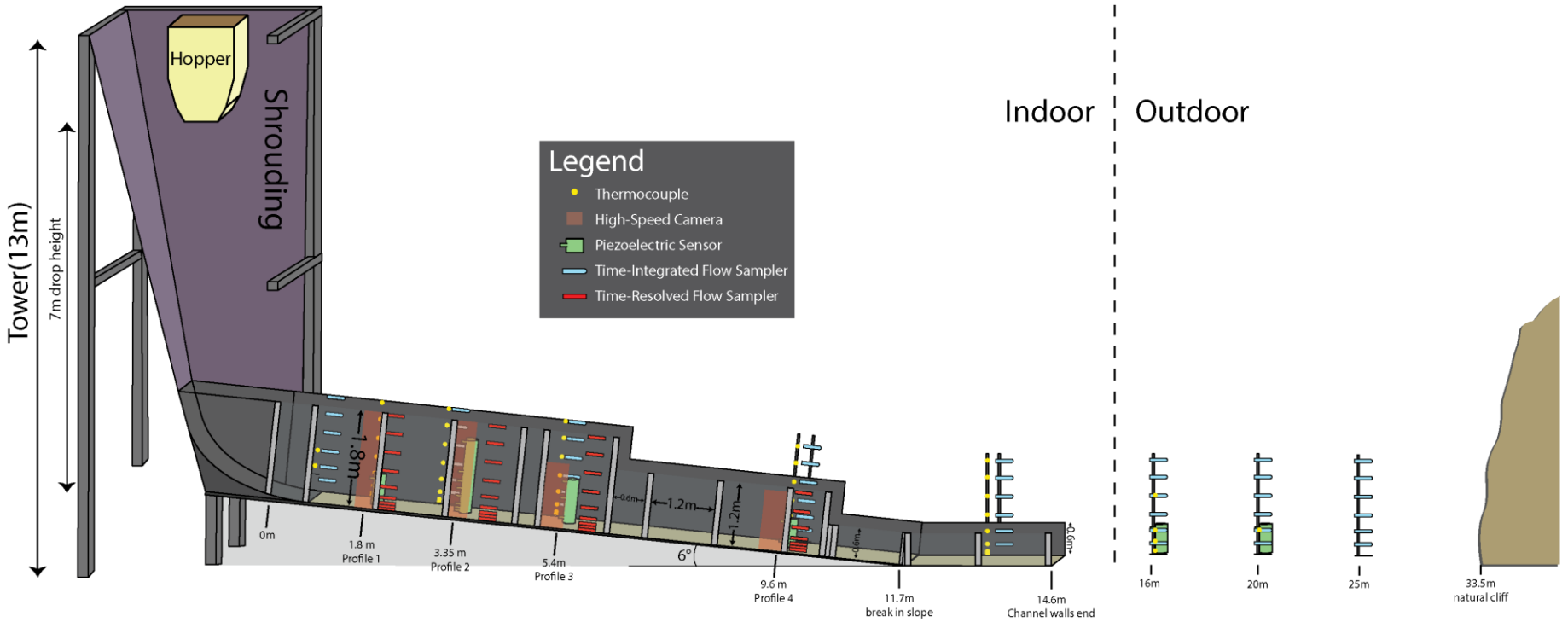

Figure 2.1 Sketch of the PELE large-scale experiment setup. *The 13* m *high tower holds a hopper with a volume of 0.7* m^3 *to hold and discharge the volcanic material into the channel. The material drops 7* m *and impacts at the 0* m *runout. The first 14.9* m *of flow propagation is channeled by a glass wall on one side and a steel wall on the other side, where different sensors are installed, and high-speed videos of the passing flow are recorded. Between 0* m *and 14.6* m*, the channel height is subsequently decreased. The confined runout ends at 14.6* m*. Shortly after the start of the unconfined runout, the flow exits the old boiler house. The propagation ends in a buoyant lift-off of the flow or with a collision with a natural cliff at 33.5* m*. Figure modified from Ardo (2022).*

2.3 Experimental Series

This PhD thesis and the M.Sc. thesis of James Ardo (Ardo, 2022) present experimental results investigating the substrate roughness's influence on the flow propagation, sedimentation, and turbulence structure inside pyroclastic density currents. All experiments were timed in a way that ensured the same weather conditions, including ambient temperature, humidity, and very low wind speeds. In this study, the following initial and boundary conditions are used, which are also summarized in Table 2-1:

- **Mass:** The mass of ash used in an experiment determines the initial potential energy contained in the system before discharge. Through energy conservation, this directly also impacts the flow of kinetic energy. The experimental material's mass also influences the PDC's duration and particle concentration and is kept constant at 125 kg for the experimental series.
- **Temperature:** The temperature of the volcanic material can be varied between 30°C and 400°C. This will strongly influence the dynamics and the buoyancy of generated PDCs.
- **Particle Phase:** The particle phase used in the experimental series is natural volcanic material with grain sizes varying from $2\ \mu m\ -\ 16\ mm\ (-4\ -\ 9\ \phi)$, a fines content of 20 wt%, and a median grain size of $245\ \mu m\ (2\ \phi)$.
- **Terrain:** When varying terrain, we can alter the bed roughness, as well as insert topographic obstacles such as hills, houses, or any other structure. The experimental series focuses on the influence of bed roughness on the propagation of pyroclastic density currents, which was varied in logarithmic steps. The roughest surface used was composed of $4\ -\ 8\ mm$ river pebbles. The intermediate roughness used was

skateboard grip tape equivalent to a P80 grid sandpaper (≈ 201 µm). The smoothest roughness used was dynamically smooth medium density fiber (MDF) boards, with roughness less than the ambient dust.

- **Hopper Height:** Variations of hopper height and with those variations of the drop height, as well as initial potential energy, determine the impact velocity. Adjusting the hopper height allows the synthesis of different source conditions of volcanic eruptions. The current setup of PELE is fixed to 7 m, and with that, an impact velocity of $7\ \mathrm{m} \cdot \mathrm{s}^{-1}$.
- **Channel Geometry:** The adjustable channel inclination and width are kept constant at $6°$ ($\approx 10.5\%$) and 0.5 m.

All initial conditions, besides the systematically varied bed roughness, are kept constant to systematically analyze the influence of the bed roughness on the flow behavior, the turbulence generation and the buoyancy. The main conditions of the experimental series are summarized in Table 2-1.

Table 2-1 Initial and boundary conditions of the experimental series

Parameter	**Rough Exp.**	**Intermediate Exp.**	**Smooth Exp.**
Mass	125 kg	125 kg	125 kg
Temperature	120°C	120°C	120°C
Bed Roughness	$4 - 8$ mm	≈ 201 µm	Hydraulically smooth
Hopper Height	7 m	7 m	7 m
Channel Width	50 cm	50 cm	50 cm
Channel Inclination	6°	6°	6°
Ambient Temperature	15°C	15°C	15°C

The roughness range was chosen as it represents a broad range of roughness with logarithmic

changes between them, a finer discretization. With that, more experiments were not feasible with the current experimental setup of PELE. In addition to these experiments, five large-scale experiments were conducted to test sensors and camera setups. In this thesis, these additional experiments will not be further focused on; all analyses will be performed on the main experimental series.

2.4 Properties of the Pyroclastic Material

The natural volcanic material used in the presented experimental series matches the experimental material used by Brosch (2020) and is composed of two well-studied 232 AD Taupo ignimbrite deposits (Wilson, 1985). The particle sizes are characterized using the ϕ grain-size scale defined as:

$$\phi = -\log_2 \frac{d}{d_0} \qquad \textit{EQN. 2-1}$$

with d being the particle diameter and d_0 being the reference diameter (1 mm).

The first component, referred to as Surge 2, is located 19 km north-east of the vent, on the side of the Thermal Explorer Highway ($38°43'8.9"S\ 176°9'56.31"E$). The Surge 2 deposit has an unimodal distribution with the primary mode at $2\ \phi$, a median grain size of 1.6 ϕ, and a fines content (particles smaller 4.5 ϕ) of 3.7 wt%, see grain size distribution Figure 2.2. The second component of the experimental mixture, referred to as Hatepe, was sampled 7 km south-east of the vent and 2 km east of Hatepe ($38°51'27.9"S\ 176°2'11.3"E$). This deposit has a polymodal grainsize distribution (see Figure 2.2) with modes at 2 ϕ, 4 ϕ, and 6.5 ϕ. Hatepe has a median grain size of 3.6 ϕ and a fines content of approx. 36.5 wt%. Upon sampling, both deposits were cleaned of organic material and sieved to grain sizes smaller than $-4\ \phi$ (16 mm). Upon arrival in the lab, all sampled material is dried in ovens

at 100°C for a minimum of 3 days to eliminate all moisture for storage and the mixing of the final experimental material.

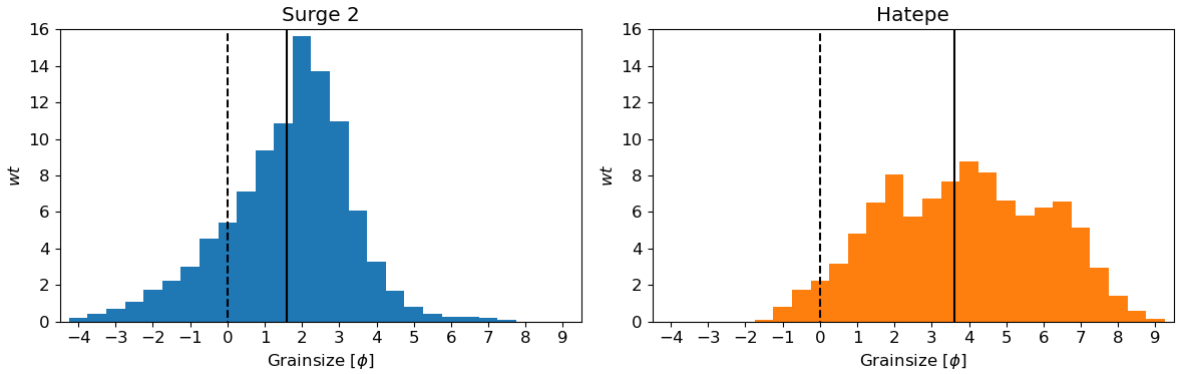

Figure 2.2 Properties of the sampled volcanic deposits. *On the left is the grain size distribution of the Surge 2 deposit. The solid vertical line shows the median grain size of* 1.6 ϕ *(solid vertical line). The right provides the grain size distribution for the Hatepe deposit, with a median grain size of* 3.6 ϕ *(solid vertical line). The vertical dashed lines both mark* 0 ϕ.

The experimental mixture consists of 60 wt% Surge 2 and 40 wt% Hatepe. This provides the experimental blend presented in Figure 2.3. The final experimental blend has a bimodal distribution with modes at $2\,\phi$ and $6.5\,\phi$, a median grainsize of $2\,\phi$ (245 µm), and a grainsize range from $-4\,\phi$ to $9\,\phi$ (2 µm to 16 mm). The average solid densities as a function of grain size measured by heavy liquids separation are shown in Figure 2.3. It is important to note that this does not represent the maximum and minimum densities for each grain size and only the averages per grain size. The mixture is composed of quartz, feldspars, titanomagnetite crystals, lithics, glassy vesicular pumice, and ash. Some of the singular clasts reach over 2700 kg/m^3 in our experimental mixture.

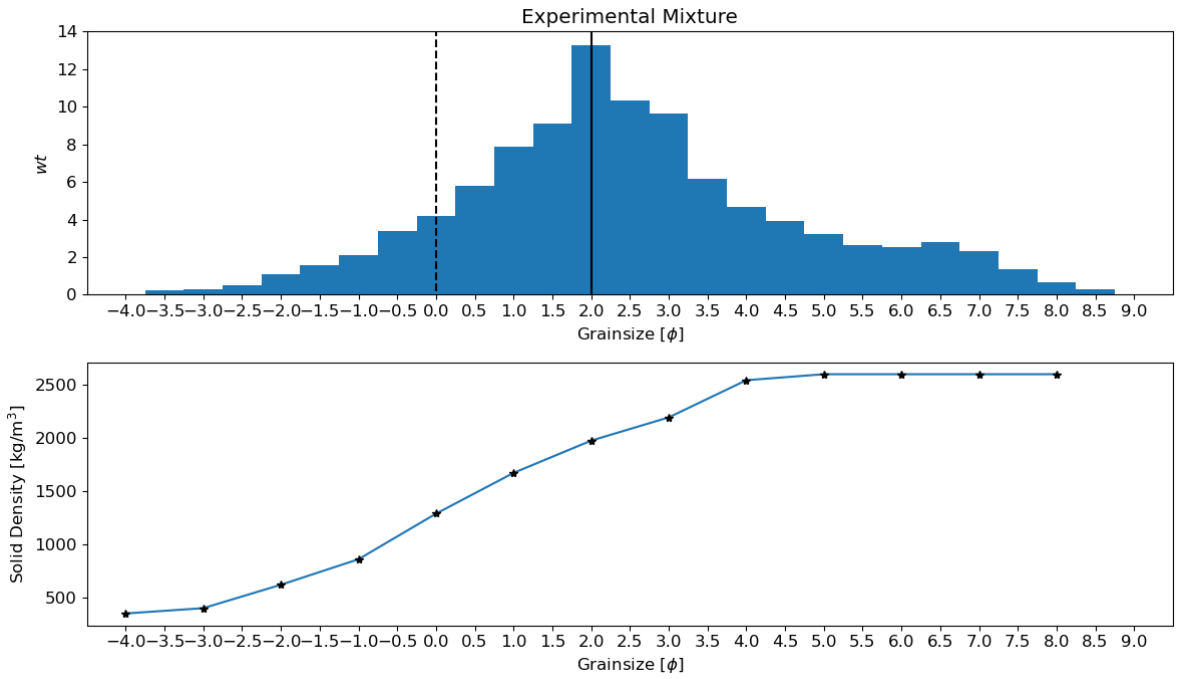

Figure 2.3 Properties of the experimental mixture. *On top the grain size distribution of the experimental material is presented. The solid vertical line shows the median grain size of* 2 ϕ *and the vertical dashed line is* 0 ϕ*. The base shows how the average particle density changes with particle diameter. The black stars show measurements from heavy liquid separation, and the blue lines are linear interpolations between the measurements.*

2.5 Scaling in PELE

In fluid dynamic experiments, dimensionless numbers assure dynamic similarity to the synthesized process. The dimensionless analysis includes fluid dynamic and thermodynamic scaling to show that the synthesized PDCs are dynamically similar to real-world PDCs. Previous extensive experimental series and scaling analyses have shown PELE to scale natural PDCs adequately for the whole scale of end members and the whole runout and to deliver reproducible results (Breard, 2016; Brosch, 2020); results of the scaling analysis are summarized in Table 2-2.

Table 2-2 Relevant dimensionless numbers, and flow properties, for PELE and natural, dilute pyroclastic currents. *The parameters are colour-coded, ambient and flow properties are marked in grey, dimensionless numbers focusing on fluid dynamics in green, dimensionless numbers focusing on fluid-particle interactions in blue, and thermodynamic dimensionless numbers in red. With μ_a ambient dynamic viscosity, C_S particle solid concentration, ρ_a ambient density, ρ_c flow density, $\Delta\rho$ density difference between flow and ambient, C_{p_c} and C_{p_a} the flow and ambient heat capacity, g is the gravitational acceleration, g' is the reduced gravitational acceleration, k is the Karman constant, θ the substrate inclination, u_T the particle terminal velocity, and Δu the eddy rotational velocity. Values for natural PDCs from Druitt (1998), Choux and Druitt (2002), and Burgisser et al. (2005). The flow dynamic viscosity description is from Wohletz (1998). The equation for the Galileo number is from Uhlmann and Doychev (2014). Table modified from Brosch et al. (2021).*

Parameter	Meaning	Definition	Generated PDCs	Natural PDCs
Particle Size		d	2 µm – 16 mm	10^{-6} – 10^{-1} m
Particle density		ρ_s	350 – 2600 kg /m^3	300 – 2600 kg/m^3
Ambient Density		ρ_a	1.06 – 1.225 kg · m^{-3}	0.6 – 1.2 kg · m^{-3}
Flow density		ρ_c	1.27 – 10 kg/m^3	
Flow Temperature		T	15 – 60 °C	
Velocities		u	≤ 10.5 m · s^{-1}	10 – 200 m · s^{-1}
Flow dynamic viscosity		$\mu_c=\mu_a\left(1+\frac{\rho_s C_s}{\rho_a(1-C_s)}\right)^2$	3×10^{-5} – 3×10^{-3} $\frac{\text{kg}}{\text{s m}}$	10^{-5} – 4×10^{-3} $\frac{\text{kg}}{\text{s m}}$
Kinetic energy density		$U_{kin}=\frac{1}{2}\rho_c u^2$	10^{-2} – 10^3 $\frac{\text{kg}}{\text{m s}^2}$	10^3 – 10^4 $\frac{\text{kg}}{\text{m s}^2}$
Buoyant thermal energy density		$U_T=\rho_c\frac{C_{p_c}}{C_{p_a}}\alpha\, T\, h\, g$	10 – 10^3 $\frac{\text{kg}}{\text{m s}^2}$	10^3 – 10^4 $\frac{\text{kg}}{\text{m s}^2}$
Reynolds number	$\frac{\text{Inertial Forces}}{\text{Viscous Forces}}$	$Re=\frac{\rho_c\, u\, h}{\mu_c}$	1.5×10^6	33×10^5 – 6.7×10^9

Richardson number	$\frac{\text{Buoyancy Term}}{\text{Flow Shear Term}}$	$Ri = \frac{\Delta\rho\, h\, g}{\rho_a u^2}$	$10^{-2} - 10$	$0 - 10$
Froude number	$\frac{\text{Inertial Forces}}{\text{Gravitational Forces}}$	$Fr = \frac{u}{\sqrt{g'\, h\, cos(\theta)}}$	$0.75 - 2$	≈ 1
Particle Stokes number	$\frac{\text{Characteristic Time Particle}}{\text{Characteristic Time Fluid}}$	$St = \frac{u_T \Delta u}{\delta g}$	$10^{-3} - 9.9$	$11 \times 10^{-4} - 97 \times 10^{6}$
Galileo Number	$\frac{\text{Gravitational Forces}}{\text{Viscous Forces}}$	$G_a = \frac{\rho_c \sqrt{\left\lvert {\rho_p}/{\rho_c} - 1 \right\rvert D^3 g}}{\mu_c}$	$5.9 \times 10^{-8} - 3.4 \times 10^{4}$	
Stability number	Defines particle transport zones	$\Sigma = \frac{u_T}{\Delta u}$	$13 \times 10^{-3} - 32$	$2.8 \times 10^{-6} - 9.7 \times 10^{9}$
Rouse number	Characterises turbulent particle transport regimes	$P = \frac{u_T}{k u_s}$	$66 \times 10^{-2} - 19$	$10^{-3} - 10^{2}$
Thermal Richardson number	$\frac{\text{Buoyancy Term}}{\text{Flow Shear Term}}$	$Ri_T = \frac{\Delta T\, \alpha\, h\, g}{u^2}$	$2 \times 10^{-2} - 4.5$	$0 - 5$

Pyroclastic density currents pose complex systems where various physical processes interplay and must be scaled to reproduce natural events. The scaling can be separated into fluid dynamics, gas-particle interactions, and thermodynamics. Relevant non-dimensional numbers to scale the fluid dynamics of pyroclastic density currents are the Reynolds number (Re) comparing inertial and viscous forces, the Richardson number (Ri) comparing buoyancy and shear terms, and the Froud number (Fr) comparing inertial and gravitational forces. With these values matching, fluid dynamic scaling is provided. Of particular interest for this thesis are the gas-particle interactions and the investigation of multiphase physics. Non-dimensional numbers that need to match are the particle Stokes number (St) comparing particle response times with fluid motion time scales, the stability number (Σ) comparing terminal fall velocities of particles to turbulent velocity fluctuations of the fluid phase, the Galileo number (Ga) comparing gravitational forces and viscous forces (Uhlmann and Doychev, 2014), and the Rouse number (P) describing the particle transport in turbulent flows. Using natural volcanic material ensures similarity in gas-particle interactions due to

the natural shape of the particles, the grain size and the density of natural PDCs (Lube et al., 2015). The thermodynamics is scaled using the thermal Richardson number (Ri_T) comparing thermal buoyancy and fluid shear terms. In addition to non-dimensional numbers, the kinetic energy density (U_{kin}), and the buoyant thermal energy density can be used to compare natural flows with large-scale experiments.

Table 2-2 shows a good overlap in non-dimensional numbers and dimensional scaling factors. Notably, ranges do not exactly match, and scaling limitations must be considered when analyzing the data. Despite these limitations, PELE is the best-scaled PDC experiment due to the achieved length scales, the use of natural volcanic material, and the variable temperature. For more details on calculating the non-dimensional numbers and the scaling analysis for dilute PDCs in PELE, the reader is referred to Brosch (2020).

2.6 Data Acquisition in PELE

In PELE, various sensors are used to collect data that can be analyzed to understand different aspects of the dynamics inside PDCs. The following describes the sensor inventory and the resulting sensor arrays.

2.6.1 Synchronization Signal

Exact time synchronization is vital to analyze physical measurements and infer temporal correlations. This is especially important for processes with small timescales and high frequencies. A 10 V signal, generated with the experimental trigger, is logged in independent data logging modules to achieve this synchronization. All visible light cameras record LEDs connected to this trigger signal and can be synchronized. This ensures time synchronization at the beginning of every experimental run. Subsequently generated 10 V trigger signals also

ensure that logging systems record data with accurate sampling rates. A quality control step investigating the synchronization signal enables the identification of systematic errors in the sampling rates due to rounding errors in logging codes or other malfunctions of the logging system. These errors can then be corrected to ensure accurate time synchronization. Due to technical limitations, the thermal camera and hopper loadcells are not synchronized with this signal.

2.6.2 Camera Inventory

Cameras have been one of the primary sources of data deployed in PELE since the first experiments. These can be separated into three categories: high-speed, conventional normal to fast, and thermal cameras. The entire camera inventory is summarized in Table 2-3.

High-Speed Cameras: Six high-speed cameras can be positioned to cover different parts of the glass walls of the channel and, with that, different portions of the flow. In the presented experimental series, these six high-speed cameras were deployed to create profiles at four different runout distances (1.8 m, 3.35 m, 5.4 m, and 9.6 m marked in Figure 2.1). For profile 1 (1.8 m), two of the Basler A2000-340km were installed on top of each other to record high-resolution data for the entire 1.8 m window height at that location. Profile 2 (3.35 m) is set up the same way using the NAC Meriam HX-7 ST-839 for the lower part and a Basler A2000-340km to record the top part of the window. For profile 3 (5.4 m), a Basler A2000-340km was installed to observe up to a height of 1.2 m. At Profile 4 (9.6 m), the NAC Hotshot 1280 was used to record data up to a height of 1.1 m. The video data recorded with the high-speed cameras is used to calculate velocity fields and visually analyze the passing flow and its features.

GoPro Hero Cameras: In addition to those high-speed cameras, PELE has an inventory of 22 GoPro Hero cameras with models ranging from GoPro Hero 3 to GoPro Hero 8, recording with framerates between $30 - 240$ fps at a resolution of 1920×1020. These cameras are installed in various locations and angles to the flow propagation. They are used to: Firstly, give overview imagery of the propagating flow, to track the propagation and geometry of the propagating flows. And secondly, record the time-resolved sampling tubes, enabling the mapping of the accumulated sediment and the calculation of flow concentrations and densities.

Table 2-3 Camera inventory in the PELE experimental facility.*Highspeed cameras are underlain with grey, and thermal cameras with red.*

Model	Qty	Resolution	Framerate	Measurement
NAC Meriam HX-7 ST-839	1	1920×1080	500 fps	RGB
NAC Hotshot 1280	1	1024×640	500 fps	Monochrome
Basler A2000-340km	4	1920×760	500 fps	Monochrome
GoPro Hero 3 to 8	20	1920×1080	30– 240 fps	RGB
Sony α6000	2	1920×1080	50 fps	RGB
Panasonic Lumix TZ110	1	1920×1080	50 fps	RGB
Canon EOS 600D	1	1280×720	50 fps	RGB
Infratec VarioCAM	1	640×480	50 fps	$7.5 - 14$ µm spectral range

Sedimentation Cameras: The 2 Sony α6000 cameras, as well as the Panasonic Lumix TZ110 and Canon EOS 600D, are used to capture the sedimentation and erosional processes at the base of the flows. All sedimentation cameras operate at a frame rate of 50 fps.

Thermal Camera: A thermal camera will be placed outside the building, accommodating the main part of PELE. This measurement enables the mapping of the flow during the

propagation on the horizontal runout, which gives valuable information about the temperature of the flow at that stage.

2.6.3 Temperature Sensors

Temperature measurements are an essential data source to infer particle concentrations, thermal buoyancy, and flow density. Previous studies used thermocouples of the type (RS Pro 409-4920 K-type thermocouple) with response times of 0.1 s. Thermal measurements using thermocouples can be described as a convolution between the temperature signal and the response function of the thermocouple ($measurement(t) = (temperature * response\ function)(t)$). This naturally leads to a smoothing of the signal where longer response times lead to stronger smoothing of the signal, and faster response times can capture more high-frequency signals. Previous thermocouples of the type RS Pro 409-4920 K-type, with a response time of 0.1 s, meaning 96% of a step change is measured in moving gas, were updated with faster 410-345 Type K thermocouples by TC Direct with response times less than 0.015 s.

A total of 49 thermocouples were deployed in eight vertical profiles along the runout (see Table 2-4). The sensors are inserted into the flow from the steel wall using small aluminum tubes (2.5 mm diameter and 5 cm length). Upon installation, the thermocouples were thermally isolated from the aluminum tubes using heat-resistant silicone. Further, it was ensured that the sensing tip did not have contact with the aluminum, which would artificially increase the thermal mass of the sensor and decrease the responsiveness.

Table 2-4 Thermocouple measurement network.

	P0	P1	P2	P3	P3.1	P4	P6	P7
Runout [m]	0.6	1.8	3.4	5.4	7	9.6	16	20
Qty.	4	8	8	8	8	8	4	1
Height [m]	0.45, 0.75, 1.1 1.45	0.035 0.085 0.21, 0.45, 0.75, 1.1, 1.45, 1.8	0.035, 0.085, 0.21, 0.45, 0.75, 1.1, 1.45, 1.8	0.035, 0.085, 0.21, 0.45, 0.75, 1.1, 1.45, 1.8	0.035, 0.085, 0.21, 0.45, 0.75, 1.1, 1.45, 1.8	0.035, 0.085, 0.21, 0.45, 0.75, 1.1, 1.45, 1.8	0.08, 0.25, 0.45, 1.1	0.45

2.6.4 Piezo Electric Pressure Sensors

Previously the only pressure sensors deployed in PELE recorded pore pressures. This PhD advanced the PELE experimental setup by deploying new Piezoelectric pressure sensors of the type PCB Piezotronics 106B51. These Piezoelectric pressure sensors were installed on wing profiles at six vertical profiles along the runout. These wing-shaped sensor mounts were installed in the center of the channel and along the flat runout. This enables the first in situ dynamic pressure measurements inside PELE and avoids potential boundary effects from the glass and steel wall. The exact locations where the sensors are installed are summarized in Table 2-5.

Table 2-5 Sensor network of the Piezoelectric pressure sensors (PCB Piezotronics 106B51).

	P1	P2	P3	P4	P5	P6
Runout [m]	1.8	3.35	5.4	9.6	16	20
Qty.	1	7	3	2	1	1
Height [m]	0.45	0.04, 0.08, 0.15, 0.30, 0.45, 0.75, 1.3	0.08, 0.45, 0.75	0.08, 0.45	0.45	0.45

2.6.5 Low-Volume Pitot Tubes

As part of this PhD thesis, low-volume Pitot tubes were designed, built, and tested. To achieve low response times, it is vital to create Pitot tubes with very low volume. Calculations by Flemmer et al. (1984) suggest that the reaction time of the gas-purged pitot tubes is proportional to the internal dead volume. Currently available commercially, Pitot tubes are either too expensive or have too high response times to be deployed in PELE to investigate the turbulence of experimental PDCs. In the following, I describe the design, prototyping, and calibration of low-volume Pitot tubes to be used with differential pressure sensors of the type SDP3x by Sensirion AG.

First, 3D-printed pitot tubes were designed, and gas-purged pitot systems (Flemmer, 1984) with 0.5 mm, 0.75 mm, and 1 mm internal tubing diameters were tested (see Figure 2.4). These Pitot tubes were printed in titanium by RAM3D, in Tauranga, New Zealand. The gas purging generated noise levels above the amplitude of the measures signal; therefore purging was eliminated, and the 3D-printed conventional low-volume Pitot tubes were tested.

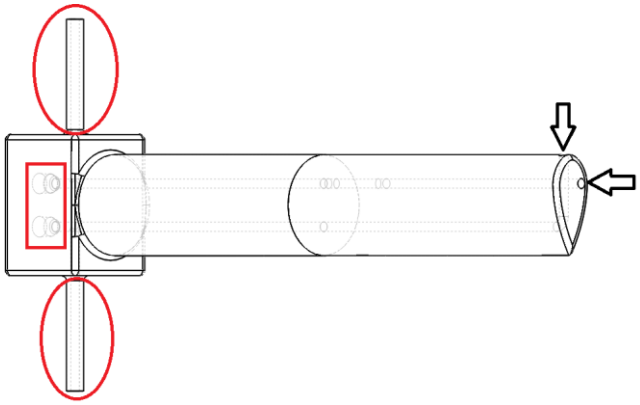

Figure 2.4 3D gas-purged Pitot tube design. *The red box marks the sensor mount, the red ovals the air supply for the gas purging, and the arrows the pressure ports (top dynamic, side static). The grey dashed lines indicate the internal tubing.*

In first experimental runs, an airflow with a velocity of approximately $14.5\ \mathrm{m \cdot s^{-1}}$ (meaning dynamic of 129 Pa) was generated in the horizontal flow tube. The flow velocity was monitored using an anemometer to ensure the right flow velocity. The 3D-printed Pitot tubes were inserted into the flow without applying any gas purging. The results for the 3D-printed pitot with 0.5, 0.75, and 1 mm internal diameter are presented in Figure 2.5.

Figure 2.5 shows the Pitot tube with 0.5 mm diameter to measure only very small signals. These low values are too small to be calibrated afterward. The pitot tubes with 1 and 0.75 mm diameters show far better results but have very large volumes and are very cost-intensive when looking at producing larger batches of over 40 Pitot tubes. Furthermore, blockages were observed after the controlled introduction of ash into the flow tubes. Blockages were not observed for Pitot tubes with 0.5 mm internal tubing.

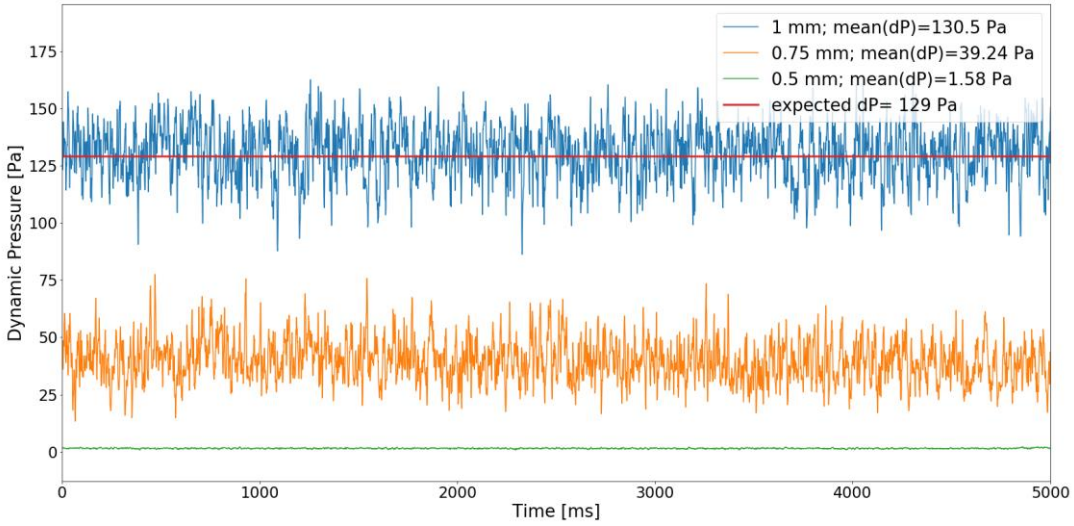

Figure 2.5 Results from the vertical flow tube using 3D printed prototypes without gas purging. *The 3D-printed prototypes were inserted in a flow with an expected dynamic pressure of approximately* 128 *Pa*.

The increasing dampening effect, with decreasing internal diameter, is caused by the increasing pressure drop. The roughness of the 3D-printing leads to increased pressure drops.

Also, the radius of the bend in the dynamic pressure port may be increased to decrease the pressure drop, as the straightening of the flow is not further necessary, which needs to be considered in the design of the gas-purged system.

Spinal anesthetic needles, providing smooth tubes with small internal diameters, are used in the second generation of prototypes. In the process of prototyping, three different needle diameters were tested: 22 g (0.413 mm inner diameter), 21 g (0.514 mm inner diameter), and 20 g (0.603 mm inner diameter). To produce these Pitot tubes and to give them a shape that will have the least influence on the probed flow possible, I designed different molds to cast the needles into an epoxy resin structure. The resin structure takes the same shape as the pitot tube in Figure 2.4. The casting process was optimized to ensure smooth production and reproducible Pitot tubes.

The resin must be heat resistant and have the right viscosity for the casting process. Two different epoxy resins, meeting the heat resistance requirements, were tested, and a heat-resistant epoxy usually used by boat builders proved most suitable to produce Pitot tubes.

Secondly, molds needed to be manufactured to assure a smooth production process. First attempts using a 3D printed mold (see Figure 2.6) were produced in cooperation with Daniel Farley, Xpeed Limited. The mold includes alignment pins and injection holes for the resin.

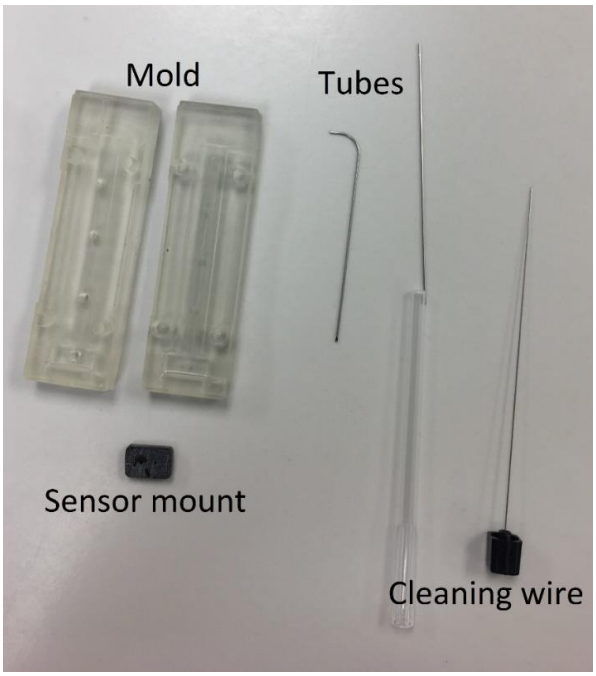

Figure 2.6 3D printed Pitot tube mold and other parts needed to cast Pitot tubes.

The sensor mounts for these casted Pitot tubes (Figure 2.6) were designed by me and 3D printed by Morio Fukuoka, Massey University. The sensor mounts are printed to achieve the highest possible quality with submillimeter precision. The spinal needles are glued into those sensor mounts and sealed off using hot glue to prevent the epoxy resin from entering the sensor mount or spinal needles. This assembly is placed in the molds (Figure 2.7), and the mold is filled with epoxy.

Figure 2.7 Placement of the sensor mount and internal tubing into the 3D-printed mold.

After the curing process, the Pitot tube was released from the mold and the slight flexibility of the 3D-printed mold provided for an easy release. This delivered the first cast Pitot tube prototype (see Figure 2.8).

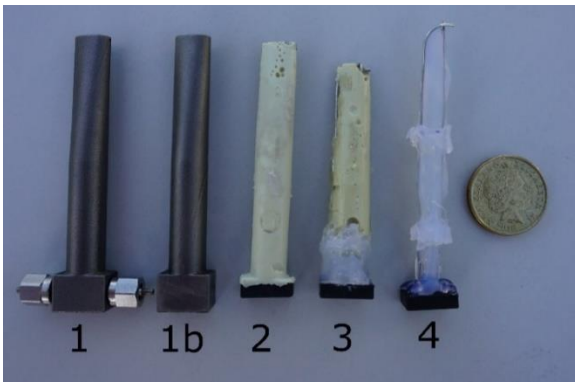

Figure 2.8 Different prototypes for the pitot tube systems with a 1 New Zealand dollar coin for scale. *1) a 3D printed pitot tube including a gas purge. 1b) a 3D printed pitot tube, where the gas purging was removed. 2) The first epoxy Pitot tube, cast using a 3D printed mold. 3) The second cast using the first 3D printed mold. 4) A provisional prototype is only fixing the tubing and the sensor mount using hot glue.*

For the first prototype, 22G spinal needles with an internal diameter of 0.413 mm were used. A second prototype using 21G spinal needles with an internal diameter of 0.514 mm was produced. Due to further hardening of the 3D printed mold, the mold got brittle, and a mold release was not possible. In the process of removing the mold from the Pitot tube, the sensor mount of the Pitot tube and the mold broke (see Figure 2.9). It was possible to fit a new sensor mount and test this second prototype (Figure 2.8).

The prototype using the 20g (0.603 mm inner diameter) spinal needles was built by provisionally connecting the spinal needles and the sensor mount using hot glue and building a support structure of hot glue (see Figure 2.8). This was done due to the emerging Covid-19 pandemic and the uncertain accessibility of lab facilities.

Provisional testing resulted in the choice of the 20g spinal needles for the final production.

Figure 2.9 Sensor mount (circled in red) and 3D printed mold after producing the second cast prototype.

A third attempt at producing a more sustainable mold was made by machining the mold from plastic, including filling holes, alignment pins, and holes for ejection pins. A clean mold release was not possible with this mold. The Pitot tube and the mold were both damaged, as the epoxy completely blocked the ejection pins. Applying force in the hope of loosening the ejection pins lead to damage to the mold and the ejection pins.

The final silicone prototypes made from silicone provided excellent mold release and reusability. To produce those molds, the male shapes of the mold halves are 3D printed, including all relevant features (see Figure 2.10). Mold Star^{TM} 15 SLOW silicone was used to cast these molds. With one set of male prints to produce the molds, the serial production of Pitot tubes and molds started simultaneously, with the production capacity growing with each iteration.

Figure 2.10 3D model of the male half for the production of silicone molds.

The Pitot tubes were set to record counts due to computational limitations of the Arduino Leonardo modules used to read the sensors and send the reading via serial connection to the logging computer. This and the residual pressure drop are corrected in a calibration step that was performed multiple times for each Pitot tube (Figure 2.11). A known pressure signal is applied to the dynamic port of the pitot tube and recorded at a calibration sensor and with the pitot tube simultaneously (Figure 2.11 b). This signal is then used to calculate a linear regression, with an intercept at zero, between Pitot reading and calibration pressure (Figure 2.11 b). A slight hysteresis is visible, which is not considered, as a linear relationship sufficiently describes the calibration. Non-linear responses of the dead-volume could

potentially cause the hysteresis. The result of the calibration is shown in Figure 2.11 c, where a sufficient match can be observed, with only slight errors towards high pressures.

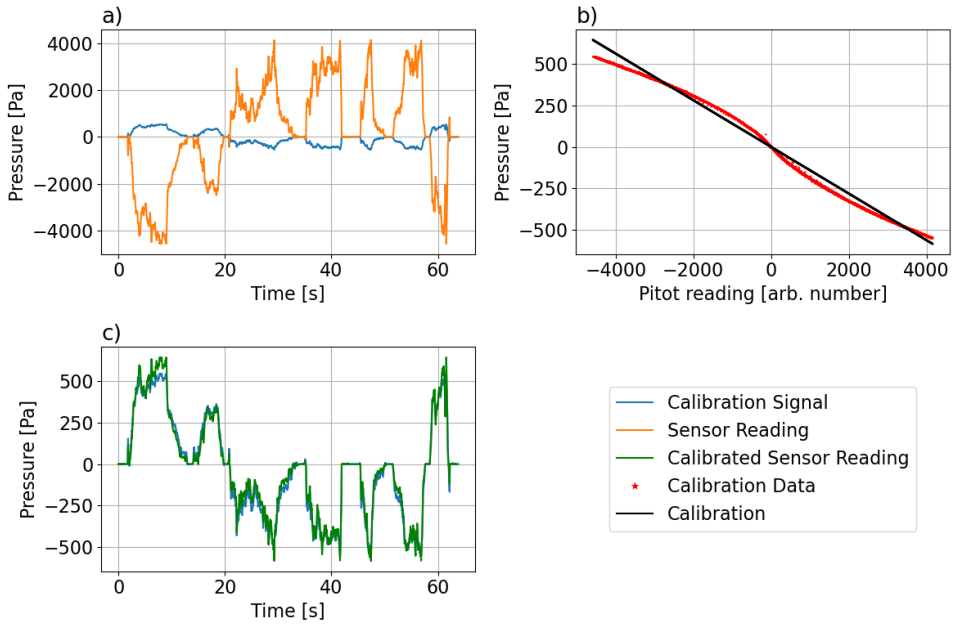

Figure 2.11 Calibration algorithm for low-volume Pitot tubes. *a) comparison of the Pitot sensor reading (orange) and the calibration signal (blue). b) the calibration curve (black) calculated from the calibration data (red) in (a). c) Comparison of the calibration signal (blue) and the calibrated Pitot sensor reading (green).*

Each Pitot tube was calibrated three times before each of the three experiments in this PhD, and for four experiments performed as part of the PhD project of Lucas Corna (Corna, 2023). This has shown reproducibility in the correlation process, as well as reproducibility and accuracy of the production process. The final Pitot tubes need a correction of c. 3.7 and the pressure range-dependent conversion factor of the SDP3x sensor.

2.6.6 Time-Integrated Flow Sampler

In PELE, time-integrated flow solid samples are collected with 2.4 × 15 cm glass test tubes. These test tubes are installed at eight vertical profiles along the runout (0.6 m, 1.9 m, 4.5 m, 9.7 m, 13 m, 16 m, and 20 m). The passive samplers are installed at heights varying from

6 cm to 180 cm. The exact positions are summarized in Table 2-6. The sampling tubes up until 13 m protrude 5 cm into the flow from the steel wall. Sampling tubes at 16 m and 20 m are positioned in the flow's center. These tubes collect time-integrated samples of the passing solid particles inside the flow, which can be analyzed to infer time-integrated masses and grain-size distributions.

Table 2-6 Time integrated flow sampler positions.

	P0	**P1**	**P2/3**	**P4**	**P4/5**	**P5**	**P6**
Runout [m]	0.6	1.9	4.5	9.7	13	16	20
Qty.	6	6	6	6	8	8	8
Height [m]	0.21, 0.45, 0.75, 1.1, 1.45, 1.8	0.21, 0.45, 0.75, 1.1, 1.45, 1.8	0.21, 0.45, 0.75, 1.1, 1.45, 1.8	0.21, 0.45, 0.75, 1.1, 1.45, 1.8	0.06, 0.11, 0.21, 0.45, 0.75, 1.1, 1.45, 1.8	0.06, 0.11, 0.21, 0.45, 0.75, 1.1, 1.45, 1.8	0.06, 0.11, 0.21, 0.45, 0.75, 1.1, 1.45, 1.8

2.6.7 Time-Resolved Flow Sampler

Next to time integrated flow samplers, time resolves flow samplers were deployed at four different runout distances (2 m, 3.4 m, 5.2 m, and 9.6 m) at heights varying from 3.5 cm to 180 cm (exact positions see Table 2-7). Thirty-four of these sampling tubes were built and deployed in the generated flows. These time-resolved sampling tubes are comprised of square glass tubing with an opening cross-section of 1.96 cm^2 with lengths varying from 5 cm to 15 cm (Brosch et al., 2021). In the back of the sampling tubes, two fine steel meshes (15 µm) ensure the passage of the gas phase while solid particles are blocked. The filling of these tubes is monitored with GoPro Hero cameras, allowing for mapping isochrones of deposited material and enabling the calculation of solid concentrations and current densities. These isochrones can also be sampled, yielding time-resolved flow grain size information.

Table 2-7 Time resolved flow sampler positions.

	P1	P2	P3	P4
Runout [m]	2	3.4	5.2	9.6
Qty.	9	9	9	7
Height [m]	0.035, 0.08, 0.15, 0.25, 0.45, 0.75, 1.1, 1.45, 1.8	0.035, 0.08, 0.15, 0.25, 0.45, 0.75, 1.1, 1.45, 1.8	0.035, 0.08, 0.15, 0.25, 0.45, 0.75, 1.1, 1.45, 1.8	0.035, 0.08, 0.15, 0.25, 0.45, 0.75, 1.1,

2.6.8 Load Cells

Four loadcells of the type Zemic H8C-C3-1.5T-4B, monitor the weight of the hopper during experimental runs. This allows to calculate time-resolved discharge rates and characterize the mass discharge during experimental runs.

2.6.9 Laser Scanner

A Leica MS50 laser scanner was used to scan the channel base before and after an experimental run to accurately determine the deposit thickness as a function of the runout and channel width. The difference between these measurements equals the deposit thickness. Two geo-reference points inside the experimental facility calibrate the laser scanner.

2.7 Data Analysis Techniques

With the vast variety of sensors installed in PELE, different physical properties are measured, summarized in Table 2-8. Throughout the existence of PELE, developing new analysis algorithms was one of the main challenges to dealing with large and diverse data

sets, extracting quantitative information, and linking different physical properties quantitively.

Table 2-8 Physical properties measured and calculated from PELE large-scale experiments.

Parameter	Unit	Mathematical representation
Image Data	0-255 grayscale	scalar
Velocity Data	m s^{-1}	vector field
Concentration		scalar
Density	kg m^{-3}	scalar
Momentum Density	Kg s^{-1} m^{-2}	vector field
Temperature	°C	scalar
Thermal Images	°C	scalar
Dynamic Pressure	Pa	scalar
Pore Pressure	Pa	scalar
Grain-size Distribution	wt.%	distribution

2.7.1 Flow Geometries

The flow geometry, such as the time-resolved flow front position, flow height at static runouts, and the whole flow geometry, are mapped using high-speed and GoPro hero cameras. For accurate results, predefined grids are overlain onto the images.

2.7.2 Particle Image Velocimetry

The data collected by the six high-speed cameras are used to calculate two-dimensional velocity fields using digital particle image velocimetry (PIV) using the PIVlab software (version 2.54) (Thielicke and Stamhuis, 2014) in MATLAB. PIV needs at least two images, one recorded at t_0 and the other one at $t_0 + \Delta t$. It measures how far particles have traveled and calculates the velocity of those particles by dividing the distance traveled by the time difference. Cross-correlating small sub-images determines the displacement. The output of

PIV is a vector field with the velocities (vertical v and horizontal u). For details on PIV, the reader is referred to Thielicke and Stamhuis (2014) and Thielicke and Sonntag (2021).

Velocity fields are extracted from image data using the following workflow, which expands the workflow used by Brosch (2020). Using VirtualDub2 (https://www.virtualdub.org/), the images of the highspeed cameras are extracted, and for the NAC Meriam HX-7 ST-839, converted into greyscale images. Followed by a first preprocessing step using Adobe Photoshop. This step corrects uneven lighting using irregularly shaped polygons (see Figure 2.12). After the external preprocessing, the images are imported to PIVlab, and a region of interest (RIO) is defined, for which velocity will be calculated.

This step is followed by the PIVlab internal image preprocessing. First, a histogram equalization using the contrast limited adaptive histogram equalization (Zuiderveld, 1994) is performed. In this algorithm, the image is subdivided into smaller regions, and the histograms for those regions the histograms are equalized, enhancing the local contrast. The region size for this filter should be chosen to be larger than the structures that want to be preserved in the image. Here, values between $50 - 100$ pixels are used. After applying the histogram equalization, a Wiener low pass filter with a size between $3 - 5$ pixels is used to denoise the images. The implemented automatic contrast stretch is also enabled. The results of the filtering are visually assessed and refined. The FFT window deformation algorithm is used to extract the velocities in combination with multiple passes of correlation windows decreasing in size and step size. The subsequent window sizes are defined to be 256 pixels, 128 pixels, 64 pixels, and 32 pixels. The step size is always defined to be half the window size. The last pass is then repeated until an error slope of less than 0.025 is achieved. A Gauss 2x3-point algorithm is used to perform sub-grid estimations and increase the accuracy of the algorithm. The Correlation robustness is set to high (Thielicke and Sonntag, 2021).

Once the calculations are completed, the sampling rate and a known length in the images are defined to calibrate the output from pixel/frame to $\mathrm{m} \cdot \mathrm{s}^{-1}$.

In the post-processing, reasonable velocity limits are defined. And a standard deviation filter with $8 \cdot std$, and a local median filter with 3 are used.

The resulting velocities have a temporal resolution of 500 Hz and a spatial resolution of around 1 cm. The spatial resolution varies slightly for each camera due to different spatial resolutions and zoom in different cameras. The data is exported as a Mat-file to be imported and analyzed in Python.

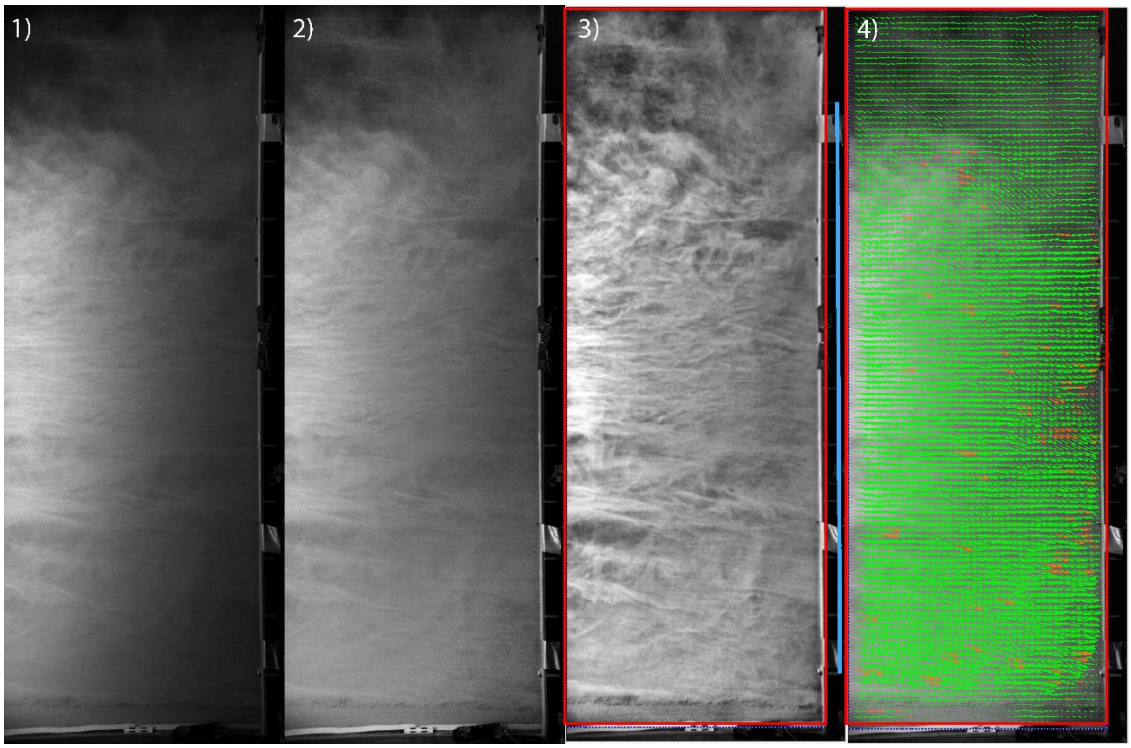

Figure 2.12 Outline of the PIV workflow used to calculate velocities from image data. *1) Raw example image from the flower Basler camera at profile one (1.8 m). 2) The results of the histogram equalization in Photoshop. 3) The results of the PIVlab (version 2.54), the region of interest is marked in red, and the known calibration length (1 m) in blue. Filter settings used in this example are a CLAHE window size of 75 pixels and a wiener low pass filter window size of 4. The auto contrast stretch is enabled. 4) The resulting vector field for this*

frame. Green vectors show valid results, and red vectors show results that are excluded due to the filtering in post-processing.

2.7.3 Calculating Time-Resolved Particle Solid Concentrations

Time-resolved particle solid concentrations are obtained using the data from the time-resolved sampling tubes, following the algorithm of Brosch and Lube (2020).

The time-resolved flow samplers are recorded using GoPro Hero cameras at a framerate of 60 fps. In the resulting images, isochrones are mapped, projecting the whole deposited material on the glass wall. The change of this area between two time-steps ΔA_i can be transferred into a deposited volume V_{d_i}, with the assumption that the deposit is constant throughout the depth of the tube w.

$$V_{d_i} = \Delta A_i \cdot w. \qquad \textit{EQN. 2-2}$$

The volume flux Q_i is calculated using the downstream component of the flow velocities u_i, determined by the PIV algorithm, and the sampling tube cross-section A_c.

$$Q_i = u_i \cdot A_c. \qquad \textit{EQN. 2-3}$$

With which the passing flow volume V_{f_i} is for a time difference Δt is calculated.

$$V_{f_i} = Q_i \cdot \Delta t \qquad \textit{EQN. 2-4}$$

Finally, time-resolved particle solid concentrations are calculated as:

$$C_{s_i} = \frac{V_{d_i}(1-\epsilon)}{V_{f_i}} \qquad \textit{EQN. 2-5}$$

With the porosity ϵ for close packing being constant at around 46%.

This yields time-resolved solid particle concentrations.

2.7.4 Calculating Time-Resolved Flow Densities and Dynamic Pressures

Using the time-resolved particle solid concentrations C_{s_i} flow densities ρ_c can be calculated as follows (Brosch and Lube, 2020; Dellino et al., 2008; Hallworth and Huppert, 1998)

$$\rho_{c_i} = (1 - C_{s_i})\rho_f + C_{s_i}\rho_p \qquad \textit{EQN. 2-6}$$

With the fluid density ρ_f and the average particle density ρ_p. For the dynamic pressure follows

$$P_{dyn_i} = \frac{\rho_{c_i} {U_i}^2}{2} \qquad \textit{EQN. 2-7}$$

with the instantaneous flow velocity magnitude U_i.

2.7.5 Flow Grainsize Distributions

Both time-integrated and time-resolved grain size distributions were obtained through a combination of sieving for particles larger 250 µm and a laser particle size analysis for all particles smaller than 250 µm. Time-resolved samplers are sampled with 0.5 s temporal resolution. GRADISTAT (Blott and Pye, 2001) was used to analyze the grain size distribution.

2.7.6 Temperature Correction for the Piezo Electric Pressure Sensors

The Piezoelectric pressure sensors are sensitive to temperature changes due to differences in thermal expansion coefficients between the sensor's internal quartz crystal, inducing a voltage when put under pressure, and the steel casing encapsulating the crystal. The measured pressure is lowered for temperature rises due to the steel expanding more than the crystal. Cooling of the sensor causes the inversed signal. The temperature signal is much larger than the expected pressure range and shows a smooth trend (see Figure 2.13). The manufacturer does not provide software or information on the removal of this signal. The following temperature correction is performed on the example of an independent experiment to test the sensors and the data processing. The results align with the final experimental runs and provide an additional example demonstrating that proposed algorithm works repeatedly.

To remove the temperature influence on the Piezoelectric pressure measurement, I assumed the resulting pressure signal to be the superposition of the flow's pressure signal and the temperature's influence on the measurement.

$$P_{measured} = P_{flow} + P_{temp} \qquad \textit{EQN. 2-8}$$

As positive dynamic pressures are expected, the temperature influence must be the lower envelope of the pressure signal. By removing this lower envelope, the temperature influence can be removed. A workflow to remove the temperature influence is defined through experimentation, cross-validation with temperature data, and comparison with independent pressure measurements.

The temperature influence is calculated as the moving average (6 ms) of the time series, subtracted by the standard deviation (of the 6 ms–interval), providing the lower envelope.

A spike removal was performed to avoid plateauing around strong pressure excursions (see Figure 2.13), where all pressure gradients larger than 150 Pa/ms are removed. Based on this spike-removed pressure data, the lower envelope is calculated.

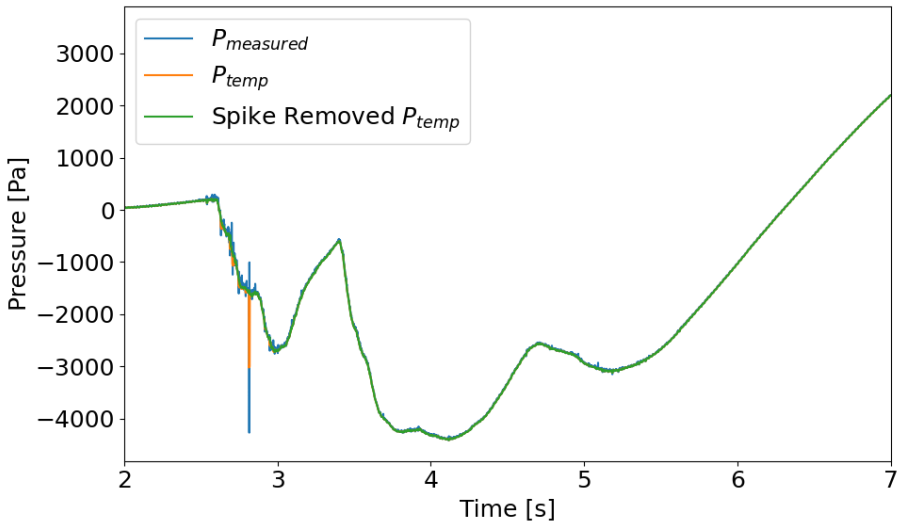

Figure 2.13 Calculation of the pressure signature of the temperature change. *The raw temperature influenced pressure signal ($P_{measured}$) is shown in blue. Orange is the temperature influence on the pressure measurement (P_{temp}) without the spike removal, and green is the spike removed temperature influence. It is apparent that the spike removal sufficiently removes plateaus in the calculated temperature influence.*

The lower envelope of the temperature data, caused by temperature changes of the sensor, is then compared to the temperature data recorded at the same position as the pressure (see Figure 2.14). This shows that the empirically calculated temperature influence and the temperature data show the same features and have an inversed correlation, as expected due to the sensor's construction.

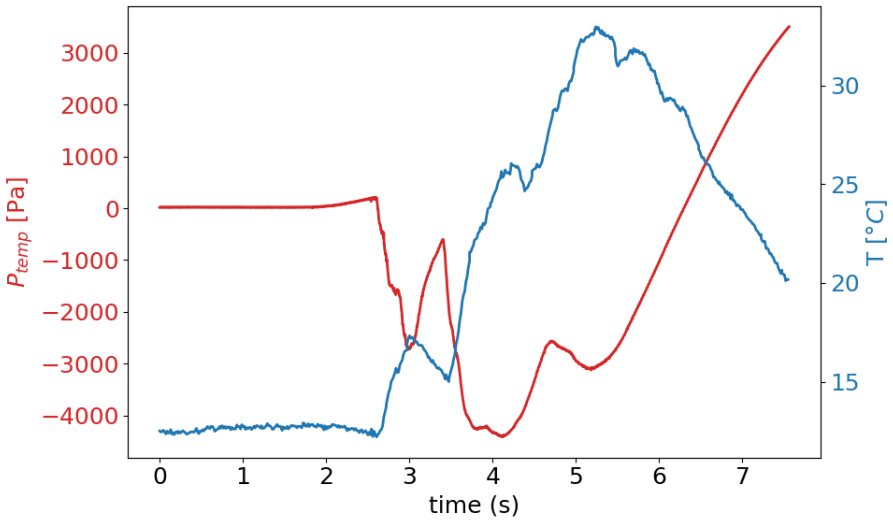

Figure 2.14 Comparing the temperature signal with the temperature-induced pressure changes. *The temperature and the temperature influence are compared, and the long-period flow features provide an excellent match. The sensor construction can explain the inversed relationship between these signals.*

In the last quality control step, the resulting pressure signal, filtered with a moving average filter to increase comparability, is compared to an independent pressure measurement derived from flow velocities and flow densities (as described in Section 2.7.4). The separate measurements show a good match, providing confidence that the temperature correction works sufficiently (see Figure 2.15). Single negative measurement values were replaced with the following adjacent values.

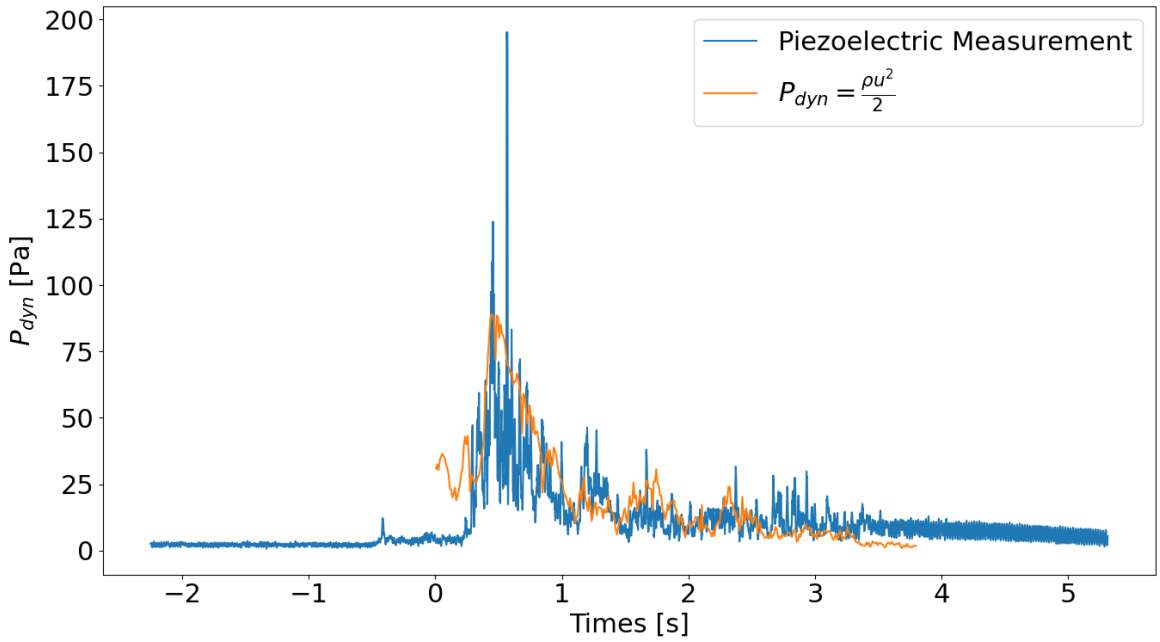

Figure 2.15 Comparison of the temperature-corrected piezoelectric pressure measurement and the dynamic pressures calculated from velocities and flow densities. *The two completely independent measurements show a good fit, both in long- and short-period processes. The Piezoelectric sensors show a more abrupt onset of the flow and higher peak values. A 10 ms average filter was applied to the piezoelectric measurement to improve comparability.*

This algorithm was developed and tested using data from four independent experiments, using different masses of experimental material, as well as different grain size distributions and a variety of temperatures. The temperature was varied from unheated volcanic material to material heated to 120℃. The unheated material was colder than the ambient air in the morning of the experimental run and produced the inverse temperature signature as hot material. The temperature removal also worked for the cold material.

Extraction of Particle Impacts and Calculation of Impact Rates: The particle impacts are identified and extracted through a 220 Pa/ms threshold gradient. This can be used to create a binary time series for each sensor, where zero denotes no particle impacts, and one denotes particle impacts (See Supplementary Figure 3.3).

Particle impact rates are then calculated through a convolution of the binary time series a,

$$a(t) = \begin{cases} 1 \; \forall \; \frac{\Delta P}{\Delta t} \geq 220 \text{ Pa/ms} \\ 0 \; otherwise. \end{cases}, \qquad \textit{EQN. 2-9}$$

with a box function v

$$v(t) = \begin{cases} n^{-1} \; \forall \; |t| \leq \frac{n}{2} \\ 0 \; \forall \; |t| > \frac{n}{2} \end{cases}, \qquad \textit{EQN. 2-10}$$

as

$$f_{impact} = (a * v). \qquad \textit{EQN. 2-11}$$

The length n of the convolutional kernel is set to $200\,ms$. This particle impact extraction leads to a smoothing and temporal blurring of the signal and provides particle impact rates (see Figure 3.3). Codes for the temperature correction and the extraction of particle impacts are included in Appendix C.

2.7.7 Reynolds Decomposition

Data (X) from turbulent flows can be interpreted as the superposition of the mean flow ($\bar{X}$) and the turbulent fluctuations (X')

$$X(x,z,t) = \overline{X(x,z,t)} + X'(x,z,t)\,. \qquad \textit{EQN. 2-12}$$

This has previously been done only for the downstream velocity components in experimental pyroclastic density currents (Brosch, 2020; Brosch et al., 2021; Cerminara et al., 2021). To calculate the mean flow, empirical Power Gaussian fits of the vertical distribution of the downstream velocity were calculated using polynomial fits (Cerminara et al., 2021).

With this approach, the analysis highly depends on analytical or empirical models to describe the mean properties. Further, the definition of the mean flow directly defines the turbulent fluctuations, and strong assumptions lead to a biased turbulence pattern and potential errors.

An alternative to using empirical models can be the use of purely data-driven approaches. This thesis calculates the mean flow properties by applying Savitzky-Golay filters (Savitzky and Golay, 1964). This means that polynomials fit the data's temporal subsets, and the central value is used as the filtered value. A convolution is then performed over the whole time series. The degree of the polynomials and the length of the data subsets (window length) can be chosen. This thesis sets the polynomial degree to one for most applications. The window length is varied, allowing to investigate different timescale turbulence structures. The Savitzki-Golay filter implementation by SciPy (Virtanen et al., 2020) is used, which results in a similar algorithm to a moving average. One key difference is that only parts of the data subsets are needed at data boundaries to fit appropriate polynomials, and no padding is applied. For example, only data with times equal to or larger than the evaluated data point are used at the beginning of the time series to fit the polynomial. This reduced the boundary effects and allowed an excellent application to transient turbulence. This algorithm can be used for any turbulence setting where temporal data is collected and any data stream (e.g. greyscale images, velocities, temperature, and pressures). The results of these algorithms are presented in Chapter 4 and Chapter 5, and codes are included in Appendix D and Appendix E.

2.7.8 Frequency Analysis and its Interpretations

Frequent spectra can be calculated with all the measurements by applying a Discrete Fourier Transformation. This way, periodic processes in the measured properties can be identified

and linked to physical processes. Identifying pronounced maxima can inform about highly energetic physical processes such as large eddies (Brosch et al., 2021). The frequency spectra for turbulent data show a logarithmic energy decay from low frequencies (large periods) to high frequencies and short periods. This is caused by the Kolmogorov cascade describing the energy transfer from large to small eddies. Spatial Fourier transforms, where the amplitude is calculated as a function of the wave number ($k = 1/\lambda$, with the wavelength/eddy size λ), the slope of the Kolmogorov cascade is $-5/3$ for single fluids (Pope, 2000). The Kolmogorov cascade is considered one of the few constants in turbulence. The presence of particles in turbulent suspensions has been shown to decrease the slope of the energy cascade (Balachandar, 2009; Bosse et al., 2006). An increased slope shows a reduced momentum transfer towards smaller turbulence structures, and a decreased slope means an enhanced momentum transfer from larger to smaller structures. In previous studies in the PELE experimental facility, only the energy cascade in the frequency domain is considered. In this thesis, I apply a coordinate transform on the temporal axis to obtain a length axis. This is achieved by temporal advection of flow structures with measured flow velocities, providing first insights into the energy cascade with relation to turbulence structure sizes.

2.7.9 Time-Height Representation of Data

Time-height representations of the data are used to obtain insights into the temporal evolution of the experimentally generated PDCs (Lube et al., 2019). To create these time-height plots, measurements or results from calculations along a vertical profile at a given observer location are plotted as pseudo-color or contour plots over time. This can be done with velocities, temperatures, pressures, and high-speed camera video data. For the generation of the video time height plot, in the following referred to as kymographs, camera

images are exported as black and white images and loaded into Python, where single-pixel columns are extracted and saved as a matrix with a height and a time dimension. Matrixes of different cameras can be aligned using the trigger signal and the measuring tool in ImageJ (Schneider et al., 2012) in combination with known marker locations, such as sensors in the camera view. These new representations allow the correlation of physical data with visual features of the flow and increase the interpretability of the time-height representations of other measurements. Furthermore, this representation can be used for fast flow and sediment height mapping. When interpreting time height presentations generated in PELE, the geometry of flow features is mirrored along the y-axis.

2.8 References

Ardo, J., 2022. Investigation of depositional processes in pyroclastic surges : a large-scale experimental approach : a thesis presented in partial fulfilment of the requirements for the degree of Master of Science in Earth Science at Massey University, Manawatū, New Zealand. Masters Thesis, Massey University.

Balachandar, S., 2009. A scaling analysis for point–particle approaches to turbulent multiphase flows. Int J Multiphas Flow, 35(9): 801-810.

Blott, S.J. and Pye, K., 2001. GRADISTAT: A grain size distribution and statistics package for the analysis of unconsolidated sediments. Earth Surf Proc Land, 26(11): 1237-1248.

Bosse, T., Kleiser, L. and Meiburg, E., 2006. Small particles in homogeneous turbulence: Settling velocity enhancement by two-way coupling. Phys Fluids, 18(2).

Breard, E.C.P., 2016. Dynamics of pyroclastic density currents: a thesis presented in partial fulfilment of the requirements for the degree of Doctor of Philosophy in Earth

Sciences at Massey University, Manawatū, Palmerston North, New Zealand. Doctoral. Massey University.

Brosch, E., 2020. Inside pyroclastic surges – a characterisation of the flow behaviour, hazard impact mechanisms and sedimentation processes through large-scale experiments: a thesis presented in partial fulfilment of the requirements for the degree of Doctor of Philosophy in Earth Sciences at Massey University, Manawatū, Palmerston North, New Zealand. Doctoral. Massey University.

Brosch, E. and Lube, G., 2020. Spatiotemporal sediment transport and deposition processes in experimental dilute pyroclastic density currents. Journal of Volcanology and Geothermal Research, 401: 106946.

Brosch, E., Lube, G., Cerminara, M., Esposti-Ongaro, T., Breard, E.C.P., Dufek, J., Sovilla, B. and Fullard, L., 2021. Destructiveness of pyroclastic surges controlled by turbulent fluctuations. Nature Communications, 12(1): 7306.

Burgisser, A., Bergantz, G.W. and Breidenthal, R.E., 2005. Addressing complexity in laboratory experiments: the scaling of dilute multiphase flows in magmatic systems. Journal of Volcanology and Geothermal Research, 141(3-4): 245-265.

Cerminara, M., Brosch, E. and Lube, G., 2021. A theoretical framework and the experimental dataset for benchmarking numerical models of dilute pyroclastic density currents. arXiv preprint arXiv:2106.14057.

Choux, C.M. and Druitt, T.H., 2002. Analogue study of particle segregation in pyroclastic density currents, with implications for the emplacement mechanisms of large ignimbrites. Sedimentology, 49(5): 907-928.

Corna, L., 2023. The interactions of pyroclastic density currents with obstacles : a large-scale experimental study : a thesis presented in partial fulfilment of the requirements for the degree of Doctor of Philosophy in Earth Sciences at Massey

University, Manawatū, Palmerston North, New Zealand. Doctoral Thesis, Massey University.

Dellino, P., Mele, D., Sulpizio, R., La Volpe, L. and Braia, G., 2008. A method for the calculation of the impact parameters of dilute pyroclastic density currents based on deposit particle characteristics. J Geophys Res-Sol Ea, 113(B7): B07206.

Dellino, P., Zimanowski, B., Buttner, R., La Volpe, L., Mele, D. and Sulpizio, R., 2007. Large-scale experiments on the mechanics of pyroclastic flows: Design, engineering, and first results. J Geophys Res-Sol Ea, 112(B4): B04202.

Druitt, T.H., 1998. Pyroclastic density currents. Geological Society, London, Special Publications, 145(1): 145-182.

Esposti Ongaro, T., Cerminara, M., Charbonnier, S.J., Lube, G. and Valentine, G.A., 2020. A framework for validation and benchmarking of pyroclastic current models. B Volcanol, 82(6): 51.

Flemmer, R.L., 1984. A pneumatic probe to detect the presence of gas bubbles in fluidized beds. 1. Method of operation. Industrial & engineering chemistry fundamentals, 23(1): 113-115.

Flemmer, R.L., Swart, H.C. and Mori, H., 1984. A pneumatic probe to detect gas bubbles in fluidized beds. 2. Response of the probe. Industrial & engineering chemistry fundamentals, 23(1): 116-119.

Hallworth, M.A. and Huppert, H.E., 1998. Abrupt transitions in high-concentration, particle-driven gravity currents. Phys Fluids, 10(5): 1083-1087.

Lube, G., Breard, E.C.P., Cronin, S.J. and Jones, J., 2015. Synthesizing large-scale pyroclastic flows: Experimental design, scaling, and first results from PELE. J Geophys Res-Sol Ea, 120(3): 1487-1502.

Lube, G., Breard, E.C.P., Jones, J., Fullard, L., Dufek, J., Cronin, S.J. and Wang, T., 2019. Generation of air lubrication within pyroclastic density currents. Nat Geosci, 12(5): 381-386.

Pope, S.B., 2000. Turbulent Flows. Cambridge University Press, Cambridge.

Savitzky, A. and Golay, M.J., 1964. Smoothing and differentiation of data by simplified least squares procedures. Analytical chemistry, 36(8): 1627-1639.

Scharff, L., Hort, M. and Varley, N.R., 2019. First in-situ observation of a moving natural pyroclastic density current using Doppler radar. Scientific Reports, 9(1): 7386.

Schneider, C.A., Rasband, W.S. and Eliceiri, K.W., 2012. NIH Image to ImageJ: 25 years of image analysis. Nature methods, 9(7): 671-675.

Thielicke, W. and Sonntag, R., 2021. Particle Image Velocimetry for MATLAB: Accuracy and enhanced algorithms in PIVlab. Journal of Open Research Software, 9(1).

Thielicke, W. and Stamhuis, E.J., 2014. PIVlab – Towards User-friendly, Affordable and Accurate Digital Particle Image Velocimetry in MATLAB. Journal of Open Research Software, 2: e30.

Uhlmann, M. & Doychev, T., 2014. Sedimentation of a dilute suspension of rigid spheres at intermediate Galileo numbers: the effect of clustering upon the particle motion. *Journal of fluid mechanics*, 752**,** 310-348.

Virtanen, P., Gommers, R., Oliphant, T.E., Haberland, M., Reddy, T., Cournapeau, D., Burovski, E., Peterson, P., Weckesser, W. and Bright, J., 2020. SciPy 1.0: fundamental algorithms for scientific computing in Python. Nature methods, 17(3): 261-272.

Wilson, C.J.N., 1985. The Taupo Eruption, New Zealand. II. The Taupo Ignimbrite. Philosophical Transactions of the Royal Society of London. Series A, Mathematical and Physical Sciences, 314(1529): 229-310.

Wohletz, K.H., 1998. Pyroclastic surges and compressible two-phase flow. Developments in Volcanology, 4.

Zuiderveld, K., 1994. Contrast limited adaptive histogram equalization. Graphics gems: 474-485.

3 Deadly coupling – hazard impacts of pyroclastic density currents exacerbated by mesoscale particle clusters

This manuscript is prepared for submission as a research article to **Nature Communications Earth and Environment**. Due to journal requirements, the methods section is included as a supplement.

Title: Deadly coupling - hazard impacts of pyroclastic density currents exacerbated by mesoscale particle clusters

Authors: Daniel Uhle[1], Gert Lube[1], Eric C.P. Breard[2], Eckart Meiburg[3], Josef Dufek[4], James Ardo[1,5], Jim Jones[6], Susanna Jenkins[7], Ermanno Brosch[1], Luke Fullard[7], Lucas Corna[1]

[1] School of Agriculture and Environment, College of Science, Massey University, Palmerston North, New Zealand

[2] School of Geosciences, University of Edinburgh, UK

[3] University of California Santa Barbara, Santa Barbara, USA

[4] Department of Earth Sciences, University of Oregon, Eugene, USA

[5] Manaaki Whenua- Landcare Research, Palmerston North, New Zealand

[6] School of Food and Advanced Technology, College of Science, Massey University, Palmerston North, New Zealand

[6] School of Food and Advanced Technology, College of Science, Massey University, Palmerston North, New Zealand

[7] Earth Observatory Singapore, Singapore

[8] Horizons Regional Council, Palmerston North, New Zealand

3.1 Abstract

Causing one-third of all volcanic fatalities, pyroclastic density currents create far greater destruction than we can currently explain scientifically. Opportunities to interrogate the mechanisms behind this hazard have long been desired, but real-world flows persistently defy direct internal observation. Here, we show, through the first high-resolution measurements of dynamic pressure in large-scale experiments, that pressure maxima exceed maximum theoretical values used in hazard assessments derived from estimates of bulk flow velocity and density by more than one order of magnitude. These distinct pressure excursions occur through the clustering of particles with high particle Stokes numbers at the peripheries of coherent turbulence structures and from the direct impact of these particles with structures. Together, they generate significant loading and piercing impacts to life and infrastructure. They account for up to 75 percent of local flow energy and must be considered in hazard models that aim to forecast and mitigate volcanic risk globally.

3.2 Introduction

Pyroclastic density currents (PDCs) are lethal and recurrent hazards from volcanoes (Sulpizio *et al.*, 2014, Dufek *et al.*, 2015, Neri *et al.*, 2015, Lube *et al.*, 2020). Over 500 million people are directly endangered by these multiphase flows of hot volcanic particles and gas (Valentine, 1987, Valentine, 1998, Baxter *et al.*, 2005, Lube *et al.*, 2011, Auker *et al.*, 2013, Cronin *et al.*, 2013, Lube *et al.*, 2014, Dufek, 2016). Over the past decade alone, and despite strong advances in understanding volcanic hazards, PDCs have caused several thousand fatalities and significant damage to infrastructure globally (Auker *et al.*, 2013). So,

how can we learn to predict PDC hazards accurately? The key hazard agents of PDCs are the volcanic particles carried inside them. PDCs fuel a 'wicked armory': as the main driver of PDC motion, the abundance of particles relative to gas, characterizing the flow density, in contrast to the density of the ambient atmosphere, controls flow speed, destructive power, and reach (Elghobashi, 1994, Burgisser *et al.*, 2005, Dellino *et al.*, 2010, Meiburg and Kneller, 2010, Andrews and Manga, 2011, Andrews and Manga, 2012, Jenkins *et al.*, 2013, Breard *et al.*, 2015, Cole *et al.*, 2015, Baxter *et al.*, 2017, Steel *et al.*, 2017, Brosch *et al.*, 2022). Carrying most of the thermal energy, particles are also responsible for PDC burn hazards, while the readily respirable particles cause inhalation injury and asphyxia (Eisele *et al.*, 1981, Baxter *et al.*, 2017). To model and mitigate against PDC hazards, we must understand the behavior of particles better, more specifically, their motion and sedimentation inside PDCs (Lube *et al.*, 2020).

However, a fundamental roadblock hinders this endeavor: the motion of particles within a PDC is modified through complex, long-hypothesized, but poorly understood one-way to four-way coupling mechanisms between particle and gas phases (Breard *et al.*, 2016, Breard and Lube, 2017, Sweeney and Valentine, 2017, Breard *et al.*, 2018, Weit *et al.*, 2018, Lube *et al.*, 2020). Unlike a homogenous suspension of particles in a fluid, these interactions modify the flow and turbulence structure in PDCs, leading to particle clustering, lubricating forces, and enhanced sedimentation (Esposti Ongaro *et al.*, 2007, Breard *et al.*, 2016, Lube *et al.*, 2019, Brosch and Lube, 2020, Neri *et al.*, 2021, Calabrò *et al.*, 2022). Recent advances through large-scale PDC experiments discovered that these interactions focus particles, and thus mechanical and thermal energies, into large eddies, turbulence mesoscale structures, and internal gravity waves (Brosch *et al.*, 2021). However, how the feedback mechanisms between particles and gas, within and across coherent turbulence structures, control the

runout and hazard behavior of PDCs remains unknown. The most advanced numerical multiphase PDC models cannot yet capture the turbulent particle-gas interactions across all relevant length scales and at the non-isotropic turbulence of PDCs (Dufek and Bergantz, 2007a, Dufek and Bergantz, 2007b, Dufek *et al.*, 2007, Esposti Ongaro *et al.*, 2007, Dufek and Manga, 2008, Dufek *et al.*, 2009, Esposti Ongaro *et al.*, 2012, Carcano *et al.*, 2014, Lube *et al.*, 2020, Neri *et al.*, 2021, Calabrò *et al.*, 2022). The opportunity to explore the multiphase physics of PDCs has long been desired, but their ferocity hampers direct observation and measurements of their internal characteristics.

An important example of the large uncertainties for hazard planning that result from this gap in understanding is the destruction-causing dynamic pressure of PDCs. To estimate local values of dynamic pressure, researchers have systematically mapped the degree of damage to structures in the aftermath of volcanic eruptions (Valentine, 1998, Baxter *et al.*, 2005, Jenkins *et al.*, 2013, Lerner *et al.*, 2022). Another approach uses relationships between sediment transport and resulting deposit characteristics in turbulent fluid flow to estimate local time-averaged flow velocity and density values, which define dynamic pressure (Dioguardi and Dellino, 2014, Mele *et al.*, 2015). Recently, direct measurements in large-scale experiments, natural PDCs, and snow avalanches demonstrated that turbulent excursions in velocity and density, which together define dynamic pressure, exceed field- and theory-derived pressure estimates (Brosch *et al.*, 2021). While this finding demonstrates the importance of turbulent multiphase flow in volcanic hazard assessments, it also raises caution about the applicability of current approaches that use (time) average flow properties.

These fundamental and applied research challenges are not unique to PDCs but are thought to govern hazard impacts caused by snow avalanches, dust storms, and the debris-laden basal parts of tornados and accidental explosions. In this study, we present the first high-resolution

direct measurements of destruction-causing dynamic pressure in large-scale PDC experiments to interrogate how dynamic pressures form and evolve in PDCs. We show that the generally assumed cause of hazard impacts of dynamic pressure, through the loading force of a continuum fluid onto an obstacle, accounts for only a fraction (as low as 25 percent) of the total dynamic pressure. Maximum values and a much wider spectrum of pressure result from piercing-like impacts of those individual particles, whose characteristic response time to fluid motion is equal to or smaller than the characteristic time-scale of fluid motion. Through this, we refine our understanding of the origin and evolution of hazard impacts of pyroclastic density currents that necessitate a re-evaluation of current hazard assessment strategies.

3.3 Results

3.3.1 Synthesizing pyroclastic density currents and measuring dynamic pressure in large-scale experiments

Over the last decade, the development of several large-scale experimental facilities to synthesize scaled analogs of PDCs (Esposti Ongaro *et al.*, 2020, Lube *et al.*, 2020) created a novel approach to studying their internal flow characteristics under safe conditions. The experimental apparatuses in Italy (Dellino *et al.*, 2007) and New Zealand (Lube *et al.*, 2015), which use heated natural volcanic material, lend themselves to interrogating the scaled fluid mechanic and thermodynamic processes inside fully turbulent PDC analogs. Here, we report the results of direct dynamic pressure measurements inside large-scale experimental PDCs conducted at the New Zealand facility PELE (the Pyroclastic flow Eruption Large-scale Experiment) (Lube *et al.*, 2015). At PELE, experimental PDCs are generated by the controlled gravitational collapse of a suspension of hot volcanic particles and air from an

elevated hopper into an instrumented runout section. For the experiments reported here, we used a 0.7 m^3 hopper in which a 124 kg mixture of natural volcanic particles was heated to 120°C (the ambient temperature was 15°C) over a period of 72 h to allow for thermal equilibration and evaporation of residual moisture inside the pre-dried mixture.

The volcanic material comprises a mixture of two well-characterized deposits of pyroclastic density currents of the 232 CE Taupo eruption in New Zealand (Wilson, 1985). The main components of the mixture are highly vesicular pumice, glass shards, free crystals, and rare lithic particles. The mixture has a weakly bimodal grain-size distribution ranging from 2 µm to 16 mm, with a main mode at 250 µm and a minor mode at 11 µm. The particle density distribution ranges from c. 300– 2,600 $kg \cdot m^{-3}$ and is skewed towards low densities. Further details of the material characteristics are provided in Supplementary Figure 1 and the Methods section.

The hopper is lifted to a vertical drop height of 7 m. It is mounted onto four load cells recording its mass discharge, which in this case lasts c. 4.6 s at an average discharge rate of c. 27 $kg \cdot s^{-1}$. On impact into a 0.5 m-wide and 12 m-long flume with a slope of 6°, the aerated particle-air mixture forms a channelized dilute gravity current with an initial front velocity of c. 5.5 $m \cdot s^{-1}$ and, on average, the particle volume concentration of c. 0.25 vol. %. The flow is characterized by a leading, c. 1.1– 2 m thick gravity current head, which is trailed by a gravity current wake that overlies a c. 0.9– 1.6 m thick gravity current body, and followed by a c. 1.8– 3.5 m thick gravity current tail region (Figure 3.1 a and b). Downstream of the inclined flume section, the experimental PDC propagates to 17 m along a horizontal, 0.5 m wide channel-confined section before spreading across an unconfined horizontal concrete pad. Around 8 s after impact, the vertically density-stratified current has propagated 23.5 m, slowed to c. 0.5 $m \cdot s^{-1}$ and has emplaced approximately 99.7% of its

total deposit volume. At 24 m, the depth-and time-integrated particle volume concentration has decreased to values smaller than 0.01 vol. % due to both deposition and entrainment of ambient air; the current becomes positively buoyant and finally ascends as a series of thermals along the flow length (Supplementary Movie 1).

To investigate the origin and evolution of dynamic pressure inside the experimental PDCs, seven vertical, wing-shaped profiles with up to six piezo-electric dynamic pressure sensors were placed into the flow centerline at runout distances of 1.8, 3.35, 5.4, 9.6, 12, 16 and 20 m (Figure 3.1 c). Measurements of time (t)-variant dynamic pressure $P_{dyn}(t,z)$ are recorded at a frequency of 1 kHz and are complemented by measurements of time series, in vertical profiles, of flow velocity $u(t,z)$, flow density $\rho_C(t,z)$, flow temperature and flow grain-size distribution, where z is the height above the flow base in the direction perpendicular to the slope (see Section 3.5 for details). Flow velocity components $u(t,z)$ are measured using high-speed video at 0.5 kHz through the flume's tempered glass sides. The sidewalls introduce boundary effects that are not present in unconfined real-world flows and in the flow centerline of the experimental flows where the dynamic pressure is measured. We minimize these boundary effects through the use of hydraulically smooth sidewalls (i.e., the thickness of laminar layer/wall roughness < 5) while the flow's Reynolds number, which is inversely related to the thickness of the viscous boundary layer, is high ($Re = 1.5 \cdot 10^6$). Velocity data, together with measurements of time-variant and height-variant grain-size distribution, flow density, and temperature, allow to calculate independent dynamic pressures, defined as:

$$P_{dyn\_Bernoulli} = \frac{1}{2}\rho_C|u|^2, \qquad \textit{EQN. 3-1}$$

where $|u|$is the magnitude of the local time-variant velocity.

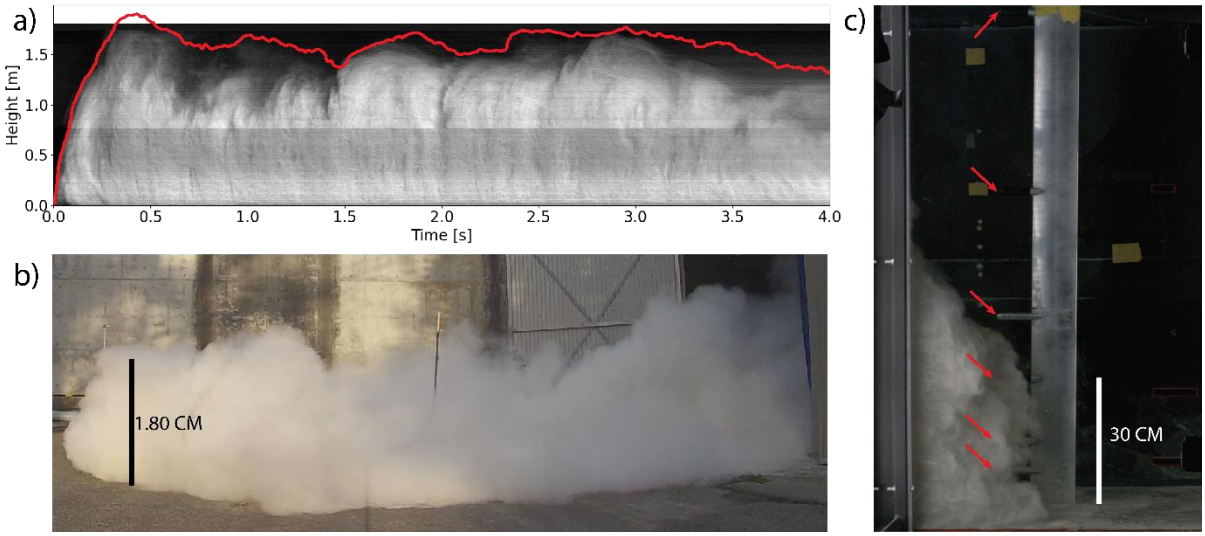

Figure 3.1 Simulation and dynamic pressure measurements of pyroclastic density currents in large-scale experiments. *a) lateral view of the experimental PDC during channel-confined propagation along a proximal measurement profile, which is located at* 1.8 *m downstream from impact of the hot mixture of volcanic material and air with the channel. The height-time kymograph of pixel intensity of the monochromatic flow structure is obtained by stacking vertical profiles of pixels recorded with a high-speed camera at the static observer location. Pixel brightness correlates positively with, both, bulk flow particle volume concentration and the abundance of highly reflective coarse-grained pumiceous glass shards and plagioclase crystals. The red line shows the time-variant height of the upper flow boundary. At this location, the density current structure is fully developed, comprising a leading head with a wake in its rear and a trailing density current body. The density current tail region is not shown. b) lateral view of the frontal c.* 7 *m of the advancing experimental PDC across the unconfined distal runout section approximately* 1.5 *m before buoyancy reversal. c) snapshot of the front of the experimental PDC approaching one of the wing-shaped vertical profiles of dynamic pressure sensors. The shape of the wings is designed to reduce flow detachment and formation of a turbulent wake behind the profile. The sensing elements of the piezoelectric dynamic pressure sensors protrude upstream from the wing into the approaching density current (marked by red arrows).*

The scaling Table 3-1 shows that the experimental PDCs generated under these conditions scale well to natural, fully dilute, fully turbulent PDCs (i.e., pyroclastic surges or blasts).

Amongst the non-dimensional products of characteristic length-, time- and temperature-scales, we highlight the Reynolds number (comparing inertial and viscous forces) reaching values of $1.5 \cdot 10^6$, Stokes number (characterizing particle coupling to turbulent flow) of $10^{-3} - 10^{10}$, Stability number (comparing time scales of particle settling and turbulent fluid motion) of $10^{-2} - 10^{1}$, Richardson number (characterizing the stability of stratification in turbulent flows) of $10^{-2} - 10^{1}$, and thermal Richardson number (assessing the ratio of forced and buoyant convection) of $0.02 - 4.5$. The overlap of ranges in Reynolds, Stokes, and Stability numbers in experimental and natural PDCs ensures that the complete range of particle-gas feedback mechanisms and turbulent particle transport is reproduced.

Table 3-1 Comparison of the scaling of natural dilute pyroclastic density currents and experimental pyroclastic density currents in PELE large-scale experiments. *Scaling is based on non-dimensional products characterizing the bulk flow with regards to the Reynolds number, the Richardson number, the thermal Richardson number, the Froude number, the Stokes number, the Stability number, and the Rouse number. h is the flow height; ρ_c is flow density, ρ_a is ambient density, and $\Delta\rho$ is the difference between flow and ambient densities; ΔT is the temperature difference between the flow and ambient air; u_T is the terminal fall velocity of particles; Δu is the eddy rotation velocity; u_s is the shear velocity; δ is the eddy diameter; α is the thermal expansion coefficient of air, μ_C is the dynamic viscosity of the flow, g is acceleration due to gravity, g' is the reduced gravity, K is the von Karman constant and Θ is the slope of the substrate. Values for natural PDCs from Druitt (1998), Choux and Druitt (2002), and Burgisser et al. (2005). The flow dynamic viscosity description is from Wohletz (1998). Table modified from Brosch et al. (2021).*

Parameter	Meaning	Definition	Generated PDCs	Natural PDCs
Particle Size		d	2 µm $-$ 16 mm	10^{-6} $-$ 10^{-1} m
Particle density		ρ_s	350 $-$ 2600 kg $/m^3$	300 $-$ 2600 kg $/m^3$

Ambient Density		ρ_a	1.06 $-$ 1.225 kg $\cdot$ m^{-3}	0.6 $-$ 1.2 kg $\cdot$ m^{-3}
Flow density		ρ_c	1.27 $-$ 10 kg /m^3	
Flow Temperature		T	15 $-$ 60 °C	
Velocities		u	$\leq$ 10.5 m $\cdot$ s^{-1}	10 $-$ 200 m $\cdot$ s^{-1}
Flow dynamic viscosity		$\mu_c=\mu_a\left(1+\frac{\rho_s C_s}{\rho_a(1-C_s)}\right)^2$	$3\times10^{-5}-3\times10^{-3}$ $\frac{\text{kg}}{\text{s m}}$	$10^{-5}-4\times10^{-3}$ $\frac{\text{kg}}{\text{s m}}$
Kinetic energy density		$U_{kin}=\frac{1}{2}\rho_c u^2$	$10^{-2}-10^3$ $\frac{\text{kg}}{\text{m s}^2}$	10^3-10^4 $\frac{\text{kg}}{\text{m s}^2}$
Buoyant thermal energy density		$U_T=\rho_c\frac{C_{p_c}}{C_{p_a}}\alpha\ T\ h\ g$	$10-10^3$ $\frac{\text{kg}}{\text{m s}^2}$	10^3-10^4 $\frac{\text{kg}}{\text{m s}^2}$
Reynolds number	$\frac{\text{Inertial Forces}}{\text{Viscous Forces}}$	$Re=\frac{\rho_c\ u\ h}{\mu_c}$	1.5×10^6	$33\times10^5-6.7\times10^9$
Richardson number	$\frac{\text{Buoyancy Term}}{\text{Flow Shear Term}}$	$Ri=\frac{\Delta\rho\ h\ g}{\mu_c}$	$10^{-2}-10$	$0-10$
Froude number	$\frac{\text{Inertial Forces}}{\text{Gravitational Forces}}$	$Fr=\frac{u}{\sqrt{g'\ h\ cos(\theta)}}$	$0.75-2$	≈1
Particle Stokes number	$\frac{\text{Characteristic Time Particle}}{\text{Characteristic Time Fluid}}$	$St=\frac{u_T\Delta u}{\delta g}$	$10^{-3}-9.9$	$11\times10^{-4}-97\times10^6$
Stability number	Defines particle transport zones	$\Sigma=\frac{u_T}{\Delta u}$	$13\times10^{-3}-32$	$2.8\times10^{-6}-9.7\times10^9$
Rouse number	Characterises turbulent particle transport regimes	$P=\frac{u_T}{ku_s}$	$66\times10^{-2}-19$	$10^{-3}-10^2$

Thermal Richardson number	$\frac{\text{Buoyancy Term}}{\text{Flow Shear Term}}$	$Ri_T = \frac{\Delta T\ \alpha\ h\ g}{u^2}$	2×10^{-2} $-$ 4.5	$0\ -\ 5$

3.3.2 Two types of dynamic pressure

Figure 3.2 a and b depict a typical example of the time series of dynamic pressure inside the experimental PDCs (here for the vertical profile 2 at a runout distance of 3.35 m at approximately mid-flow height of 0.45 m from the flow base). The spectrum of measured dynamic pressures ranges over five orders of magnitude with a local time-integrated value of 45 Pa and maximum values of several kilopascals. The wide range between average and maximum pressures and the absolute values of recorded maximum pressure are surprising. A recent analysis of dynamic pressure in experimental PDCs using measurements of flow velocity and flow density and EQN. 3-1 showed that turbulent fluctuations in velocity and density generate dynamic pressures that exceed average values by a factor of 3–5 (Brosch *et al.*, 2021). This coincides with our measurements of dynamic pressure through velocity and density time series (that is $P_{dyn\_Bernoulli}$) and EQN. 3-1 giving maximum and average values of 79 and 24 Pa, respectively (i.e., a ratio of c. 3.3). In stark contrast, time-averaged (45 Pa) and maximum dynamic pressures (4830 Pa) recorded by the dynamic pressure sensors (Figure 3.2 a) differ more than two orders of magnitude. They can, therefore, not be explained by turbulent fluctuations in velocity and density of the multiphase flow. Thus, from the perspective of understanding and mitigating the hazard impacts of PDCs, an important question arises on the origin and nature of these unexpectedly large pressures.

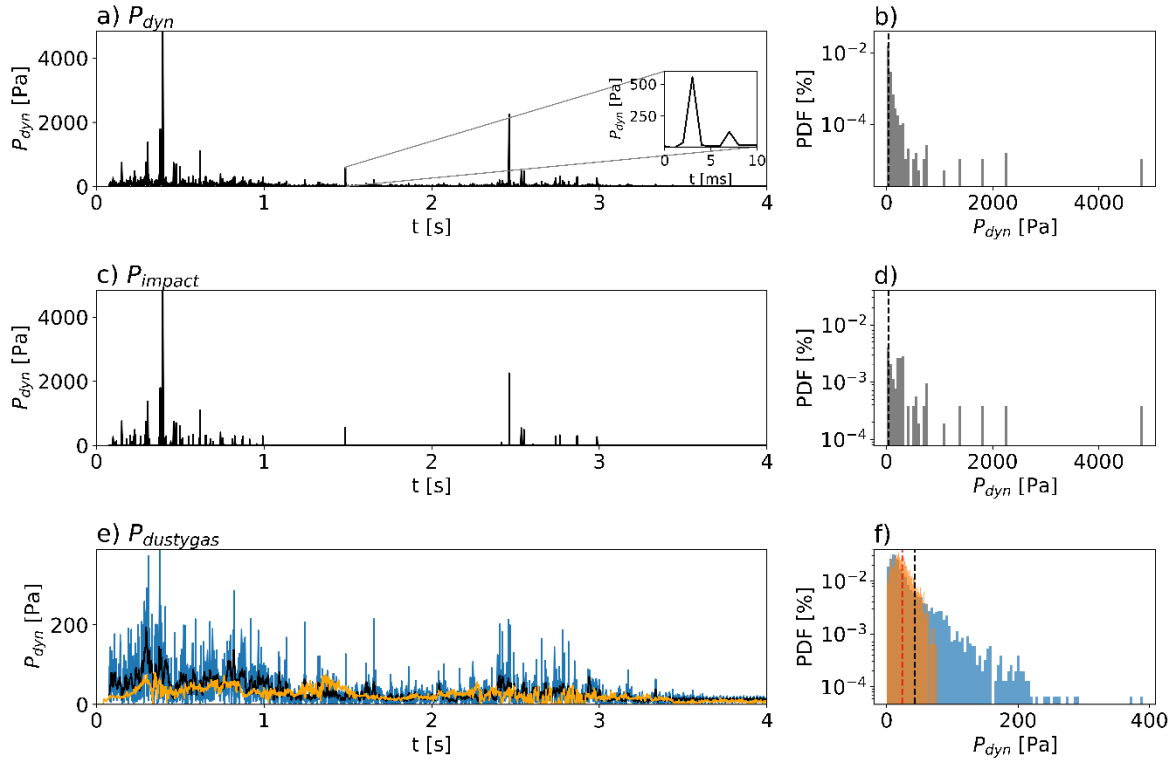

Figure 3.2 Two types of dynamic pressure and their probability density spectra. All measurements of dynamic pressure shown in this figure are obtained at the location of 3.35 m from impact at a height 0.45 m above the flow base. a) variation of the entire dynamic pressure P_{dyn} as a function of time as recorded by piezoelectric sensor and the corresponding probability density function shown in b). The pressure signal of P_{dyn} shows abundant near-instantaneous high-pressure peaks of several hundred to thousands of Pascal, which are characterized by pressure increases in less than one millisecond followed immediately by a pressure decrease in less than one millisecond. The inset highlights an example of one of the near-instantaneous high-pressure signals, which are associated with impacts from individual particles with the pressure sensor. c) Variation of the partial dynamic pressure signal P_{impact} as a function of time recorded by the piezoelectric sensor, which shows only those parts of the entire pressure signal P_{dyn} that are associated with near-instantaneous pressure peaks. d) shows the probability density function of P_{impact}. e) Variation of the partial dynamic pressure signal $P_{dusty\ gas}$ as a function of time, which is the dynamic pressure of the continuous dusty gas phase computed as the difference between $P_{dyn}(t)$ and $P_{impact}(t)$ via EQN. 3-2. The black line shows a 20 ms average of the time series $P_{dusty\ gas}$ (depicted in blue). The orange line shows the corresponding time

series of the dynamic pressure $P_{Bernoulli}$, computed independently from time series of flow velocity and flow density via Eq. (1). f) probability density functions of $P_{dusty\ gas}$ (blue) and $P_{Bernoulli}$ (orange).

An important clue is given by the form of those pressure signals that exceed the theoretical values of dynamic pressure calculated through turbulent fluctuations of flow velocity and density (EQN. 3-1). These high-pressure signals are characterized by an instantaneous pressure increase to a maximum in less than one millisecond followed by an immediate pressure decrease in less than one millisecond (inset of Figure 3.2 a). Furthermore, we determined that in all occurrences of these near-instantaneous high-pressure signals, the rate of pressure change with time is always larger than c. $220\ \mathrm{Pa \cdot ms^{-1}}$. These characteristics in the form of pressure signals are consistent with the impacts of individual particles with the pressure sensor. Considering particle diameters and size-averaged particle densities determined from flow samples and local velocities measured in the high-speed video, theoretical values of dynamic pressure caused by impacts of individual particles can be estimated (Supplementary Note 1 and Supplementary Figure 3.2). At time-averaged local velocities, impacts of particles with diameters larger than c. $100\ \mu\mathrm{m}$ generate dynamic pressures larger than $500\ \mathrm{Pa}$, and thus, considerably larger than theoretical values of dynamic pressure calculated through turbulent fluctuations of flow velocity and density and EQN. 3-1. Maximum measured values of dynamic pressure (for instance, 4.8 kPa at profile 2) can be explained as impacts of both low-density pumiceous particles with particle diameters larger than c. 2 mm and abundant high-density plagioclase particles with particle diameters larger than c. $600\ \mu\mathrm{m}$. Hence, the near-instantaneous high-pressure signals are explained by individual particle impacts.

This finding allows a sub-division of the total dynamic pressure signal P_{dyn} into the dynamic pressure associated with impacts from individual particles P_{impact} (Figure 3.2 c and d) and the dynamic pressure of the (continuous) dusty gas phase $P_{dusty\ gas}$ (Figure 3.2 e) where:

$$P_{dyn} = P_{dusty\ gas} + P_{impact}. \qquad \textit{EQN. 3-2}$$

Probability density functions of the thus derived dynamic pressure of the dusty gas phase $P_{dusty\ gas}$ and the dynamic pressure $P_{dyn\_Bernoulli}$ derived from flow velocity and flow density (via EQN. 3-1) coincide markedly well (Figure 3.2 f). This justifies the subdivision of the total dynamic pressure into its continuous dusty gas, $P_{dusty\ gas}$, and particle impact, P_{impact}, components. Furthermore, the piezo-electric signal of the dynamic pressure sensor has a superior temporal resolution (1 kHz) in comparison to the time series of dynamic pressure $P_{dyn\_Bernoulli}$ computed, via EQN. 3-1, from time series of flow density data (with a sampling rate of 20 Hz) and velocity (sampled at 0.5 kHz). Thus, the piezo-electric signal shows a much more detailed record of the dynamic pressure of the continuous dusty gas phase in the high-pressure end of its spectrum.

Despite the big differences in pressure ranges between the dynamic pressures of the dusty gas phase (up to 390 Pa at profile 2) and particle impacts (up to 4.8 kPa at profile 2), the probability density functions and the time series of both signals and hence that of the total dynamic pressure, share two characteristics: First, the pressure distributions are strongly skewed towards large pressures (Figure 3.2 b, d and f). Second, the highest pressures and highest occurrences of large pressures occur during passages of the head (c. 0–1 s in Figure 3.2 a, c, and e) and distal body regions (c. 2.4–3 s in Figure 3.2 a, c, and e) of the experimental PDC. For the dynamic pressure of particle impacts P_{impact}, time series of the

rate of particle impacts f_{impact} (number of particle impacts per unit time) provide further insights (Figure 3.3 e-h). Along flow runout, the rate of particle impacts, at approximately mid-flow height (i.e., at $z = 0.45$ m), decays strongly from more than 275 Hz at a distance of 1.8 m, to 95 Hz at 5.4 m, and no recorded impacts at 9.6 m and beyond (Figure 3.4). This suggests that dynamic pressure signals associated with impacts from individual particles are limited to particles with a critical minimum momentum. We note that the pattern of decay of the number of particle impacts with runout distance is similar to the decay of particles with diameters of 125–500 µm in flow samples (Figure 3.4). This grain-size range constitutes the coarse tail of flow grain-size distributions in proximal to distal runout reaches. Interestingly, this is also the particle size range characterized by intermediate particle densities between rare, large, low-density particles and highly abundant but small high-density particles (Supplementary Figure 3.1).

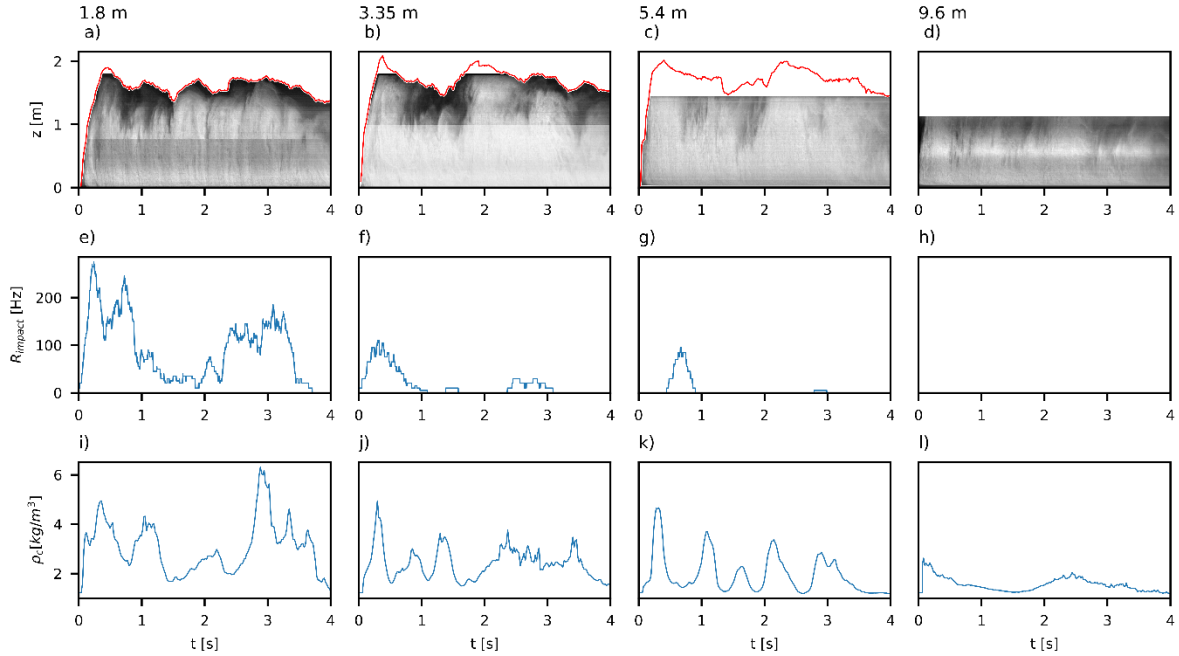

Figure 3.3 Spatiotemporal variation of the frequency of particle impacts. *a–d) Height-time kymographs (also see Figure 3.1 a) of the monochromatic flow structure at four different flow runout distances (*1.8, 3.35, 5.4, *and* 9.6 *m from impact). The flow height is marked in red. e-h) time-series of the frequency of particle impacts* f_{impact} *at the four different distances. The frequency strongly declines with distance. i-l) time-series of the depth-integrated flow density* $\overline{\rho_C(t)}$ *at the four different distances. The regular low-frequency oscillations in flow density are positively correlated in time with the fluctuations of particle impact rates.*

The low numbers of particle impacts at medial to distal profile locations limit further analysis. However, at the proximal profiles, impact numbers are sufficiently large to see that the rate of impacts obeys a regular low-frequency oscillation (Figure 3.3 e), which is positively correlated in time with a low-frequency oscillation in flow density (Figure 3.3 i and j).

Supplementary Figure 3.3 depicts a time series of particle impacts in binary form (that is: times during which an impact occurs are assigned a value of 1, and times where no impacts occur a value of 0). This shows that if a particle impact occurs, it is typically followed by multiple further impacts. By contrast, isolated single-particle impacts are rare. The mean of

the number of successive (in other words, clustered) impacts ranges from 2– 14 impacts with an average number of clustered impacts of c. 4.

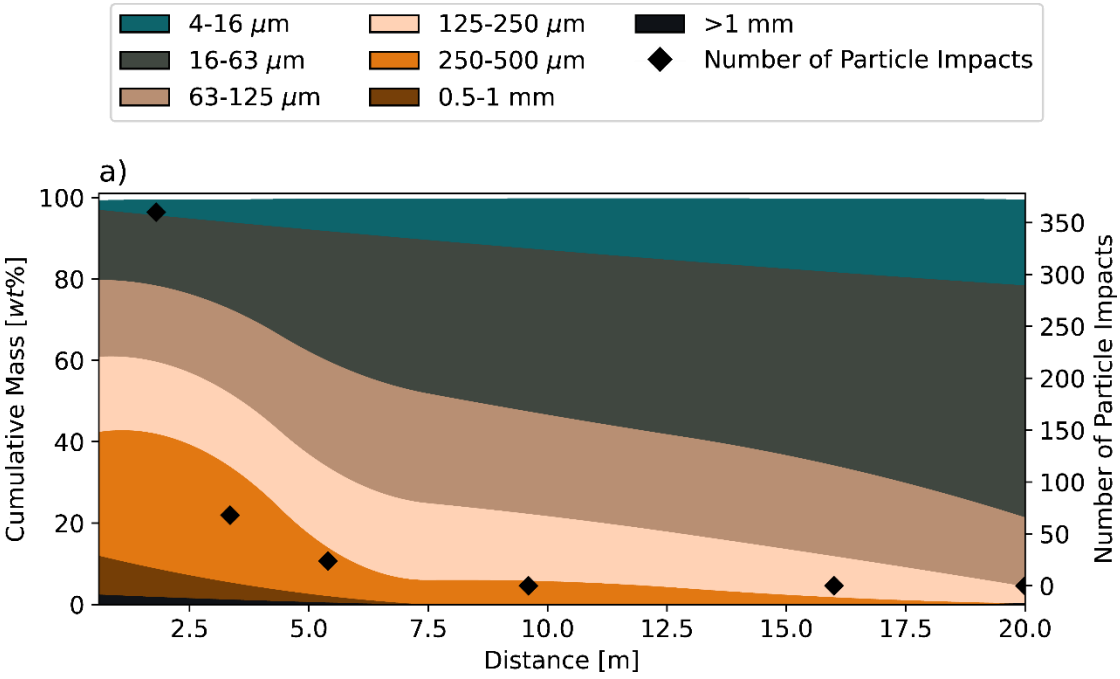

Figure 3.4 Spatial evolution of particle impacts and flow grain-size distribution. *The number of particle impacts with the piezoelectric dynamic pressure sensors at mid-flow height (*0.45 *m from the flow base) as a function of flow distance (black diamond symbols). In comparison, the time-integrated cumulative grain-size distribution of the flow captured in flow samplers at heights of* 0.45 *m is shown as a function of flow distance. The decrease of particle impacts with distance follows a similar trend as the decay of particle sizes* 125– 500 μ*m in flow samples. Particles with diameters larger than* 2 *mm (not shown) completely sediment from the flow by c.* 1.8 *m; particles with diameters* > 1 *mm and* > 500 μ*m sediment from the flow at distances of c.* 5 *m and c.* 7.5 *m, respectively.*

3.3.3 Energy spectra of dynamic pressure from particle impacts and dusty gas

Recently, low-frequency oscillations in flow density, velocity, and, hence, dynamic pressure have been linked to the occurrence of large-scale coherent turbulence structures inside experimental and real-world PDCs and snow avalanches (Brosch *et al.*, 2021). The

frequency f of the most energetic coherent structure in a turbulent flow is given by the Strouhal number Str as

$$Str = f\frac{L}{U}, \qquad \textit{EQN. 3-3}$$

where L and U are the flows' characteristic length- and velocity- scales (Strouhal, 1878, Turner, 1969). For highly turbulent flow conditions with Reynolds numbers $Re > 10^5$, the Strouhal number approaches a constant value of approximately 0.3 (Brosch *et al.*, 2021). In our high-Reynolds number experimental dilute PDCs ($Re = 1.5 \cdot 10^6$), the measured main frequencies of flow density oscillations (c. 1.26 Hz (i.e., a period of 794 ms) and dynamic pressure of particle impacts (c. 1.33 Hz (a period of 752 ms)) coincide closely and correspond with the period of the visually observed occurrences of the largest flow structures (Supplementary Figure 3.3). Substituting the experimentally determined frequency $f \sim 1.3$ Hz, the time-averaged height of the gravity current body region $L \sim 1.15$ m and the time-averaged flow velocity $U \sim 4.76\, m \cdot s^{-1}$ into EQN. 3-3, gives a Strouhal number $Str = 0.31$ close to the commonly observed value.

The energy peak associated with the most energetic coherent structures, at a frequency of $f \sim 1.3$ Hz, is clearly visible in the energy spectra of the total dynamic pressure P_{dyn}, the dynamic pressure of particle impacts $P_{impacts}$ and the dynamic pressure of the continuum dusty gas phase $P_{dusty\ gas}$ at the top of their respective energy cascades (orange bars in Figure 3.5). The energy of $P_{dusty\ gas}$ decreases strongly with increasing frequency, up until c. 7 Hz, consistent with the transfer of turbulent kinetic energy (per unit volume) to smaller scales of coherent structures (Figure 3.5 c). By contrast, the energy of particle impacts (Figure 3.5 b) and the energy associated with the total dynamic pressure (Figure 3.5 a) show

a markedly flatter decay of pressure energy with increasing frequency (and decreasing length-scale of coherent turbulence structure). Importantly, the maximum energy values of both, $P_{impacts}$ and P_{dyn}, which also exceed the energy values of the most energetic coherent structures at $f = 1.3$ Hz, occur across a defined band of frequencies f of c. $7 - 16$ Hz (grey bars in Figure 3.5 a and b). The wavenumbers associated with this frequency band correspond to length scales of c. $0.25 - 0.6$ m (Figure 3.5 d and e).

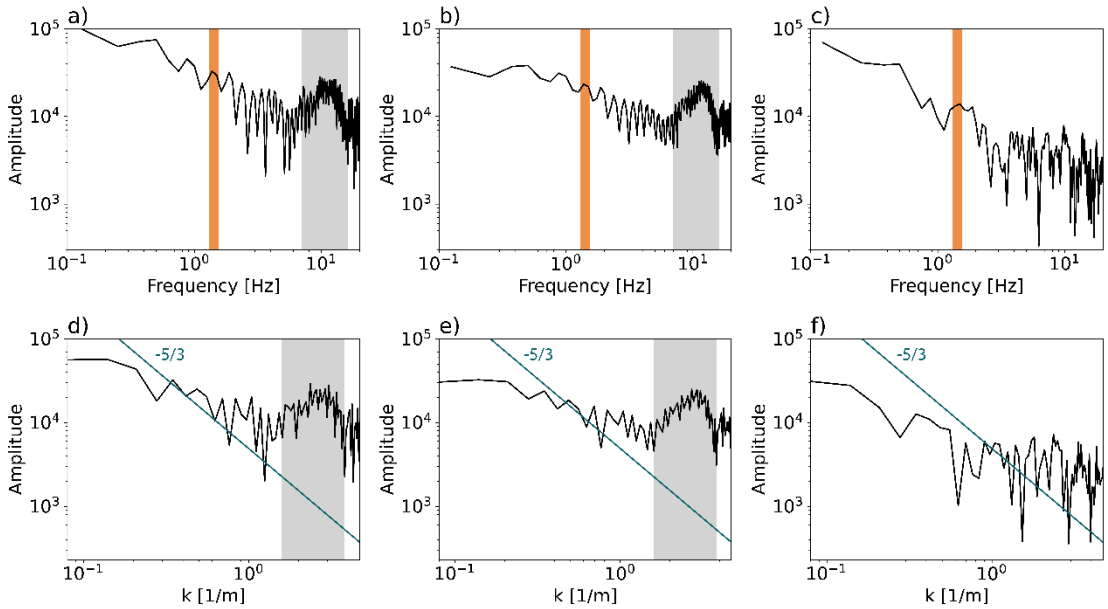

Figure 3.5 Energy spectra of dynamic pressure in Fourier space. *a–c) Energy spectra of dynamic pressure against frequency for P_{dyn} (a), P_{impact} (b) and $P_{dusty\ gas}$ (c). Energy peaks at a frequency $f \sim 1.3$ Hz associated with the largest coherent structures are highlighted by an orange bar. The highest-pressure energies occur in P_{dyn} (a) and P_{impact} (b) across a narrow band of frequencies f_{max} from c. $7 - 16$ Hz highlighted by a grey bar. d–f) Energy spectra of dynamic pressure against wavenumber k for P_{dyn} (d), P_{impact} (e) and $P_{dusty\ gas}$ (f). For P_{dyn} and P_{impact}, the high-energy band associated with f_{max} is highlighted by grey bars. This band corresponds to the wavenumber of c. $1.\bar{6} - 4\ m^{-1}$ or length-scales of coherent structures k^{-1} of c. $0.25 - 0.6\ m$. The green line with slope of $-5/3$ shows the Kolmogorov scaling of the inertial range.*

3.3.4 The multiphase origin of dynamic pressure fluctuations

We hypothesize that the origin of the unusually high and temporally clustered dynamic pressures is rooted in the concentration of particles at the peripheries of coherent turbulence structures. PDCs are characterized by extremely wide ranges of characteristic length- (c. eight orders of magnitude) and time scales (c. three orders of magnitude) (Burgisser *et al.*, 2005). They also comprise a broad spectrum of particle sizes (approximately five and six orders of magnitudes in our experimental and natural dilute PDCs, respectively) and a wide range of particle volume concentration (excluding concentrated, dense granular-fluid regimes, this spans from c. 10^{-5}–$3 \cdot 10^{-1}$ vol. %). Together, these characteristics allow for a wide spectrum of gas-particle feedback mechanisms from simple one-way coupled suspensions where the motion of particles is affected by the motion of the fluid phase but not vice versa, over two-way coupled particle-gas systems where particle-gas interactions can modify the flow and turbulence structure, to four-way coupling that strongly alters the flow structure also leading to inter-particle lubrication and collision forces (Elghobashi, 1994, Breard *et al.*, 2016, Weit *et al.*, 2018, Lube *et al.*, 2019, Lube *et al.*, 2020). The degree of coupling of particles to turbulence structures can be approximated through the particle Stokes number St, defined as

$$St = \frac{\tau_p}{\tau_\varepsilon}, \qquad \textit{EQN. 3-4}$$

where τ_p is the characteristic timescale of particles and τ_ε is the turbulence timescale. Particles with low Stokes numbers $St \ll 1$ are well coupled with the fluid phase and tend to follow the fluid motion; particles with $St \sim 1$ accumulate at the margins of coherent turbulence structures, while high Stokes number particles $St \ll 1$ are decoupled from fluid turbulence and move independent of the turbulence motion (Burgisser and Bergantz, 2002).

For the condition $St = 1$ of particles concentrating at the peripheries of coherent structures, it follows:

$$\tau_p = \tau_\varepsilon \leftrightarrow \tau_p^{-1} = f_\varepsilon, \text{ and} \qquad \textit{EQN. 3-5}$$

$$\leftrightarrow f_\varepsilon = \tau_p^{-1} = \frac{18\rho_F \nu_F F}{\rho_P d^2}, \qquad \textit{EQN. 3-6}$$

where f_ε is the frequency associated with this condition, ρ_F and ρ_P are fluid and particle densities, respectively, ν_F is the kinematic viscosity of the fluid, F is the Stokes drag factor as defined by Clift and Gauvin (1971) (see Section 3.5) and d the particle diameter. EQN. 3-6 and our experimental data of the particle size-averaged particle density $\overline{\rho_P(d)}$ can be combined to calculate the critical frequency $f_\varepsilon(d)$ of particle clustering at margins of coherent structures as a function of particle diameter (Figure 3.6 a). For the polydisperse volcanic mixture used in our experiments (Supplementary Figure 3.1), these critical frequencies range over four orders of magnitude from $3 \cdot 10^{-1} - 4 \cdot 10^{3}$ Hz. However, the particle sizes associated with the measured energy maximum in $P_{impacts}$ and P_{dyn}, at $f_{\varepsilon\_max} \sim 7 - 16$ Hz (Figure 3.5 a and b), constitute a narrow band of particle diameters of $117 - 229$ µm (grey horizontal bar in Figure 3.6 a). In flow samples, this particle size range occupies the coarse tail of grain size distributions (Figure 3.6 b). Due to sedimentation of the strongly vertically density stratified current, the proportion of particles larger than 117 µm strongly decreases from c. 60 wt. % in the initial mixture to c. 8 wt. % at a flow distance of 20 m (Figure 3.4 and Figure 3.6 b). Similarly, the dynamic pressure energy associated with particle impacts $P_{impacts}$, which, at a runout distance of 1.8 m, accounts to c. 75 % of the total dynamic pressure P_{dyn}, decreases strongly downstream approximately following a power law decay (Figure 3.6 c).

The largest particle size supported by turbulence in the experimental flows, which is limited by the characteristic length- and velocity-scales of the most energetic coherent turbulence structure (EQN. 3-3) and associated with a measured frequency $f \sim 1.3$ Hz, corresponds to c. 2 mm (black dashed line in Figure 3.6 a and b). Therefore, the experimental PDC strongly depletes in particles larger than 2 mm even before a proper gravity current structure has formed at around 1.8 m after impact. Particle sizes smaller than 2 mm (associated with the frequency of the largest coherent structure) but larger than $117-229$ µm (associated with the frequencies at the energy maximum of dynamic pressure f_{ε_max}) do not form notable peaks in dynamic pressure energy (Figure 3.5). This is explained by the rare abundance of particles of this size range, which occupy the coarse tail of flow grain size distributions (Figure 3.6 b).

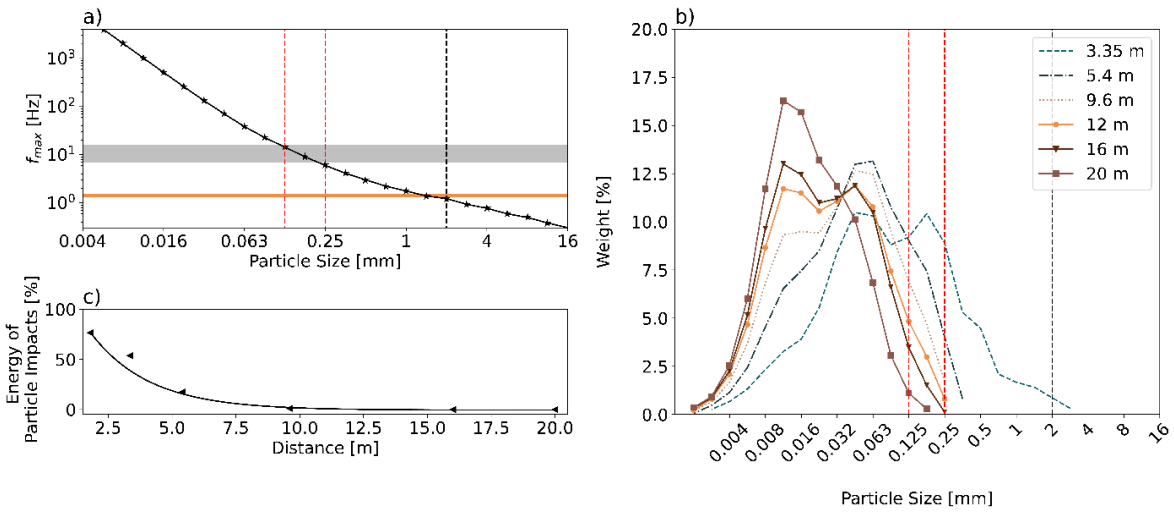

Figure 3.6 Particle sizes of critical Stokes numbers and their sequential sedimentation. *a) The frequency f_{max} associated with the condition of particle Stokes number $St = 1$ as a function of grain size. The grey horizontal bar depicts the frequency band in f_{max} of c. $7 - 17$ Hz of highest-pressure energies, the orange horizontal bar marks the largest coherent structures at c. 1.3 Hz. The two vertical dashed red lines delimit the experimentally determined corresponding critical grain sizes for $St = 1$ at f_{max} of c. $127 - 224$ µm. The red horizontal bar and the black vertical dashed line mark the frequency associated with the most energetic coherent flow structure at a frequency $f \sim 1.3$ Hz and the corresponding grain size of c. 2 mm, respectively. b) histograms of time-integrated flow grain size distributions captured in flow samplers at flow heights of 0.45 m above the flow base for various flow distances. As in (a), the two vertical dashed red lines delimit the grain-size range of c. $127 - 224$ µm associated with f_{max}, while the black dashed line marks the critical grain size of c. 2 mm supported by the most energetic coherent turbulence structures at $f \sim 1.3$ Hz. Note the downstream depletion of the flow in critical Stokes number particles associated with f_{max} (c. $127 - 224$ µm). c) The fractional time-integrated energy of particle impacts P_{impact} relative to the entire pressure energy P_{dyn} as a function of flow distance. The black line is a best-fit power law to the data.*

To visualize the process of clustering of particles with critical Stokes numbers at the margins of coherent turbulence structures, we conducted a numerical simulation of the experimental dilute PDC using an Eulerian-Eulerian approach with particle-fluid four-way coupling. In this multiphase simulation, five different particle sizes are modeled (2 mm, 0.5 mm,

0.125 mm, 0.032 mm, and 0.008 mm) whose relative proportions and particle size-dependent densities are the same as in the physical experiment (see Section 3.5 for details). Figure 3.7 depicts contour plots of particle volume concentration of the evolving current at approximately half of the total runout length for each particle size. High Stokes number particles (2 mm in diameter; Figure 3.7 a) do not highlight any coherent turbulence structures and have sedimented into the basal flow. Low Stokes number particles (0.032 mm and 0.008 mm in diameter; Figure 3.7 d and e) remain homogeneously suspended throughout the flow or tend to concentrate slightly in the central regions of coherent structures. By contrast, particles with diameters of 0.5 and 0.125 mm concentrate at the peripheries of eddies, highlighting the coherent turbulence structure of the flow (Figure 3.7 b and c). Similar to our physical experiment, the highest particle concentration in eddy peripheries occurs for particles with diameters of 0.125 mm. The average size of the large coherent structures (highlighted by concentrated margins) in the numerical simulation accounts for approximately 0.5 m (Figure 3.7 c). This corresponds with the length scales of c. 0.25– 0.6 m that are associated with the narrow band of maxima in dynamic pressure as seen in the energy spectra of dynamic pressure as a function of wavenumber (where the length-scale is the inverse of the wavenumber k; Figure 3.5 d and e).

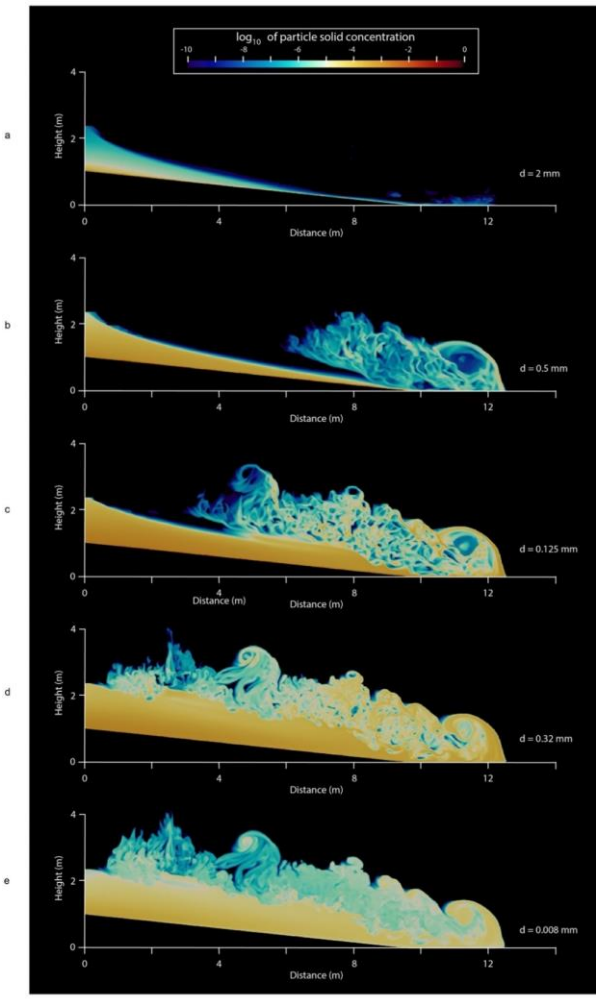

Figure 3.7 Clustering of critical Stokes number particles at the peripheries of coherent structures. *a-e) snapshots from a numerical multiphase Eulerian-Eulerian fluid particle four-way coupled simulation of the physical experiment at approximately mid-flow runout distance. The contour plots show the spatial variation across the simulated PDC in the particle concentration of five modeled grain sizes of* $2\ mm$ *(a),* $500\ \mu m$ *(b),* $125\ \mu m$ *(c),* $32\ \mu m$ *(d), and* $8\ \mu m$ *(e). Technical aspects of the numerical simulation are detailed in the Methods section. Particles with Stokes numbers* $St > 1$ *(a), which are only supported by turbulence at the scales of the largest coherent structures, have sedimented into the basal flow and do highlight any coherent structures at mid-flow runout. Particles with critical Stokes numbers* $St = 1$ *(b and c) concentrate at the peripheries of coherent structures. The effect is stronger for particle sizes of* $125\ \mu m$ *than for particle sizes of* $500\ \mu m$ *because of the significantly higher abundance of the* $125\ \mu m$ *particles over* $500\ \mu m$ *particles. Particles with low Stokes numbers* $St < 1$ *(d and e) tend to be homogeneously suspended or slightly concentrated in the central parts of coherent structures.*

3.3.5 Spatiotemporal evolution of dynamic pressure fluctuations

To assess the destruction potential of PDCs, volcanologists routinely use estimates of either bulk flow or local time-integrated flow velocity and density values to evaluate average dynamic pressures (Dufek, 2016). Our finding of the accumulation of particles with critical Stokes numbers (i.e., $St = \mathcal{O}(1)$,) at the peripheries of coherent turbulence structures imply strong fluctuations of dynamic pressure to occur at the characteristic frequency f_{ε_max} of these coherent structures. To prevent underestimation of the destruction potential of PDCs, it is important to understand how turbulent fluctuations of dynamic pressure around field-estimated average values evolve during flow propagation.

Figure 3.8 a compares the time-averaged dynamic pressure $P_{dusty\ gas\_ave}$, the maximum dynamic pressure of the continuum phase $P_{dusty\ gas\_max}$ and the maximum dynamic pressure associated with particle impacts P_{impact_max} as a function of flow distance. $P_{dusty\ gas\_ave}$ (i.e, the equivalent of the time-averaged loading pressure estimated in hazard assessments to assess damage to infrastructure) steadily decreases with flow distance D following a powerlaw of the form $P_{dusty\ gas\_ave} \propto 1/D$. By contrast, and up to 9.6 m, the maximum loading pressure $P_{dusty\ gas\_max}$ exceeds the time-averaged pressure by an order of magnitude. In distal reaches, D > 15 m, $P_{dusty\ gas\_max}$ starts to decline more strongly. Maximum dynamic pressures from particle impacts P_{impact_max} exceed $P_{dusty\ gas\_ave}$ by two orders of magnitude, strongly decline with distance and are restricted to the proximal flow reaches of $D \leq$ 5.6 m.

Figure 3.8 b shows the pressure ratio of $P_{dusty\ gas\_max}$ over $P_{dusty\ gas\_ave}$ against flow distance. This ratio assesses by how much current field-based estimates of dynamic pressure

underestimate actual turbulence-enforced maximum loading pressures and can be expressed as:

$$\frac{P_{dusty\ gas\_max}}{P_{dusty\ gas\_ave}} = \frac{\rho_{max}{U_{max}}^2}{\rho_{ave}U_{ave}^2}. \qquad \textit{EQN. 3-7}$$

The dynamic pressure ratio is independent of scale, and experimental estimates can be applied to natural flow scales. However, the spatiotemporal evolution of the dynamic pressure ratio is limited by the abundance of particles with $St = \mathcal{O}(1)$ inside the flows. Following the decoupling of high Stokes number particles from the margins of coherent structures, their motion is independent of fluid turbulence and results in their rapid sedimentation from the flow. Figure 3.8 b illustrates the evolution of the dynamic pressure ratio against flow distance in the experimental PDCs. Immediately following formation of a gravity current structure at c. 1.8 m and up to 5.6 m, the pressure ratio continuously increases from initial values of c. 11.8 to maxima of c. 13 in c. 0.74 s. This duration coincides with the characteristic eddy timescale of the largest coherent structure of $\tau_\varepsilon = 1/f \sim 1/1.3 = 0.77\ s$. This suggests that the characteristic timescale of the motion of high Stokes number particles from a homogeneous suspension into eddy peripheries can be estimated by the overturn time of the largest coherent structure.

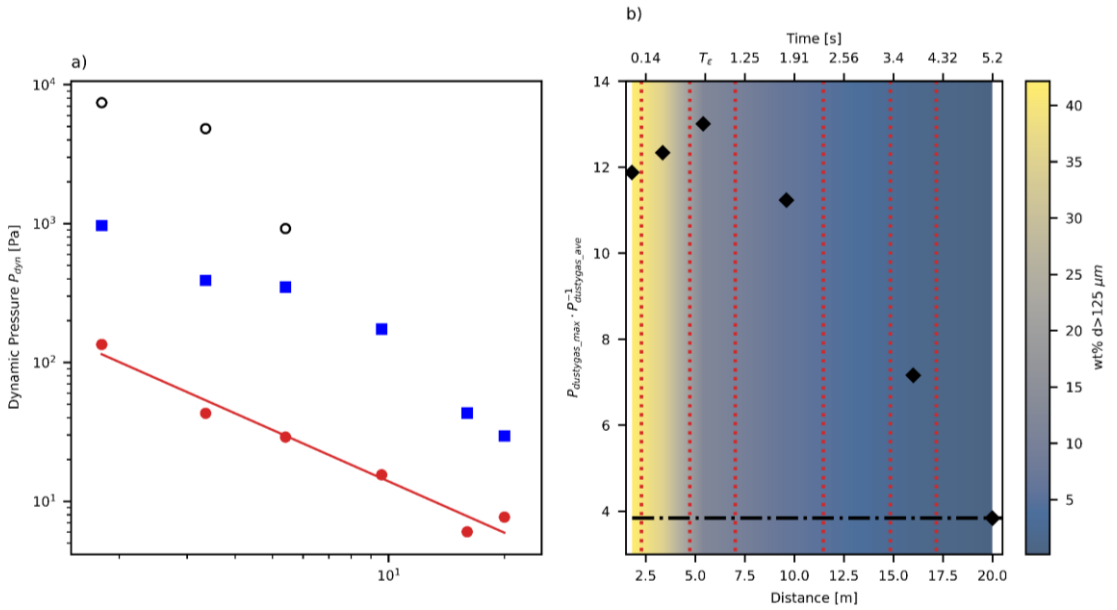

Figure 3.8 Spatiotemporal evolution of dynamic pressures during flow propagation. *a) Dynamic pressure as a function of flow distance D. The red circles show time-averaged values of dynamic pressure* $P_{dusty\ gas\_ave}$*. The red line is a best-fit powerlaw through the data that yields* $P_{dusty\ gas\_ave} = 136D^{-1.019}$*. The blue square symbols represent the maximum dusty gas pressure* $P_{dusty\ gas\_max}$*. The black circles show measurements of the maximum particle impact pressure* P_{impact_max}*. b) The ratio of time-integrated maximum and average dusty gas pressures* $P_{dusty\ gas}$ *as a function of flow distance (black diamonds), the underlay color shows the concentration of particles with diameters* > 125 μm *in weight percent, with red vertical dashed lines demark particle concentrations of* $40\ wt.\%$, $20\ wt.\%$, $10\ wt.\%$, $5\ wt.\%$, $2.5\ wt.\%$, *and* $1.25\ wt.\%$*. The secondary non-linear horizontal time axis depicts the times of flow front arrival corresponding to these distances. After the formation of a gravity current structure at c. 1.8 m and up until 5.4 m, the pressure ratio increases slightly to maximum values of around 13. The flow duration associated with this increase coincides with the eddy time scale* t_ε *highlighted on the secondary x-axis. Downstream from 5.4 m, the pressure ratio decreases in association with a reduction in the particle concentration of critical Stokes number particles larger than 125 μm, which is a function of distance as a colour contour plot. The horizontal dashed line corresponds to the condition predicted by EQN. 3-8 where the pressure ratio takes a critical value of c. 3.9, when the flow is depleted in particles with* $St \geq 1$.

After the time τ_ε, the abundance of particles with $St = \mathcal{O}(1)$ declines below 10 wt.%. This appears to be the limiting mass loading for maximum particle clustering to occur and,

downstream of 5.6 m, the pressure ratio decreases strongly. At 20 m, where the abundance of particles with $St = \mathcal{O}(1)$ is around 2 wt. %, the pressure ratio approaches a value of 3.84. In the case of exhaustion of $St = \mathcal{O}(1)$ particles carried inside the flow, EQN. 3-7 reduces to:

$$\frac{P_{dusty\ gas\_max}}{P_{dusty\ gas\_ave}} \sim \left(\frac{U_{max}}{U_{ave}}\right)^4, \qquad \textit{EQN. 3-8}$$

(see Supplementary note 2). Our velocity measurement of the maximum and average velocity at 20 m give a value of $(U_{max}/U_{ave})^4$ of 3.9 closely corresponding with the measured pressure ratio of 3.84.

3.4 Discussion

Current approaches to assess the destruction potential of pyroclastic density currents envisage the loading force of a continuum multiphase fluid of characteristic velocity and density across structural surfaces opposing flow direction (Valentine, 1998, Dioguardi and Dellino, 2014, Dufek, 2016, Lube *et al.*, 2020, Brosch *et al.*, 2021). In the absence of detailed measurements inside flows, volcanologists estimate local time-integrated values of flow velocity and density from deposit characteristics to guide assessments of potential hazard impact (Dioguardi and Dellino, 2014, Mele *et al.*, 2015). Our simulations of pyroclastic density currents through large-scale physical experiments and numerical modeling demonstrate a fundamental shortcoming of this approach: the modification of the flow and turbulence structure due to coupled feedbacks between particle and gas phases. Our large-scale experiments demonstrate that these feedbacks lead to the preferential clustering of large, high-momentum particles at the margins of coherent turbulence structures and

generate two different types of dynamic pressure that result in distinct hazard impacts (see Figure 3.9).

The first type, the dynamic pressure of the continuous dusty gas phase $P_{dusty\ gas}$, significantly exceeds the average dynamic pressure by more than one order of magnitude. The cause of these strong turbulent pressure fluctuations is the modification of the flow into coherent structures with high-density margins, spatially separating the flow into high-density (eddy peripheries) and lower-density domains (central regions of eddies). The size of the coherent structures, and hence the characteristic frequency of high-density/high dynamic pressure flow pulsing f_{ε_max}, is determined by the abundance of particles whose characteristic response time to fluid motion is equal to or smaller than the characteristic time-scale of changes in the fluid motion (that is, particle Stokes numbers $St \geq 1$). Depending on the mass loading of particles with this critical Stokes number condition, the ratio of the clustering-enforced maximum dynamic pressure $P_{dusty\ gas}$ and the field-estimated average pressure can range between c. $4-13$. To prevent an underestimation of the intensity of hazard impact, we strongly suggest that these factors are applied to conventional estimates of dynamic pressure that apply bulk values of flow velocity and density (Dioguardi and Dellino, 2014, Mele *et al.*, 2015). For instance, for two-story buildings, a mean dynamic pressure of 5–10 kPa results in failure or doors, while four-times larger maximum clustering-enforced dynamic pressures lead to failure of exterior building walls constructed from brick, stone or concrete (Valentine, 1998). Oscillation in dynamic pressure at the frequency f_{ε_max} further intensifies the destructiveness of flows due to the progressive structural weakening of materials amid repeated high-pressure loading.

The second type, the dynamic pressure of particle impacts P_{impact}, can exceed average dynamic pressures, even stronger than $P_{dusty\ gas}$, by two orders of magnitude. Unlike a

loading continuum pressure, this pressure results when particles with Stokes numbers $St \geq 1$ uncouple from the flow that engulfs a structure and directly impinge onto it. The resulting piercing pressure impacts can be seen as pockmarks onto trees and infrastructure and are illustrated for the case of the Merapi 2010 eruption in Supplementary Figure 3.5. Piercing dynamic pressure impacts from PDCs are also the likely cause for the failure of brittle structures such as glass windows. Current estimates of a continuous fluid loading pressure to explain window damage (Valentine, 1998) must thus be re-assessed to prevent false hazard prediction. Importantly, the large magnitude of particle impact pressures must be considered as a potential contributor to the high fatality and injury rates in PDC-forming eruptions.

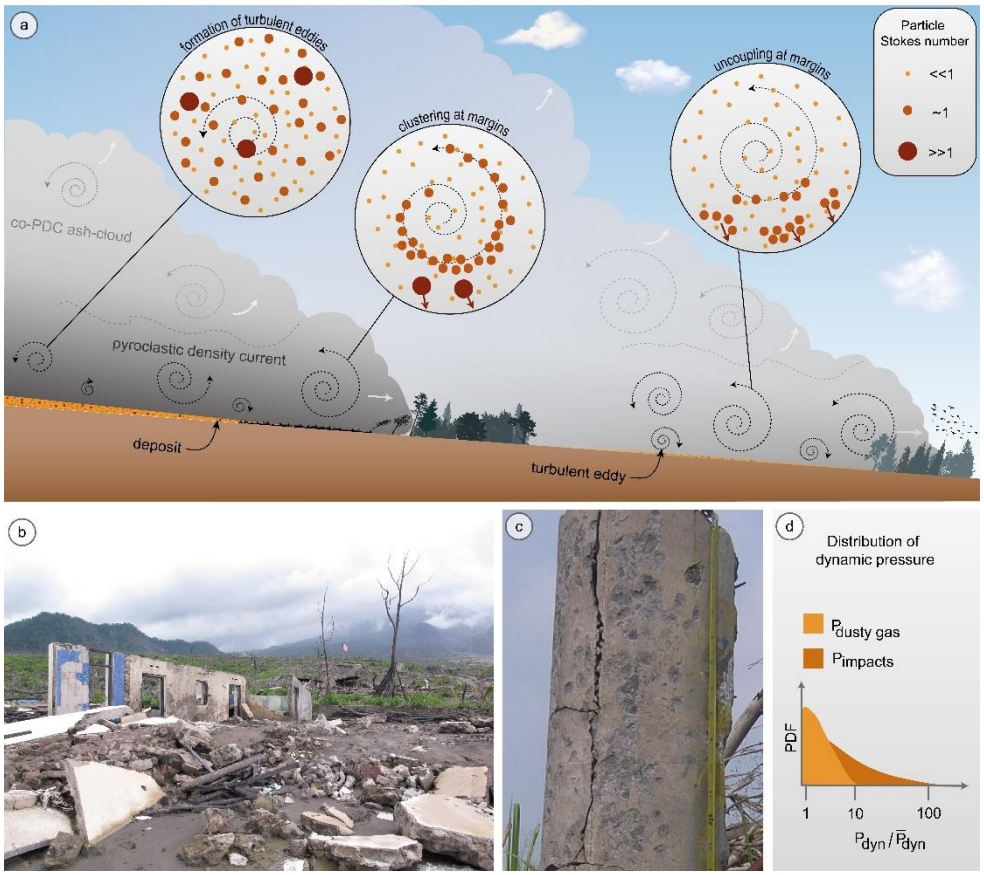

Figure 3.9 Effects of gas-particle feedback on pyroclastic density current hazards. a) Schematic sketch visualizing a dilute PDC propagating down the side of a volcano. The insets visualize the formation of vortices in proximal locations, how particles preferentially accumulate at the vortex boundaries, and finally are, decoupled and sediment from the dilute PDC. Abundance of particles shows further the increase of densities at vortex margins. b) Photo of typical destruction patterns caused by the dusty gas pressure $P_{dusty\ gas}$, showing complete destruction of a house besides flow parallel walls remaining due to their low area exposed to the destruction causing dynamic pressure. c) Pockmarks on an electricity pole showing a characteristic destruction pattern of particle impacts. d) Conceptual distributions of the dusty gas pressure $P_{dusty\ gas}$ and particle impact pressures $P_{impacts}$. Dusty gas pressures are predominantly low, with values reaching up to one magnitude higher than average pressures, whereas particle impact pressures extend the distributions and reach values up to two magnitudes larger than average dynamic pressure values $\overline{P_{dyn}}$.

Our experiments demonstrate the role of turbulent gas-particle feedbacks in modifying the flow and turbulence structure and exacerbating hazard impacts. These findings are also

applicable to other types of high-Reynolds number, polydisperse particle-gas flows, such as powder snow avalanches, dust storms, and the debris-laden basal flow regions of tornados and explosions and should be considered in the assessments of their potential hazard impacts.

3.5 Methods

3.5.1 Large-scale experiments

The Pyroclastic flow Eruption Large-scale Experiment (PELE), fully described in Lube *et al.* (2015), is an international test facility to synthesize, view, and measure inside pyroclastic density currents. Experimental PDCs of up to six tonnes of volcanic material and gas move at velocities of $7-32\ \mathrm{m}\cdot\mathrm{s}^{-1}$, are $2-4.5$ m thick and propagate to runout length of >35 m (Lube *et al.*, 2015). The currents are generated by the controlled gravitational collapse of variably diluted suspensions of pyroclastic particles and gas from an elevated hopper into an instrumented runout section. PELE is operated inside a 16 m high, 25 m long, and 18 m wide disused boiler house. The apparatus is composed of four main structural components: (i) Tower. A 13 m-high construct that lifts either a $4.2\ \mathrm{m}^3$ hopper (for moderate to high discharge rates of $300-1{,}500\ \mathrm{k}\cdot\mathrm{s}^{-1}$) or a $0.7\ \mathrm{m}^3$ hopper (for discharge rates of $30-200\ \mathrm{k}\cdot\mathrm{s}^{-1}$) to the desired discharge height. The hoppers are equipped with internal hopper heating units to heat the pyroclastic material to target temperatures of up to 400 °C. The heating process is monitored by thermocouples, and the hopper is mounted onto four load cells to capture the time-variant mass discharge. (ii) Column. A ≤ 9 m high shroud of heat-resistant cloth through which the discharged particle-air mixture accelerates under gravity. (iii) Chute. A 17 m long and 0.5 m wide multi-instrumented channel section with $0.6-1.8$ m high side walls of temperature-resistant glass. The first 12 m are variable adjustable to slope angle between 5° and 25° while the last 5 m of the channel is horizontal. (iv) Outflow. A

25 m-long flat instrumented, unconfined runout section extends outside the building. The physical properties of the particle-gas suspensions prior to impact with the channel (velocity, mass flux, volume flux, particle concentration), the characteristics of the solid components (grain-size distribution, particle density distribution, particle temperature), and boundary conditions (substrate roughness, chute slope, and channel width) can be modified to generate a wide range of reproducible natural flow conditions (Lube *et al.*, 2015, Brosch and Lube, 2020). For the experiments reported in this study, the small hopper with 0.7 m^3 is used to generate fully turbulent experimental PDCs with a basal bedload region but without a dense basal underflow, which would form at the high discharge rates in the large hopper setup condition.

The use of pyroclastic solids material and air is an important prerequisite to generate natural stress coupling between the fluid and solid phases. The pyroclastic material, containing particle sizes from 2 µm to 16 mm, consists of a mixture of two well-characterized ignimbrite deposits F1 and F2 from the 232 CE Taupo eruption(Wilson and Walker, 1982). The first component (F1) is a proximal medium-ash-dominated ignimbrite deposit with an unimodal grain-size distribution, a median diameter of 366 µm, and 4.5 wt. % of extremely fine ash (< 63 µm). The second component (F2) is a fine ash-rich facies from the base of the proximal Taupo ignimbrite deposit with a polymodal grain-size distribution, a median diameter of 103 µm, and 36.5 wt. % of extremely fine ash. The experiments reported in this study involve a material blend with F1= 60 wt. % and F2= 40 wt. % (the grain-size distribution is shown in Supplementary Figure 3.1 a), yielding a mixture with 20 wt. % of particles smaller than 63 µm. The main solids components of the pyroclastic material are highly vesicular pumice, glass shards, free crystals, and lithic particles. The relative

proportion of these components varies with grain size. The average particle density as a function of particle diameter is shown in Supplementary Figure 3.1 b.

The resulting experimental pyroclastic density currents are fully turbulent with Reynolds numbers in the lower 10^6 (and up to 10^7 in proximal regions). Dimensionless products quantifying the scaling similarity of natural and experimental currents for the bulk flow are depicted in Table 3-1. Further details of the experimental protocol, properties the volcanic material, and measurement techniques are reported in Lube *et al.* (2015) and Brosch and Lube (2020), but the measurements and analytical methods specific to the results presented here are detailed below.

3.5.2 Sensors and analytical methods

Twenty fast cameras (60– 120 fps) and three normal-speed cameras (24– 30 fps) positioned at different distances and viewing angles recorded the downstream propagation of the experimental pyroclastic density currents. At flow distances of 1.8 m, 3.35 m, 5.4 m, and 9.6 m, four highspeed camera profiles consisting of six highspeed cameras recorded vertical profiles of the passing flows at 500 fps. LED floodlight arrays were used to achieve sufficient and even illumination, which allowed for a detailed analysis of the gas-particle transport and sedimentation with particle image analysis (PIV; using the algorithm PIVlab (Thielicke and Stamhuis, 2014, Thielicke and Sonntag, 2021)). Two-dimensional velocity fields were derived with PIV from the highspeed videos at time intervals of 2 ms.

Time series of dynamic pressure $P_{dyn}(t)$ were measured with piezoelectric pressure sensors (PCB Piezotronics 106B51 and signal conditioners PCB 483C) at the flow centerline, at flow distances of 1.8 m, 3.35 m, 5.4 m, 9.6 m, 16 m, and 20 m from impact and were recorded at a sampling rate of 1 kHz. The pressure sensors, which comprise a circular, 15 mm

diameter, frontal steel diaphragm, were mounted into 0.1 m-long bullet-shaped encasing to reduce flow separation at the upstream-directed sensor head. The encased pressure sensors protruded out of 1.8 m-heigh wing-shaped profiles designed to reduce flow separation behind the profiles and to guide cabling. In this study, we report the results of dynamic pressure measurements obtained at approximately the mid-depth of the density current body region at a slope-normal height $z = 0.45$ m above the flow base.

At flow distances of 0.5, 1.8, 3.35, 5.4, 9.6, 12, 16, and 20 m from impact vertical arrays of transparent sediment samplers collected the flowing mixture. During the experiment, the sequential filling the flow samplers was filmed with highspeed cameras. These samplers are open on the upstream side, allowing the flow to enter through the 1.69 cm^2 cross-sectional area, while on the downstream side, a 16 μm mesh allows only the gas-phase of the flow to exit, leading to the accumulation of the transported particles inside the sampler. From this, we measure continuous data of flow sediment passing a position as a function of time. Downslope velocity components $u(t)$ of the flow at a position 5 cm upstream of each flow sampler were obtained through PIV. The weight and density of the material deposited inside the flow samplers was measured at selected time intervals to calculate the time-variant porosity of the captured sediment, as well as the sediment grain-size distribution. Particle solids-concentration C_S is defined as

$$C_s(z,t) = \frac{V_d\ (1-\varepsilon)}{u\ A_o t} \qquad \textit{Supplementary EQN. 3-1}$$

where V_d is the time-variant sediment accumulated volume inside the flow sampler, u is the time-variant downslope velocity obtained through PIV at the entrance of the flow sampler, A_0 is the cross-sectional area of the flow sampler, t the selected time intervals, ε the time-variant sediment porosity, and z the height in slope-perpendicular direction.

At each of the flow sampler locations, time-variant and height-variant temperature $T(z,t)$ is measured in vertical arrays of fast thermocouples (410-345 Type K). Together with the time-series of time-variant and height-variant flow velocity $u(z,t)$, grain-size distributions, volumetric particle concentrations $CS\,(z,t)$, the temperature time-series allow for the calculation of dynamic pressure $P_{dyn\_Bernoulli}$ defined by EQN. 3-1 where bulk flow density $\rho_C(z,t)$ is given by

$$\rho_C = C_S\rho_P + \frac{P_a}{\gamma_g R_g T}(1 - C_S) \qquad \textit{Supplementary EQN. 3-2}$$

where ρ_P is the particle density, P_A is the ambient pressure, γ_g is the mass fraction of the gas components (including moisture) and R_g their gas constants.

3.5.3 Energy spectra

Fourier spectra are computed via Fast Fourier Transform (FFT) using the Python implementation by Numpy (Harris *et al.*, 2020). Further, only the positive real output is considered due to the symmetry of the Fourier transform and physical meaning. The time axis (t) of the data is transferred into advected distances (x) by multiplication with time-averaged velocities ($x = \bar{u} \cdot t$), to calculate energy spectra with wave numbers. These data series are functions of advected distance. Using the Numpy implementation of the FFT spectra as a function of the wave number (inverse wavelength) are calculated. Also, for these spectra, only the real and positive output is considered.

The pressure data is sampled at 1 kHz, and time series with 8 s length are analyzed, providing a Nyquist frequency of 500 Hz and a frequency resolution of 0.125 Hz. Long time-series were used to improve the frequency resolution and capture the flow's natural

onset and fading. The advected data was analyzed for an 11.24 m advected distance at a resolution of ~1.4 mm. This provides minimum wave numbers and a wave number resolution of $0.09\,\mathrm{m}^{-1}$ and Nyquist wave numbers of $\sim 16 \cdot 10^4\,\mathrm{m}^{-1}$. Flow height measurements with 60 Hz lead to a Nyquist frequency of 30 Hz. The time series has a length of ~5.8 s, leading to minimum frequencies and a frequency resolution of ~0.17 Hz. Flow densities are recorded at 500 Hz for 4 s, leading to 250 Hz Nyquist frequencies and 0.25 Hz minimum frequency and frequency resolution. Greyscale data recorded at 500 Hz is analyzed for 3.5 s, producing 250 Hz Nyquist frequencies and ~0.29 Hz frequency resolution.

3.5.4 Multiphase flow simulation of the PELE experiments

Numerical simulations using the Eulerian-Eulerian approach, also known as the two-fluid method (TFM), were performed to reproduce the experimental currents. We employed the open-source Multiphase Flow with Interphase eXchanges (MFIX) solver, developed by the National Energy Technology Laboratory (NETL) within the US Department of Energy. This technique enables us to solve mass, momentum, and energy equations for both fluid and solid phases, capturing solid-fluid 4-way coupling. A comprehensive description of all equations can be found in Musser *et al.* (2021).

We executed the 3D flow simulation on the ARCHER2 cluster utilizing 1200 CPU cores with 3 Tb of RAM for 15 days, employing the large-eddy-simulations (LES) with the wall-adapting local eddy-viscosity subgrid model WALE of (Ducros *et al.*, 1998) to model subgrid turbulence. The initial and boundary conditions for the simulations were established based on the international benchmarking and validation exercise for PDC model. (Esposti Ongaro *et al.*, 2020)

The top boundary of the domain is described as a pressure boundary that creates a stratified "atmosphere". All other boundaries, except the inlet, follow the no-slip boundaries for the fluid phase and partial slip for the solid phase, following the work of Johson and Jackson (1987). The experimental geometry was uploaded in MFIX as an STL file upon which we created a roughness of approximately 0.01 m in height to emulate the basal boundary conditions. The mesh was cut to follow the geometry using the cutcell method. (Musser *et al.*, 2021)

The inlet boundary is treated as a mass inflow, where a flux of temperature, fluid and solid concentration, and velocity were prescribed. The continuous grain-size distribution of the experimental mixture was discretized in five bins of particles with a diameter of $2 \cdot 10^{-3}$ m, $5 \cdot 10^{-4}$ m, $125 \cdot 10^{-6}$ m, $32 \cdot 10^{-6}$ m and $8 \cdot 10^{-6}$ m. This representation preserves the mean size diameter D[3,2] (surface-mean diameter) and D[4,3] (volume-mean diameter) consistent with the experimental counterpart. We also discretized the solid density distribution into the same respective five bins to ensure accurate gas-particle coupling in the simulation. In order to match experiments closely, the inlet used time- and height-variant velocity, concentration, grain-size distribution, and temperature profiles described by Cerminara *et al.* (2021).

At the inlet, we assumed thermal and kinetic equilibria, resulting in uniform temperature and no-slip velocity across all phases in each inlet computational cell. However, the numerical simulation captured thermal and kinetic decoupling, dictated by particle Stokes number as shown in Figure 3.7. Using the finite volume method with a second-order solver and Superbee limiter, the MFIX solves mass, momentum, and energy equations. This approach allows us to derive the temperature, velocity, and concentration fields for the fluid and each

solid phase in each computation cell. The results were saved as binary VTK files, which were loaded in Paraview® v5.11 and subsequently exported as images.

3.6 Supplementary Material

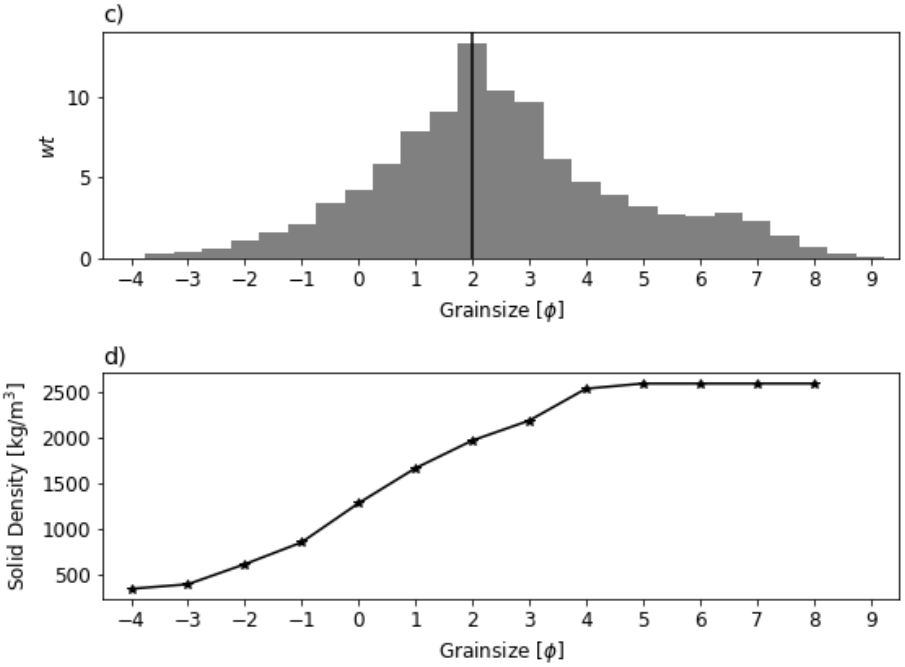

Supplementary Figure 3.1 Grain size and particle density distributions of the initial volcanic mixture. *a) grain size distribution of the initial mixture of volcanic material from the Taupo ignimbrite. b) density distribution as a function of particle diameter of the initial volcanic mixture.*

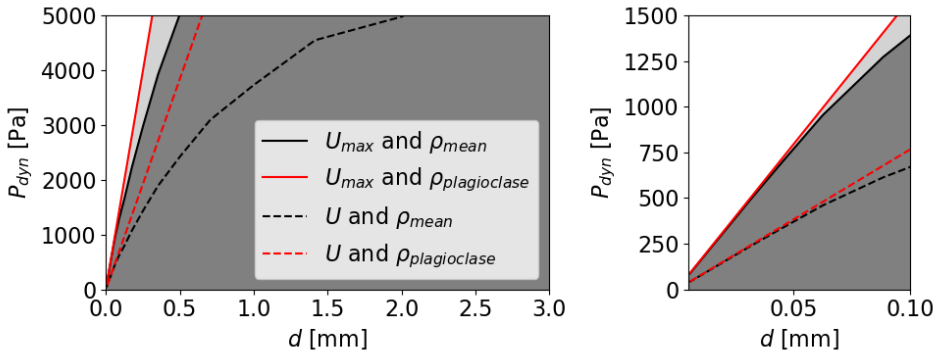

Supplementary Figure 3.2 Theoretical values of dynamic pressure due to particle impacts $P_{impact\ theoretical}$ in large-scale experiments. *$P_{impact\ theoretical}$ as a function of particle size using Supplementary EQN. 3-3. Results for two different experimentally determined particle velocity values are shown. The solid curves show theoretical impact pressure values for the case where particle velocity u takes the experimentally measured maximum values (at a flow distance of 3.35 m and 0.45 m above the flow base). The dashed curves illustrate the case where particle velocity u takes the experimentally measured time-averaged value (at a flow distance of 3.35 m and 0.45 m above the flow base). Solutions of Supplementary EQN. 3-3 using grain-size averaged particle density values (Supplementary Figure 3.1) are shown as black solid and dashed lines. Solutions of Supplementary EQN. 3-3 using a constant particle density of $2{,}650\ kg \cdot m^3$ to estimate $P_{impact\ theoretical}$ for abundant free crystals of plagioclase are shown as red solid and dashed lines. The estimated values of $P_{impact\ theoretical}$ indicate that maximum dynamic pressures recorded with the piezoelectric dynamic pressure sensors of up to $4{,}830\ Pa$ at this location, can be explained, at average flow velocities, as impacts of two types of particles: low-density, rare pumiceous particles larger than c. $1.5-2\ mm$ in diameter, and abundant free crystals of plagioclase that are larger than c. $0.6\ mm$ in diameter. The left panel shows an enlarged version of the right figure to highlight the variation of $P_{impact\ theoretical}$ with particle size at the lower end of dynamic pressures. This shows that, at average velocity, $P_{impact\ theoretical}$ exceeds values of $500\ Pa$, and thus maximum measured values of $P_{dusty\ gas}$ (i.e., $390\ Pa$ at $3.35\ m$ runout distance) and $P_{dyn\_Bernoulli}$ (i.e., $79\ Pa$ at $3.35\ m$ runout distance) for particles larger than approximately $0.1\ mm$ in diameter.*

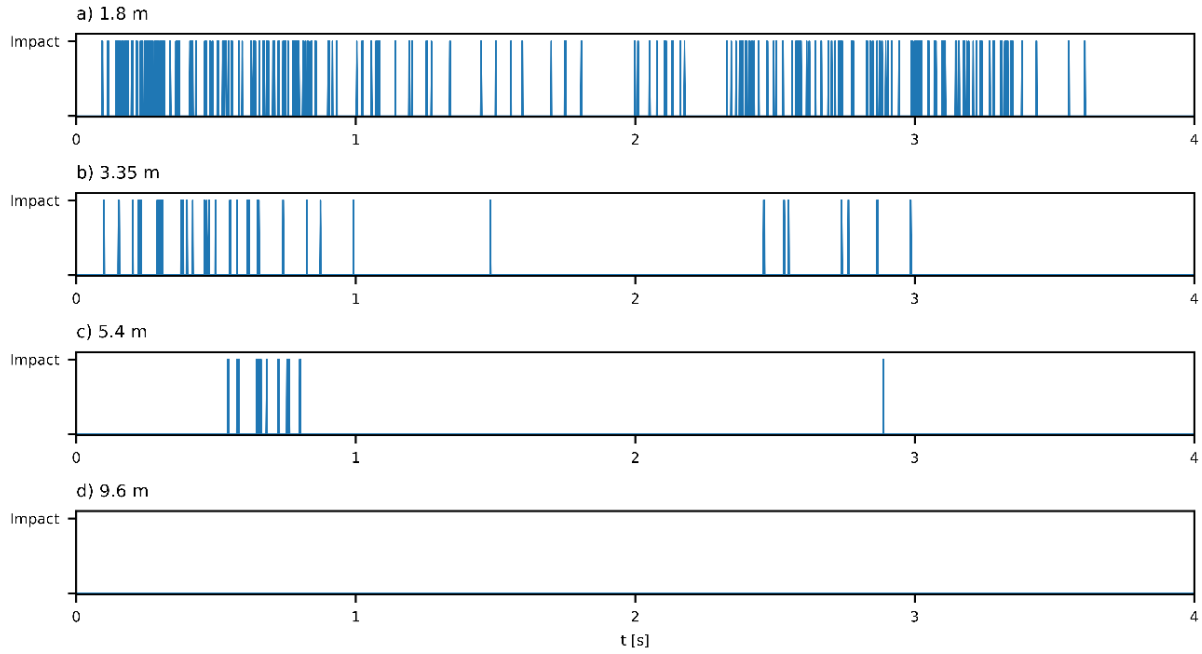

Supplementary Figure 3.3 Spatiotemporal characteristics of occurrences of particle impacts. *a-d) Time series of particle impacts at 0.45 m above the flow base at four different distances from impact:* 1.8 *m (a),* 3.35 *m (b),* 5.4 *m (c), and* 9.6 *m (d). Occurrences of particle impacts are shown in binary form. That is, times of impacts are assigned a value of* 1 *and times without impacts are assigned a value of zero. The number of particle impacts is strongly decreasing with flow distance, and no particle impacts are recorded at the position at* 9.6 *m. When particle impacts occur, they tend to occur in clusters of several successive impacts. Non-clustered particle impacts are rare. Most particle impacts occur in the head region (c.* 0 – 1 *s) and in the mid-body region (c.* 2.4 – 3 *s) of the experimental dilute PDC.*

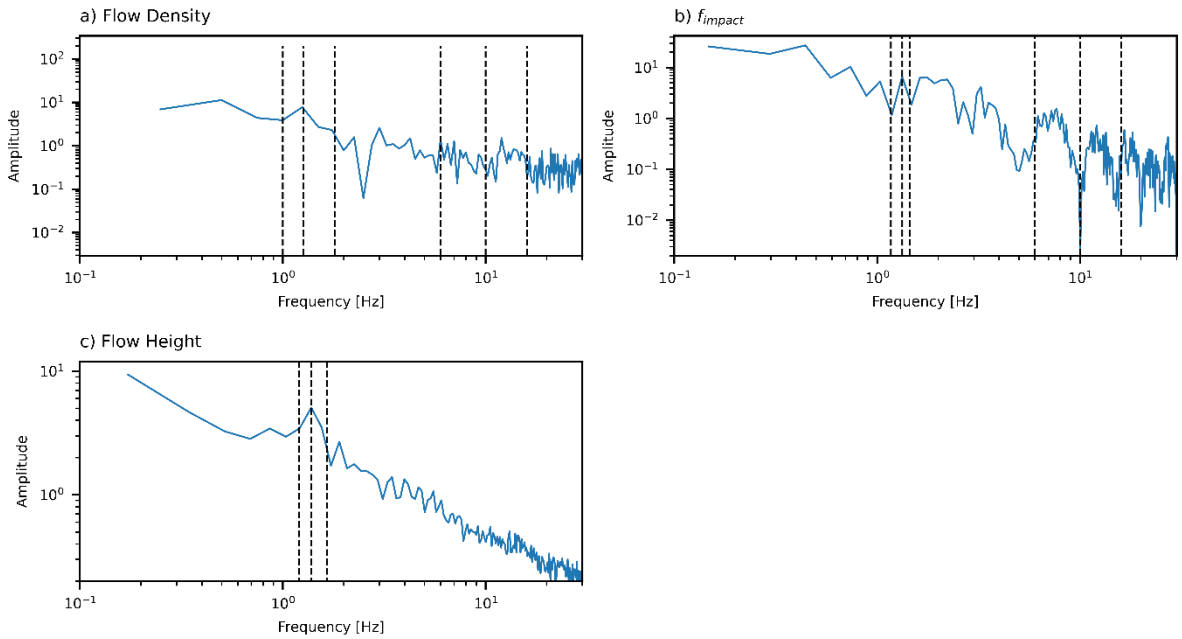

Supplementary Figure 3.4 Fourier spectra of flow density, particle impact rate, and flow height. *a-c) Fourier spectra of flow density (a), particle impact rate (b), and flow height (c). All spectra show a main amplitude peak at a frequency f ~ 1.3 Hz (red vertical bar), which coincides with the visibly observed period of the largest coherent structures of approximately* 700 – 800 *ms (Figure 3.4 a-c).*

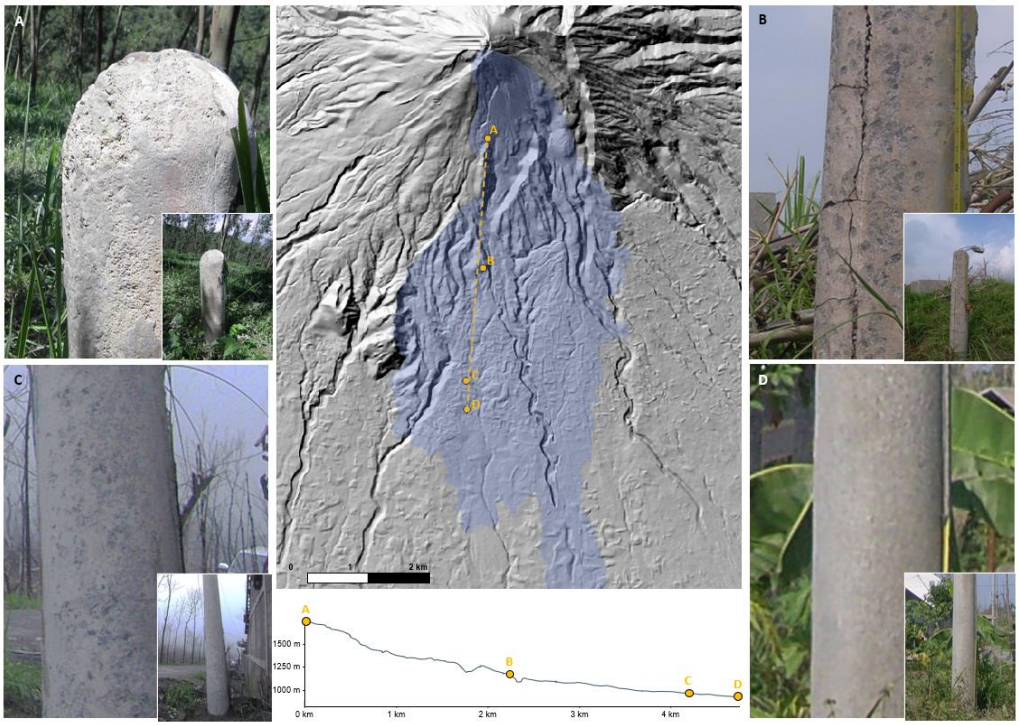

Supplementary Figure 3.5 Observed particle impacts at Merapi (Indonesia). *Reduced particle impact on concrete structures, with increased distance along flow: a) scoured concrete marker, with flow direction from left to right (August 2013); b) snapped and deeply pockmarked electricity pole, with flow direction from left to right (July 2011); c) lightly pockmarked electricity pole, tilted but not felled, flow direction into the photo (December 2010); and d) Upright electricity pole with little to no pockmarking, flow direction into the photo (July 2011). All photos S.F. Jenkins. The upper middle map shows the PDC outline from November 2010 in blue and the four photo locations, with the dashed line representing the elevation profile (no vertical exaggeration) shown below.*

3.6.1 Supplementary Note 1: Estimating dynamic pressure due to impacts by individual particles

The recorded time series of dynamic pressure include near-instantaneous high-pressure signals of several kPa (e.g., up to 4,830 Pa at 3.35 m runout distance; Figure 3.2 a). These high-pressure signals largely exceed maximum dynamic pressure of the dusty gas phase $P_{dusty\ gas}$ (e.g. 390 Pa at 3.35 m runout distance) obtained from direct high-resolution

piezoelectric measurements of dynamic pressure and EQN. 3-2, as well as maximum dynamic pressures $P_{dyn\_Bernoulli}$ (e.g., 79 Pa at 3.35 m runout distance) calculated through EQN. 3-1 using lower-resolution measurements of turbulent fluctuations of velocity and density of the multiphase flow.

The form of the near-instantaneous high-pressure signals suggest their origin as impacts of individual particles with the pressure sensors (see main text and Figure 3.2). Assuming, for simplicity, spherical particles, theoretical values of dynamic pressure due to particle impacts can be estimated from our measurements of flow velocity $u(t,z)$, particle diameter d and grain-size averaged particle density ρ_P obtained from flow samples as:

$$P_{impact\ theoretical} = \frac{4}{3}\rho_P d \frac{\Delta u}{\Delta t}, \qquad \textit{Supplementary EQN. 3-3}$$

where Δt is the time for an impacting particle to decelerate from flow velocity u to rest. To prevent the overestimation of $P_{impact\ theoretical}$, Δt is assigned a value of 1 ms coinciding with both the observed duration of the sudden pressure increases during the near-instantaneous high-pressure peaks and the maximum sampling frequency. The results from this analysis considering measured maximum and time-averaged values of flow velocity at the profile at a flow distance of 3.35 m at approximately mid-flow height (0.45 m above the flow base) are shown in Supplementary Figure 3.2.

3.6.2 Supplementary Note 2: Dimensional scaling of the ratio of maximum and time-averaged dynamic pressures $P_{dusty\ gas}$

In EQN. 3-7 in the main text, we express the ratio of maximum and time-averaged dynamic pressures of $P_{dusty\ gas}$, as it is only the time-averaged values that are estimated from field evidence and hence deviations are important to know for hazard assessments as:

EQN. 3-7 in the main text defines the ratio of maximum and time-averaged dynamic pressures of $P_{dusty\ gas}$ as:

$$\frac{P_{dusty\ gas\_max}}{P_{dusty\ gas\_ave}} = \frac{\rho_{max} {U_{max}}^2}{\rho_{ave} U_{ave}^2} \qquad \textit{Supplementary EQN. 3-4}$$

Field evidence only allows estimating bulk flow or local time-averaged dynamic pressure values. To prevent an underestimation of the destructiveness of PDCs in hazard assessments it is important to evaluate by how much turbulence fluctuations in dynamic pressure exceed time-averaged pressure values.

In Figure 3.8, we show that initially, the pressure ratio is increasing over a duration that coincides with the eddy timescale τ_ε of the largest coherent structure. We interpret this to suggest that τ_ε is the characteristic timescale for critical Stokes number particles (i.e., $St = 1$) to move to the peripheries of coherent structures where they concentrate relative to the average flow density. After a time τ_ε, the pressure ratio decreases monotonically, coinciding with the decrease in the volume fraction of critical Stokes number particles carried by the flow. That is when $St = 1$ particles eventually decouple from the peripheries of coherent structures and sediment through the flow unsupported by fluid turbulence.

The clustering of critical Stokes number particles at the peripheries of coherent structures represents a modification of the flow and turbulence structure into concentrated and less concentrated domains. These domains represent density discontinuities inside the flow. From gravity wave theory, density discontinuities in shallow flows, with thickness L, travel at the speed of gravity waves. Thus, for U_{max} and U_{ave} in EQN. 3-7 (also Supplementary EQN. 3-4) we may write:

$U_{max} \sim \sqrt{(\rho_{max} - \rho_{ambient})/\rho_{ambient}\, L}$, and $U_{ave} \sim \sqrt{(\rho_{ave} - \rho_{ambient})/\rho_{ambient}\, L}$, where $\rho_{ambient}$ is the density of the ambient air. In natural dilute PDCs and in our experimental dilute PDCs, $\rho_{max} \gg \rho_{ambient}$ and $\rho_{ave} \gg \rho_{ambient}$ and hence:

$$\frac{{U_{max}}^2}{{U_{ave}}^2} \sim \frac{\rho_{max}}{\rho_{ave}} \qquad \textit{Supplementary EQN. 3-5}$$

Substituting this relationship into Supplementary EQN. 3-4, which is EQN. 3-7 in the main text, yields:

$$\frac{P_{dusty\ gas\_max}}{P_{dusty\ gas\_ave}} \sim \left(\frac{U_{max}}{U_{ave}}\right)^4, \qquad \textit{Supplementary EQN. 3-6}$$

which is EQN. 3-8 in the main text.

3.7 References

Andrews, B.J. & Manga, M., 2011. Effects of topography on pyroclastic density current runout and formation of coignimbrites. *Geology*, 39**,** 1099-1102.

Andrews, B.J. & Manga, M., 2012. Experimental study of turbulence, sedimentation, and coignimbrite mass partitioning in dilute pyroclastic density currents. *Journal of Volcanology and Geothermal Research,* 225**,** 30-44.

Auker, M.R., Sparks, R.S.J., Siebert, L., Crosweller, H.S. & Ewert, J., 2013. A statistical analysis of the global historical volcanic fatalities record. *Journal of Applied Volcanology,* 2**,** 2.

Baxter, P.J., Boyle, R., Cole, P., Neri, A., Spence, R. & Zuccaro, G., 2005. The impacts of pyroclastic surges on buildings at the eruption of the Soufriere Hills volcano, Montserrat. *Bulletin of Volcanology,* 67**,** 292-313.

Baxter, P.J., Jenkins, S., Seswandhana, R., Komorowski, J.C., Dunn, K., Purser, D., Voight, B. & Shelley, I., 2017. Human survival in volcanic eruptions: Thermal injuries in pyroclastic surges, their causes, prognosis and emergency management. *Burns,* 43**,** 1051-1069.

Breard, E.C.P., Dufek, J. & Lube, G., 2018. Enhanced Mobility in Concentrated Pyroclastic Density Currents: An Examination of a Self-Fluidization Mechanism. *Geophysical Research Letters,* 45**,** 654-664.

Breard, E.C.P. & Lube, G., 2017. Inside pyroclastic density currents – uncovering the enigmatic flow structure and transport behaviour in large-scale experiments. *Earth and Planetary Science Letters,* 458**,** 22-36.

Breard, E.C.P., Lube, G., Cronin, S.J. & Valentine, G.A., 2015. Transport and deposition processes of the hydrothermal blast of the 6 August 2012 Te Maari eruption, Mt. Tongariro. *Bulletin of Volcanology,* 77**,** 1-18.

Breard, E.C.P., Lube, G., Jones, J.R., Dufek, J., Cronin, S.J., Valentine, G.A. & Moebis, A., 2016. Coupling of turbulent and non-turbulent flow regimes within pyroclastic density currents. *Nature Geoscience,* 9**,** 767-771.

Brosch, E. & Lube, G., 2020. Spatiotemporal sediment transport and deposition processes in experimental dilute pyroclastic density currents. *Journal of Volcanology and Geothermal Research,* 401**,** 106946.

Brosch, E., Lube, G., Cerminara, M., Esposti-Ongaro, T., Breard, E.C.P., Dufek, J., Sovilla, B. & Fullard, L., 2021. Destructiveness of pyroclastic surges controlled by turbulent fluctuations. *Nature Communications,* 12**,** 7306.

Brosch, E., Lube, G., Esposti-Ongaro, T., Cerminara, M., Breard, E.C.P. & Meiburg, E., 2022. Characteristics and controls of the runout behaviour of non-Boussinesq particle-laden gravity currents – A large-scale experimental investigation of dilute pyroclastic density currents. *Journal of Volcanology and Geothermal Research,* 432**,** 107697.

Burgisser, A. & Bergantz, G.W., 2002. Reconciling pyroclastic flow and surge: the multiphase physics of pyroclastic density currents. *Earth and Planetary Science Letters,* 202**,** 405-418.

Burgisser, A., Bergantz, G.W. & Breidenthal, R.E., 2005. Addressing complexity in laboratory experiments: the scaling of dilute multiphase flows in magmatic systems. *Journal of Volcanology and Geothermal Research,* 141**,** 245-265.

Calabrò, L., Esposti Ongaro, T., Giordano, G. & De' Michieli Vitturi, M., 2022. Reconstructing Pyroclastic Currents' Source and Flow Parameters From Deposit Characteristics and Numerical Modeling: The Pozzolane Rosse Ignimbrite Case Study (Colli Albani, Italy). *Journal of Geophysical Research: Solid Earth,* 127**,** e2021JB023637.

Carcano, S., Esposti Ongaro, T., Bonaventura, L. & Neri, A., 2014. Influence of grain-size distribution on the dynamics of underexpanded volcanic jets. *Journal of Volcanology and Geothermal Research,* 285**,** 60-80.

Cerminara, M., Brosch, E. & Lube, G., 2021. A theoretical framework and the experimental dataset for benchmarking numerical models of dilute pyroclastic density currents. *arXiv preprint*, https://arxiv.org/abs/2106.14057. .

Choux, C.M. & Druitt, T.H., 2002. Analogue study of particle segregation in pyroclastic density currents, with implications for the emplacement mechanisms of large ignimbrites. *Sedimentology,* 49**,** 907-928.

Clift, R. & Gauvin, W.H., 1971. Motion of entrained particles in gas streams. *The Canadian Journal of Chemical Engineering,* 49**,** 439-448.

Cole, P.D., Neri, A. & Baxter, P.J., 2015. Hazards from Pyroclastic Density Currents. *In* H. Sigurdsson (ed.) *The Encyclopedia of Volcanoes (Second Edition).* Amsterdam: Academic Press, 943-956.

Cronin, S.J., Lube, G., Dayudi, D.S., Sumarti, S., Subrandiyo, S. & Surono, 2013. Insights into the October–November 2010 Gunung Merapi eruption (Central Java, Indonesia) from the stratigraphy, volume and characteristics of its pyroclastic deposits. *Journal of Volcanology and Geothermal Research,* 261**,** 244-259.

Dellino, P., Buttner, R., Dioguardi, F., Doronzo, D.M., La Volpe, L., Mele, D., Sonder, I., Sulpizio, R. & Zimanowski, B., 2010. Experimental evidence links volcanic particle characteristics to pyroclastic flow hazard. *Earth and Planetary Science Letters,* 295**,** 314-320.

Dellino, P., Zimanowski, B., Buttner, R., La Volpe, L., Mele, D. & Sulpizio, R., 2007. Large-scale experiments on the mechanics of pyroclastic flows: Design, engineering, and first results. *Journal of Geophysical Research-Solid Earth,* 112**,** B04202.

Dioguardi, F. & Dellino, P., 2014. PYFLOW: A computer code for the calculation of the impact parameters of Dilute Pyroclastic Density Currents (DPDC) based on field data. *Computers & Geosciences,* 66**,** 200-210.

Druitt, T.H., 1998. Pyroclastic density currents. *Geological Society, London, Special Publications,* 145**,** 145-182.

Ducros, F., Nicoud, F. & Poinsot, T., 1998. Wall-adapting local eddy-viscosity models for simulations in complex geometries. *Numerical Methods for Fluid Dynamics,* vi**,** 293-299.

Dufek, J., 2016. The Fluid Mechanics of Pyroclastic Density Currents. *Annual Review of Fluid Mechanics, Vol 48,* 48**,** 459-485.

Dufek, J. & Bergantz, G.W., 2007a. Dynamics and deposits generated by the Kos Plateau Tuff eruption: Controls of basal particle loss on pyroclastic flow transport. *Geochemistry Geophysics Geosystems,* 8.

Dufek, J. & Bergantz, G.W., 2007b. Suspended load and bed-load transport of particle-laden gravity currents: the role of particle–bed interaction. *Theoretical and Computational Fluid Dynamics,* 21**,** 119-145.

Dufek, J., Esposti Ongaro, T. & Roche, O., 2015. Pyroclastic Density Currents: Processes and Models. *In* H. Sigurdsson (ed.) *The Encyclopedia of Volcanoes.* Amsterdam: Academic Press, 617-629.

Dufek, J. & Manga, M., 2008. In situ production of ash in pyroclastic flows. *Journal of Geophysical Research-Solid Earth,* 113.

Dufek, J., Manga, M. & Staedter, M., 2007. Littoral blasts: Pumice-water heat transfer and the conditions for steam explosions when pyroclastic flows enter the ocean. *Journal of Geophysical Research,* 112.

Dufek, J., Wexler, J. & Manga, M., 2009. Transport capacity of pyroclastic density currents: Experiments and models of substrate-flow interaction. *Journal of Geophysical Research: Solid Earth,* 114.

Eisele, J.W., O'halloran, R.L., Reay, D.T., Lindholm, G.R., Lewman, L.V. & Brady, W.J., 1981. Deaths during the May 18, 1980, eruption of Mount St. Helens. *New England Journal of Medicine,* 305**,** 931-936.

Elghobashi, S., 1994. On predicting particle-laden turbulent flows. *Applied Scientific Research,* 52**,** 309-329.

Esposti Ongaro, T., Cavazzoni, C., Erbacci, G., Neri, A. & Salvetti, M.V., 2007. A parallel multiphase flow code for the 3D simulation of explosive volcanic eruptions. *Parallel Computing,* 33**,** 541-560.

Esposti Ongaro, T., Cerminara, M., Charbonnier, S.J., Lube, G. & Valentine, G.A., 2020. A framework for validation and benchmarking of pyroclastic current models. *Bulletin of Volcanology,* 82**,** 51.

Esposti Ongaro, T., Clarke, A.B., Voight, B., Neri, A. & Widiwijayanti, C., 2012. Multiphase flow dynamics of pyroclastic density currents during the May 18, 1980 lateral blast of Mount St. Helens. *Journal of Geophysical Research: Solid Earth,* 117**,** B06208.

Harris, C.R., Millman, K.J., Van Der Walt, S.J., Gommers, R., Virtanen, P., Cournapeau, D., Wieser, E., Taylor, J., Berg, S., Smith, N.J., Kern, R., Picus, M., Hoyer, S., Van Kerkwijk, M.H., Brett, M., Haldane, A., Del Río, J.F., Wiebe, M., Peterson, P., Gérard-Marchant, P., Sheppard, K., Reddy, T., Weckesser, W., Abbasi, H., Gohlke, C. & Oliphant, T.E., 2020. Array programming with NumPy. *Nature,* 585**,** 357-362.

Jenkins, S., Komorowski, J.C., Baxter, P.J., Spence, R., Picquout, A., Lavigne, F. & Surono, 2013. The Merapi 2010 eruption: An interdisciplinary impact assessment methodology for studying pyroclastic density current dynamics. *Journal of Volcanology and Geothermal Research,* 261**,** 316-329.

Johson, P.C. & Jackson, R., 1987. Frictional-collisional constitutive relations for the granular materials, with application to plane shearing. *journal of Fluid Mechanics***,** 223-233.

Lerner, G.A., Jenkins, S.F., Charbonnier, S.J., Komorowski, J.-C. & Baxter, P.J., 2022. The hazards of unconfined pyroclastic density currents: A new synthesis and classification according to their deposits, dynamics, and thermal and impact characteristics. *Journal of Volcanology and Geothermal Research,* 421**,** 107429.

Lube, G., Breard, E.C.P., Cronin, S.J. & Jones, J., 2015. Synthesizing large-scale pyroclastic flows: Experimental design, scaling, and first results from PELE. *Journal of Geophysical Research-Solid Earth,* 120**,** 1487-1502.

Lube, G., Breard, E.C.P., Cronin, S.J., Procter, J.N., Brenna, M., Moebis, A., Pardo, N., Stewart, R.B., Jolly, A. & Fournier, N., 2014. Dynamics of surges generated by hydrothermal blasts during the 6 August 2012 Te Maari eruption, Mt. Tongariro, New Zealand. *Journal of Volcanology and Geothermal Research,* 286**,** 348-366.

Lube, G., Breard, E.C.P., Esposti-Ongaro, T., Dufek, J. & Brand, B., 2020. Multiphase flow behaviour and hazard prediction of pyroclastic density currents. *Nature Reviews Earth & Environment,* 1**,** 348-365.

Lube, G., Breard, E.C.P., Jones, J., Fullard, L., Dufek, J., Cronin, S.J. & Wang, T., 2019. Generation of air lubrication within pyroclastic density currents. *Nature Geoscience,* 12**,** 381-386.

Lube, G., Cronin, S.J., Thouret, J.C. & Surono, 2011. Kinematic characteristics of pyroclastic density currents at Merapi and controls on their avulsion from natural and engineered channels. *Geological Society of America Bulletin*, 123**,** 1127-1140.

Meiburg, E. & Kneller, B., 2010. Turbidity Currents and Their Deposits. *Annual Review of Fluid Mechanics*, 42**,** 135-156.

Mele, D., Dioguardi, F., Dellino, P., Isaia, R., Sulpizio, R. & Braia, G., 2015. Hazard of pyroclastic density currents at the Campi Flegrei Caldera (Southern Italy) as deduced from the combined use of facies architecture, physical modeling and statistics of the impact parameters. *Journal of Volcanology and Geothermal Research*, 299**,** 35-53.

Musser, J., Vaidheeswaran, A. & Clarke, M.A., 2021. MFIX Documentation Volume 3: Verification and Validation Manual; 3rd ed. NETL-PUB-22050; NETL Technical Report Series; U.S. Department of Energy, National Energy Technology Laboratory: Morgantown, WV.

Neri, A., Esposti Ongaro, T., De'michieli Vitturi, M. & Cerminara, M., 2021. Multiphase flow modeling of explosive volcanic eruptions. *Transport phenomena in multiphase systems.* Springer, 243-281.

Neri, A., Esposti Ongaro, T., Voight, B. & Widiwijayanti, C., 2015. Pyroclastic Density Current Hazards and Risk. *In* J.F. Shroder & P. Papale (eds.) *Volcanic Hazards, Risks and Disasters.* Boston: Elsevier, 109-140.

Steel, E., Buttles, J., Simms, A.R., Mohrig, D. & Meiburg, E., 2017. The role of buoyancy reversal in turbidite deposition and submarine fan geometry. *Geology*, 45**,** 35-38.

Strouhal, V., 1878. Ueber eine besondere Art der Tonerregung. *Annalen der Physik*, 241**,** 216-251.

Sulpizio, R., Dellino, P., Doronzo , D.M. & Sarocchi, D., 2014. Pyroclastic density currents: state of the art and perspectives. *Journal of Volcanology and Geothermal Research,* 283**,** 36-65.

Sweeney, M.R. & Valentine, G.A., 2017. Impact zone dynamics of dilute mono- and polydisperse jets and their implications for the initial conditions of pyroclastic density currents. *Physics of Fluids,* 29**,** 093304.

Thielicke, W. & Sonntag, R., 2021. Particle Image Velocimetry for MATLAB: Accuracy and enhanced algorithms in PIVlab. *Journal of Open Research Software,* 9.

Thielicke, W. & Stamhuis, E.J., 2014. PIVlab – Towards User-friendly, Affordable and Accurate Digital Particle Image Velocimetry in MATLAB. *Journal of Open Research Software,* 2**,** e30.

Turner, J.S., 1969. Buoyant Plumes and Thermals. *Annual Review of Fluid Mechanics,* 1**,** 29-44.

Valentine, G.A., 1987. Stratified flow in pyroclastic surges. *Bulletin of Volcanology,* 49**,** 616-630.

Valentine, G.A., 1998. Damage to structures by pyroclastic flows and surges, inferred from nuclear weapons effects. *Journal of Volcanology and Geothermal Research,* 87**,** 117-140.

Weit, A., Roche, O., Dubois, T. & Manga, M., 2018. Experimental Measurement of the Solid Particle Concentration in Geophysical Turbulent Gas-Particle Mixtures. *Journal of Geophysical Research-Solid Earth,* 123**,** 3747-3761.

Wilson, C.J.N., 1985. The Taupo Eruption, New Zealand. II. The Taupo Ignimbrite. *Philosophical Transactions of the Royal Society of London. Series A, Mathematical and Physical Sciences,* 314**,** 229-310.

Wilson, C.J.N. & Walker, G.P.L., 1982. Ignimbrite Depositional Facies - the Anatomy of a Pyroclastic Flow. *Journal of the Geological Society*, 139**,** 581-592.

Wohletz, K.H., 1998. Pyroclastic surges and compressible two-phase flow. *Developments in Volcanology*, 4.

4 Characterizing the Flow and Turbulence Structure of Dilute Pyroclastic Density Currents Through Large-Scale Experiments

This chapter is prepared for submission as a full-length research article to the **Journal of Geophysical Research: Solid Earth**.

Title: Characterizing the Vertical Structure of Dilute Pyroclastic Density Currents in Large-Scale Experiments

Authors: Daniel Uhle[1], Gert Lube[1], Jim Jones[2], James Ardo[1,3], Ermanno Brosch[1]

[1] School of Agriculture and Environment, College of Science, Massey University, Palmerston North, New Zealand

[2] School of Food and Advanced Technology, College of Science, Massey University, Palmerston North, New Zealand

[3] Manaaki Whenua- Landcare Research, Palmerston North, New Zealand

4.1 Abstract

Dilute pyroclastic density currents (PDCs) are hazardous volcanic phenomena frequently occurring on volcanoes around the world. To improve analytical and lower-order numerical PDC models used for hazard assessments, it is necessary to characterize the vertical velocity and density structures of PDCs and how they are modulated during flow propagation due to particle sedimentation, entrainment of air, and the onset of buoyancy reversal.

In the absence of direct measurements of the vertical structure of PDCs, large-scale experiments, and high-resolution computational multiphase simulations can provide missing insight. Here, we present data from a series of dynamically scaled large-scale experiments, where column collapse PDCs are simulated using hot volcanic material and air. The bed roughness and, with this, the lower flow boundary were systematically varied from hydraulic smooth to roughnesses in scales of the viscous sublayer. The deployed substrates geometrically scale to the conditions of sandy to bouldery substrates in natural volcanic landscapes. The resulting data is used to investigate the effects of bed roughness changes on the vertical flow structure.

We show that the time-averaged velocity and particle concentration follow self-similar vertical distributions. Combining vertical distributions of velocity and density, we derive a vertical distribution of the time-averaged flow dynamic pressure, which defines the heights and values of maximum and average (time-averaged) dynamic pressures for arbitrary bulk flow densities and velocities. The self-similar vertical structure of the experimental dilute PDCs is unmodulated by the basal roughness conditions.

Reynolds decompositions are performed using temporal Savitzki-Golay filters to separate and investigate the turbulent and mean components of dilute PDCs, showing that turbulence

is most pronounced in the head and wake of dilute PDCs. We show that the main production of turbulence occurs at the upper free boundary, where concentrations and density gradients are low. At the basal interface, high concentrations and large density gradients hinder the generation of turbulence. We show the generation of an actively mixing layer reaching into the main flow body and actively driving the entrainment of ambient air.

4.2 Introduction

Dilute pyroclastic density currents (dilute PDCs), also called pyroclastic surges, are fully turbulent multiphase flows of hot volcanic particles and gas that present a frequent volcanic hazard at many volcanoes at the Earth's surface (Valentine, 1987, Wohletz, 1998, Lube *et al.*, 2014, Sulpizio *et al.*, 2014). These density-stratified flows constitute a type of particle-laden gravity current, where the suspended particles carry a significant part of the flows' momentum, and the flow runout behavior is strongly controlled by the entrainment of ambient air and the sedimentation of particles inside the flow (Burgisser and Bergantz, 2002, Andrews and Manga, 2012, Dellino *et al.*, 2019, Brosch *et al.*, 2022). Related but isothermal phenomena include turbidity currents (Meiburg and Kneller, 2010, Wells and Dorrell, 2021), dust storms or haboobs (Knippertz *et al.*, 2007), and powder snow avalanches (Hopfinger, 1983, Ancey, 2004).

An essential characteristic of dilute PDCs is their vertical velocity and density structure. Together, they define destruction-causing dynamic pressure, and their spatiotemporal evolution is critical for estimating hazard footprints and impacts in risk assessments (Dioguardi and Mele, 2018, Dellino *et al.*, 2021). The quantitative characterization of the vertical velocity and concentration structure of dilute PDCs is a crucial ingredient for the testing and further development of theoretical and numerical PDC flow models (e.g., Dade

and Huppert, 1995, Dufek and Bergantz, 2007, Neri *et al.*, 2015, Fauria *et al.*, 2016). This is particularly the case for multi-layer flow models (Doyle *et al.*, 2008, Doyle *et al.*, 2010, Kelfoun, 2017, Shimizu *et al.*, 2019, Shimizu *et al.*, 2021) that rely on empirical models of the vertical velocity and concentration structure to describe exchanges of mass, energy, and momentum between layers.

The destructiveness of PDCs makes direct field measurements inside natural flows challenging. Recently, measurements inside PDCs of particle velocities with Doppler-Radar at Colima volcano (Scharff *et al.*, 2019) and pressure via micro barometers at Whakaari White Island (Brosch *et al.*, 2021) provided direct observation of the internal flow structure. However, the spatial resolution of these measurements was either too coarse (Colima) or limited to one measurement location (Whakaari) to allow for a detailed characterization of the vertical flow structure.

To describe the vertical velocity structure of dilute PDCs, Dellino *et al.* (2008) suggested the use of the law of the wall (Prandtl, 1905, Batchelor and Proudman, 1956), which is used to characterize average velocity profiles of turbulent, wall-bounded flows. The law of the wall velocity profile was demonstrated not to match the velocity structure of dilute PDCs due to the effects of free shear of the current with the ambient atmosphere (Brosch *et al.*, 2021, Cerminara *et al.*, 2021). Instead, similarity to the vertical velocity distribution in turbidity currents has been shown, which is characterized by an inner wall region due to solid shear at the lower flow boundary and an outer jet region due to free shear with the ambient atmosphere (Parker *et al.*, 1987, Altinakar *et al.*, 1996, Cantero-Chinchilla *et al.*, 2015).

Brosch *et al.* (2021) and Cerminara *et al.* (2021) suggested an empirical, fully differentiable Power-Gaussian function to describe the form of vertical profiles of velocity magnitude that

accounts for the basal solid-shear and upper free-shear flow boundaries. The Power-Gaussian is defined as:

$$u(z) = U_m \left(\frac{z}{h_m}\right)^{\xi} exp\left[-\left(\frac{z-h_m}{\chi}\right)^2 - \xi\left(\frac{z}{h_m} - 1\right)\right], \qquad \textit{EQN. 4-1}$$

where z is the height in the slope-normal direction, h_m the height of the wall region, at which the maximum velocity U_m occurs, ξ is the inner layer exponent, and χ is the outer layer exponent. EQN. 4-1 describes the wall/jet layer boundary at the height h_m, where shear vanishes to zero $\left(\left.\frac{du}{dz}\right|_{z=h_m} = 0\right)$. EQN. 4-1 has a similar shape to velocity functions published by Altinakar *et al.* (1996) and Cantero-Chinchilla *et al.* (2015) to describe vertical profiles of the downstream velocity component in the density current body region of turbidity currents. Unlike the velocity functions for turbidity currents of Altinakar *et al.* (1996) and Cantero-Chinchilla *et al.* (2015), the velocity profiles of EQN. 4-1 do not approach zero at the top of the gravity current body region but exponentially decay into the gravity current wake region that overlies the body.

Brosch *et al.* (2021) and Cerminara *et al.* (2021) showed the fit of EQN. 4-1 to data of velocity magnitude in a large-scale PDC experiment for a proximal observer location and calculated time-varying mean flow fields by fitting temporal polynomials for the fit parameters U_m, h_m, ξ and χ. Empirical functions for the downslope (u) and vertical (slope-normal) (v) velocity components for pyroclastic currents, if they are related, and how velocity profiles evolve downstream remain unknown. Still, empirical descriptions of v are of particular importance to characterize particle settling, the generation of vertical density stratification, and the effects of fluid buoyancy changes.

Existing empirical models for the vertical distribution of particle concentration originate from analog experiments of low-concentration turbidity currents under both subcritical and supercritical flow conditions (Parker *et al.*, 1987, Garcia and Parker, 1993, Altinakar *et al.*, 1996, Nourmohammadi *et al.*, 2011). These studies show a strong relationship between the vertical particle concentration and velocity distributions, with the velocity maximum at the boundary between wall and jet regions delineating two distinct zones of concentration distributions. Above U_m, concentration is decreasing asymptotically, while below U_m, the vertical concentration distribution closely follows a boundary layer approximation.

While Altinakar *et al.* (1996) suggested separate empirical laws for the concentration distribution in wall and jet regions in the body of turbidity currents, Cantero-Chinchilla *et al.* (2015) derived a fully differentiable function of the variation of particle concentration with height defined as

$$C(z) = C|_{z=h_m} \cdot e^{-\phi\left[\left(\frac{z}{h_f}\right)^{\zeta} - \eta_w{}^{\zeta}\right]}, \qquad EQN.\ 4\text{-}2$$

with z the height above the substrate, h_f the thickness of the gravity current body region, $C|_{z=h_m}$ the concentration at the wall-jet boundary ($z = h_m$), $\eta_w = h_m/h_f$ the dimensionless height of the wall-jet boundary, and ϕ and ζ are unknown fit parameters. EQN. 4-2 has been assessed at a single observer location in large-scale experiments of pyroclastic surges and was found to represent the data well, except for the lower flow region where sedimentation is enhanced by particle clustering (Brosch and Lube, 2020, Brosch *et al.*, 2021).

In this study, we present results from large-scale experiments interrogating the vertical structure and turbulence generation of dilute PDCs. We test the ability of empirical laws to capture the time-averaged vertical velocity and concentration structure of downstream evolving large-scale experimental PDCs. These empirical laws are further investigated, and

an empirical function describing the dynamic pressure is suggested. Further, the influence of the basal roughness is tested, and the presence of a basal slip is investigated. We extract and interrogate the turbulence structure of dilute PDCs from the velocity measurements and investigate the turbulence field using the turbulence intensity and turbulent kinetic energy. The results are used to characterize and interpret the spatiotemporally evolving turbulence structure of the experimental PDCs and the engines of turbulence generation.

4.3 Methods

Experimental dilute PDCs of hot volcanic particles and air were synthesized at the large-scale eruption simulator facility PELE in New Zealand. The set-up, experimental protocol, scaling similarity to natural PDCs, and sensors and measurement principles are described in detail in Lube *et al.* (2015) and Brosch *et al.* (2021). The experimental flows were generated by the seven-meter vertical fall of heated pyroclastic material from an elevated hopper into an instrumented runout section. The volcanic material used in the presented experimental series is a mixture of two well-characterized deposits of the 232 CE Taupo ignimbrite (Wilson, 1985), with particle diameters ranging from 2 µm to 16 mm ($-4\,\phi$ to $9\,\phi$). The particle mixture is characterized by a weakly bimodal grain-size distribution with a main mode at 245 µm ($2\,\phi$) and a minor mode at 11 µm ($6.5\,\phi$) (Brosch and Lube, 2020, Brosch *et al.*, 2021, Brosch *et al.*, 2022). Particle densities averaged over full ϕ-grain-size classes vary from $350 - 2650\ \mathrm{kg \cdot m^{-3}}$, constituted from a wide range of different clast types ranging from low-density pumices to high-density glass shards, lithic clasts, and free crystals. The utilization of natural volcanic material ensures realistic stress coupling between particles and gas and particle settling.

The instrumented runout section is comprised of two variably sloping parts: an upstream 12.8 m long and 6° sloping channel-confined section before a 23 m long, horizontal, and partially (first 4 m) channel-confined section. The open channel has a constant width of 0.5 m and variably high side walls (0– 6.4 m: 1.8 m high; 6.4– 11.6 m: 1.2 m high; 11.6– 16.8 m: 0.6 m high). To film the experimental currents with high-speed video, while also minimizing sidewall boundary effects, one side of the channel is constructed out of 10 mm thick, high-quality glass sheets.

At flow distances of 1.8 m, 3.35 m, 5.4 m, and 9.6 m from impact of the mixture onto the channel base, six high-speed cameras were deployed to record four vertical profiles of the passing flow at 500 Hz. The resulting video footage was used to calculate two-dimensional velocity fields ($\vec{U} = (u, v)$) using Particle Image Velocimetry (PIV), utilizing the PIVlab software (version 2.54) (Thielicke and Stamhuis, 2014, Thielicke and Sonntag, 2021). The resulting spatial resolution of the velocity fields is c. 1 cm. The resulting velocity fields were processed in Python to calculate temporal averages, mean velocity fields, and empirical velocity fits.

At the four vertical profile locations, high-speed video also recorded the filling of transparent flow sediment samplers at heights of 0.035– 1.8 m perpendicularly above the channel base. The flow sediment samplers allow the flow to enter through a 1.69 cm^2 opening on the upstream side. On the downstream side, only the gas phase exits the sampler through a 16 µm mesh, while the accumulation of solid particles inside the sampler is continuously recorded. Downslope velocity components $u(t)$ of the flow 0.05 m upstream of each flow sampler were computed from PIV. The weight and density of the material inside the flow samplers was measured at selected time intervals to calculate the time-variant porosity of the

captured sediment and its grain-size distribution. The time series of particle solids concentration at each sampler location was computed as

$$C_s(z,t) = \frac{V_d\,(1-\varepsilon)}{u_e\,A_o t}, \qquad \textit{EQN. 4-3}$$

where V_d is the time-variant volume of sediment accumulated inside the sampler, u_e the time-variant velocity obtained through PIV at the entrance of the flow sampler, A_o the cross-sectional area of the flow sampler, t the selected time intervals, ε the time-variant sediment porosity, and z the height above the channel in slope-normal direction.

At each of the four vertical profile locations, additional high-resolution video cameras recorded the sediment transport, erosion, and deposition processes in the basal c. 0.15 m of the flow. Together with the high-speed videos, this imagery was used to measure time-series of the height of the lower flow boundary at a spatial resolution of < 0.5 mm.

Three large-scale experiments were conducted at the same starting conditions (summarized in Table 4-1), except for the bed roughness, using 125 kg of volcanic material heated to 120 °C at an ambient temperature of 15 °C. The choice of the experimental basal roughness conditions was guided by the idea of simulating a variety of natural volcanic substrates in the range from sandy to boulder terrains. In the first experiment, hereafter referred to as the rough experiment, a layer of $4-8$ mm diameter, subrounded pebbles was glued to the channel base. In the second experiment, hereafter referred to as the intermediate experiment, a layer of skateboard grip tape equal to P80 sandpaper ($\sim$201 µm) was used as the channel base. In the third experiment, hereafter referred to as the smooth experiment, a high-quality medium-density fiberboard (MDF) with roughness scales of less than ten microns was inserted into the channel base. For natural PDCs with $100-500$ m thicknesses, these conditions represent geometrically scaled natural roughness (Table 4-1) of $0.2-2.2$ m for

the rough experiment, $1.1 - 5.5$ cm for the medium experiment, and $0.56 - 2.8$ mm for the smooth experiment. In the experimental flows, the thickness of the boundary layer (also referred to as the wall region in density currents), on average, is c. 0.3 m thick, and the thickness of the viscous sublayer (the lower c. $0.1 - 1$ percent of the boundary layer thickness (Cebeci, 2013) where strong vertical gradients in velocity and viscosity occur) has a thickness of < 3 mm. This means that only in the rough experiment are roughness elements larger than the viscous sublayer.

Table 4-1 Summary of the experimental series investigating the influence of bed roughness on the PDC's propagation. *The roughness scaling is performed for* $100 - 500\ m$ *thick natural PDCs (*$R = r \cdot {H_{PELE}}/{H_{Nature}}$*, with R the scaled roughness, r the deployed roughness,* H_{PELE} *flow thickness in Pele, and the natural flow thickness* H_{Nature} *of* $100 - 500\ m$*).*

Parameter	**Rough Exp.**	**Intermediate Exp.**	**Smooth Exp.**
Mass of Volcanic Material	125 kg	125 kg	125 kg
Initial Temperature of Volcanic Material	120°C	120°C	120°C
Bed Roughness (r)	$4 - 8$ mm	≈ 201 µm	≈ 10 µm
Scaled Roughness (R)	$0.2 - 2.2$ m	$1.1 - 5.5$ cm	$0.56 - 2.8$ mm
Ambient Temperature	15°C	15°C	15°C

The scaling analysis, summarized in Table 4-2, shows that the experimental PDCs scale well to natural dilute PDCs (Brosch and Lube, 2020, Brosch *et al.*, 2021, Brosch *et al.*, 2022). From the dimensionless numbers that demonstrate fluid dynamical scaling we highlight the Reynolds number that reaches $1.5 \cdot 10^6$, the Richardson number with a range of $10^{-2} - 10$, the Froude numbers of $0.75 - 2$, and the thermal Richardson number with a range of $2 \cdot 10^{-2} - 4.5$. Using natural volcanic material ensures accurate gas-particle feedback. Which

is shown by the particle Stokes number ($10^{-3} - 9.9$), stability number ($13 \times 10^{-3} - 32$), and Rouse number ($66 \times 10^{-2} - 19$).

Table 4-2 Scaling parameters comparing natural and experimental dilute PDCs. *With μ_a ambient dynamic viscosity, C_S particle solid concentration, ρ_a ambient density, ρ_c flow density, $\Delta\rho$ density difference between flow and ambient, C_{p_c} and C_{p_a} the flow and ambient heat capacity, respectively, g the gravitational acceleration, g' the reduced gravitational acceleration, k the Karman constant, θ the substrate inclination, u_T the particle terminal velocity, and Δu the eddy rotational velocity. Values for natural PDCs are collected from Druitt (1998), Choux and Druitt (2002), and Burgisser et al. (2005). The equation for the flow dynamic viscosity is from Wohletz (1998). Table modified from Brosch et al. (2021).*

Parameter	Meaning	Definition	Generated PDCs	Natural PDCs
Particle Size		d	$2\ \mu m - 16\ mm$	$10^{-6} - 10^{-1}\ m$
Particle density		ρ_s	$350 - 2600\ kg/m^3$	$300 - 2600\ kg/m^3$
Ambient Density		ρ_a	$1.06 - 1.225\ kg/m^3$	$0.6 - 1.2\ kg/m^3$
Flow density		ρ_c	$1.27 - 10\ kg/m^3$	
Flow Temperature		T	$15 - 60\ °C$	
Velocities		u	$\leq 10.5\ m/s$	$10 - 200\ m/s$
Flow dynamic viscosity		$\mu_c = \mu_a \left(1 + \frac{\rho_s C_s}{\rho_a (1 - C_s)}\right)^2$	$3 \times 10^{-5} - 3 \times 10^{-3}\ \frac{kg}{s\ m}$	$10^{-5} - 4 \times 10^{-3}\ \frac{kg}{s\ m}$
Kinetic energy density		$U_{kin} = \frac{1}{2}\rho_c u^2$	$10^{-2} - 10^{3}\ \frac{kg}{m\ s^2}$	$10^{3} - 10^{4}\ \frac{kg}{m\ s^2}$

Buoyant thermal energy density		$U_T = \rho_c \frac{C_{p_c}}{C_{p_a}} \alpha\, T\, h\, g$	$10 - 10^3 \frac{\text{kg}}{m\, s^2}$	$10^3 - 10^4 \frac{\text{kg}}{m\, s^2}$
Reynolds number	$\frac{\text{Inertial Forces}}{\text{Viscous Forces}}$	$Re = \frac{\rho_c\, u\, h}{\mu_c}$	1.5×10^6	$33 \times 10^5 - 6.7 \times 10^9$
Richardson number	$\frac{\text{Buoyancy Term}}{\text{Flow Shear Term}}$	$Ri = \frac{\Delta\rho\, h\, g}{\mu_c}$	$10^{-2} - 10$	$0 - 10$
Froude number	$\frac{\text{Inertial Forces}}{\text{Gravitational Forces}}$	$Fr = \frac{u}{\sqrt{g'\, h\, cos(\Theta)}}$	$0.75 - 2$	≈ 1
Particle Stokes number	$\frac{\text{Characteristic Time Particle}}{\text{Characteristic Time Fluid}}$	$St = \frac{u_T \Delta u}{\delta g}$	$10^{-3} - 9.9$	$11 \times 10^{-4} - 97 \times 10^6$
Stability number	Defines particle transport zones	$\Sigma = \frac{u_T}{\Delta u}$	$13 \times 10^{-3} - 32$	$2.8 \times 10^{-6} - 9.7 \times 10^9$
Rouse number	Characterises turbulent particle transport regimes	$P = \frac{u_T}{k u_s}$	$66 \times 10^{-2} - 19$	$10^{-3} - 10^2$
Thermal Richardson number	$\frac{\text{Buoyancy Term}}{\text{Flow Shear Term}}$	$Ri_T = \frac{\Delta T\, \alpha\, h\, g}{u^2}$	$2 \times 10^{-2} - 4.5$	$0 - 5$

4.4 Results

4.4.1 Density Current Structure

After the impact of the vertically falling particle-air mixture with the channel, a density current forms, whose velocity and concentration distributions are measured at four vertical profiles at 1.8 m, 3.35 m, 5.4 m, and 9.6 m from the impact zone. Over this distance, the flow front velocity decreases from c. 5.5 $\text{m} \cdot \text{s}^{-1}$ to c. 4 $\text{m} \cdot \text{s}^{-1}$. The time- and height-integrated volumetric particle concentration declines from c. 0.25 vol% to c. 0.05 vol. % through deposition and entrainment of ambient air. Using the example of the first two profile

locations at 1.8 and 3.35 m, Figure 4.1 depicts the general flow structure in height-time contour plots of velocity magnitude $U(z,t)$; the slope-normal velocity component $v(z,t)$ and particle volume concentration $C(z,t)$. The experimental PDC is comprised of a c. 1.85–2 m high-density current head region (from flow arrival until c. 0.9 s) and a c. 1–1.15 m high-density current body region (from c. 0.9–4 s). Behind the head, the density current body region is overlain by a c. 0.5–0.9 m-thick density current wake region.

The head forms an upslope rotating vortex structure that is visible as strong changes in the slope-normal vertical (slope normal) velocity components (Figure 4.1 c and d). Above the leading, c. 0.15 m high-density current nose, the head is comprised of a frontal, c. 0.5 m wide, low-velocity region in front of the high-velocity head center and rear regions (Figure 4.1 a and b). This low-velocity frontal region, which is in direct contact with and thus vigorously entrains ambient air, has the largest positive (upwards-directed) slope-normal velocities of the entire current. At the rear of the upper head region, free shear with the ambient air sheds off material that produces the frontal part of the gravity current wake region, which trails the rear of the head region. However, the bulk of the density current wake region above the body region is formed by rapid particle sedimentation and the development of a strong vertical density stratification approximately 0.2 s after impact. Behind the head, this leads to the segregation of the density current into (i) an upper, strongly entraining and well-mixed, low-velocity region (typically $< 2\ \mathrm{m \cdot s^{-1}}$) of low particle concentration (10^{-2}–10^{-3} vol. %) and high vorticity, which we refer to as the wake; and (ii) a lower, faster-moving (typically $> 4\ \mathrm{m \cdot s^{-1}}$), denser ($10^{-2}$–$10^{0}$ vol. %), strongly vertically density-stratified body region (Figure 4.1 e and f). The boundary between the body and wake flow regions is delineated by a strong increase in vorticity and by the change from dominantly downward to dominantly upward-directed velocity components. Over the 9.4 m

travel distance of our measurement profiles, and despite the entrainment of ambient air and evolving particle sedimentation, the bulk density of the wake (c. $1.4\ \mathrm{kg \cdot m^{-3}}$) remains higher than that of the ambient air (c. $1.225\ \mathrm{kg \cdot m^{-3}}$).

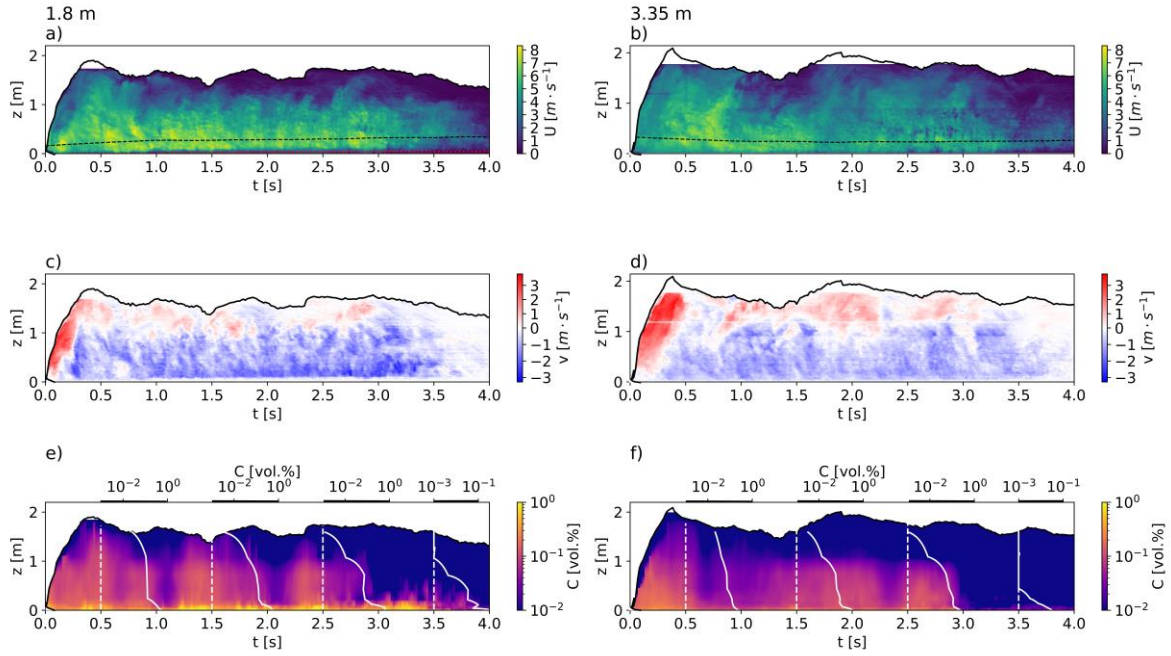

Figure 4.1 Velocity and concentration data from large-scale experiments. *The first column shows time-height contour plots of velocity magnitude, vertical velocity, and concentrations measured at* $1.8\ m$ *from impact. The second column shows velocity magnitude, vertical velocity, concentrations measured at* $3.35\ m$ *from impact. All data is shown to the flow height, marked by blackline. a,b) Time-height presentation of the velocity magnitude at* $1.8\ m$ *and* $3.35\ m$*, respectively. The black dashed line shows the height of the velocity maximum, where the boundary between the wall and jet region sits. The dashed red line in (a) marks the time-variant thickness of the aggrading deposit. With* $\sim 2\ mm$*, the deposit in b is smaller than the PIV resolution (*$\sim 1\ cm$*) and therefore not shown. c,d) Vertical velocities as time-height plots at* $1.8\ m$ *and* $3.35\ m$*, respectively. The definition of vertical velocities follows the definition of the coordinate system, with positive velocities (red) going upward and negative velocities going downward. The colormap diverges at* $0\ m \cdot s^{-1}$ *and marks the transition from positive to negative velocities white. e,f) time-height plots of particle solid concentrations in vol.%. White dashed vertical lines at* 0.5*,* 1.5*,* 2.5*, and* $3.5\ s$ *anchor the concentration profiles (white lines). The x-axes for these concentration profiles are shown at the upper x-axis.*

As in turbidity currents, the height $h_m(t)$ of the velocity maximum $U_m(z,t)$ and vanishing shear divides the lower wall region (also inner region) from the upper jet region (also outer region). Unlike in turbidity currents and as described in detail in Brosch and Lube (2020), the lower wall region is characterized by the accumulation of fast-settling mesoscale particle clusters and the formation of a cluster-rich, so-called transient region of c. 0.1– 1.5 vol. % above the bedload region. The dynamic thinning and thickening of the transient region coincides with a pinching and swelling of the bedload region (which has a concentration of c. 0.5 to several volume percent) and an alternation of depositional, non-depositional, and erosive flow phases. The variably erosive and depositional nature of the lower flow boundary towards the static deposit (or substrate) results in a variably strong basal slip at the lower flow boundary.

4.4.2 Vertical Profiles of Flow Velocity and Flow Particle Concentration

***Velocity magnitude**:* Figure 4.2 shows the time-averaged velocity magnitude $\overline{U}$ with height z for the three experiments over rough (Figure 4.2 a-d), intermediate (Figure 4.2 e-h), and smooth (Figure 4.2 i-l) substrates at the four observer locations. All of the vertical velocity profiles are characterized by a pronounced velocity maximum $U_m(z,t)$. The height $h_m(t)$ where the velocity maximum occurs divides the flow into a lower wall region (inner region) and an upper jet region (outer region). In the wall region, shear strongly decreases upwards from maximum values at the lower flow boundary to zero at $h_m(t)$. In the jet region above $h_m(t)$, shear initially increases upwards before decreasing again with closer proximity to the upper flow boundary. Figure 4.2 also shows the height-dependent maximum values of velocity magnitude $\overline{U_m}$. In the flow body, profiles of $\overline{U_m}$ and $\overline{U}$ have roughly similar forms with an approximately constant ratio of maximum and mean velocity values of around 1.5. However, in the uppermost part of the body and the entire wake, $\overline{U_m}(z)/\bar{u}(z)$ strongly

increases with height to values larger than 5, highlighting a systematic increase in turbulence fluctuations with increasing proximity to the free-shear flow boundary. Similarly, $\overline{U_m}(z)/\bar{u}(z)$ also increases towards the lower flow boundary.

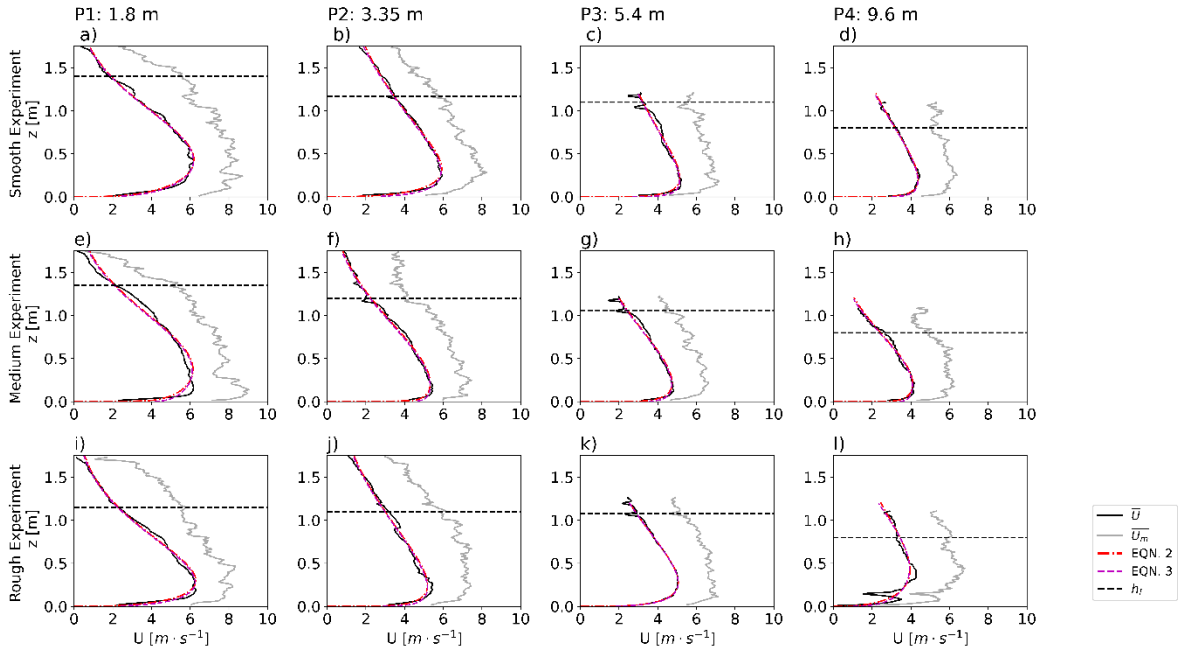

Figure 4.2 Spatial evolution of the velocity magnitude. *The four columns show the data of different experiments along the flow runout. The first row is the smooth, the second row is the medium, and the last row is the rough experiment. In a-l, each plot shows the time-averaged velocity data $\overline{U}$ (black), the maximum velocity magnitudes $\overline{U_m}$ (grey), the fit of the Power-Gaussian without slip (EQN. 4-2) (red dashed line), the fit of the Power-Gaussian including a basal slip (EQN. 4-3) (purple dashed line), and the height of the body-wake boundary (vertical black dashed line). The legend is shared for the entire figure.*

Figure 4.2 a-l shows that the data $\overline{U}(z)$ are well described by best-fits of the Power-Gaussian velocity model of EQN. 4-1 and the correlation coefficient for these fits range from 0.96 to 0.99. It is noteworthy that the velocity data is similarly well fit with an alternative Power-Gaussian velocity model with a basal Navier-Maxwell slip condition of the form:

$$U(z) = U_{max}\left(\frac{z+n}{h_m}\right)^{\xi} exp\left[-\left(\frac{z+n-h_m}{\chi}\right)^2 - \xi\left(\frac{z+n}{h_m} - 1\right)\right], \qquad EQN.\ 4\text{-}4$$

where n is the Navier slip length. Correlation coefficients for the fit of EQN. 4-4 to the downslope velocity data range between 0.97 and 0.99 (Figure 4.2 a-l), therefore showing slight improvements of correlation coefficients.

***Downstream velocity**:* Figure 4.3 presents measurements of the time-averaged downslope velocity component $\bar{u}$ and of the maximum values of the downslope velocity component $\overline{u_m}$ against height z for the three experiments over rough (Figure 4.3 a-d), intermediate (Figure 4.3 e-h), and smooth substrate roughness (Figure 4.3 i-l) at the four observer locations. Profiles of the downstream velocity have the same characteristics as the velocity magnitude. Markedly, for the same experiment and measurement location, the heights of the velocity maximum of $\bar{u}$ are virtually identical to those obtained for $\overline{U}$. Figure 4.3 a-l also shows that, similar to $\overline{U}$, the data $\bar{u}(z)$ are well described by best-fits of the Power-Gaussian velocity model of EQN. 4-1 (correlation coefficient for these fits range between 0.96 and 0.99) and by the alternative Power-Gaussian velocity model with a basal Navier-Maxwell slip condition of EQN. 4-4 (regression coefficients ranging between 0.97 and 0.99), again showing slight improvements in correlation coefficients.

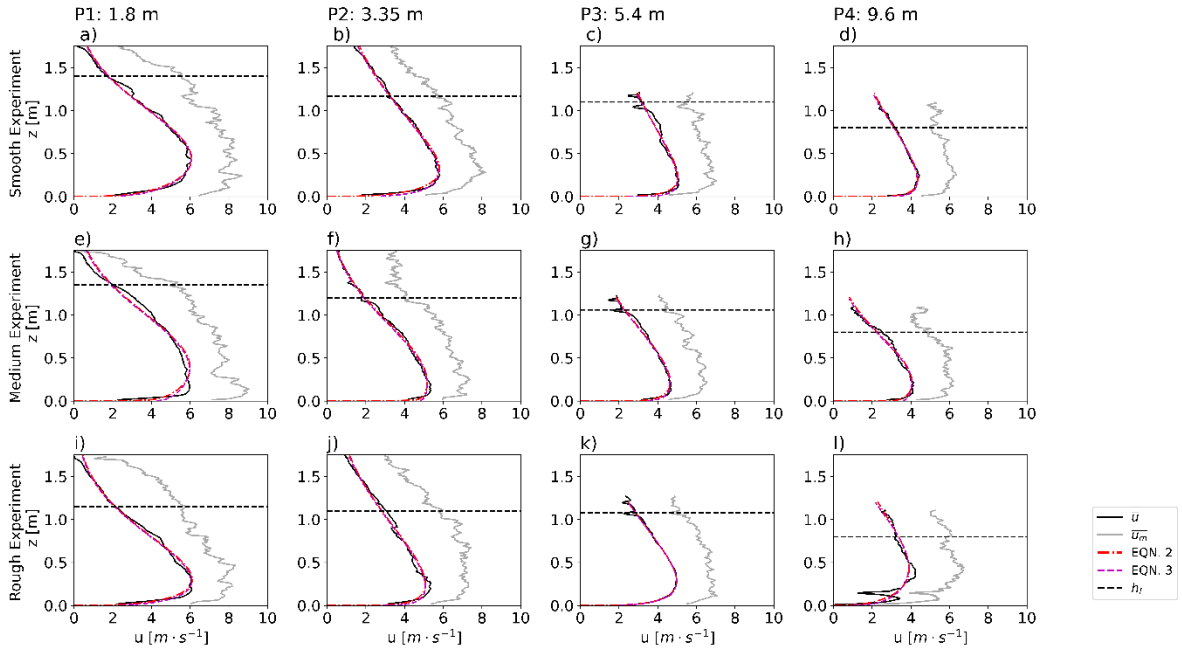

Figure 4.3 Spatial evolution of the downstream velocity component. *The columns show the downstream velocity data of all experiments along the flow runout. The first row shows data from the smooth, the second row the medium, and the last row the rough experiment. Each panel shows the time-averaged velocity data* $\bar{u}$ *(black), the maximum downstream velocity* $\overline{u_m}$ *(grey), the Power-Gaussian fit without basal slip (EQN. 4-2) (red dashed line), the Power-Gaussian fit with basal slip (EQN. 4-3) (purple dashed line), and the body-wake boundary (vertical black dashed line). The legend at the bottom right corner is shared for all panels.*

***Vertical (slope normal) velocity*:** Figure 4.4 a-n shows the measurements of the time-averaged vertical (slope normal) velocity ($\bar{v}$) component against height z for all experiments and measurement locations. This depicts the occurrence of downward motion (negative vertical velocities) in the flow body and upward motion (positive vertical velocities) in the wake with the time-averaged height of the body-wake boundary h_f, with $\bar{v}|_{z=h_f} = 0\ m \cdot s^{-1}$, shown as vertical dashed lines for each velocity profile. For $z < h_f$, the form of $\bar{v}$ velocity profiles show a marked similarity to the power-Gaussian form of the measurements of the downslope velocity ($\bar{u}$) components and the velocity magnitude ($\overline{U}$). However, the height h_{m_v} of the maximum downward velocity values V_{max} is systematically lower than

h_m. Figure 4.4 demonstrates, that vertical profiles of v are well described by a power-Gaussian function of the form:

$$v(z) = V_{max}\left(\frac{z}{h_{m_v}}\right)^{\xi_v} exp\left[-\left(\frac{z-h_{m_v}}{\chi_v}\right)^2 - \xi_v\left(\frac{z}{h_{m_v}} - 1\right)\right], \qquad EQN.\ 4\text{-}5$$

where ξ_v is the inner layer exponent, and χ_v the outer layer coefficients describing the vertical velocity distribution. However, unlike the measurements, EQN. 4-5 cannot mathematically describe the divergence (y-intercept and associate change from downward to upward motion) at the body-wake boundary at h_f. Therefore EQN. 4-5 is only valid in the flow body.

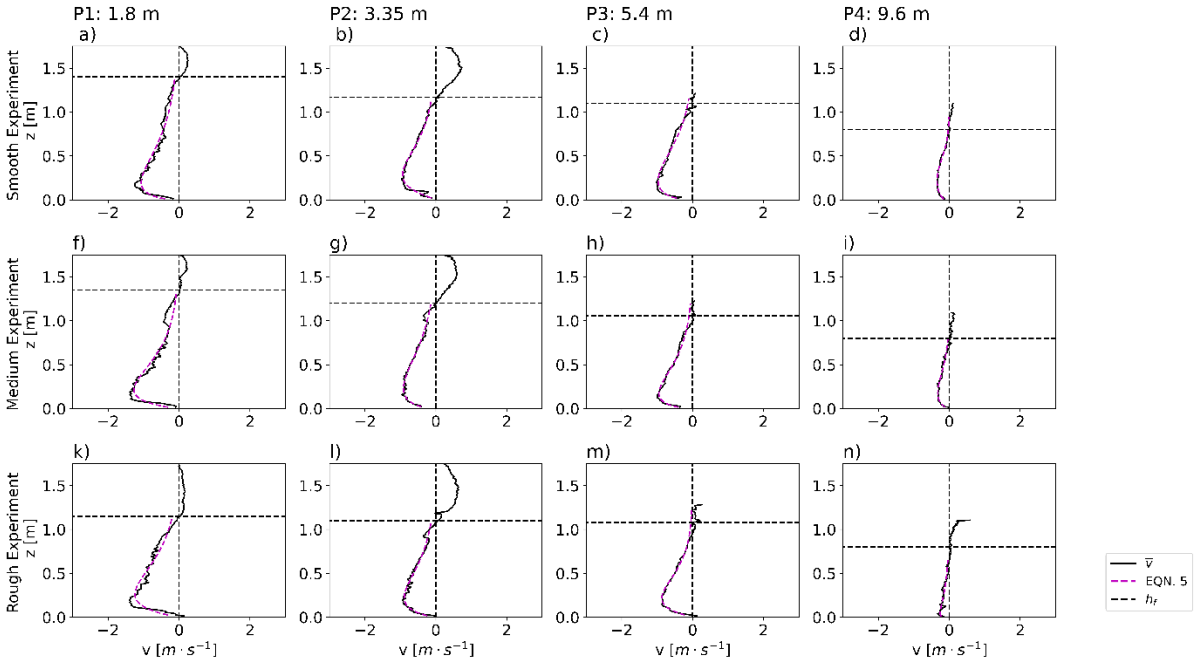

Figure 4.4 Vertical profiles of the vertical velocity component. *The columns show the vertical velocities of all experiments along the runout. The first row shows vertical velocity data from the smooth, the second row the medium, and the last row the rough experiment. Each panel shows the dimensional time-averaged vertical velocity data $\bar{v}$ (black), the Power-Gaussian fit for the vertical velocity (EQN. 4-5) (purple dashed line) and the body-wake boundary (vertical black dashed line). The legend is shared for the whole figure.*

4.4.3 Self-Similarity of Time-Averaged Velocity Profiles

For the case of sub-critical and supercritical experimental turbidity currents, Cantero-Chinchilla *et al.* (2015) demonstrated that vertical profiles of the streamwise (downstream) velocity component have a self-similar form. To test if such a self-similarity also occurs in dilute PDCs and how this is modified by the substrate roughness, the velocity data of our experiments is shown in non-dimensional forms in Figure 4.5 by normalizing measurements of $\bar{U}(z)$, $\bar{u}(z)$ and $\bar{v}(z)$ velocities with their respective maximum velocity values U_{max}, u_{max} and V_{max}, extracted from the Power-gaussian fits in Figure 4.2-Figure 4.4, and height z by the flow height h_f, mapped in time-averaged vertical velocities (shown in Figure 4.5).

The non-dimensional Power-Gaussian of the velocity magnitude takes the form

$$\frac{U(\eta)}{U_{max}} = \left(\frac{\eta}{\eta_m}\right)^{\xi} exp\left[-\left(\frac{\frac{\eta}{\eta_m}-1}{\chi}\right)^2 - \xi\left(\frac{\eta}{\eta_m}-1\right)\right], \qquad EQN.\ 4\text{-}6$$

with $\eta = \frac{z}{h_f}$ the non-dimensional height and $\eta_m = \frac{h_m}{h_f}$. The velocity distributions of the downstream and vertical velocity components are normalized in the same way as:

$$\frac{u(\eta)}{\overline{u_{max}}} = u_m\left(\frac{\eta}{\eta_{m_u}}\right)^{\xi_u} exp\left[-\left(\frac{\frac{\eta}{\eta_{m_u}}-1}{\chi_u}\right)^2 - \xi_u\left(\frac{\eta}{\eta_{m_u}}-1\right)\right], \qquad EQN.\ 4\text{-}7$$

with $\eta_{m_u} = \frac{h_{m_u}}{h_f}$ the height of the maximum downstream velocity; and

$$\frac{v(z)}{V_{max}} = \left(\frac{\eta}{\eta_{m_v}}\right)^{\xi_v} exp\left[-\left(\frac{\frac{\eta}{\eta_{m_v}}-1}{\chi_v}\right)^2 - \xi_v\left(\frac{\eta}{\eta_{m_v}}-1\right)\right], \qquad EQN.\ 4\text{-}8$$

with $\eta_{m_v} = \frac{h_{m_v}}{h_f}$ the non-dimensional height of the maximum downward velocity.

For the vertical velocity component, we also tested a mathematical law of Cantero-Chinchilla *et al.* (2015) derived for the downstream velocity component of turbidity currents without dilute wake:

$$v(z) = \sigma \left(\frac{z}{h_f}\right)^{\Pi} \left(\frac{1-z}{h_f}\right)^{\Sigma}, \qquad \textit{EQN. 4-9}$$

with σ, Π, and Π being empirically determined fit parameters.

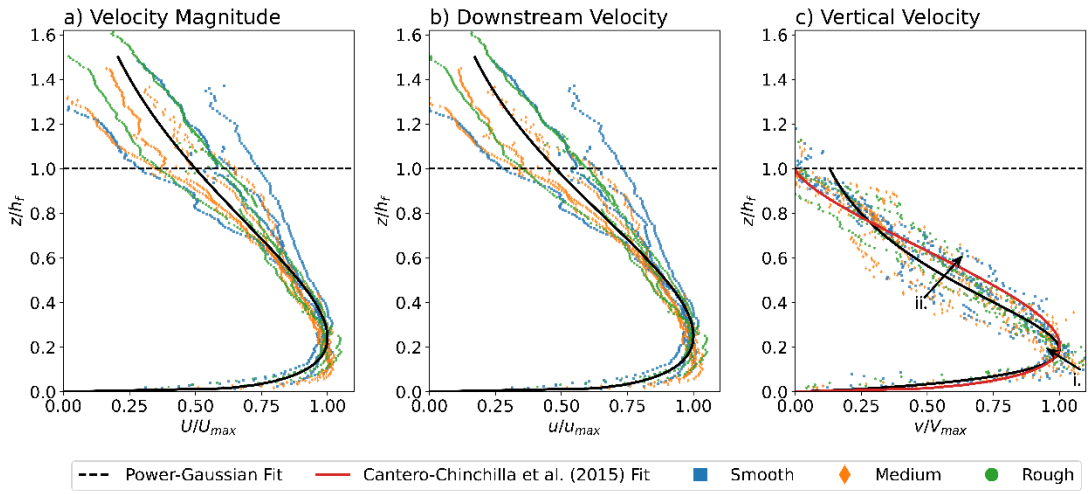

Figure 4.5 Self-Similarity of the velocity distributions in dilute pyroclastic density currents. *a) Self-similarity of the velocity magnitude U. The data all profiles of the smooth (blue squares), medium (orange diamonds), and rough (green circles) is shown in non-dimensional form. For the normalization, the height z is divided by the flow height (h_f). Further, each time-averaged velocity profile is divided by the maximum velocity U_{max}, u_{max}, and V_{max}, for the velocity magnitude, downstream velocity, and vertical velocity, respectively. The Fits using Power-Gaussian functions are marked by black lines. For the vertical velocity (c), a velocity fit after EQN. 4-9 is shown in red. Further arrows marked with i and ii in (c) indicate the velocity profile trends along the runout. A shared legend is provided below.*

Figure 4.5 shows the best fits for all normalized velocity-height data with the non-dimensional Power-Gaussian models EQN. 4-6, EQN. 4-7, and EQN. 4-8 for the velocity magnitude, downstream velocity, and vertical velocity, respectively.

For velocity magnitude and the downstream velocity component (Figure 4.5 a and b), for the entire wall region and approximately the lower two-thirds of the jet region $\left(\frac{z}{h_f} \leq 0.7\right)$, the normalized velocity data for all tested roughness conditions and all locations collapses onto a universal curve. Scatter around this curve shows no systematic dependence on the substrate roughness, the flow distance, and the downstream-decreasing thickness of the transient and bedload layers. In the uppermost part of the jet region and particularly in the turbulent wake $\left(\frac{z}{h_f} \geq 0.7\right)$, the normalized velocity data show increasing scatter around the universal curve. The resulting fit parameters for the velocity magnitude are $h_m/h_f = 0.24$, $\xi = 0.25$, and $\chi = 6.06$, and for the downstream velocity $h_{m_u}/h_f = 0.25$, $\xi_u = 0.23$, and $\chi_u = 4.89$. Therefore, the velocity magnitude and downstream velocity show differences in their fit parameters, most pronounced in the outer layer coefficients χ and χ_u. The resulting correlation coefficient for the velocity magnitude is 0.926 and for the downstream velocity 0.931. The vertical velocity component produces correlation coefficients of 0.94 and fit parameters $h_{m_v}/h_f = 0.189$, $\xi_v = 0.78$, and $\chi_v = 4.9 \cdot 10^3$. This demonstrates that the velocity distribution of the vertical velocity deviates significantly in the fit parameters from the velocity magnitude and downstream velocity. Unlike, velocity magnitude and the downstream velocity component, normalised profiles of the vertical velocity component show slight but systematic variation with travel distance as marked with arrows i and ii in Figure 4.5 c.

The fit of EQN. 9 to the data of the vertical velocity component, defined to be zero at the body wake boundary ($\bar{v}|_{z=h_f} = 0$) is shown as a red line in Figure 4.5 c. The fit results in a correlation coefficient of 0.917, and fit parameters $\sigma_{Cantero-Chinchilla} = 2.4$, $\xi_{Cantero-Chinchilla} = 0.39$, and $\xi_{Cantero-Chinchilla} = 1.48$..

4.4.4 Self-Similarity of Time-Averaged Concentration Distributions

Figure 4.6 shows the time-averaged concentration distribution to also follow a self-similar shape, following EQN. 4-2 (Cantero-Chinchilla *et al.*, 2015). Due to time constraints and data availability, only concentrations for the smooth and rough experiments were computed. For both experiments and all observer locations, the dimensional concentration distributions are well fit by the concentration distribution of Eqn. 2 suggested by Cantero-Chinchilla *et al.* (2015) for turbidity currents.

Normalization with the flow height h_f and the concentration at the body wake boundary ($C|_{z=h_m}$) provides the non-dimensional concentration distribution as:

$$\frac{C(z)}{C|_{z=h_m}} = e^{-\phi\left[\left(\frac{z}{h_f}\right)^{\zeta} - \eta_w{}^{\zeta}\right]}. \qquad \textit{EQN. 4-10}$$

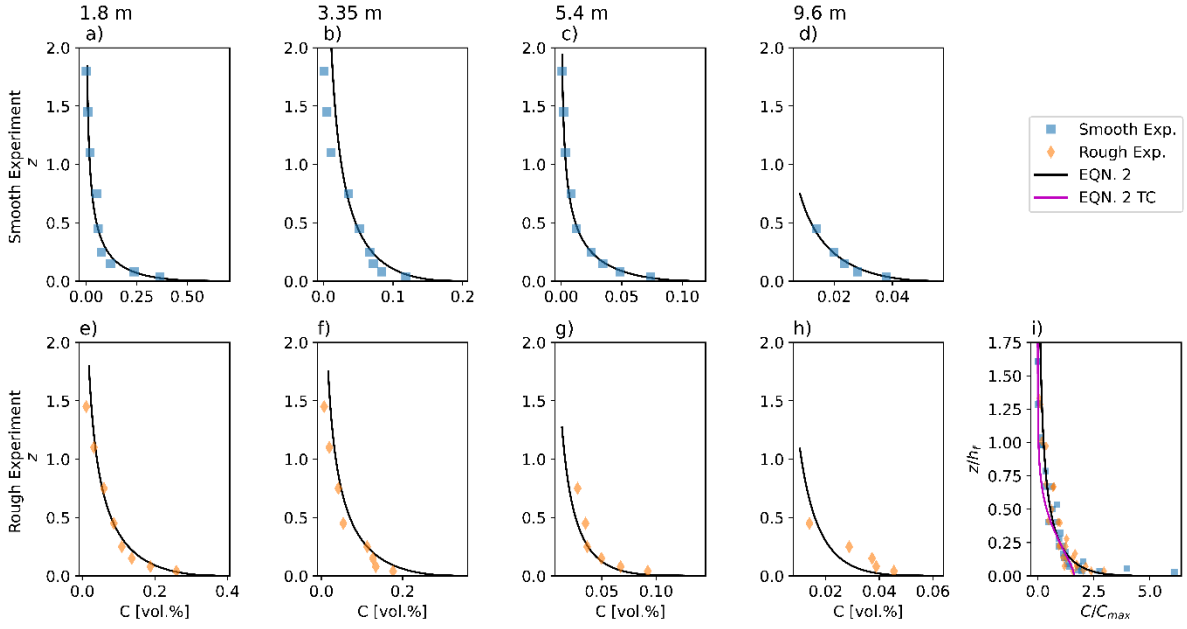

Figure 4.6 Evolution and self-similarity of concentration distribution. *The first row (a-d) shows time-averaged concentration distributions from the smooth experiment, at a)* 1.8, *b)* 3.35, *c)* 5.4, *d)* 9.6 *m. Each panel shows the time-averaged data (blue squares), and the concentration fits with EQN. 4-2 (Cantero-*

Chinchilla et al., 2015) (black). The second row (e-h) shows time-averaged concentration distributions from the rough experiment, at e) 1.8, *f)* 3.35, *g)* 5.4, *h)* 9.6 *m. Each panel shows time-averaged data (orange diamonds), and the concentration fits using EQN. 4-2 after Cantero-Chinchilla et al. (2015) (black). i) Shows the non-dimensional concentration data of the smooth experiment (blue squares), and the rough experiment (orange diamonds), each normalized by the flow height* h_f *and the concentration at the height of the velocity maximum* $C|_{z=h_f}$*, the fit of EQN. 4-10 to the time-averaged non-dimensional data. For comparison, the fit of EQN. 4-10 for turbidity currents was computed by Cantero-Chinchilla et al. (2015) (purple line).*

Figure 4.6 i shows the nondimensional concentration data of the smooth and rough experiments. The data is normalized by the flow height h_f and the concentration at the height of the velocity maximum $C|_{z=h_m}$. The data shows a collapse and self similar distribution with height. Fits of EQN. 4-10 provide correlation coefficients of 0.85 and fit parameters $\phi = 2.87$ and $\zeta = 0.454$. For comparison fit parameters for turbidity current data are calculated to be $\phi = 4$ and $\zeta = 1.5$ (Cantero-Chinchilla *et al.*, 2015). The fit parameters in EQN. 4-10 control different proportions of the concentration distribution. Here ϕ controls how the concentration profile decays with height, with the decay being larger for large ϕ. Lower values of ϕ, therefore, show that the concentration decays slower with height, compared to turbidity currents presented in Cantero-Chinchilla *et al.* (2015). ζ, on the other hand, describes the increase towards the base, and if the lowermost region has a concave ($\zeta < 1$) or convex ($\zeta > 1$)trend. The smaller $\zeta < 1$, the stronger the concave trend, and with it, the increase of concentrations towards the base. The value of $\zeta = 1.5$ for turbidity currents (Cantero-Chinchilla *et al.*, 2015) presents a convex trend in the wall region. This is contrasted by a concave trend presented by dilute PDCs with $\zeta = 0.56$ that highlight stronger increases in concentration toward the flow base.

4.4.5 Self-Similarity of dynamic pressure

Through the self-similarity of the concentration profiles follows self-similarty of the density profiles defined as:

$$\rho(z) = (1 - C(z))\rho_f + C(z)\rho_p, \qquad \textit{EQN. 4-11}$$

with the ambient density $\rho_f = 1{,}293\ \mathrm{kg \cdot m^{-3}}$, and the average solid density $\rho_p = 1950\ \mathrm{kg \cdot m^{-3}}$.

Using EQN. 4-2, the self-similar density as a function of height is defined as:

$$\rho(z) = \left[1 - C|_{z=h_m} \cdot e^{-\phi\left[\left(\frac{z}{h_f}\right)^{\zeta} - \eta_w{}^{\zeta}\right]}\right]\rho_f + C|_{z=h_m} \cdot e^{-\phi\left[\left(\frac{z}{h_f}\right)^{\zeta} - \eta_w{}^{\zeta}\right]}\rho_p. \qquad \textit{EQN. 4-12}$$

As the velocity magnitude was shown to be self-similar, the dynamic pressure must be self-similar and is defined as:

$$P_{dyn}(z) = \frac{\rho(z) \cdot U(z)^2}{2} = \frac{{U_m}^2\left(\frac{z}{h_m}\right)^{2\xi} e^{\left[\frac{-2\left(\frac{z}{h_m}-1\right)\xi - \left(2\left(\frac{z}{h_m}-1\right)^2\right)}{\chi^2}\right]} \cdot \left(\left(1 - C_{max} \cdot e^{-\phi\left[\left(\frac{z}{z_f}\right)^{\zeta} - \left(\frac{h_m}{z_f}\right)^{\zeta}\right]}\right)\rho_f + C_{max} \cdot e^{-\phi\left[\left(\frac{z}{z_f}\right)^{\zeta} - \left(\frac{h_m}{z_f}\right)^{\zeta}\right]}\rho_p\right)}{2}. \qquad \textit{EQN. 4-13}$$

With the fit parameters determined from the concentration and velocity fits. Figure 4.7 shows the non-dimensional self-similar distributions of the velocity magnitude, concentrations, densities, and dynamic pressure.

The proposed functions can be used to calculate the non-dimensional time- and height-averaged velocity magnitude $\bar{U} = 0.81$, concentration $\bar{C} = 0.8$, flow density $\bar{\rho} = 0.8$, and dynamic pressure $\overline{P_{dyn}} = 0.58$. These average values are marked as dashed vertical lines in Figure 4.7 a-c. The maximum of dynamic pressure is approximately 2.46 times higher than the bulk, depth- and time-integrated value ($P_{dyn_{max}} = 2.46 \cdot \overline{P_{dyn}}$). The height of the maximum dynamic pressure sits at $h_{P_{max}} \sim 0.0675 \cdot h_f$, and thus lower than the height of the velocity maximum $h_m = 0.24 \cdot h_f$. Using bulk flow densities $\bar{\rho}$ and velocities $\bar{U}$ the maximum time-averaged dynamic pressure can be calculated as

$$P_{dyn_{max}} = 2.72 \cdot \bar{U}^2 \cdot \bar{\rho}. \qquad \textit{EQN. 4-14}$$

Figure 4.7d compares the vertical profile of the self-similar time-averaged dynamic pressure with the similarly normalised, direct measurements of the 95th percentile of dynamic pressure (measured with Piezoelectric pressure sensors). The 95th percentile is chosen as a statistically relevant maximum value of turbulent fluctuations in dynamic pressure that is characteristic for the vertical variation pressure of the entire current. While the forms of the mean and turbulent pressure profiles are broadly similar, the significantly larger turbulence excursions show comparably lower reduction in dynamic pressure towards the solid-shear lower and free-shear upper flow boundaries than the time-averaged pressure profile.

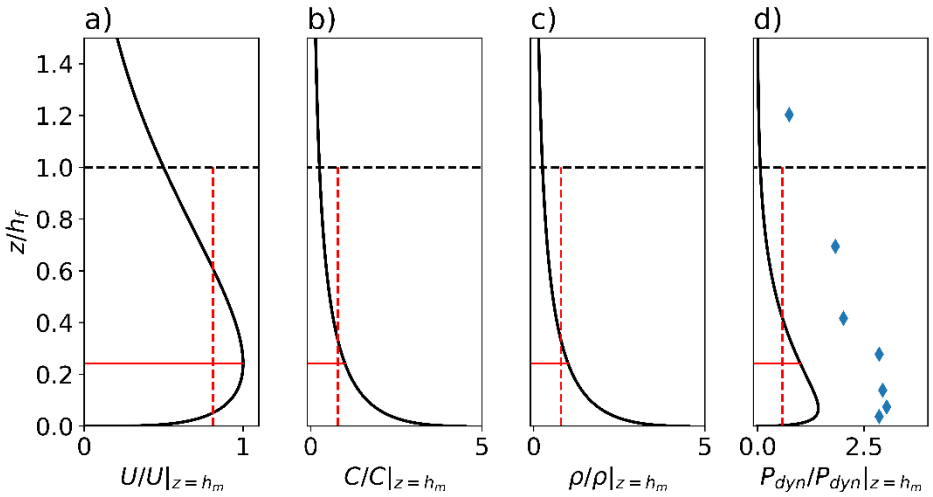

Figure 4.7 Self-similarity of the normalized velocity magnitude, concentration, density, and dynamic pressure. *a) non-dimensional Power-Gaussian fit (EQN. 4-6) of the velocity magnitude, normalized by the velocity magnitude* $U|_{z=hm}$ *at* h_m*, and the flow height* h_f*. b) non-dimensional concentration fits of EQN. 4-10, normalized by the concentration at the wall jet boundary* $C|_{z=hm}$ *and the flow height* h_f*. c) Densities calculated from concentrations shown in b (EQN. 4-11). The density distribution is normalized by the density at the wall jet boundary* $\rho|_{z=hm}$ *and the flow height* h_f*. d) Distribution of dynamic pressures calculated after EQN. 4-13 as* $P_{dyn} = \frac{U^2\rho}{2}$*. The for the velocity magnitude, the Power-Gaussian velocity fit is used, and densities from pannel (c) are used. The distribution of dynamic pressure is normalized using the dynamic pressure at the body wake boundary* $P_{dyn}|_{z=hm}$*, marked in red.The height axis is normalized by the flow height* h_f*. Blue diamonds mark the 90s percentile of the dusty gas pressure measured using Piezoelectric pressure sensors (PCB Piezotronics 106B51). a-d) for each non-dimensional profile, the height average over the flow body (*$z \leq 1$*) is marked with vertical dashed red lines.*

4.4.6 Mean and Turbulent Components of the Flow Structure

Analysis of the time-averaged velocity and concentration distributions has shown self-similarity, and comparing with maximum values revealed that turbulence excursions do not necessarily follow the time-averaged self-similar vertical structure of dilute PDCs. To further investigate the temporal evolution of the generated dilute PDCs, Reynolds

decompositions were performed at $3.35\,m$ from impact for the rough experiment. The Reynolds decomposition is defined as:

$$U(t,z) = \bar{U}(t,z) + U'(t,z), \qquad \textit{EQN. 4-15}$$

with the flow field $U(t,z)$, the mean flow field $\bar{U}(t,z)$, and the turbulence fluctuations $U'(t,z)$. Previous work by Cerminara *et al.* (2021) and Brosch *et al.* (2021) used Power-Gaussian profiles with temporal polynomials as fit parameters to calculate the mean flow field $\bar{U}(t,z)$. Here, the mean flow fields are computed using first-degree temporal Savitzki-Golay filters (Savitzky and Golay, 1964) with filter lengths of $1\,s$. This algorithm allows for the extraction of turbulence fluctuations from all velocity components (U, u, and v) and for both the body and wake of the dilute PDC. Results of the turbulence fluctuations are shown in Figure 4.8.

The velocity fields for the velocity magnitude, downstream velocity, and vertical velocity exhibit complex features, as shown in Figure 4.8 a, b, and c, respectively. The full flow field of the velocity magnitude (Figure 4.8 a) and the downstream velocity (Figure 4.8 b) show similar features including the flow head ($t < 1\,s$) and a dominant flow body (c. $2-3\,s$). The vertical velocity (Figure 4.8 c) provides more insights into the flow structure. The vertical velocity shows the leading upstream rotating head vortex and the divergence at the body wake boundary. Calculating the mean velocity fields using temporal Savitzki-Golay filters with $1\,s$ filter length (Figure 4.8 d, e, and f) provides mean velocity fields that still show a signature of the flow's head and body regions. The vertical velocity further shows the evolution of the body wake boundary in the flow body (Figure 4.8 f). Maximum values of the mean velocity magnitude and downstream velocity reach values $> 6\ \mathrm{m \cdot s^{-1}}$. The

mean field of vertical velocities takes values between c. -1.14 and $2\ \mathrm{m \cdot s^{-1}}$, and with it, smaller, significantly smaller values than the raw vertical velocities (c. -2.3 to $3.9\ \mathrm{m \cdot s^{-1}}$).

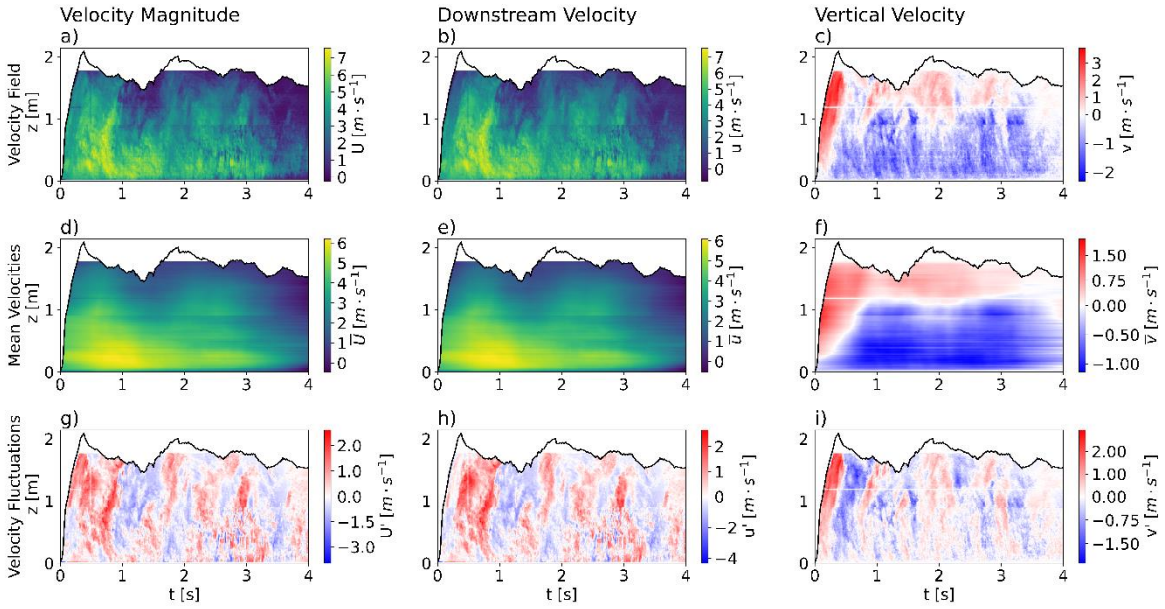

Figure 4.8 Reynolds decomposition of the velocity magnitude, downstream velocity, and vertical velocity. *The first coloumn (a, d, and g) shows the Reynolds decompositon of the velocity magnitude at 3.35 from impact. The second coloumn (b, e, and h) shows the Reynolds decomposition of the downstream velocity at 3.35 m from impact. The third coloums (c, f, and i) shows the Reynolds decomposition of the vertical velocity at 3.35m from impact. All Reynolds decompositions ($X = \bar{X} + X'$) where performed using temporal Savitzki-Golay filters with filter length of $1\ s$ to calculate the mean velocity fields $\bar{X}$. For each coloumn the first row shows the raw velocities X, the second row the mean velocites $\bar{X}$, and the third row the turbulence fluctuations X'. The flow height is marked black in all panels and all data is recorded at 3.35 m. The first row shows the raw velocities of a) velocity magnitude, b) downstream velocity c) vertical velocity. The second row shows the mean velocity fields of a) the velocity magnitude, b) the downstream velocity, and c) the vertical velocity. The last row shows the turbulence fluctuations of a) the velocity magnitude, b) the downstream velocity, and c) the vertical velocity.*

Velocity fluctuations of the velocity magnitude (Figure 4.8 g) and downstream velocity component (Figure 4.8 h) show similar features with slight deviations. Noteworthy, the range of velocity fluctuations of the downstream velocity exceeds the range of velocity fluctuations

in the velocity magnitude. The vertical velocity fluctuations show a strong signature of the frontal head vortex and subsequent low-period fluctuations with lower magnitude.

To investigate how dominant turbulence fluctuations are compared to the mean flow turbulence intensities defined as

$$I = \frac{\sqrt[2]{\frac{u'^2+v'^2}{2}}}{\sqrt[2]{\bar{u}^2+\bar{v}^2}}, \qquad \textit{EQN. 4-16}$$

are calculated. Time-height contour plots of turbulence intensities along the runout ($1.8 - 5.4$ m) are shown, for the example of the rough experiment, in Figure 4.9. The turbulence intensities take high values throughout the entire flow with values > 0.05, for all observer locations. For the first two observer locations, 1.8 and 3.35 m, the turbulence intensities reach values larger 1.5, in the first two profiles. At the third profile at 3.35 m the turbulence intensities reach lower values, and an overall decrease with distance is observed. The temporal evolution for all observed locations shows strong similarities with maximum values in the head (approximately the first second of the flow passage). Especially the higher portions of the head at 1.8 m and 3.35 m show the largest turbulence intensities. During the passage of the flow body c. $1 - 3$ s, a stratification in the turbulence intensities occurs. At 1.8 m (Figure 4.9 a), this stratification is most clearly visible. The flow wake shows the highest values, which decrease at a height of c. 1 m, below the body wake boundary at c. 1.15 m. Below this, the flow body composed of the wall and jet region shows lower turbulence intensities, followed by an increase in turbulence intensities in the last few centimeters above the flow base. At 3.35 and 5.4 m from impact, these trends are also observed. With the waning of the flows after c. 3 s, turbulence intensities increase for all observer locations.

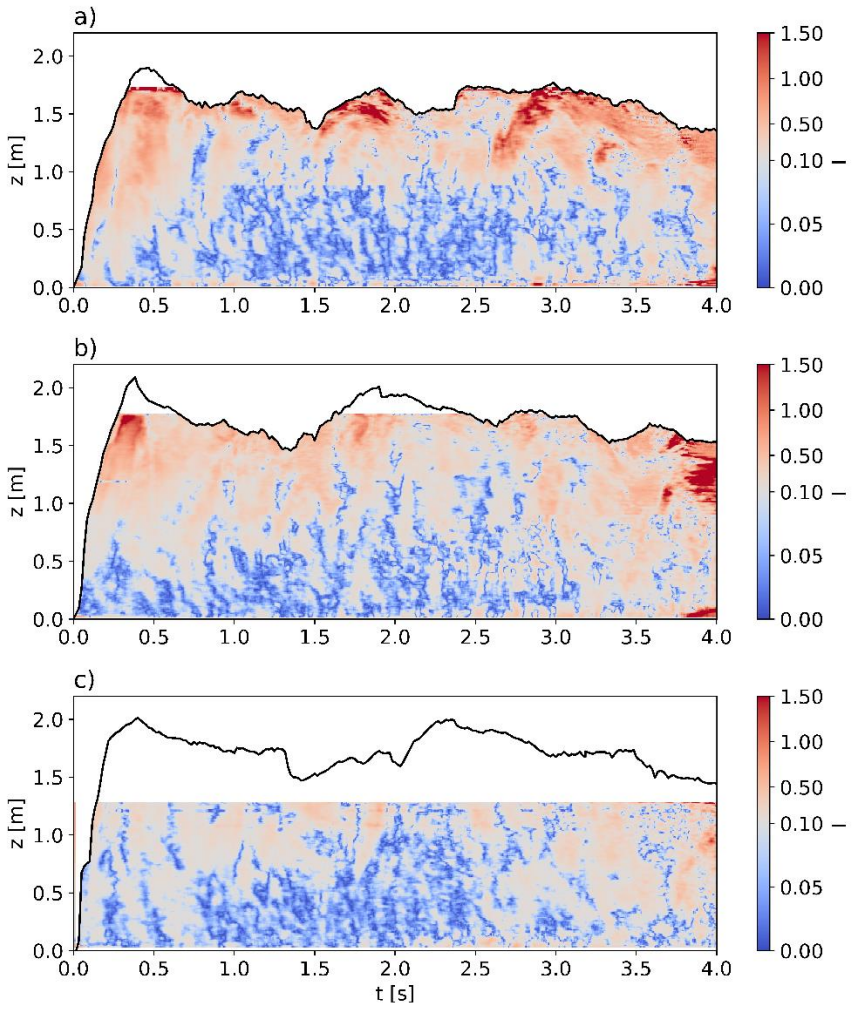

Figure 4.9 Spatio-temporal evolution of turbulence intensities (EQN. 4-16). *Each panel shows the turbulence intensities from the rough experiment at different distances from impact: a) 1.8 m, b) 3.35 m, and c) 5.4 m. Turbulence fluctuations are extracted using temporal Savitzki Golay filters with 1 s filter length. For each panel, the flow height is marked in black.*

Figure 4.10 shows time-integrated profiles of the turbulence intensities. Figure 4.10 a compares the time averaged turbulence intensity for 1.8, 3.35, and 5.4 m from impact. All locations show the same trend, with high turbulence intensities at the base, dropping off until $\frac{z}{h_f}$~0.1. Between $\frac{z}{h_f}$~0.1 to $\frac{z}{h_f}$~0.7, a slight increase in turbulence intensities can be observed until a strong increase starts at $\frac{z}{h_f}$~0.7, where also deviations of the self-similarity

are observed in the velocity magnitude and downstream velocity (see Figure 4.5 a and b). A comparison of the different experiments in Figure 4.10 b shows no substantial influence of the bed roughness.

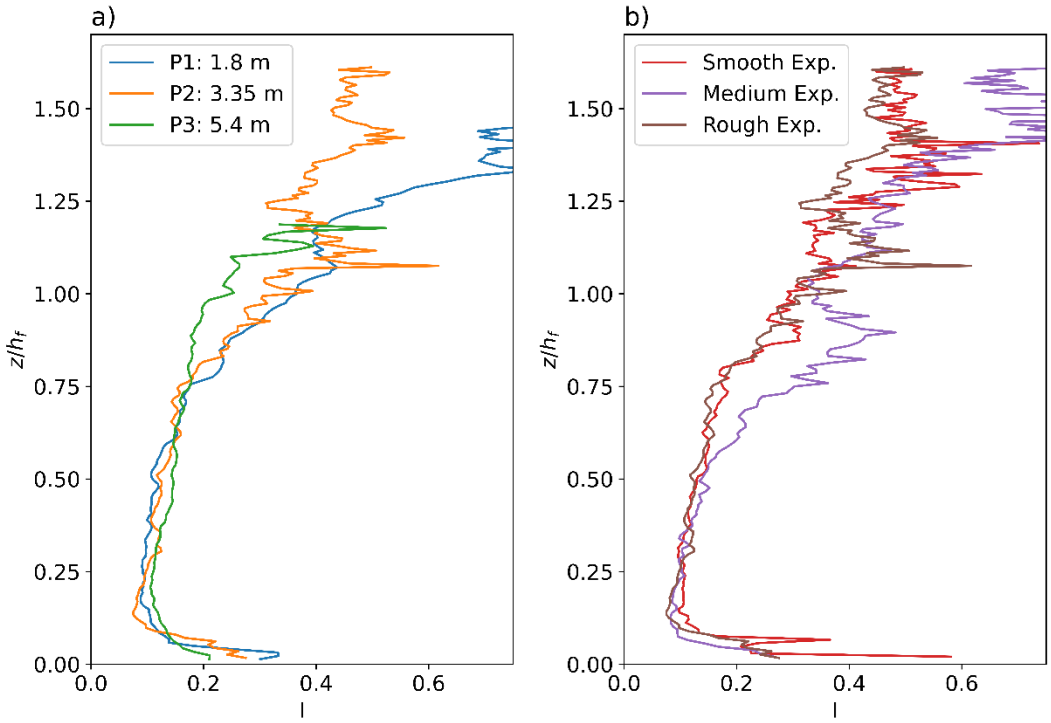

Figure 10 Time-integrated normalized profiles of turbulence intensities and turbulence kinetic energy. *a) Time-integrated profiles of the turbulence intensities (EQN. 4-16) of the rough experiment for 1.8 (blue),3.35 (orange), and 5.4* m *(green) from impact. b) Time-integrated turbulence intensities for different experimental runs, smooth experiment (red), medium experiment (purple), and rough experiment (brown), at 3.35* m *runout. Turbulence intensities are calculated using temporal Savitzki Golay filters with 1 s filter length and averaged over the central flow body (1-2.5 s).*

Another measure of turbulence is turbulence kinetic energy (TKE), defined as:

$$TKE = \frac{1}{2}\left(\overline{u'^2} + \overline{v'^2}\right), \qquad \textit{EQN. 4-17}$$

with $\overline{u'^2}$ the time-averaged squared downstream velocity fluctuation, and $\overline{v'^2}$ the time-averaged squared vertical velocity component. For the transient case of dilute PDCs, such

as presented here, the squared turbulence fluctuations are not time-averaged; therefore, the presented time-dependent TKE is defined as:

$$TKE = \frac{1}{2}(u'^2 + v'^2), \qquad \textit{EQN. 4-18}$$

providing the kinetic energy contained in the turbulence per unit mass. Results for the TKE for for the rough experiment at 1.8, 3.35, and 5.4 m, from impact, extracted with 1 s and 250 ms filter lengths, are shown in Figure 4.10.

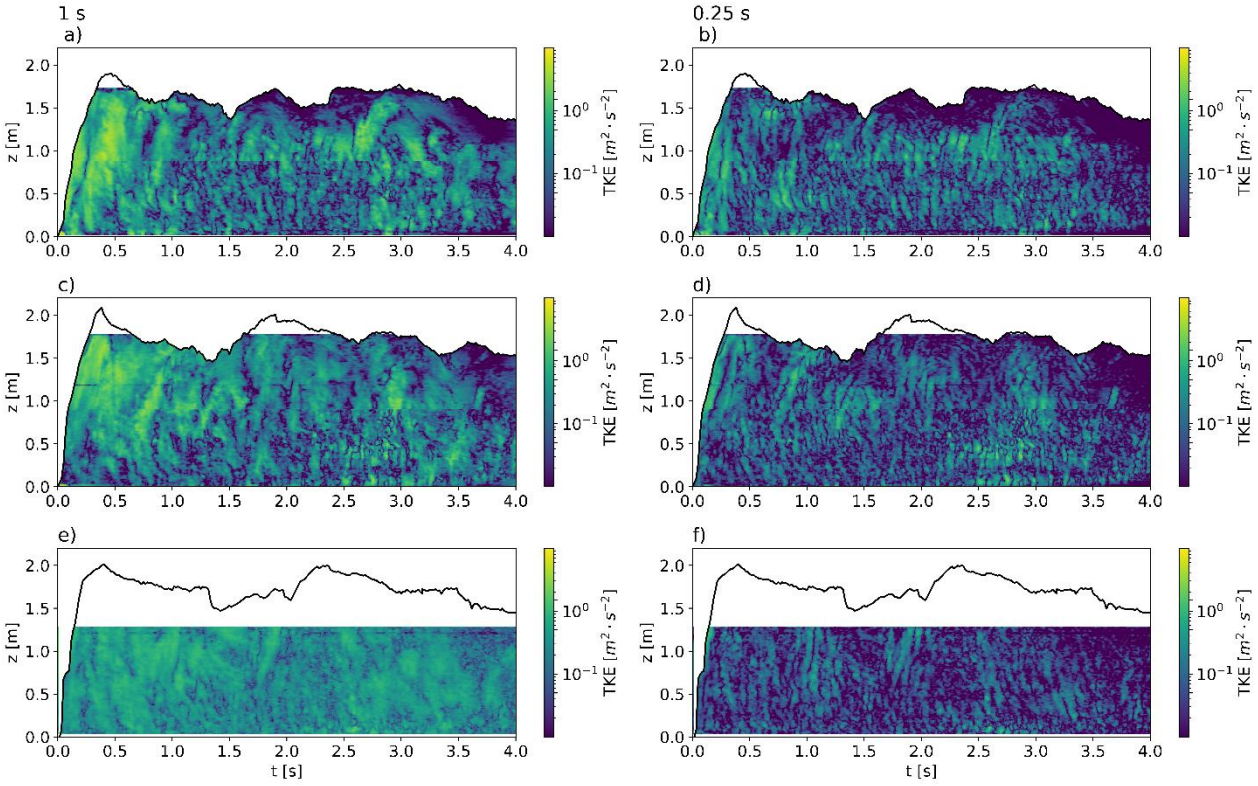

Figure 4.10 Spatio-temporal evolution of turbulence kinetic energy (EQN. 4-18) inside dilute PDCs. *The turbulence kinetic energy (EQN. 4-18) extracted from velocity measurements obtained during the rough experiment are shown at* 1.8, 3.35, *and* 5.4 m *from impact in panel a, b, and c, respectively. Turbulence fluctuations to calculate the TKE are extracted via Reynolds decomposition, using* 1 s *long temporal Savitzki Golay filters to calculate the mean flow fields for the downstream and vertical velocity.*

The TKE at 1.8 m from impact (Figure 4.10 a) shows variations over multiple orders of magnitude. The TKE is maximal in the flow head, which constitutes the largest turbulence structure in dilute PDCs. Following the head, between c. 1 and 2.5 s, the TKE reduces and, similarly to the turbulence intensity, shows higher values in the wake than in the main flow body. Interestingly, features with small duration (~100 ms) and spatial extend are dominant within the main flow body. With the waning of the flow (~3 s onward), an increase in TKE can be observed, and the TKE shows a more even distribution with height. As opposed to the turbulence intensity I, no dominant increase in TKE is observed towards the substrate. TKE at 1.8 m from impact, extracted with a shorter window length of 250 ms (Figure 4.10 b), shows that sub-vertical high-frequency features superimpose large turbulence structures throughout the flow passage. At 3.35 m from impact (Figure 4.10 b), the TKE shows similar features in the head until c. 1 s. Particularly the upper head shows maximum values. After the head passage, between c. 1 and 3 s, the turbulence kinetic energy shows consistently higher values in the wake and is dominated by small-scale high-frequency structures in the flow body. Also, at $5.4\,m$ from impact (Figure 4.10 b), this same pattern is shown. Comparing these three observer locations, it is apparent that the TKE decreases during the flow propagation, from initially c.19 $\mathrm{m^2 \cdot s^{-2}}$ to 1.85 $\mathrm{m^2 \cdot s^{-2}}$ at 5.4 m from impact. Extracting higher frequency turbulence structures using shorter filter lengths reveals the superposition of larger and smaller turbulence structures also to occur at 3.35 and 5.4 m, Figure 4.10 d and f, respectively.

4.5 Discussion

4.5.1 Self-Similar Vertical Structure of Dilute PDCs

We presented the first dataset interrogating the time-averaged vertical structure of velocity and concentration of dilute PDCs. We conducted three experiments with varying bed roughness, from dynamically smooth to roughness larger than the viscous sublayer. The results show that the Power-Gaussian velocity profile suggested by Brosch *et al.* (2021) and Cerminara *et al.* (2021) fits the dimensional velocity magnitude and downstream velocity at all observer locations and experiments. These results show the similarity to velocity distributions used to describe turbidity currents (Altinakar *et al.*, 1996, Cantero-Chinchilla *et al.*, 2015). Investigations on the presence of a basal slip did not provide conclusive results due to the slightly too coarse spatial resolution of our PIV analysis. The slight increase in fit quality of the Power-Gaussian profile with a Navier slip condition (Eqn. 4) in comparison to the normal Power-Gaussian description (Eqn. 1) is not significant enough to be interpreted and may stem from overfitting due to the employment of an additional fitting parameter.

Unlike distributions of velocity magnitude and downstream velocity in turbidity currents, the velocity distributions of dilute PDCs do not approach zero at the upper boundary of the flow body. Here, dilute PDCs develop a turbulent wake where downstream velocity and velocity magnitude are not zero, and the vertical (slope normal) velocity component changes sign and transitions from predominantly downward to predominantly upward motion. Up to the body wake boundary, we further show a Power-Gaussian fit to describe the vertical velocity component well. At the body-wake boundary, the vertical velocities switch signs, leading to predominantly upward motion in the flow's wake. The Power-Gaussian profile of the vertical velocity does not describe the body-wake boundary well. Fitting a velocity distribution such as Cantero-Chinchilla *et al.* (2015) suggested for the downstream velocity

components to the vertical velocity data satisfies the boundary condition at the body wake boundary. However, the fit parameters of Power-Gaussian velocity distributions provide valuable information about the data (Cerminara *et al.*, 2021), whereas the fit parameters of EQN. 4-9 are less easily interpretable (Cantero-Chinchilla *et al.*, 2015).

Analyzing the non-dimensional velocity data reveals the self-similarity of all velocity components, and no clear influence of the substrate roughness can be identified. This does not match the results of Kashefipour *et al.* (2017), investigating water particle currents. An important difference between the presented experiments and the experiments presented by Kashefipour *et al.* (2017) is the range of roughness used. With wall region heights of $2-6$ cm, Kashefipour *et al.* (2017) used $0-1.5$ cm roughnesses in 0.5 cm steps. Scaling these roughness scales to the PELE set-up would correspond to maximum roughness scales of $10-33$ cm, exceeding the used roughness scales ($4-8$ mm) by more than an order of magnitude. These roughness scales match obstacle heights used by Corna (2023), who investigated the influence of topographic obstacles on the propagation of dilute PDCs. Therefore, the roughness scales used in this study might be too small to influence the vertical structure. Further, with strongly sedimenting flows such as described here, the flows rapidly generate their own substrate that they propagate on overprinting the preexisting terrain. Further studies applying wider ranges of bed roughness are suggested.

Time-averaged concentration distributions along the runout were shown to be well fit by EQN. 4-2, first suggested by Cantero-Chinchilla *et al.* (2015), and tested at one observer location by Brosch and Lube (2020). The main differences between concentration profiles of dilute PDCs and turbidity currents, as shown by Cantero-Chinchilla *et al.* (2015), are a strong increase towards the base and a slower fading with height. This is presented in the fit parameters and is constituted in a concave rise of concentrations towards the base as opposed

to a convex trend for turbidity currents. Also, the decrease in concentrations of dilute PDCs decreases slower towards the top in dilute PDCs. It is noteworthy that turbidity currents investigated by Cantero-Chinchilla *et al.* (2015) did not develop a dominant wake.

Using the self-similar distributions of velocity magnitude and concentration, a self-similar distribution of the dynamic pressure is derived. This self-similar distribution has the same shape as dynamic pressure distributions presented in Dellino *et al.* (2010). The main difference here is that EQN. 4-13 has maximum values at c. $\frac{z}{h_f} = 0.068$ compared to smaller values observed by Dellino *et al.* (2010). For natural PDCs, such as the PDC generated during the 9th of December eruption of Whakaari (White Island), New Zealand, a flow height of 26 m (Brosch *et al.*, 2021) would, according to our results, generate a dynamic pressure maximum at c. 1.77 m. For other natural flows between $100 - 500$ m flow height, the dynamic pressure maximum would result at $6.8 - 34$ m, and thereby within the height of built infrastructures.

The self-similarity of all velocity components, as well as the concentration, dynamic pressure, and, therefore, the momentum, provides valuable information for depth-averaged models (Doyle *et al.*, 2008, Doyle *et al.*, 2010, Kelfoun, 2017, Shimizu *et al.*, 2019, Shimizu *et al.*, 2021). To attempt to improve these models, the vertical distributions suggested in this research could be implemented in those models. The similarity of the dynamic pressure distributions (EQN. 4-13) to results by Dellino *et al.* (2010), obtained using a law of the wall velocity profile, suggests changing the vertical distributions may not significantly change the model outputs.

4.5.2 Engines of Turbulence in Dilute Pyroclastic Density Currents

Turbulence fluctuations of the velocity magnitude, downstream, and vertical velocity were extracted using temporal Savitzki Golay filters to calculate the mean flow fields. The resulting turbulence fluctuations reveal the head to be the most dominant structure and to be followed by a range of large turbulence structures. These turbulence structures are presented through the entire flow height and show strong similarities to structures presented by Brosch *et al.* (2021). Turbulence intensities calculated from the mean and turbulent components extracted from the Reynolds decomposition revealed the turbulence to be dominant in lowermost part of the wall region and to strongly increase and be dominant above $\frac{z}{h_f} > 0.7$. This matches the main deviations from the self-similar velocity profiles shown in Figure 4.5. This pattern is shown throughout the entire flow passage, least dominant in the turbulent head, constituting the largest and most dominant turbulence structure in the described PDCs. Time-integrated height profiles of the turbulence intensities reconfirm this pattern and suggest no significant differences along the runout or the substrate roughness.

Turbulence kinetic energies extracted with 1 s long Savitzki Golay filters also revealed the most dominant turbulence structure to be the head and the turbulence to be higher in the flow wake than in the body. Interestingly, the body is dominated by higher frequency turbulence structures than the rest of the flow, and no significant increase to the base was observed. This pattern is most visible at 1.8 m from impact. The turbulence kinetic energy decreases strongly along the runout. These results suggest that the turbulence generation is dominated by the outer free shear, creating an actively mixing wake that protrudes into the main flow body. In upper flow portions low density gradients and low stratification stability (Brosch and Lube, 2020) lead to unhindered turbulence production. Strong density stratifications and high particle concentrations in lower flow portions hinder turbulence generation

(Elghobashi, 1994, Breard *et al.*, 2016, Lube *et al.*, 2020). Outer shear and the actively mixing layer are therefore suggested to be one of the main drivers of turbulent entrainment (Burgisser and Bergantz, 2002, Andrews and Manga, 2012, Dellino *et al.*, 2019, Brosch *et al.*, 2022) and the generation of large destructive turbulence structures (Brosch *et al.*, 2021). Extracting turbulence kinetic energies with smaller window lengths further showed the superposition of smaller sub-vertical high-frequency turbulence structures.

4.6 References

Altinakar, M.S., Graf, W.H. & Hopfinger, E.J., 1996. Flow structure in turbidity currents. *Journal of Hydraulic Research,* 34**,** 713-718.

Ancey, C., 2004. Powder snow avalanches: Approximation as non-Boussinesq clouds with a Richardson number–dependent entrainment function. *Journal of Geophysical Research: Earth Surface,* 109.

Andrews, B.J. & Manga, M., 2012. Experimental study of turbulence, sedimentation, and coignimbrite mass partitioning in dilute pyroclastic density currents. *Journal of Volcanology and Geothermal Research,* 225**,** 30-44.

Batchelor, G.K. & Proudman, I., 1956. The large-scale structure of homogenous turbulence. *Philosophical Transactions of the Royal Society of London. Series A, Mathematical and Physical Sciences,* 248**,** 369-405.

Breard, E.C.P., Lube, G., Jones, J.R., Dufek, J., Cronin, S.J., Valentine, G.A. & Moebis, A., 2016. Coupling of turbulent and non-turbulent flow regimes within pyroclastic density currents. *Nature Geoscience,* 9**,** 767-771.

Brosch, E. & Lube, G., 2020. Spatiotemporal sediment transport and deposition processes in experimental dilute pyroclastic density currents. *Journal of Volcanology and Geothermal Research,* 401**,** 106946.

Brosch, E., Lube, G., Cerminara, M., Esposti-Ongaro, T., Breard, E.C.P., Dufek, J., Sovilla, B. & Fullard, L., 2021. Destructiveness of pyroclastic surges controlled by turbulent fluctuations. *Nature Communications,* 12**,** 7306.

Brosch, E., Lube, G., Esposti-Ongaro, T., Cerminara, M., Breard, E.C.P. & Meiburg, E., 2022. Characteristics and controls of the runout behaviour of non-Boussinesq particle-laden gravity currents – A large-scale experimental investigation of dilute pyroclastic density currents. *Journal of Volcanology and Geothermal Research,* 432**,** 107697.

Burgisser, A. & Bergantz, G.W., 2002. Reconciling pyroclastic flow and surge: the multiphase physics of pyroclastic density currents. *Earth and Planetary Science Letters,* 202**,** 405-418.

Burgisser, A., Bergantz, G.W. & Breidenthal, R.E., 2005. Addressing complexity in laboratory experiments: the scaling of dilute multiphase flows in magmatic systems. *Journal of Volcanology and Geothermal Research,* 141**,** 245-265.

Cantero-Chinchilla, F.N., Dey, S., Castro-Orgaz, O. & Ali, S.Z., 2015. Hydrodynamic analysis of fully developed turbidity currents over plane beds based on self-preserving velocity and concentration distributions. *Journal of Geophysical Research-Earth Surface,* 120**,** 2176-2199.

Cebeci, T., 2013. Chapter 4 - General Behavior of Turbulent Boundary Layers. *In* T. Cebeci (ed.) *Analysis of Turbulent Flows with Computer Programs (Third Edition).* Oxford: Butterworth-Heinemann, 89-153.

Cerminara, M., Brosch, E. & Lube, G., 2021. A theoretical framework and the experimental dataset for benchmarking numerical models of dilute pyroclastic density currents. *arXiv preprint arXiv:2106.14057*.

Choux, C.M. & Druitt, T.H., 2002. Analogue study of particle segregation in pyroclastic density currents, with implications for the emplacement mechanisms of large ignimbrites. *Sedimentology,* 49**,** 907-928.

Corna, L., 2023. The interactions of pyroclastic density currents with obstacles : a large-scale experimental study : a thesis presented in partial fulfilment of the requirements for the degree of Doctor of Philosophy in Earth Sciences at Massey University, Manawatū, Palmerston North, New Zealand. Doctoral. Massey University.

Dade, W.B. & Huppert, H.E., 1995. A Box Model for Non-Entraining, Suspension-Driven Gravity Surges on Horizontal Surfaces. *Sedimentology,* 42**,** 453-471.

Dellino, P., Buttner, R., Dioguardi, F., Doronzo, D.M., La Volpe, L., Mele, D., Sonder, I., Sulpizio, R. & Zimanowski, B., 2010. Experimental evidence links volcanic particle characteristics to pyroclastic flow hazard. *Earth and Planetary Science Letters,* 295**,** 314-320.

Dellino, P., Dioguardi, F., Doronzo, D.M. & Mele, D., 2019. The Entrainment Rate of Non-Boussinesq Hazardous Geophysical Gas-Particle Flows: An Experimental Model With Application to Pyroclastic Density Currents. *Geophysical Research Letters,* 46**,** 12851-12861.

Dellino, P., Dioguardi, F., Rinaldi, A., Sulpizio, R. & Mele, D., 2021. Inverting sediment bedforms for evaluating the hazard of dilute pyroclastic density currents in the field. *Scientific Reports,* 11**,** 21024.

Dellino, P., Mele, D., Sulpizio, R., La Volpe, L. & Braia, G., 2008. A method for the calculation of the impact parameters of dilute pyroclastic density currents based on deposit particle characteristics. *Journal of Geophysical Research-Solid Earth,* 113**,** B07206.

Dioguardi, F. & Mele, D., 2018. PYFLOW_2.0: a computer program for calculating flow properties and impact parameters of past dilute pyroclastic density currents based on field data. *Bulletin of Volcanology,* 80**,** 28.

Doyle, E.E., Hogg, A.J., Mader, H.M. & Sparks, R.S.J., 2008. Modeling dense pyroclastic basal flows from collapsing columns. *Geophysical Research Letters,* 35.

Doyle, E.E., Hogg, A.J., Mader, H.M. & Sparks, R.S.J., 2010. A two-layer model for the evolution and propagation of dense and dilute regions of pyroclastic currents. *Journal of Volcanology and Geothermal Research,* 190**,** 365-378.

Druitt, T.H., 1998. Pyroclastic density currents. *Geological Society, London, Special Publications,* 145**,** 145-182.

Dufek, J. & Bergantz, G.W., 2007. Suspended load and bed-load transport of particle-laden gravity currents: the role of particle–bed interaction. *Theoretical and Computational Fluid Dynamics,* 21**,** 119-145.

Elghobashi, S., 1994. On predicting particle-laden turbulent flows. *Applied Scientific Research,* 52**,** 309-329.

Fauria, K.E., Manga, M. & Chamberlain, M., 2016. Effect of particle entrainment on the runout of pyroclastic density currents. *Journal of Geophysical Research-Solid Earth,* 121**,** 6445-6461.

Garcia, M. & Parker, G., 1993. Experiments on the Entrainment of Sediment into Suspension by a Dense Bottom Current. *Journal of Geophysical Research-Oceans,* 98**,** 4793-4807.

Hopfinger, E.J., 1983. Snow Avalanche Motion and Related Phenomena. *Annual Review of Fluid Mechanics,* 15**,** 47-76.

Kashefipour, S.M., Daryaee, M. & Ghomeshi, M., 2017. Effect of bed roughness on velocity profile and water entrainment in a sedimentary density current. *Canadian Journal of Civil Engineering,* 45**,** 9-17.

Kelfoun, K., 2017. A two-layer depth-averaged model for both the dilute and the concentrated parts of pyroclastic currents. *Journal of Geophysical Research: Solid Earth,* 122**,** 4293-4311.

Knippertz, P., Deutscher, C., Kandler, K., Müller, T., Schulz, O. & Schütz, L., 2007. Dust mobilization due to density currents in the Atlas region: Observations from the Saharan Mineral Dust Experiment 2006 field campaign. *Journal of Geophysical Research: Atmospheres,* 112.

Lube, G., Breard, E.C.P., Cronin, S.J. & Jones, J., 2015. Synthesizing large-scale pyroclastic flows: Experimental design, scaling, and first results from PELE. *Journal of Geophysical Research-Solid Earth,* 120**,** 1487-1502.

Lube, G., Breard, E.C.P., Cronin, S.J., Procter, J.N., Brenna, M., Moebis, A., Pardo, N., Stewart, R.B., Jolly, A. & Fournier, N., 2014. Dynamics of surges generated by hydrothermal blasts during the 6 August 2012 Te Maari eruption, Mt. Tongariro, New Zealand. *Journal of Volcanology and Geothermal Research,* 286**,** 348-366.

Lube, G., Breard, E.C.P., Esposti-Ongaro, T., Dufek, J. & Brand, B., 2020. Multiphase flow behaviour and hazard prediction of pyroclastic density currents. *Nature Reviews Earth & Environment,* 1**,** 348-365.

Meiburg, E. & Kneller, B., 2010. Turbidity Currents and Their Deposits. *Annual Review of Fluid Mechanics,* 42**,** 135-156.

Neri, A., Esposti Ongaro, T., Voight, B. & Widiwijayanti, C., 2015. Pyroclastic Density Current Hazards and Risk. *In* J.F. Shroder & P. Papale (eds.) *Volcanic Hazards, Risks and Disasters.* Boston: Elsevier, 109-140.

Nourmohammadi, Z., Afshin, H. & Firoozabadi, B., 2011. Experimental observation of the flow structure of turbidity currents. *Journal of Hydraulic Research,* 49**,** 168-177.

Parker, G., Garcia, M., Fukushima, Y. & Yu, W., 1987. Experiments on Turbidity Currents over an Erodible Bed. *Journal of Hydraulic Research,* 25**,** 123-147.

Prandtl, L., 1905. Uber Flussigkeitsbewegung bei sehr kleiner Reibung. *Verhandl. 3rd Int. Math. Kongr. Heidelberg (1904), Leipzig*.

Savitzky, A. & Golay, M.J., 1964. Smoothing and differentiation of data by simplified least squares procedures. *Analytical chemistry,* 36**,** 1627-1639.

Scharff, L., Hort, M. & Varley, N.R., 2019. First in-situ observation of a moving natural pyroclastic density current using Doppler radar. *Scientific Reports,* 9**,** 7386.

Shimizu, H.A., Koyaguchi, T. & Suzuki, Y.J., 2019. The run-out distance of large-scale pyroclastic density currents: A two-layer depth-averaged model. *Journal of Volcanology and Geothermal Research*.

Shimizu, H.A., Koyaguchi, T., Suzuki, Y.J., Brosch, E., Lube, G. & Cerminara, M., 2021. Validation of a two-layer depth-averaged model by comparison with an experimental dilute stratified pyroclastic density current. *Bulletin of Volcanology,* 83**,** 73.

Sulpizio, R., Dellino, P., Doronzo , D.M. & Sarocchi, D., 2014. Pyroclastic density currents: state of the art and perspectives. *Journal of Volcanology and Geothermal Research,* 283**,** 36-65.

Thielicke, W. & Sonntag, R., 2021. Particle Image Velocimetry for MATLAB: Accuracy and enhanced algorithms in PIVlab. *Journal of Open Research Software,* 9.

Thielicke, W. & Stamhuis, E.J., 2014. PIVlab – Towards User-friendly, Affordable and Accurate Digital Particle Image Velocimetry in MATLAB. *Journal of Open Research Software,* 2**,** e30.

Valentine, G.A., 1987. Stratified flow in pyroclastic surges. *Bulletin of Volcanology,* 49**,** 616-630.

Wells, M.G. & Dorrell, R.M., 2021. Turbulence processes within turbidity currents. *Annual Review of Fluid Mechanics,* 53**,** 59-83.

Wilson, C.J.N., 1985. The Taupo Eruption, New Zealand. II. The Taupo Ignimbrite. *Philosophical Transactions of the Royal Society of London. Series A, Mathematical and Physical Sciences,* 314**,** 229-310.

Wohletz, K.H., 1998. Pyroclastic surges and compressible two-phase flow. *Developments in Volcanology*, 4.

5 Turbulence Structures in Dilute Pyroclastic Density Currents and their Implications on Turbulent Gas Particle Coupling

This chapter is prepared for submission as a research article to Journal of Geophysical Research: Solid Earth.

Title: Turbulence Structures in Dilute Pyroclastic Density Currents and their Implications on Turbulent Gas Particle Coupling

Authors: Daniel Uhle[1], Gert Lube[1], Jim Jones[2], Eric C.P. Breard[3], Eckart Meiburg[4], James Ardo[1,5], Ermanno Brosch[1], Lucas Corna[1], Anja Moebis[1], Kevin Alexander Kreutz[1]

[1] School of Agriculture and Environment, College of Science, Massey University, Palmerston North, New Zealand

[2] School of Food and Advanced Technology, College of Science, Massey University, Palmerston North, New Zealand

[3] School of Geosciences, University of Edinburgh, UK

[4] University of California Santa Barbara, Santa Barbara, USA

[5] Manaaki Whenua- Landcare Research, Palmerston North, New Zealand

5.1 Abstract

Dilute pyroclastic density currents (dilute PDCs) are amongst the most hazardous volcanic phenomena globally. *In situ* measurements are highly challenging due to their high destructiveness. Therefore, most research has focused on deposit interpretations, analog experiments, and numerical simulations. Large-scale experiments have shown that turbulence structures significantly enhance the destructiveness of dilute PDCs. However, the formation of the turbulence structures and their modification by gas-particle interactions inside dilute PDCs remain poorly understood.

We present experimental results synthesizing high Reynolds number dilute PDCs formed by the gravitational collapse of hot volcanic material falling from a hopper onto an inclined chute. The turbulence structures and gas-particle coupling are investigated through measurements of flow-internal velocity fields, flow temperature, and dynamic pressure. The recorded time series are analyzed for their turbulence characteristics by performing Reynolds decompositions and investigations of their frequency spectra. Our observations show large turbulence structures to be superimposed by smaller sub-vertical sub-structures. The Fourier spectra of dynamic pressure are characterized by maxima and slope changes, corresponding to discrete frequency bands at $6 - 17$ Hz and $35 - 95$ Hz, where flow energies are focused, and amplitude maxima occur. Analyzing the particle Stokes number, these frequencies can be linked to characteristic modes of the flow grain-size distributions, $114 - 252$ μm and $39 - 67$ μm, respectively. The Fourier spectra of dynamic pressure, vertical velocity, and temperature also show characteristic decreases in slope and, therefore, enhanced energy transfer from large to small structures. Energy maxima in the Fourier spectra of dynamic pressure on frequency bands between $6 - 17$ Hz coincide with the slope changes at 6 Hz and sub-vertical structures with $\sim$10 Hz.

We hypothesize that particles cluster at eddy peripheries, from which they finally decouple, generating sub-vertical sedimentation pathways. Through this process, turbulent gas-particle feedbacks cause selective sedimentation, producing polymodal flow grain-size distributions and modulations of the turbulent energy cascade.

5.2 Introduction

Dilute pyroclastic density currents (also dilute PDCs or pyroclastic surges and blasts) are frequently occurring and highly destructive volcanic processes at the Earth's surface (Wohletz, 1998, Sulpizio et al., 2014, Lube et al., 2020). Dilute PDCs represent strongly vertically density stratified, turbulent multiphase flows of hot volcanic particles and gas. Dilute PDCs frequently occur for all eruption magnitudes, but their destructiveness and unpredictability make systematically planned *in situ* measurements inside flows challenging. Only a few incidental direct geophysical measurements of PDCs exist (Scharff et al., 2019, Brosch et al., 2021). Due to this lack of observations, an understanding of the detailed internal flow and turbulence structure of dilute PDCs remains incomplete.

Much of the complexity of dilute PDCs stems from their polydispersity and wide range of particle concentrations occurring concurrently within a single flow (Branney and Kokelaar, 2002, Roche, 2012). In turbulent multiphase flows, different degrees of gas-particle feedback are envisaged to occur. At particle concentrations $\phi_p \leq 10^{-6}$ one-way coupling is expected to be dominant where particles follow the fluid motion but do not modulate the fluid motion (Elghobashi, 1994). With increasing particle concentrations ($10^{-6} < \phi_p \leq 10^{-3}$), two-way coupling becomes dominant and the particles and fluid phases affect each other's dynamics (Elghobashi, 1994). For concentrations $\phi_p > 10^{-3}$, interparticle collisions and friction are important and four-way coupling characterizes gas-particle interaction and feedbacks

(Elghobashi, 1994, Carrara et al., 2019). In polydisperse systems, the particle Stokes number (St) and the Stability number (Σ) describe how particles are affected by turbulent eddies of different time and length scales (Burgisser and Bergantz, 2002, Breard and Lube, 2017). For particle Stokes numbers of around one, particles tend to accumulate and cluster at the peripheries of turbulence structures (Burgisser and Bergantz, 2002). Strong polydispersity and a wide range of particle densities result in a broad range of coupling and transport regimes (Burgisser and Bergantz, 2002, Burgisser et al., 2005, Lube et al., 2020, Breard and Lube, 2017). While particle clustering in multiphase turbulence occurs predominantly for $St = \mathcal{O}(1)$, it also occurs at conditions of smaller Stokes numbers (Fessler et al., 1994, Aliseda et al., 2002, Wang and Maxey, 1993). Particle clustering remains a main research avenue in multiphase turbulence (Brandt and Coletti, 2022).

How the multiphase properties like coupling regimes and polydispersity affect the turbulence structures and the energy cascades inside dilute PDCs has not been quantified. Several studies on multiphase flows suggest that particles enhance the energy transfer from larger to smaller turbulence structures (Yang and Shy, 2005, Bosse et al., 2006, Poelma and Ooms, 2006). The mechanism by which particles enhance this energy cascade is not known. Ferrante and Elghobashi (2003) suggest that the accumulation of particles with $St \sim 1$ at eddy peripheries increases the local momentum.

Experimental studies by Brosch et al. (2021) have shown that turbulence plays a crucial role in the destructive potential of dilute PDCs. They observed that fluctuating maxima in dynamic pressure, which are up to $3-5$ times the mean dynamic pressure, are associated with the largest coherent turbulence structures. However, it remains to be shown how pressure energy enhances inside turbulence structures and how these evolve during flow propagation.

We present measurements into experimental dilute pyroclastic density currents conducted at the large-scale facility PELE in New Zealand (Pyroclastic flow Eruption Large-scale Experiment) (Lube et al., 2015). We extract turbulence fluctuations for two different time and length scales from direct dynamic pressure measurements, flow internal velocities, specific kinetic energy, and flow temperature. Based on these turbulence fluctuations, we identify turbulence structures and describe their evolution along flow runout. Further, we investigate the Fourier spectra of these measurements, showing how turbulent energy is transferred from large to small structures and focused into distinct frequency bands. The particle Stokes number is analyzed to link the particle size distributions of the flow to turbulence timescales. The presented study aims to address three specific research questions concerning turbulent gas-particle coupling in dilute PDCs: How is turbulence presented in measurements of different flow parameters? How do turbulence characteristics change along the runout? Which gas-particle interactions occur in polydisperse dilute PDCs?

5.3 Methods

The large-scale experiment was conducted at the PELE facility, designed to generate and measure inside experimental PDCs that dynamically scale to natural flows (Lube et al., 2015, Brosch and Lube, 2020). The experimental dilute PDC is generated through a gravitational collapse by discharging heated volcanic material from an elevated hopper into an instrumented flume. An experimental dilute PDC forms on impact, propagating down the flume. The volcanic material used in the experimental runs is a mixture of two well-studied volcanic deposits from the AD232 Taupo ignimbrite (Wilson, 1985), with particle sizes from 2 µm to 16 mm, a fines content (particles < 64 µm) of 20%, and particle densities $350 - 2600\ \mathrm{kg \cdot m^{-3}}$ (Figure 5.1). The initial grain-size distribution presents an approximately

Gaussian shape with a primary mode at 250 µm, a secondary mode at 11 µm, and a d_{50} median grain size of 245 µm.

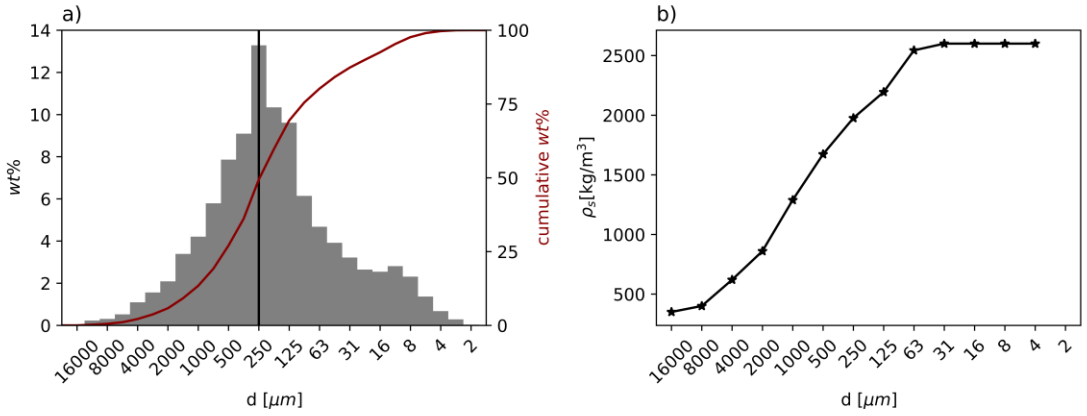

Figure 5.1 Properties of the experimental mixture. *a) Grain size distribution in weight percent (grey histogram) and cumulative grain size distribution in weight percent (dark red), with a* d_{50} *median grain size of* 241 µm *(vertical black line), and fines content (particles* $<$ 64 µm*) of c.* 20%*. The grain size distribution is near unimodal, with a primary mode at* 250 µm *and a secondary minor mode at* 11 µm*. b) Grain size-dependent average hydraulic densities of the particles. The average particle density, ranging from* $350 - 2600\ kg \cdot m^{-3}$*, was measured using heavy liquid separation by Breard (2016).*

In the experiment described here, 125 kg of volcanic material was heated to a temperature of 120 °C (the ambient temperature during the experiment was 15 °C) inside a hopper with a volume of 0.7 m^3, which is mounted 7 m above an instrumented flume inclined at 6°. The material is discharged over 5 s at an average discharge rates of $25\ \mathrm{kg \cdot s^{-1}}$, peaking at $40\ \mathrm{kg \cdot s^{-1}}$. The material impacts the instrumented flume approximately 1.5 s after the experimental trigger. At a distance of 1.8 m, a fully developed density current structure is formed.

The runout section comprises an instrumented confined channel and a horizontal unconfined runout section. The confined channel is 14.6 m long and 50 cm wide and inclined at 6°. One

sidewall is constructed from tempered glass, and the other side is made of steel. The confining side wall height reduces along the runout from 1.8 m ($0 - 6.4$ m runout) to 1.2 m ($6.4 - 10.6$ m) to finally 0.6 m (until 14.6 m), from 14.6 m onwards. The substrate is made from $4 - 8$ mm subrounded river pebbles glued into the channel as a closely packed monolayer.

The glass wall on one side of the channel allows viewing inside the flows to record flow internal processes and the flow structure, using 20 GoPro cameras (recording at $30 - 240\ frames\ per\ second$(fps) and six high-speed, high-resolution cameras (recording at 500 fps). To illustrate the flow structure at static observer location, time-height graphs of the high-speed video footage (as shown in Figure 5.2 and Figure 5.3) are generated by extracting pixel columns for each time step. The high-speed camera data is also used to calculate two-dimensional velocity fields ($\vec{U} = (u, v)$) utilizing the particle image velocimetry (PIV) implementation PIVlab (version 2.54) (Thielicke and Stamhuis, 2014). Velocity fields generated have a spatial resolution of c. 1 cm and a temporal resolution of 500 Hz (2 ms). The velocity fields are further processed in Python to compute fast Fourier transforms and to perform Reynolds decompositions.

In the confined runout, time-integrated sampling tubes were positioned on the steel wall side at runout distances of 3.35, 5.4, and 9.6 m at 45 cm height. In contrast, time-integrated sampling tubes were set at 45 cm in the center of the flow at 16 and 20 m. The particle size distributions of these flow samples was obtained through a combination of sieving and laser particle sizing.

Flow temperature was recorded in vertical profiles at 1.8, 3.4, 5.4, 9.6, 16 and 20 m with fast responding (< 0.015 s response time) Type K thermocouples a sampling rate of 75 Hz. The thermocouples intruded 5 cm into the flow from side walls to reduce boundary effects.

In the center of the flow, piezoelectric dynamic pressure sensors (manufacturer: PCB Piezotronics, model: 106B51) measured high-resolution pressure data at a sampling rate of 1 kHz.

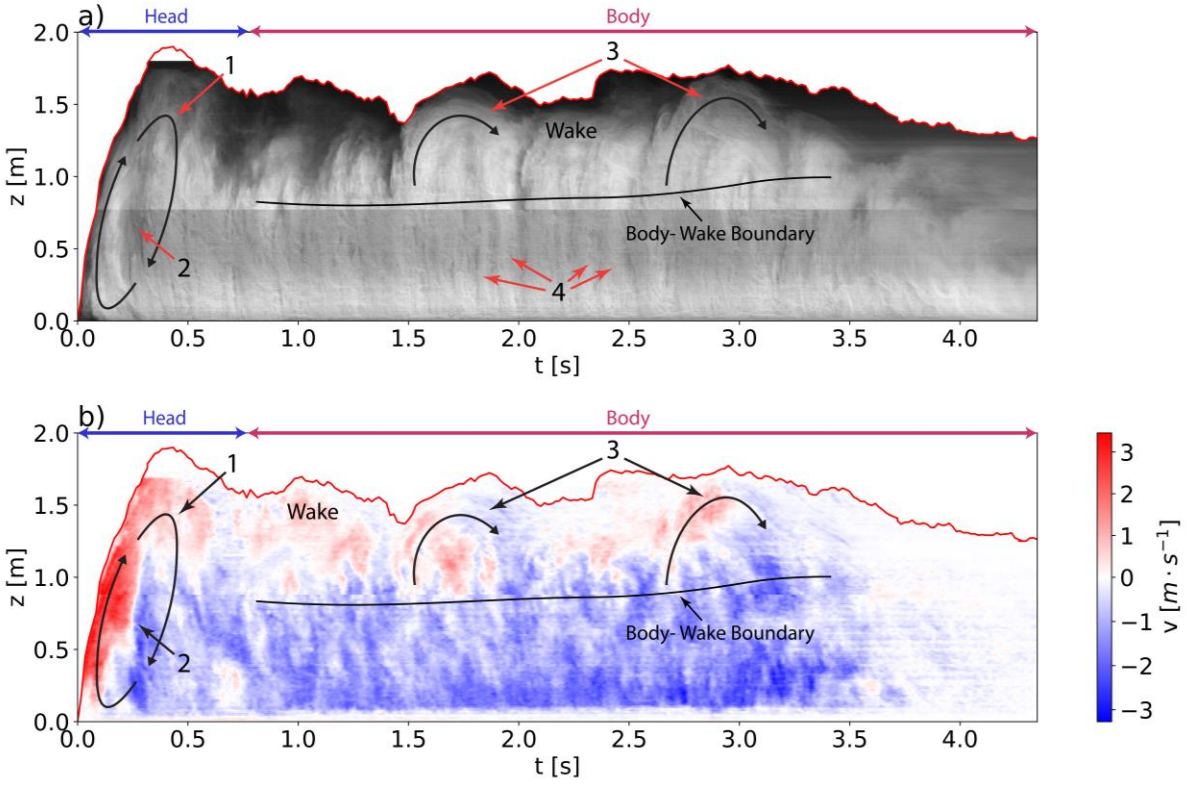

Figure 5.2 PDC structure at 1.8 m from impact. *a) Time-height graph of the high-speed video footage of showing the passing flow showing. The time-height graph is assembled from vertical pixel columns of highspeed camera videos. The greyscale is a proxy for observed particle densities. b) Time-height plot of vertical velocities. The red line gives the flow height in both plots. Zonations into flow head, and body are indicated on top. Both plots also have the same height axes (z [m]) and time axes (t [s]), where the time starts at flow arrival. The numbers mark flow features: 1) head vortex, 2) low concentration zone in the center of the head indicated by low reflectance, 3) Kelvin-Helmholtz instabilities at the upper flow boundary, 4) examples of visual sub-vertical flow structures.*

The scaling analysis summarized in Table 5-1 shows that the experimental dilute PDCs scale well to natural dilute PDCs (Brosch and Lube, 2020, Brosch et al., 2021, Brosch et al., 2022)

The fully turbulent flow with Reynolds numbers of $1.5 \cdot 10^6$ is characterized by Richardson numbers of $10^{-2} - 10$, Froude numbers of $0.75 - 2$, and thermal Richardson number of $2 \cdot 10^{-2} - 4.5$ demonstrating fluid dynamical scaling. The use of natural volcanic material further ensures realistic gas-particle feedbacks, reflected in the particle Stokes number ($10^{-3} - 9.9$), stability number ($13 \times 10^{-3} - 32$) (particle stokes numbers and stability numbers are calculated for the largest eddies), Galileo Number ($5.9 \times 10^{-8} - 3.4 \times 10^4$), and Rouse number ($66 \times 10^{-2} - 19$). Calculating the Kolmogorov length scale as $\eta = h \cdot Re^{-3/4}$ (Pope, 2000) yields Kolmogorov length scales ranging from $1.33 - 42$ µm, which is significantly smaller than the d_{50} median grain-size of the initial mixture of c. 245 µm.

Table 5-1 Dynamic scaling parameters, comparing experimental and natural dilute PDCs. *The scaling parameters are grouped into ambient and flow properties (grey), fluid dynamics (green), gas-particle coupling (blue), and thermodynamics (red). μ_a ambient dynamic viscosity, C_S particle solid concentration, ρ_a ambient density, ρ_c flow density, $\Delta\rho$ density difference between flow and ambient, C_{p_c} and C_{p_a} the flow and ambient heat capacity, g is the gravitational acceleration, g' is the reduced gravitational acceleration, k is the Karman constant, θ the substrate inclination, u_T the particle terminal velocity, and Δu the eddy rotational velocity. Values for natural PDCs are collected from Druitt (1998), Choux and Druitt (2002), and Burgisser et al. (2005). The equation for the flow dynamic viscosity is from Wohletz (1998). The equation for the Galileo number is from Uhlmann and Doychev (2014). Table modified from Brosch et al. (2021).*

Parameter	Meaning	Definition	Generated Dilute PDCs	Natural Dilute PDCs
Particle Size		d	2 µm $- 16$ mm	$10^{-6} - 10^{-1}$ m
Particle density		ρ_s	$350 - 2600$ kg $/\mathrm{m}^3$	$300 - 2600\ kg /m^3$
Ambient Density		ρ_a	$1.06 - 1.225$ kg $/\mathrm{m}^3$	$0.6 - 1.2\ kg /m^3$

Flow density		ρ_c	$1.27 - 10\ \mathrm{kg/m^3}$	
Flow Temperature		T	$15 - 60\ ^\circ\mathrm{C}$	
Velocities		u	$\leq 10.5\ \mathrm{m/s}$	$10 - 200\ \mathrm{m/s}$
Flow dynamic viscosity		$\mu_c = \mu_a \left(1 + \frac{\rho_s C_s}{\rho_a (1 - C_s)}\right)^2$	$3 \times 10^{-5} - 3 \times 10^{-3}\ \frac{\mathrm{kg}}{s\ m}$	$10^{-5} - 4 \times 10^{-3}\ \frac{\mathrm{kg}}{s\ m}$
Kinetic energy density		$U_{kin} = \frac{1}{2}\rho_c u^2$	$10^{-2} - 10^3\ \frac{\mathrm{kg}}{m\ s^2}$	$10^3 - 10^4\ \frac{\mathrm{kg}}{m\ s^2}$
Buoyant thermal energy density		$U_T = \rho_c \frac{C_{p_c}}{C_{p_a}} \alpha\ T\ h\ g$	$10 - 10^3\ \frac{\mathrm{kg}}{m\ s^2}$	$10^3 - 10^4\ \frac{\mathrm{kg}}{m\ s^2}$
Reynolds number	$\frac{\text{Inertial Forces}}{\text{Viscous Forces}}$	$Re = \frac{\rho_c\ u\ h}{\mu_c}$	1.5×10^6	$33 \times 10^5 - 6.7 \times 10^9$
Richardson number	$\frac{\text{Buoyancy Term}}{\text{Flow Shear Term}}$	$Ri = \frac{\Delta\rho\ h\ g}{\mu_c}$	$10^{-2} - 10$	$0 - 10$
Froude number	$\frac{\text{Inertial Forces}}{\text{Gravitational Forces}}$	$Fr = \frac{u}{\sqrt{g'\ h\ cos(\Theta)}}$	$0.75 - 2$	≈ 1
Particle Stokes number	$\frac{\text{Characteristic Time Particle}}{\text{Characteristic Time Fluid}}$	$St = \frac{u_T \Delta u}{\delta g}$	$10^{-3} - 9.9$	$11 \times 10^{-4} - 97 \times 10^6$
Galileo Number	$\frac{\text{Gravitational Forces}}{\text{Viscous Forces}}$	$G_a = \frac{\rho_c \sqrt{\left\lvert \rho_p/\rho_c - 1 \right\rvert D^3 g}}{\mu_c}$	$5.9 \times 10^{-8} - 3.4 \times 10^4$	
Stability number	Defines particle transport zones	$\Sigma = \frac{u_T}{\Delta u}$	$13 \times 10^{-3} - 32$	$2.8 \times 10^{-6} - 9.7 \times 10^9$
Rouse number	Characterises turbulent particle transport regimes	$P = \frac{u_T}{k u_s}$	$66 \times 10^{-2} - 19$	$10^{-3} - 10^2$

Thermal Richardson number	$\frac{\text{Buoyancy Term}}{\text{Flow Shear Term}}$	$Ri_T = \frac{\Delta T\ \alpha\ h\ g}{u^2}$	$2 \times 10^{-2} - 4.5$	$0 - 5$

5.4 Results

The experimental dilute PDC reaches the first observation profile at 1.8 m from impact at 0.28 s after the impact of the gas-particle mixture with the channel. The current propagates a total distance of 24 m within c. 12 s, where the propagation ends in a buoyant lift-off. The flow propagation is characterized by strong dilution from bulk concentrations of 0.25 vol% to 0.01 vol% due to sedimentation and entrainment of ambient air. Initial flow front velocities reach $5.5\ \text{m} \cdot \text{s}^{-1}$ which stay approximately constant until c. 0.6 s after impact. The flow front goes through three deceleration stages from 0.6 to 5.6 s ($3.6 - 20.3$ m) before the buoyant lift-off at 24 m Supplementary Figure 5.1.

Figure 5.2 shows the flow structure at the first observer location at 1.8 m from the impact, which is composed of the density current head region (c. $0 - 0.8$ s), the density current body region (c.0.8 s onward), which is overlain by a density current wake region. From c. 3.5 s onward, the flow starts to wane. The head vortex (1) is characterized by an upward motion at the head front and a downward motion in the rear of the head (Figure 5.2 a and b). The center of the head shows a zone of low reflectance in video recordings (reflectance increases with particle volume concentration and with the abundance of coarse-grained particles of highly reflective crystals and coarse ash) (2) and a transition from upward to downward motion (Figure 5.2 a and b). The wake is characterized by predominantly upward movement and shear-induced Kelvin-Helmholtz instabilities (3) at the upper flow boundary (Figure 5.2 a and b). The flow body visually shows sub-vertical structures (4) (Figure 5.2 a), which can

also be seen as a striped pattern in the downward velocity v (Figure 5.2 b). These sub-vertical structures have an approximate frequency of ~10 Hz.

Turbulence fluctuations are extracted using a Reynolds decomposition of velocity.

$$U = \overline{U} + U' \qquad \textit{EQN. 5-1}$$

Where $\overline{U}$ is the mean flow field and U' are the turbulence fluctuations. The mean flow field is calculated through temporal averaging using a Savitzki-Golay filter with a filter length of 2 s (Figure 5.3) and 250 ms (Figure 5.4). The two time periods allow us to identify (so-defined) low and high-frequency turbulence structures.

Figure 5.3 shows turbulence structures extracted with the mean flow calculated with a Savitzki-Golay Filter of 2 s. These structures are mainly low-frequency features, such as the flow head and subsequent shear-induced low-frequency turbulence structures. At 1.8 m from impact, the turbulence structures in u and v (Figure 5.3b and c) are not fully developed, and the turbulence field is characterized by a well-established head region ($0 - 0.8$ s) and subsequent turbulence structures with varying periodicity. More coherent and distinct turbulence structures are developed at 3.35 m (Figure 5.3 d-f). The frontal head ($0 - 1$ s) is presented by an initial low-velocity zone in u ($0 - 0.2$ s), followed by an acceleration feature ($0.2 - 0.8$ s). In vertical velocities, the head is presented by an initial upward motion ($0 - 0.2$ s) followed by a downward motion ($0.2 - 0.8$ s) (Figure 5.3 f). The duration of the head passage increases with time as the flow decelerates, following the Strouhal number relationship

$$Str = \frac{fL}{U} \qquad \textit{EQN. 5-2}$$

with L the characteristic length, U the characteristic velocity, and f the frequency. For dilute gravity currents, the Strouhal number is constant at Str ~ 0.3 (Brosch et al., 2021). From this follows the frequency of the largest eddies

$$f = \frac{Str\ U}{L} \qquad \textit{EQN. 5-3}$$

With an approximately constant flow height of c. 1.1 m for the proximal locations, including 5.4 m, the frequency of the most energetic coherent turbulence structure is proportional to the characteristic velocity, decreasing from 4.6 $\mathrm{m \cdot s^{-1}}$ over 4.3 $\mathrm{m \cdot s^{-1}}$ to 4 $\mathrm{m \cdot s^{-1}}$ along the initial runout up to 5.4 m. This change corresponds to head durations of 0.8, 0.85, and 0.91 s (1.25, 1.18, and 1.1 Hz), for the runouts 1.8, 3.35, and 5.4 m, respectively. This increase in durations corresponds with the visually determined duration of the head passage in Figure 5.3 a, d, and g and the largest turbulence structures. For the location at 9.6 m, structural limitations inhibit the mapping of flow height, and the head duration can only be roughly mapped. The expected head duration at 9.6 m, with a characteristic length $L = 1$ m and a characteristic velocity $U = 3.4\ \mathrm{m \cdot s^{-1}}$, is 0.98 s or 1.02 Hz, corresponding to observations from the turbulence fluctuations in Figure 5.3 k and l.

The turbulence features following the head vortex are least pronounced at 1.8 m runout (Figure 5.3 a-c). At 1.8 m runout, the turbulence following the frontal head contains more high frequencies than turbulence structures observed further along the runout. At 3.35 m runout, the turbulence shows more coherent structures and a second distinct high downstream velocity feature at c.$1.75 - 3.25$ s (Figure 5.3 e), which corresponds with an initial upward turbulence motion (c. $1.75 - 2.25$ s) followed by a downward turbulence

motion (Figure 5.3 f). This feature corresponds with the passage of the gravity current main body. It can also be identified for subsequent observer locations at 5.4 m (Figure 5.3 h-i) and 9.6 m runouts (Figure 5.3 k-l). The observed turbulence structures occur throughout the entire flow depth. Along the runout, the magnitude of these turbulence structures decreases. The most substantial decrease in magnitude occurs between 3.35 and 5.4 m.

Calculating mean velocities using a filter length of the Saviztki-Golay algorithm of 0.25 s extracts lower period turbulence structures (Figure 5.4). A comparison of Figure 5.3 and Figure 5.4 shows that large low-frequency turbulence structures in Figure 5.3 are superimposed by smaller sub-vertical turbulence structures with an approximate average frequency of ~10 Hz. These turbulence structures occur most pronounced in the vertical velocity component at proximal locations (1.8 – 5.4 m). Along the runout, these sub-vertical structures become less pronounced. At 9.6 m, only the first second after flow arrival shows these structures clearly (Figure 5.4 l). The overall turbulence pattern at 9.6 m is well-defined for low-frequency fluctuations (Figure 5.3 k and i) but less for high-frequency fluctuations (Figure 5.4 g and h).

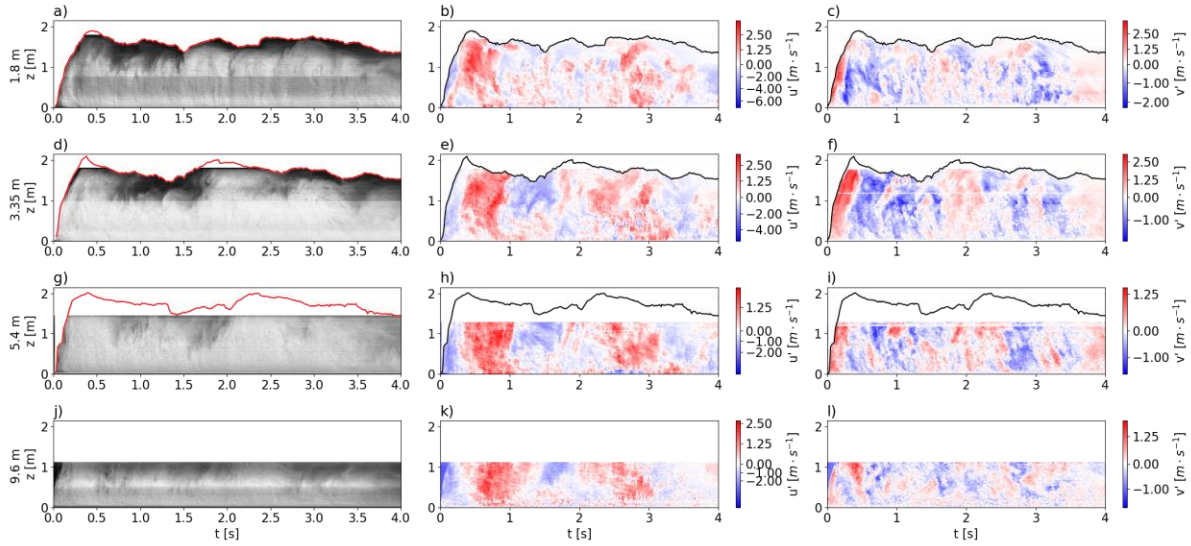

Figure 5.3 Spatio-temporal propagation of low-frequency turbulence structures. *Comparison Time-height graph of the high-speed video footage (left column), giving a visual context of the anatomy of the passing flow, with turbulence fluctuations of the downstream velocity (center column) and turbulence fluctuations of the vertical velocity (right column). The Reynolds decomposition ($U = \bar{U} + U'$) is performed utilizing temporal Savitzki-Golay filters, with a filter length of 2 s, to calculate the mean velocity fields. All y axes are scaled the same. The time axes show the time after flow arrival at the respective location. The rows are distances from impact of* 1.8, 3.35, 5.4, *and* 9.6 *m. The red and black lines give the flow height. a,d,g,j) Time-height graph of the high-speed video footage of the passing flow at1.8, 3.35, 5.4, and 9.6 m, respectively, and the flow height (red). The time axis is shared and starts after the flow arrives at the profile. b,e,h,k). Turbulence fluctuations of the downstream velocity (u') extracted with a Reynolds decomposition ($u' = u - \bar{u}$), and the flow height (black). c,f,i,l) Turbulence fluctuations of vertical velocities (v') extracted through Reynolds decomposition ($v' = v - \bar{v}$), and flow height (black). The first row a-c presents data recorded at 1.8 m runout, the second row d-f data recorded at 3.35 m, the third row g-i) data recorded at 5.4 m, and the fourth row j-l) data recorded at 9.6 m. At 9.6 m, structural limitations did not allow manual mapping of the flow height.*

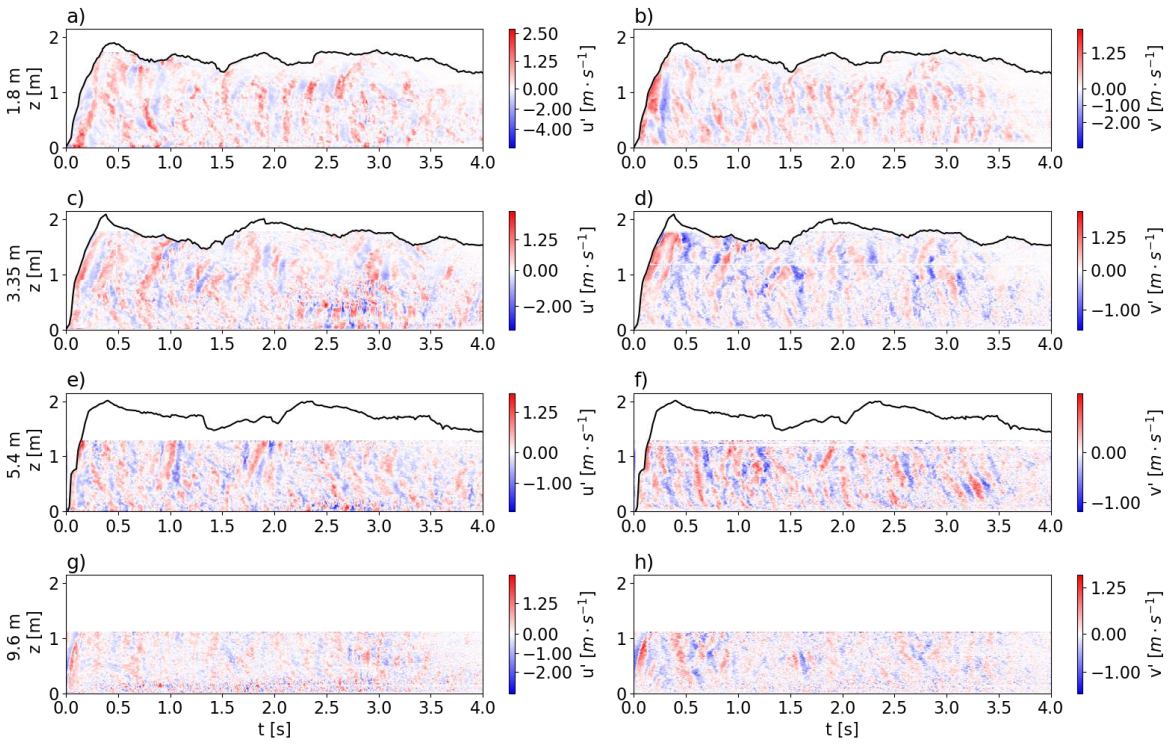

Figure 5.4 Spatio-temporal evolution of low-periodic turbulence fluctuations. *Comparison of turbulence fluctuations in downstream (left column) and vertical velocities (right column). Mean velocity fields ($\bar{U}$) for Reynolds decompositions ($U = \bar{U} + U'$) were calculated using temporal Savitzki-Golay filters with a filter length of 250 ms. The rows show data from profiles 1.8, 3.35, 5.4, and 9.6 m from impact. Black lines mark flow heights. a,c,e,g) Turbulence fluctuations of the downstream velocity (u') extracted via Reynolds decomposition ($u' = u - \bar{u}$), and flow height (black). b,d,f,h) Turbulence fluctuations of vertical velocities (v') extracted by Reynolds decomposition ($v' = v - \bar{v}$), as well as flow height (black). a-b) Data recorded at* 1.8 *m runout, c-d) data recorded at* 3.35 *m, e-f) data recorded at* 5.4 *m, and g-h) data recorded at* 9.6 *m. Structural limitations inhibited flow height mapping at* 9.6 *m from impact.*

5.4.1 Reynolds Decomposition in Independent Measurements

Figure 5.5 presents time series data of velocity magnitude (U), downstream velocity (u), vertical velocity (v), flow temperature above ambient (T), and dynamic pressure (P) at 45 cm height and 3.35 m runout. The velocity magnitude U and downstream velocity u are nearly identical. The experimental PDC is head-dominated, with the head initially showing

low velocities of c. $4.2\ \mathrm{m \cdot s^{-1}}$ $(0 - 0.2\ \mathrm{s})$ followed by an increase peaking at $0.68\ \mathrm{s}$ $(7.2\ \mathrm{m \cdot s^{-1}})$ and declining afterward. Both long- and short-period fluctuations are present in the data, with the fluctuation magnitude increasing in the flow body $(2 - 3.5\ \mathrm{s})$ before the beginning of the flow waning. The vertical velocity initially shows an upward motion $(0 - 0.33\ \mathrm{s})$, followed by a downward motion that persists for the rest of the flow passage. The flow temperature (Figure 5.5 d) shows the lowest temperatures occurring in the flow head and initial flow body. Temperatures sharply increase after c. $1.77\ \mathrm{s}$ in the flow body. These fluctuations in flow temperature are dominated by long periods of c. $0.5 - 1\ \mathrm{s}$ $(1 - 2\ \mathrm{Hz})$.

Dynamic pressures averaged with a temporal Savitzki-Golay filter with a window length of $51\ \mathrm{ms}$ are presented in Figure 5.5 e. Dynamic pressure values are initially around $50\ \mathrm{Pa}$, and increase sharply at $0.15\ \mathrm{s}$. The dynamic pressure peaks at $0.22\ \mathrm{s}$ and $126\ \mathrm{Pa}$, drops to $78\ \mathrm{Pa}$ at $0.27\ \mathrm{s}$ and increases again to $100\ \mathrm{Pa}$ at $0.33\ \mathrm{s}$. The dynamic pressure signature of the head ends with a drop to c. $\sim 35\ \mathrm{Pa}$ at $0.38\ \mathrm{s}$. This alternating pattern is associated with the head and the generation of a low-concentration and low-pressure zone in the center of the head vortex. After the head vortex, the average pressure drops significantly to c. $50\ \mathrm{Pa}$ (at c. $0.4\ \mathrm{s}$). A second drop in dynamic pressure occurs at c. $1.1\ \mathrm{s}$ to c. $25\ \mathrm{Pa}$.

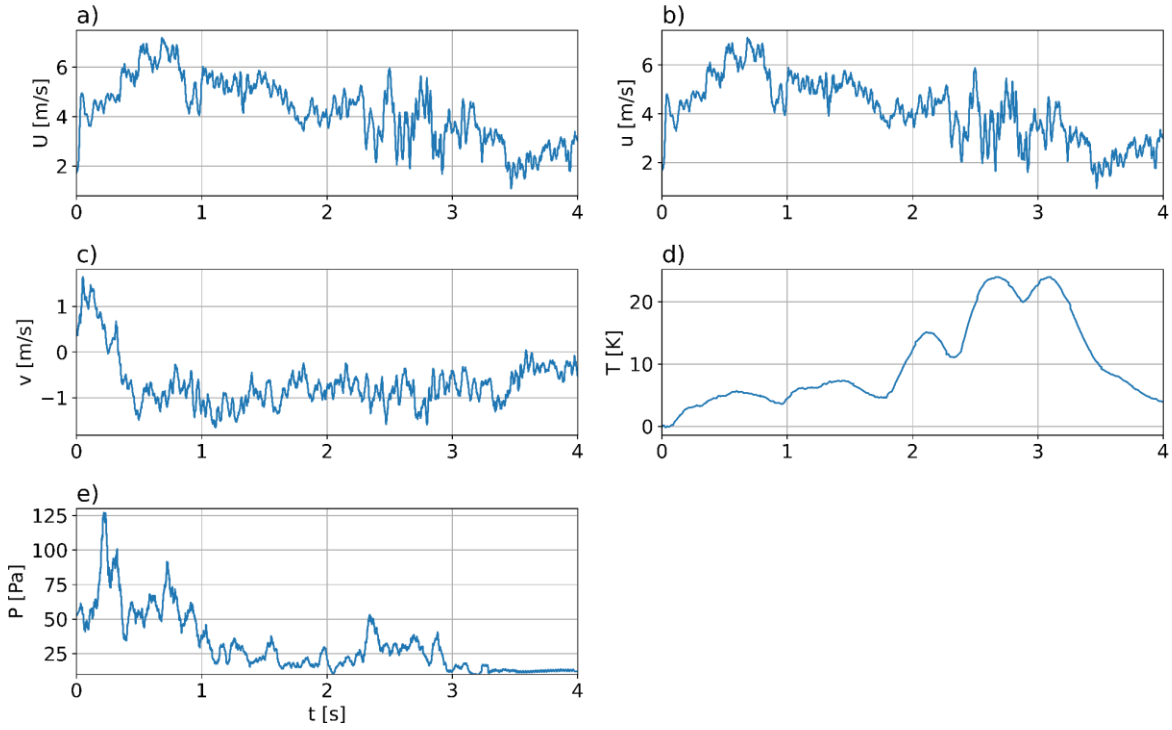

Figure 5.5 Time series data recorded at 3.35 m from impact and 45 cm height. *Data include a) velocity magnitude (U), b) downstream velocity (u), c) vertical velocity (v), d) flow temperature (T), and e) dynamic pressure (P). Velocity data (a-c) is recorded at 500 Hz and filtered with temporal Savitzki-Golay filters with filter lengths of 18 ms. Flow temperature (d) is recorded at 70 Hz and unfiltered. Dynamic pressure data (e) is recorded at 1 kHz and filtered using temporal Savitzki-Golay filters with filter lengths of 51 ms. All data shown is recorded at* 3.35 *m runout and* 45 *cm height.*

Using the Savitzki-Golay filters to calculate time-variant mean properties, the Reynolds decomposition ($X = \bar{X} + X'$) can be performed with any measured time series, where X is the measured time series, $\bar{X}$ the time-variant mean, and X' the fluctuating component.

Figure 5.6 presents turbulence fluctuations extracted from time series data of the velocity magnitude (U), downstream velocity (u), vertical velocity (v), temperature above ambient (T), and dynamic pressure (P_{dyn}) recorded at 3.35 m runout and 45 cm height, shown in Figure 5.5. To calculate mean flow properties ($\bar{X}$), first-order Savitzki-Golay filters with c.

2 s long windows were used. Turbulence fluctuations of the velocity magnitude (U') and the downstream velocity (u') are near-identical (Figure 5.6 a and c). The frontal head ($0 - 0.35$ s) is characterized by a negative excursion of turbulent fluctuations, followed by a positive excursion until 0.85 s. Fluctuations around 0 $\mathrm{m \cdot s^{-1}}$·, with magnitudes of c. ± 1 $\mathrm{m \cdot s^{-1}}$ follow this. At 2 s, the magnitude of fluctuations increases to c. ± 2 $\mathrm{m \cdot s^{-1}}$ until 2.5 s, after which the magnitude decreases again. Throughout the whole signal, large oscillations are superimposed by oscillations with higher frequencies (c. 8 Hz and above). In turbulence fluctuations of vertical velocities v' (Figure 5.6 e), the most dominant feature is the frontal head, characterized by a strong upward motion ($0 - 0.35$ s) with a subsequent downward motion ($0.35 - 0.78$ s). The head is followed by low-frequency oscillations around a value of c. 0 $\mathrm{m \cdot s^{-1}}$, superimposed by higher frequency oscillations. The magnitudes of these turbulence fluctuations decrease with the fading of the flow (c. 3.5 s onward).

Turbulence fluctuations of temperature (Figure 5.6 g) show more dominant low-frequency (< 2 Hz) and minimal superimposed oscillations. The frontal head starts with a negative temperature excursion ($0 - 0.25$ s), followed by a positive excursion until 0.84 s. At 1.5 s after a period of low turbulence, the magnitude of turbulence fluctuations of temperature increase in the flow body.

Turbulence fluctuations of dynamic pressure (Figure 5.6 k) clearly show the flow head with a negative excursion at the beginning, followed by two peaks. Low-frequency oscillations superimposed by high-frequency signals characterize the rest of the flow.

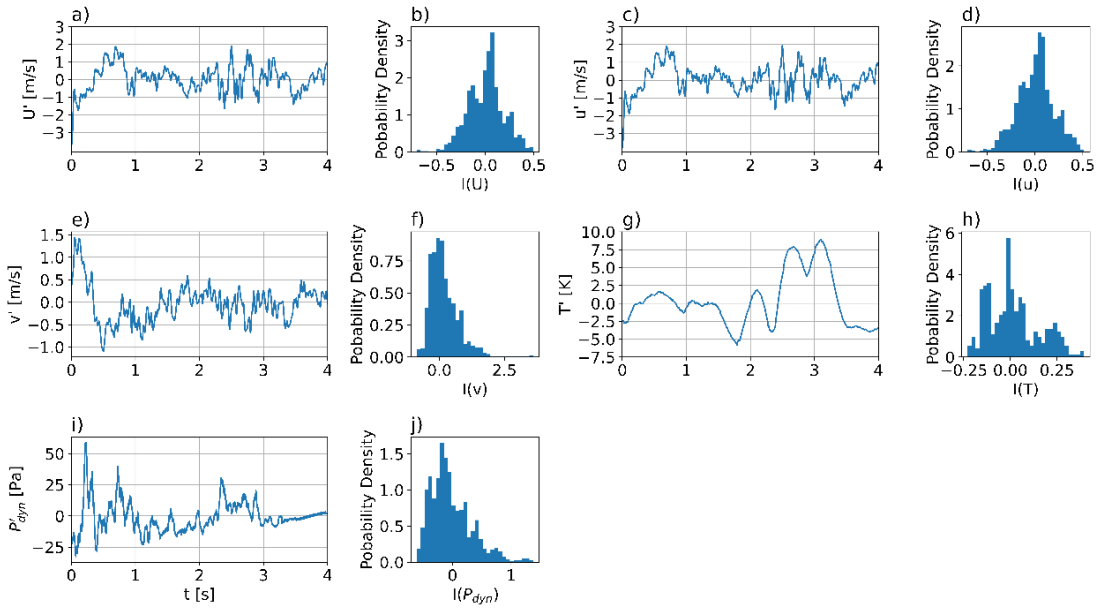

Figure 5.6 Multiparametric turbulence fluctuations. Turbulence fluctuations obtained via Reynolds decomposition ($X = \bar{X} + X'$) of a) velocity magnitude (U), c) downstream velocity (u), e) vertical velocity (v), g) flow temperature (T), and i) dynamic pressure (P). Mean properties $\bar{X}$ for the Reynolds decomposition are calculated using temporal Savitzki-Golay filters with filter length of 2 s. Probability density functions of turbulence intensities ($I(X) = X'/\bar{X}$) corresponding to the turbulence fluctuations are shown in b) velocity magnitude (U), d) downstream velocity (u), f) vertical velocity (v), h) flow temperature (T), and j) dynamic pressure (P). All data is recorded at 3.35 m from impact at a height of 45 cm. All time axes start at flow arrival and span 4 s. a) Turbulence fluctuations of the velocity magnitude (U'), recorded at 500 Hz and filtered with temporal Savitzki-Golay filters with a window length of 18 ms, with the time axis starting at flow arrival. b) Distribution of turbulence intensities of the velocity magnitude ($I(U) = U'/\bar{U}$). The distribution is polymodal, with a mean value of $7.4 \cdot 10^{-3}$and standard deviation of 0.18. c) Turbulence fluctuations of the downstream velocity (u'), recorded at 500 Hz and filtered with temporal Savitzki-Golay filters with a window length of 18 ms. The time axis starts at flow arrival. d) Distribution of turbulence intensities of the downstream velocity u, with a mean of $7.5 \cdot 10^{-3}$ and 0.19 standard deviation. e) Turbulence fluctuations of the vertical velocity v' sampled at 500 Hz and filtered with temporal Savitzki-Golay filters with a window length of 18 ms. f) Distribution of turbulence intensities of vertical velocities excluding the frontal head (0.5 s onward) ($mean = 0.18$, $standard\ deviation = 0.57$). g) shows the turbulence fluctuations of flow temperature sampled at 70 Hz. h) distribution of turbulence intensities of the flow temperature ($mean = 0.016$, $standard\ deviation = 0.14$) i) Turbulence fluctuations of direct dynamic pressure measurements smoothed with a temporal Savitzky-

Golay filter with 51 ms filter length. j) Probability density function of the turbulence intensities from dynamic pressures ($mean = -0.026$, $standard\ deviation = 0.35$).

The probability density functions (PDFs) of turbulence intensity for velocity magnitude ($I(U) = U'/\bar{U}$), downstream velocity ($I(u) = u'/\bar{u}$), vertical velocity ($I(v) = v'/\bar{v}$), flow temperatures ($I(T) = T'/\bar{T}$), and dynamic pressure ($I(P_{dyn}) = P'_{dyn}/\overline{P_{dyn}}$) are shown in Figure 5.6 b, d, f, h, j, and l, respectively. Turbulence intensities for the velocity magnitude, downstream velocities, flow temperature, flow densities, and dynamic pressure are characterized by polymodal PDFs with mean values < 0.16. The PDF of turbulence intensities of the vertical velocity $I(v)$ (Figure 5.6 f) is unimodal and skewed to large excursions, with a mean of 0.19. Standard deviations of the turbulence fluctuations for different parameters range from 0.14 to 0.57 and are summarized in the caption of Figure 5.6. These large turbulence intensities indicate strong modulations of all parameters through the turbulence field of the generated dilute PDCs.

Performing a Reynolds decomposition with a Savitzki-Golay filter length of c. 250 ms extracts higher frequency turbulence structures than extracted in Figure 5.6 (Supplementary Figure 5.2). These high-frequency turbulence structures occur throughout the entire flow passage for the velocity magnitude, downstream velocity, vertical velocity, flow temperature, flow density, and dynamic pressure Supplementary Figure 5.2 a-f, respectively. For the velocity magnitude and downstream velocity, the amplitude range of high-frequency oscillations is maximal for the flow body ($\sim$2.5 s). The magnitude of high-frequency vertical velocity fluctuations stays approximately constant until 3.5 s after which the magnitude decreases. The temperature shows only small high-frequency fluctuations of less than c. ± 1 K until 1.76 s. Stronger excursions occur until 3.5 s. These excursions match the timing of turbulence features shown in Figure 5.6 d. The dynamic pressure (Figure 5.6 e) shows the

same dominant ~10 Hz fluctuations, with maximum amplitude in the flow head ($0 - 0.5$ s) and a sharp decrease at 3.25 s with the onset of the flow fading.

5.4.2 Frequency Content and Turbulent Energy Cascade

These findings highlight that all presented measurements have sufficient temporal resolution to capture turbulence at different time scales. The Fourier spectra of the measured time series are analyzed to investigate the frequency content and the energy transfer from large to small turbulence structures. Figure 5.7 a-e shows the Fourier spectra for a) dynamic pressure, b) specific kinetic energy, c) vertical velocity, and d) flow temperature at 3.35 m runout and 45 cm height. The energy cascade of dynamic pressure (Figure 5.7 a) shows distinct behavioral changes and maxima. The energy cascade does not follow the Kolmogorov $-5/3$ slope and has a shallower slope in a log-log representation. The initial frequency range $<$ 6 Hz (until the first vertical grey bar) shows an approximately constant slope. At c. 6 Hz (start of the first vertical grey bar), slope decrease coincides with the onset of a maximum at c. $6 - 17$ Hz (grey bar marks $6 - 17$ Hz). A second frequency maximum occurs between c. 35 and 95 Hz (dark grey bar). A series of maxima is observed for higher frequencies ($>$ 95 Hz) until the amplitudes decay strongly at frequencies larger than c. 250 Hz (onset of light grey surface).

The Fourier spectrum of specific kinetic energy ($e_k = 0.5 \cdot U^2$) (Figure 5.7 b) shows a slope shallower than the $-5/3$ Kolmogorov energy cascade. Besides frequency maxima between $1 - 1.4$ Hz and at c. 1.86 Hz (Figure 5.7 b i), the energy cascade does not present significant maxima or slope changes. The vertical velocity (Figure 5.7 c) follows a $-5/3$ slope for the initial frequency range ($<$ 6 Hz). At ~6 Hz (Figure 5.7 c start of the first grey bar), the slope decreases abruptly, followed by an increased slope between c. 17 and 35 Hz (Figure 5.7 c

between the vertical grey bars). The slope gradually decreases again after 35 Hz (Figure 5.7 c left boarder of dark grey bar). The Fourier spectrum of flow temperature (Figure 5.7 d) closely follows a $-5/3$ slope until ~ 6 Hz (Figure 5.7 d left border of the grey bar). For frequencies > 6 Hz, the slope decreases.

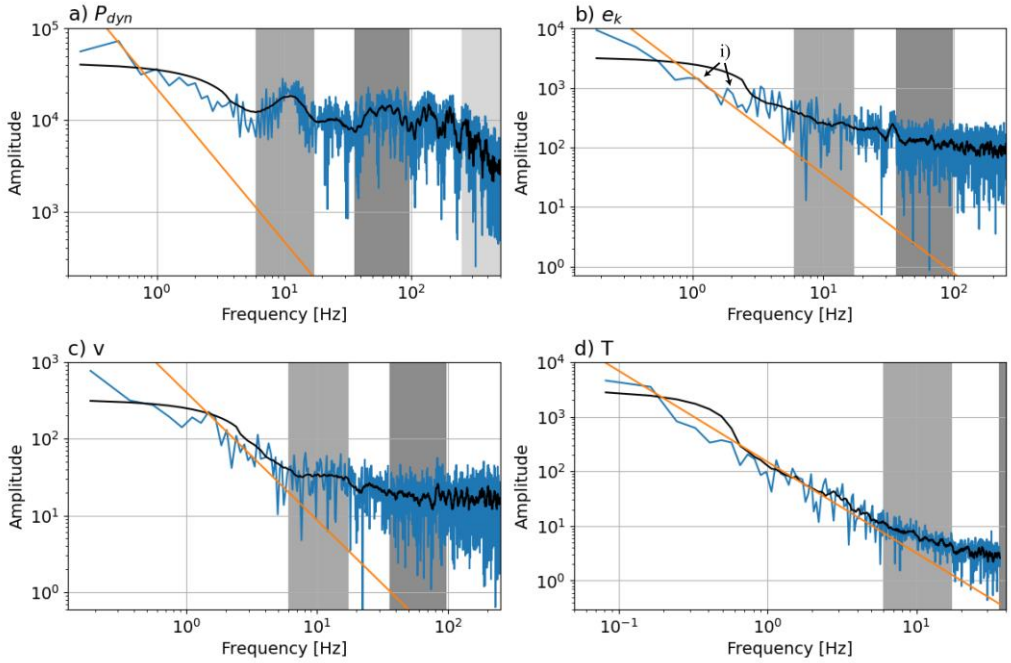

Figure 5.7 Fourier spectra of independent physical measurements. *Each section shows the Fourier spectra of the physical measurements (blue), the filtered Fourier spectra (black), the -5/3 Kolmogorov slope (orange), and the Frequency bands* $6 - 17$ *Hz (grey surface),* $35 - 95$ *Hz (dark grey surface), and* $0.25 - 2$ *kHz (light grey surfaces). All measurements are performed at 45 cm (mid-flow height) and 3.35 m runout. The Fourier spectra are only calculated up to the respective Nyquist frequencies, resulting in varying x-axis ranges. a) Fourier spectrum of direct dynamic pressure spectra, also shown in Figure 5.8 b. Dynamic pressure data is recorded at 1 kHz, resulting in a Nyquist frequency of 500 Hz. b) Fourier spectra of specific kinetic energy* ($e_k = 0.5 \cdot U^2$). *Velocity data is recorded at 500 Hz resulgint in a Nyquist frequency of 250 Hz. i) marks maxima at c. 1-1.4 Hz and 1.86 Hz. c) Fourier spectra of vertical velocities, recorded at 500 Hz resulting in a Nyquist frequency of 250 Hz. d) Shows the Fourier spectra of flow temperature. The sampling rate is 70 Hz, and the Nyquist frequency is 35 Hz.*

Figure 5.8 a-f show energy cascades for the dynamic pressure at 45 cm height for distances of 1.8, 3.35, 5.4, 9.6, 16, and 20 m, respectively. The energy cascade at 1.8 m runout has an initially steep slope, which decreases at ~6 Hz (Figure 5.8 a left border of the grey bar). The slope increases towards high frequencies >250 Hz (Figure 5.8 a marked in light grey). At 3.35 m (Figure 5.8 b), the slope of the Fourier spectrum is approximately constant for frequencies < 6 Hz. A first maximum between c. $6 - 17$ Hz (Figure 5.8 b marked by first grey bar) coincides with a decrease in slope at c. 6 Hz. A secondary frequency maximum occurs between c. $35 - 95$ Hz (Figure 5.8 b marked by dark grey bar), followed by a sequence of frequency maxima and a gradual decrease for frequencies larger than c.250 Hz (Figure 5.8 b marked by light grey surface). At profile three at 5.4 m (Figure 5.8 c), the Fourier transform of dynamic pressure initially has a steep slope until 6 Hz, where the slope decreases for higher frequencies. A frequency maximum occurs between c. 6 and 17 Hz (Figure 5.8 c first grey bar). For frequencies > 95 Hz (Figure 5.8 c left of the dark grey surface), the slope of the Fourier spectra increases. The Fourier spectrum at 9.6 m from impact shows no apparent features, such as slope changes or maxima, besides a minimum between c. $17 - 35$ Hz (Figure 5.8 d between the first and second grey bar). The Fourier spectrum of dynamic pressure at 16 m from impact shows a concave shape initially (< 6 Hz) (Figure 5.8 e i). At c. 6 Hz (Figure 5.8 e left boundary of the first grey surface), the slope increases until ~50 Hz (Figure 5.8 e ii), after which the slope gradually decreases again. At 20 m (Figure 5.8 f) from impact shortly before the final stalling of the flow and the buoyant lift-off, the Fourier spectrum does not show significant features.

5.4.3 The Interplay Between Polydispersity and Turbulence in Dilute PDCs

The initial grain-size distribution (Figure 5.1 a) is near unimodal, with the primary mode and d_{50} median grain-size coinciding at c. 250 µm. Time-integrated flow samplers show alternating stages of unimodal and bimodal grain-size distributions at different flow distances. Two bimodality stages can be recognized during flow propagation (Supplementary Figure 5.3). The first stage of bimodality, at 3.35 m runout, shows modes for particle diameters at c. 50 and 175 µm. The second stage of bimodality, observed at 9.6 and 16 m, has modes at c. 10 and 50 µm.

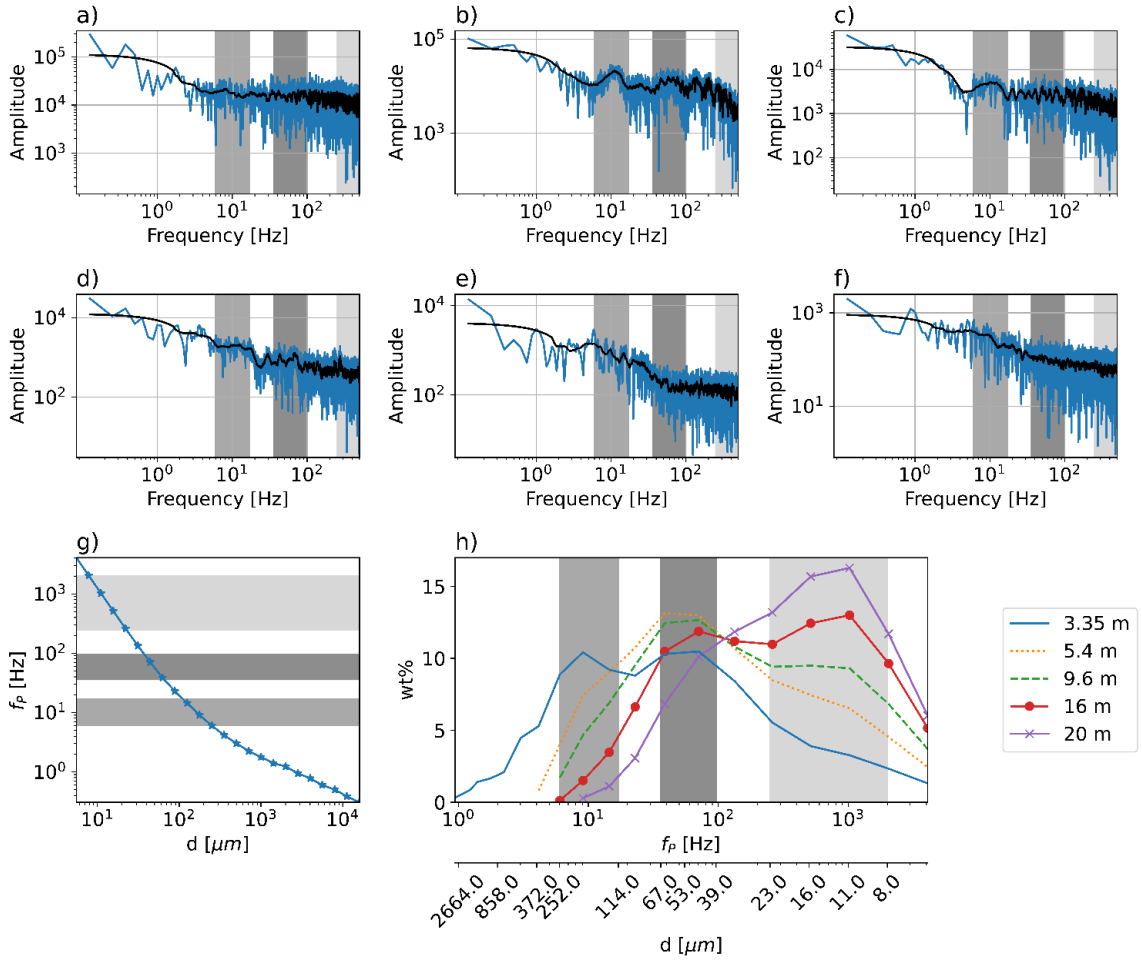

Figure 5.8 Evolution of the Fourier spectra of dynamic pressure and time-integrated flow grain-size distributions along the runout. *a-f) Shows the Fourier spectra of direct dynamic pressure measurements along the runout (a) 1.8 m, b) 3.35m, c) 5.4 m, d) 9.6 m, e) 16 m, and f) 20 m), recorded with piezoelectric pressure sensors (PCB Piezotronics 106B51). Sampling rates of 1 kHz result in 500 Hz Nyquist frequency. The raw frequency spectra (blue) are filtered (black) with a linear Savitzki-Golay filter with* $3.125\ Hz$ *filter length to improve interpretability. Vertical grey bars mark frequency ranges, grey 6-17 Hz, dark grey 35-95 Hz, and light grey >250 Hz. g) Shows grain-size dependent characteristic frequencies for which particles accumulate at eddy peripheries (EQN. 13). Horizontal grey bars mark frequency ranges, 6-17 Hz (grey), 35-95 Hz (dark grey), and 250-2000 Hz (light grey). h) Shows time-integrated particle size distribution, in weight percent, as a function of their characteristic frequency* $f_p(d)$ *(upper x-axis) and associated particle diameters* $d(\mu m)$ *for reference (lower x-axis). Grey bars mark the frequency and grain-size ranges* $6-17\ Hz$ *and* $114-252\ \mu m$ *(grey),* $35-95\ Hz$ *and* $39-67\ \mu m$ *(dark grey), and* $0.25-2\ kHz$ *and* $8-23\ \mu m$ *(light grey).*

We hypothesize that the clustering of particles at eddy margins and grain and vortex size-dependent gas-particle feedbacks lead to the maxima and slope changes in the Fourier spectra. The particle Stokes number St lends itself to describe the particle size- and vortex size-dependent gas particle feedbacks as:

$$St = \frac{\tau_P}{\tau_E}, \tag{8}$$

with τ_P the particle's characteristic timescale and τ_E the eddy turnover time. For $St \ll 1$, particles are well coupled to the fluid and follow the fluid trajectories. For $St \sim 1$, particles accumulate at the eddy margins, and for $St \gg 1$, particles decouple from the turbulence structure (Burgisser and Bergantz, 2002, Breard and Lube, 2017) At the condition St ~ 1, the eddy turn over time τ_E and the characteristic particle timescale τ_P are equal for particles to accumulate at eddy margins. The characteristic time of a particle with a density ρ_P, and diameter d can be calculated as

$$\tau_P = \frac{\rho_P d^2}{18\mu_F f} \tag{10}$$

With μ_F the fluid's dynamic viscosity and stokes drag factor f (Burgisser and Bergantz, 2002)

$$f = 1 + \left(0.15 {Re_P}^{0.687}\right) + \frac{0.0175}{1+\left(42500 Re_P^{-1.16}\right)} \tag{11}$$

The particle Reynolds numbers Re_P are defined as

$$Re_P = \frac{U_T d}{\nu}, \tag{12}$$

with the terminal fall velocity U_T and ν the kinematic viscosity. We calculated the particle Reynolds numbers using the empirical drag law by Dioguardi et al. (2018).

The largest eddy frequencies for which a particle of the diameter d, and density ρ_P accumulates in the margins are defined as

$$f_P(d) = {\tau_P}^{-1} = f_E(d) = \frac{\rho_P d^2}{18\mu_F f} \quad (13)$$

Using EQN. 13, the size axis in grain size distributions can be converted into characteristic particle frequencies (shown in Figure 5.8 h). This allows linking energy cascades with flow grain-size distributions. Along the runout, the initially unimodal flow grain-size distribution with a primary mode at c. 250 µm develops two stages of bimodality.

In the first stage of bimodality at 3.35 m (Supplementary Figure 5.3), the coarse mode sits at 175 µm (c. 114 – 252 µm) particle diameter corresponding to 9 Hz (c. 6 – 17 Hz) particle characteristic frequency, matching the first frequency maxima in Figure 5.7 a and Figure 5.8 b and c. A second finer mode occurs at c. 50 µm (c. 39 – 67 µm) particle diameter matching the frequency maximum at 50 Hz (c. 35 – 95 Hz) matching the second frequency maximum in Figure 5.7 a and Figure 5.8 b. Along the runout, the coarse mode is sedimented out, and an unimodal distribution is established at 5.4 m with the mode at particle diameters of c. 50 µm and 50 Hz particle frequencies. At the following sampling locations of 9.6 and 16 m (Figure 5.8 d and e), a second stage of bimodality is established with one mode at diameters of c. 50 µm (39 – 67 µm) and characteristic particle frequencies of ca. 50 Hz (35 – 95 Hz), corresponding to the finer mode in flow grain-size distributions at 3.35 m. At 16 m runout, a second mode is established at particle diameters of 10 µm (8 – 23 µm) corresponding to particle characteristic frequencies of 1 kHz (0.25 – 2 kHz) (Figure 5.8 h).

5.5 Discussion

Experimental dilute PDCs reaching Reynolds numbers up to $1.5 \cdot 10^6$ develop distinct turbulence patterns along the initial runout. The turbulence pattern encompasses large (low frequency) vortices superimposed by sub-vertical structures with higher frequencies around ~10 Hz. The large turbulence structures span the entire flow depth and include the upstream rotating turbulent head vortex and low-frequency structured generated by free shear with the ambient air at the upper flow boundary. The head vortex visually and in pressure data shows that particles cluster at the margins and create a low concentration and low-pressure zone in the center of the head vortex. Along the runout, the periods of these large turbulence structures increase, consistent with the constant Strouhal numbers of c. 0.3 in dilute PDCs (Brosch et al., 2021). A separation of turbulence regions by the wall jet boundary, as shown by Salinas et al. (2021) for turbidity currents with Reynolds numbers of $1.8 \cdot 10^4 - 2 \cdot 10^4$ was not observed. The experimental flow presented in this study had Reynolds numbers $1.5 \cdot 10^6$, therefore, much lower stratification stability and a higher degree of turbulence. Decreasing the Reynolds number of their experimental turbidity currents to $6 \cdot 10^3 - 9 \cdot 10^3$ Salinas et al. (2021) further show the formation of an intermediate zone. This non-turbulent intermediate zone separates the wall and the jet region in these subcritical currents. Brosch et al. (2021) identified a similar separation of turbulence features in the wall and jet region. Brosch et al. (2021) did not show a non-turbulent intermediate zone, showing the importance of the Reynolds number on stratification stability. This difference in our findings for dilute PDCs with the same starting conditions could be attributed to the algorithms used to perform the Reynolds decomposition. Brosch et al. (2021) used temporal polynomials to fit Power-Gaussian velocity profiles, assuming maximum mean velocities to occur at the wall-jet boundary. Therefore, this algorithm leads to a minimum turbulence fluctuation at the wall jet boundary, potentially causing an artificial separation in turbulence structures at the wall

jet boundary. The algorithm used to perform the Reynolds decomposition in this study does not make these assumptions. Lagrangian coherent structures need to be studied to show the coherence of flow structures (Peacock and Haller, 2013, Haller, 2015) and the separation of flow features in experimental dilute PDCs. Extracting Lagrangian coherence from our PIV outputs in the form of Lagrangian-averaged vorticity deviation (LAVD) (Farazmand and Haller, 2016, Haller et al., 2016) and finite-time Lyapunov exponents (Haller and Yuan, 2000, Haller, 2002), where unsuccessful due to the lack of smoothness in extracted velocity fields (Brandt and Coletti, 2022).

The dominant frequency of 1.3 Hz observed in previous studies (Brosch et al., 2021, Brosch et al., 2022) coincides with the largest coherent turbulence structures in the presented experiment. Temperature measurements also show these low-frequency oscillations and dynamic pressure shows dominant frequencies between 1 and 2 Hz. The largest turbulence structures are superimposed by sub-vertical structures with frequencies of ~10 Hz. These sub-vertical structures occur in both the downstream and vertical velocity components. The sub-vertical structures are also presented in the time series data and turbulence fluctuations of the flow temperature and dynamic pressure (Figure 5.5 and Figure 5.6) with frequencies between c. $6 - 17$ Hz (or ~10 Hz). This ~10 Hz signal is most dominant in the vertical velocity and dynamic pressure. The Fourier spectra of the dynamic pressure, vertical velocity, and flow temperature show distinct slope changes (modulation of the energy transfer from large to small structures) at ~6 Hz and maxima (focusing of turbulent energy in specific frequency ranges) between $6 - 17$ Hz and $35 - 95$ Hz. For the critical condition of particle Stokes number of unity, frequencies for which each particle size is accumulated at the eddy peripheries can be calculated (Burgisser and Bergantz, 2002, Breard and Lube, 2017). Transforming the particle sizes to frequencies in flow grain-size distributions (Figure

5.8 h) reveals frequencies of 6 Hz correspond to ~252 µm. Therefore, the 6 Hz slope change corresponds closely with the initial d_{50} median grain size of ~241 µm. Furthermore, maxima in the Fourier spectra of dynamic pressure between $6 - 17$ Hz and $35 - 95$ Hz can be linked to grain size modes at 175 µm ($114 - 252$ µm) and 50 µm ($39 - 67$ µm). The occurrence of distinct maxima suggests the presence of dominant turbulence structures that can be linked to selective sedimentation and a turbulent segregation mechanism. Cyclone separation, removing specific particle sizes from gas-particle suspensions (Hoffmann et al., 2003, Rhodes, 2008), might be an analog for this turbulent segregation mechanism. In contrast to previous studies (Burgisser and Bergantz, 2002, Breard and Lube, 2017), we neglected the stability number and, with it gravitational effects, showing that the Stokes number sufficiently characterizes fluid particle feedback. This is confirmed by minimum Galileo numbers of 5.9×10^{-8}, as shown in the scaling analysis. Maximum Galileo numbers of 3.4×10^{4} show that the largest particles are mostly affected by gravitational forcing and that neglecting gravitational forcing is only valid for the investigated particle size range ($< 250\ \mu m$). Experiments at different scales and using volcanic material with other grain size distributions are needed to determine the origin of dominant frequencies.

Observed slopes of the Fourier spectra are shallower than the Kolmogorov $-5/3$ law expected at conditions of isotropic turbulence. The initial frequency range (< 6 Hz) of the flow temperature and vertical velocity, following an approximate $-5/3$ law, poses an exception to this. These shallower slopes indicate an enhanced energy transfer from larger to smaller structures through the presence of particles. This is consistent with findings from experimental and numerical studies showing an enhanced energy transfer from larger to smaller scales in the presence of particles in one- and two-way coupling (Yang and Shy, 2005, Bosse et al., 2006, Poelma and Ooms, 2006, Rosa et al., 2020, Frankel et al., 2016).

Slope changes associated with frequencies of ~6 Hz and particle sizes of ~252 µm closely coincide with the initial median grain-size (241 µm), the onset of the first maxima in the Fourier spectra of dynamic pressure ($6 - 17$ Hz), and the first establishing grain-size mode (Figure 5.8 h). Secondary slope changes around c. 35 Hz and c. 50 Hz are coincide with the secondary maxima at c. 50 Hz ($35 - 95$ Hz) and the establishment of the grain-size mode around particle diameters of 50 µm corresponding to characteristic particle frequencies of c. 50 Hz.

The slope of the Fourier spectra of the flow temperature is expected to be steepened due to the response time of the thermocouples, effectively suppressing high-frequency changes in temperature. Thus, the change in slope at c. 6 Hz in the Fourier spectra of the temperature data, gives confidence in interpreting changes in slopes observed in also other measurements. Furthermore, all Fourier spectra of the flow temperature at 45 cm along the runout show this deviation (Supplementary Figure 5.4).

Being most pronounced in the vertical velocity and dynamic pressure, we hypothesize the sub-vertical structures are the origin of the selective sedimentation. For particle-eddy combinations with Stokes numbers $St = \mathcal{O}(1)$, most turbulence-induced particle clustering is expected (Fessler et al., 1994, Aliseda et al., 2002, Wang and Maxey, 1993). Therefore, we suggest that the particle accumulation at eddy margins is the origin of the formation of sub-vertical sedimentation pathways, which preferentially sediment out selected grain-size ranges, leading to bimodalities in flow grain-size distributions. The successive preferential sedimentation of progressively finer-grained particles with critical particle Stokes numbers based on the mass loading of these particle sizes is consistent with qualitative models of particle sedimentation in pyroclastic surges (Breard et al., 2015). These studies describe outward-gradational sedimentary facies that are characterized by exponential thinning and

coarse-tail grading-dominated fining with radial distance. These observations can be explained by the early clustering, decoupling and rapid sedimentation of the coarsest particles with conditions of $St = \mathcal{O}(1)$ along preferential sedimentation pathways, which is followed by the successive decoupling and sedimentation of progressively finer-grained and initially more abundant Stokes-critical particles.

The final drop in amplitudes in the Fourier spectra of the dynamic pressure at 3.35 m runout at the height of 45 cm coincides with the finally establishing grain-size mode of 11 µm but cannot robustly be linked. Through division of the energy cascade into energy containing range, intertial subrange, and dissipation range, this drop-off could indicate the end of the inertial subrange and the onset of the dissipation range at this frequency. As this only occurs at one observer location, this cannot be robustly linked.

The maxima in the Fourier transform of dynamic pressure, the onset of the enhancement of energy transfer towards smaller structures, and their selective sedimentation show large degrees of correspondence. This correspondence suggests a physical link between these processes. Figure 5.9 summarizes the main findings and conceptually puts them into context for PDCs. Figure 5.9 a shows a conceptual sketch of the Kolmogorov energy cascade, where shear generates the largest structures in the energy-containing range. The energy then decays from large to small eddies on the inertial subrange. The inertial subrange finally ends in the dissipation range, where kinetic energy is viscously dissipated. Figure 5.9 b visualizes size-dependent preferential accumulation of particles in eddy peripheries. We suggest that the accumulation of particles at eddy peripheries increases the total energy of eddies, leading to the focusing of energies. We suggest that the increased energy transfer is attributed to increased viscosities caused by particle accumulation at the eddy margins, as described by the description of dynamic viscosities by Wohletz (1998) (Table 5-1). The systematic

correspondence of dominant eddy frequencies with the initial d_{50} median grain-size, established through analysis of the critical particle Stokes number, suggests that this process only happens with sufficient mass loading for particles with $St = \mathcal{O}(1)$.

Further systemic studies are needed to investigate particle coupling mechanisms and turbulence-induced selective sedimentation. Experiments using different starting grain-size distributions could test if the turbulence structures are determined by the initial grain-size or by other dynamic properties of the flow, such as length scale and velocity. To investigate the scale dependence, larger experiments or real-world data are needed. Data such as the infrasound signal recorded during the December 9, 2019, eruption of Whakaari (White Island) (Brosch et al., 2021) and Doppler radar data from Volcán de Colima (Scharff et al., 2019) can potentially provide information on the scale dependence. The presented research only investigated time-integrated flow grain-size distributions. The runout-dependent deposit grain-size distributions need to be measured during future experiments to link grain-size modes with polymodal deposit grain-size distributions.

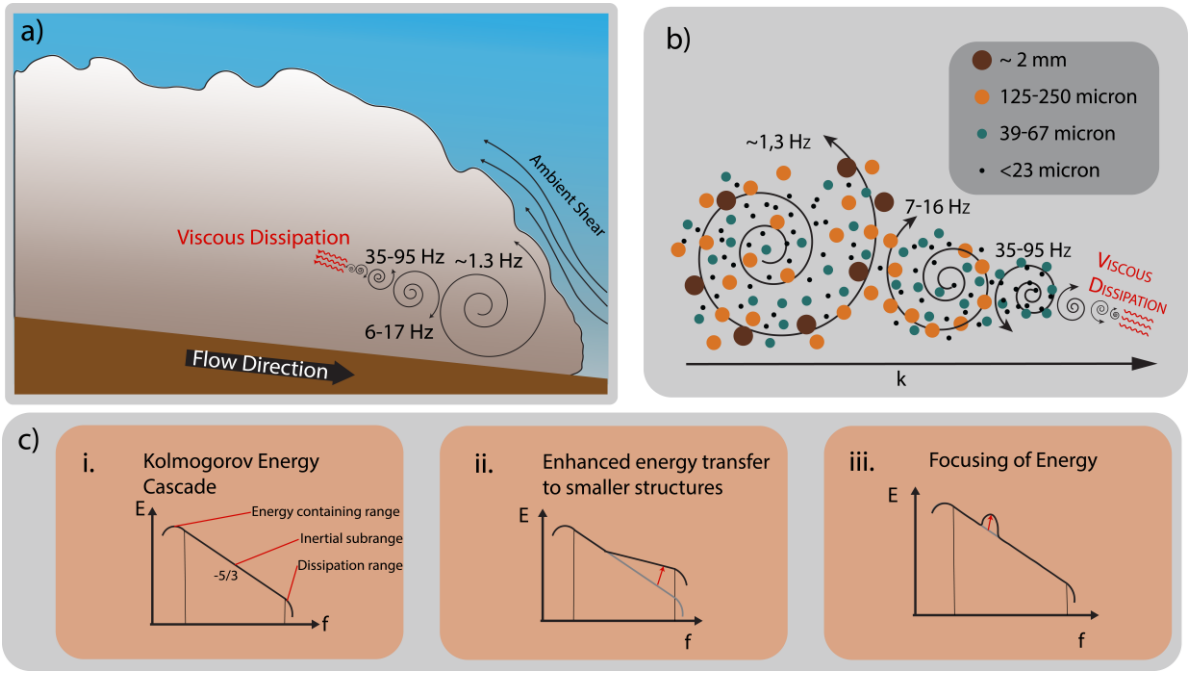

Figure 5.9 Conceptual of the grain-size dependent particle clustering and its influence on the turbulence energy cascade on PDCs. a) conceptual sketch of a PDC propagating down a slope. The frontal head consists of a large vortex generated through ambient shear. This frontal head vortex constitutes the largest turbulence structure and the start of the initial subrange, where large vortices start an energy cascade to ever smaller vortices. This generates a sequence of vortices that ends at the Kolmogorov length scale, after which energy viscously dissipates. b) Conceptual sketch of the energy cascade as a function of wave number (inverse vortex size), frequencies above estimate vortex rotational frequencies. Particles are distributed over the vortices according to their grain-size dependent particle Stokes number ($St = \frac{\tau_P}{\tau_E}$). For small particles with low Stokes numbers, the particles evenly distribute across the vortex. Particles with critical Stokes numbers around 1 accumulate at eddy margins. Large particles with high Stokes numbers ($St \gg 1$) decouple from vortices. The largest eddies support a wide range of particle sizes. The range of supported particle sizes decreases with decreasing vortex sizes. The energy cascade ends in viscous dissipation. c) i. The most basic turbulent energy cascade is split into three sections. The energy-containing range is the origin of the turbulence, and external influences such as shear generate the largest eddies. These largest eddies afterward transfer their energy down to smaller structures and start a -5/3 Kolmogorov slope in specific kinetic energy, the inertial subrange. The inertial subrange ends in the dissipation range, where energy viscously dissipates. ii) The energy cascade under the presence of particles is shown. The particles increase the energy transfer from large to small eddies. In this research, a discrete change in slope was observed and linked to the presence of particles in the turbulent system. iii) Kolmogorov energy cascade, including discrete focusing of energies due to particle clustering at eddy margins. Particles of certain grain-size accumulate at eddy margins, leading to focusing energy and generating energy maxima over distinct frequency bands.

5.6 Supplementary Material

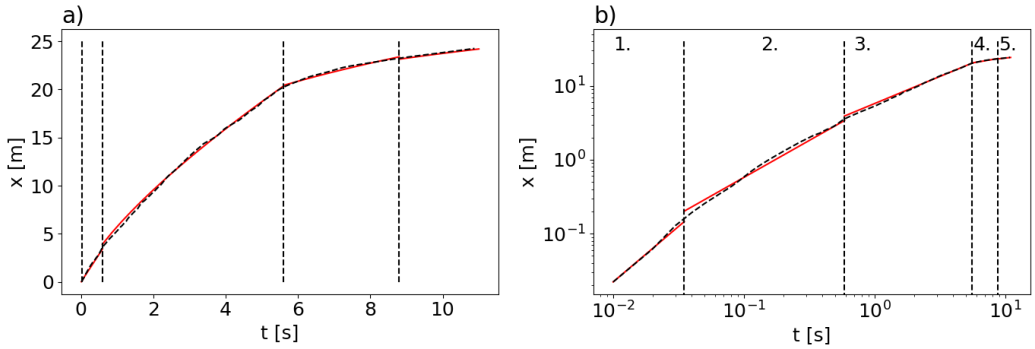

Supplementary Figure 5.1 Flow front propagation after impact. *a) Position of the flow front as a function of time after impact (dashed black line). b) Flow front position as a function of time in a log-log presentation (dashed black line). Dashed vertical lines show kinematic phases where the flow front position shows linear behavior in the log-log plot (b). Five kinematic stages are observed (red lines in a and b) and delimited by vertical dashed lines: 1. Acceleration to* $5.5\,m \cdot s^{-1}$ *2. constant velocities 3. first stage of deceleration 4. second stage of deceleration 5. final deceleration ending in the buoyant lift-off.*

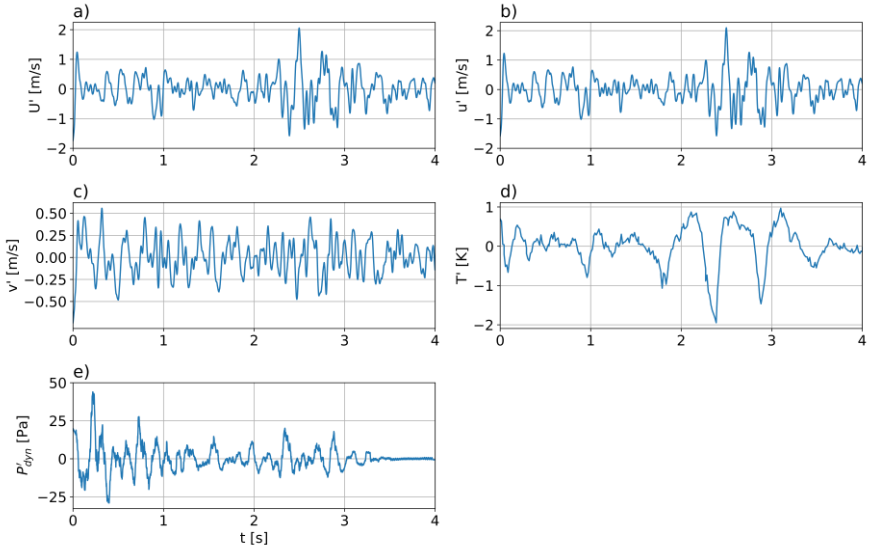

Supplementary Figure 5.2 Extracting high-frequency turbulence fluctuations from independent measurements. Turbulence fluctuations are extracted through Reynolds decomposition ($X = \bar{X} + X'$) using temporal Savitzki-Golay filters with a filter length of 250 ms to calculate the time-dependent mean parameters. All data was measured at 3.35 m runout and 45 cm height. All time axes start at flow arrival. a) Turbulence fluctuations of velocity magnitude (U'). The velocity magnitude is recorded at 500 Hz and filtered with

temporal Savitzki-Golay filters with an 18 ms filter length. b) Turbulence fluctuations of the downstream velocity, recorded at 500 Hz and filtered with temporal Savitzki-Golay filters with 18 ms filter length. c) Turbulence fluctuations extracted from the vertical velocity component, recorded at 500 Hz, and filtered with temporal Savitzki-Golay filters with 18 ms filter length. d) Turbulence fluctuations extracted from flow temperatures. Flow temperatures are recorded at 70 Hz and unfiltered. f) turbulence fluctuations of the dynamic pressure recorded with 1 kHz, filtered with a temporal Savitzky-Golay filter with 51 ms filter length.

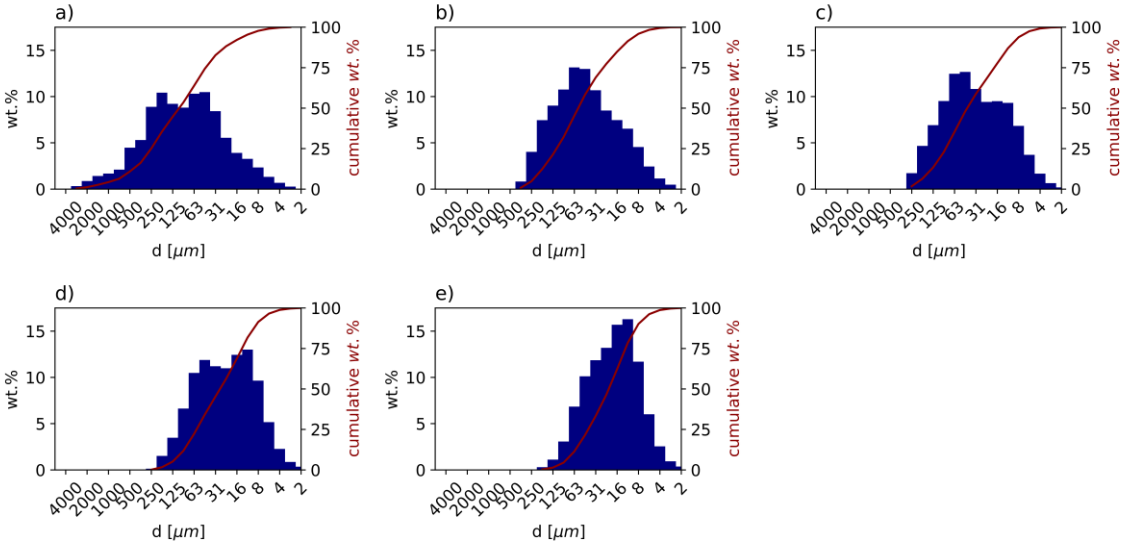

Supplementary Figure 5.3 Time-integrated flow grain-size distributions along the runout. *The probability density functions (histograms) and cumulative (red lines) time-integrated flow grain-size distributions at 45 cm height are shown along the runout: a) 3.35 m, b) 5.4 m, c) 9.6 m, d) 16 m, e) 20 m. Two stages of bimodality establish along the runout at 3.35 m (a), 9.6 m (c), and 16 m (d).*

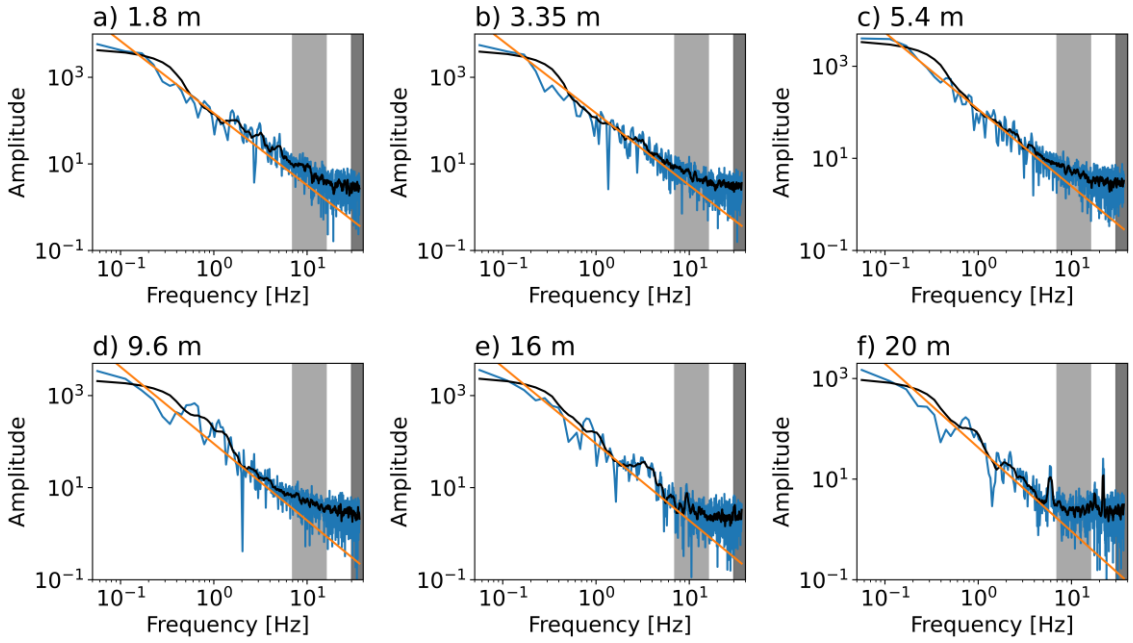

Supplementary Figure 5.4 Fourier spectra of flow temperatures. The Fourier spectra of flow temperatures were recorded at 45 cm height and 1.8 m (a), 3.35 m (b), 5.4 m (c), 9.6 m (d), 16 m (e), and 20 m (f) from impact. The temperature data was recorded with a 70 Hz sampling frequency resulting in a Nyquist frequency of 35 Hz. Each plot shows the Fourier spectra for the flow density (blue), the filtered Fourier spectra (black) filtered using linear Savitzki-Golay filters with 0.62 Hz window length, the -5/3 Kolmogorov slope (orange), and the Frequency bands $6 - 17$ Hz (grey vertical bar), $35 - 95$ Hz (dark grey vertical bar).

5.7 References

Aliseda, A., Cartellier, A., Hainaux, F. & Lasheras, J. C. 2002. Effect of preferential concentration on the settling velocity of heavy particles in homogeneous isotropic turbulence. *Journal of Fluid Mechanics,* 468**,** 77-105.

Bosse, T., Kleiser, L. & Meiburg, E. 2006. Small particles in homogeneous turbulence: Settling velocity enhancement by two-way coupling. *Physics of Fluids,* 18. Available: 10.1063/1.2166456

Brandt, L. & Coletti, F. 2022. Particle-Laden Turbulence: Progress and Perspectives. *Annual Review of Fluid Mechanics,* 54**,** 159-189. Available: 10.1146/annurev-fluid-030121-021103

Branney, M. J. & Kokelaar, B. P. 2002. *Pyroclastic Density Currents and the Sedimentation of Ignimbrites,* Geological Society.

Breard, E. C. P. 2016. *Dynamics of pyroclastic density currents*: a thesis presented in partial fulfilment of the requirements for the degree of Doctor of Philosophy in Earth Sciences at Massey University, Manawatū, Palmerston North, New Zealand. Doctoral. Massey University.

Breard, E. C. P. & Lube, G. 2017. Inside pyroclastic density currents – uncovering the enigmatic flow structure and transport behaviour in large-scale experiments. *Earth and Planetary Science Letters,* 458**,** 22-36. Available: 10.1016/j.epsl.2016.10.016

Breard, E. C. P., Lube, G., Cronin, S. J. & Valentine, G. A. 2015. Transport and deposition processes of the hydrothermal blast of the 6 August 2012 Te Maari eruption, Mt. Tongariro. *Bulletin of Volcanology,* 77**,** 1-18. Available: ARTN 100

10.1007/s00445-015-0980-5

Brosch, E. & Lube, G. 2020. Spatiotemporal sediment transport and deposition processes in experimental dilute pyroclastic density currents. *Journal of Volcanology and Geothermal Research,* 401**,** 106946. Available: https://doi.org/10.1016/j.jvolgeores.2020.106946

Brosch, E., Lube, G., Cerminara, M., Esposti-Ongaro, T., Breard, E. C. P., Dufek, J., Sovilla, B. & Fullard, L. 2021. Destructiveness of pyroclastic surges controlled by turbulent fluctuations. *Nature Communications,* 12**,** 7306. Available: 10.1038/s41467-021-27517-9

Brosch, E., Lube, G., Esposti-Ongaro, T., Cerminara, M., Breard, E. C. P. & Meiburg, E. 2022. Characteristics and controls of the runout behaviour of non-Boussinesq particle-laden gravity currents – A large-scale experimental investigation of dilute pyroclastic density currents. *Journal of Volcanology and Geothermal Research,* 432**,** 107697. Available: https://doi.org/10.1016/j.jvolgeores.2022.107697

Burgisser, A. & Bergantz, G. W. 2002. Reconciling pyroclastic flow and surge: the multiphase physics of pyroclastic density currents. *Earth and Planetary Science Letters,* 202**,** 405-418. Available: Pii S0012-821x(02)00789-6

Doi 10.1016/S0012-821x(02)00789-6

Burgisser, A., Bergantz, G. W. & Breidenthal, R. E. 2005. Addressing complexity in laboratory experiments: the scaling of dilute multiphase flows in magmatic systems. *Journal of Volcanology and Geothermal Research,* 141**,** 245-265. Available: 10.1016/j.jvolgeores.2004.11.001

Carrara, A., Burgisser, A. & Bergantz, G. W. 2019. Lubrication effects on magmatic mush dynamics. *Journal of Volcanology and Geothermal Research,* 380**,** 19-30. Available: https://doi.org/10.1016/j.jvolgeores.2019.05.008

Choux, C. M. & Druitt, T. H. 2002. Analogue study of particle segregation in pyroclastic density currents, with implications for the emplacement mechanisms of large ignimbrites. *Sedimentology,* 49**,** 907-928. Available: DOI 10.1046/j.1365-3091.2002.00481.x

Dioguardi, F., Mele, D. & Dellino, P. 2018. A New One-Equation Model of Fluid Drag for Irregularly Shaped Particles Valid Over a Wide Range of Reynolds Number. *Journal of Geophysical Research: Solid Earth,* 123**,** 144-156. Available: https://doi.org/10.1002/2017JB014926

Druitt, T. H. 1998. Pyroclastic density currents. *Geological Society, London, Special Publications,* 145**,** 145-182. Available: 10.1144/gsl.sp.1996.145.01.08

Elghobashi, S. 1994. On predicting particle-laden turbulent flows. *Applied Scientific Research,* 52**,** 309-329. Available: 10.1007/bf00936835

Farazmand, M. & Haller, G. 2016. Polar rotation angle identifies elliptic islands in unsteady dynamical systems. *Physica D: Nonlinear Phenomena,* 315**,** 1-12.

Ferrante, A. & Elghobashi, S. 2003. On the physical mechanisms of two-way coupling in particle-laden isotropic turbulence. *Physics of fluids,* 15**,** 315-329.

Fessler, J. R., Kulick, J. D. & Eaton, J. K. 1994. Preferential concentration of heavy particles in a turbulent channel flow. *Physics of Fluids,* 6**,** 3742-3749. Available: 10.1063/1.868445

Frankel, A., Pouransari, H., Coletti, F. & Mani, A. 2016. Settling of heated particles in homogeneous turbulence. *Journal of Fluid Mechanics,* 792**,** 869-893.

Haller, G. 2002. Lagrangian coherent structures from approximate velocity data. *Physics of fluids,* 14**,** 1851-1861.

Haller, G. 2015. Lagrangian coherent structures. *Annual review of fluid mechanics,* 47**,** 137-162.

Haller, G., Hadjighasem, A., Farazmand, M. & Huhn, F. 2016. Defining coherent vortices objectively from the vorticity. *Journal of Fluid Mechanics,* 795**,** 136-173. Available: 10.1017/jfm.2016.151

Haller, G. & Yuan, G. 2000. Lagrangian coherent structures and mixing in two-dimensional turbulence. *Physica D: Nonlinear Phenomena,* 147**,** 352-370. Available: https://doi.org/10.1016/S0167-2789(00)00142-1

Hoffmann, A. C., Stein, L. E. & Bradshaw, P. 2003. Gas cyclones and swirl tubes: principles, design and operation. *Appl. Mech. Rev.,* 56**,** B28-B29.

Lube, G., Breard, E. C. P., Cronin, S. J. & Jones, J. 2015. Synthesizing large-scale pyroclastic flows: Experimental design, scaling, and first results from PELE. *Journal of Geophysical Research-Solid Earth,* 120**,** 1487-1502. Available: 10.1002/2014jb011666

Lube, G., Breard, E. C. P., Esposti-Ongaro, T., Dufek, J. & Brand, B. 2020. Multiphase flow behaviour and hazard prediction of pyroclastic density currents. *Nature Reviews Earth & Environment,* 1**,** 348-365. Available: 10.1038/s43017-020-0064-8

Peacock, T. & Haller, G. 2013. Lagrangian coherent structures: The hidden skeleton of fluid flows. *Physics Today,* 66**,** 41-47. Available: 10.1063/pt.3.1886

Poelma, C. & Ooms, G. 2006. Particle-Turbulence Interaction in a Homogeneous, Isotropic Turbulent Suspension. *Applied Mechanics Reviews,* 59**,** 78-90. Available: 10.1115/1.2130361

Pope, S. B. 2000. *Turbulent Flows,* Cambridge, Cambridge University Press. Available: DOI: 10.1017/CBO9780511840531

Rhodes, M. 2008. Storage and Flow of Powders-Hopper Design. *Introduction to particle technology***,** 265-292.

Roche, O. 2012. Depositional processes and gas pore pressure in pyroclastic flows: an experimental perspective. *Bulletin of Volcanology,* 74**,** 1807-1820. Available: 10.1007/s00445-012-0639-4

Rosa, B., Pozorski, J. & Wang, L.-P. 2020. Effects of turbulence modulation and gravity on particle collision statistics. *International Journal of Multiphase Flow,* 129**,** 103334.

Salinas, J. S., Balachandar, S., Shringarpure, M., Fedele, J., Hoyal, D., Zuñiga, S. & Cantero, M. I. 2021. Anatomy of subcritical submarine flows with a lutocline and

an intermediate destruction layer. *Nature Communications,* 12**,** 1649. Available: 10.1038/s41467-021-21966-y

Scharff, L., Hort, M. & Varley, N. R. 2019. First in-situ observation of a moving natural pyroclastic density current using Doppler radar. *Scientific Reports,* 9**,** 7386. Available: 10.1038/s41598-019-43620-w

Sulpizio, R., Dellino, P., Doronzo , D. M. & Sarocchi, D. 2014. Pyroclastic density currents: state of the art and perspectives. *Journal of Volcanology and Geothermal Research,* 283**,** 36-65. Available: 10.1016/j.jvolgeores.2014.06.014

Thielicke, W. & Stamhuis, E. J. 2014. PIVlab – Towards User-friendly, Affordable and Accurate Digital Particle Image Velocimetry in MATLAB. *Journal of Open Research Software,* 2**,** e30. Available: 10.5334/jors.bl

Uhlmann, M. & Doychev, T., 2014. Sedimentation of a dilute suspension of rigid spheres at intermediate Galileo numbers: the effect of clustering upon the particle motion. *Journal of fluid mechanics,* 752**,** 310-348.

Wang, L.-P. & Maxey, M. R. 1993. Settling velocity and concentration distribution of heavy particles in homogeneous isotropic turbulence. *Journal of fluid mechanics,* 256**,** 27-68.

Wilson, C. J. N. 1985. The Taupo Eruption, New Zealand. II. The Taupo Ignimbrite. *Philosophical Transactions of the Royal Society of London. Series A, Mathematical and Physical Sciences,* 314**,** 229-310.

Wohletz, K. H. 1998. Pyroclastic surges and compressible two-phase flow. *Developments in Volcanology,* 4.

Yang, T. S. & Shy, S. S. 2005. Two-way interaction between solid particles and homogeneous air turbulence: particle settling rate and turbulence modification

measurements. *Journal of Fluid Mechanics*, 526**,** 171-216. Available: 10.1017/S0022112004002861

6 Synthesis and Conclusion

This chapter reviews the three research questions that motivated and guided this PhD thesis and summarizes the main findings. The findings are discussed in the scientific context of volcanology and multiphase fluid dynamics. A link between PDC hazards and sedimentation behavior is established through the multiphase physics of dilute PDCs. Lastly, the chapter concludes the findings, presenting future perspectives, showing additional preliminary data, and providing new research opportunities.

6.1 Research Objectives

Pyroclastic density currents are the most lethal (Auker *et al.*, 2013) but least understood (Lube *et al.*, 2020) hazards of explosive volcanism. To help shed light on some of the unexplained processes, as identified in Chapter 1, this PhD research investigated the vertical structure and multiphase gas particle feedbacks inside dilute PDCs. In this context, three large-scale experiments were conducted in PELE across basal surfaces of varying roughness. These large-scale experiments focused on answering three main research questions:

i. ***What are the processes behind the destruction-causing dynamic pressure in pyroclastic density currents, and how do these processes relate to hazard impacts?*** *This was further motivated by recent experimental results published during this PhD by others in the group (Brosch et al., 2021), and supported by coincidental measurements into natural PDCs, revealed the dynamic pressure to be focused in large turbulence structures and to span a wider spectrum than previously expected.*

The mechanisms causing these broad dynamic pressure spectra remain enigmatic, necessitating more detailed experimental work.

ii. ***How can the internal flow and turbulence structure of PDCs be characterized, and how does it evolve during flow propagation?*** *To date, the ferocity and unpredictability of PDCs have prohibited most efforts to obtain direct measurements inside flows, limiting the ability to validate flow models of dilute PDCs. This motivates continued experimental efforts to characterize the internal structure of dilute PDCs and to understand the hazard potential of PDCs better.*

iii. ***What are the effects of turbulent gas-particle feedback mechanisms on the behavior of PDCs, and how do these feedback mechanisms modify the flow and turbulence structure of dilute PDCs?*** *Theoretical models about the gas-particle interactions in pyroclastic density currents have been suggested (Burgisser and Bergantz, 2002, Breard and Lube, 2017), but comprehensive understanding on the interplay between particles and turbulence has not been developed yet, also for other turbulent systems this is not fully understood (Brandt and Coletti, 2022).*

6.2 Key Findings

6.2.1 Components of Dynamic Pressure and Their Implications on PDC Hazards

Chapter 3 focused on the research question (i): The processes behind destruction causing dynamic pressures and how they relate to hazard impacts. This was achieved through the first high-resolution dynamic pressure measurements in large-scale experimental PDCs and the development of new analysis algorithms. The results of Chapter 3 show the dynamic pressure to consist of two main contributions, which are the continuous **dusty gas pressure** and discrete **particle impacts**, and that these need to be considered separately for hazard

planning. Through investigations of the spectrum of these two contributions to dynamic pressure, it was demonstrated that dusty gas pressures exceed mean values commonly estimated for hazard assessments (e.g., Burgisser and Bergantz, 2002, Burgisser *et al.*, 2005, Dellino *et al.*, 2008, Dioguardi and Mele, 2018), by more than one order of magnitude. However, particle impacts, which occur as clusters, exerted dynamic pressures that exceed mean pressures by up to two orders of magnitude.

The **dusty gas pressure** equates to the fluid dynamic pressure, also considered by Brosch *et al.* (2021). The density in this equation is the bulk density of the gas and well-coupled particles ($St \ll 1$), creating a dusty gas envisaged to act like a continuous fluid. The hazard impact caused by the dusty gas is a continuum loading to structures such as walls and trees. The force exerted onto these structures is the dusty gas dynamic pressure integrated over the area orthogonal to the flow direction. In structural damages caused by PDCs, walls that are orthogonal to the flow direction are often destroyed, while walls in the flow direction may not collapse (Figure 6.1). Also, tree blowdowns can be caused by the dusty gas dynamic pressure (Voight, 1981, Brand *et al.*, 2023). For the Mount Saint Helens eruption, tree damage was used to define areas of destructiveness (Esposti Ongaro *et al.*, 2012). Brosch *et al.* (2021) have shown the dusty gas dynamic pressure to be focused within turbulence structures, leading to amplifications up to 3-5 times the mean pressure. The results from Chapter 3 and Chapter 5 confirm this, focusing on dynamic pressure within turbulence structures, but found, as mentioned above, that maximum pressures exceed average pressures by more than one order of magnitude. The work also sheds light on the mechanism at play, where turbulence induces particle clustering at the margins of coherent turbulence structures, which, it is argued, creates high pressures in the margins and low pressures in the center of these structures. It was also shown how maximum clustering is established during

the first rotation of the largest coherent turbulence structures. The focusing of energy peaks at an amplification of 11.8 and then decreases to 3.9, matching the previously suggested amplification of $3-5$ by Brosch *et al.* (2021). This pattern is linked to the depletion of high Stokes number particles that initially cluster at eddy peripheries, leading to the establishment of a concentration maxima, which was shown by both the large-scale experiments in this work and supported by numerical simulations (Figure 3.7 and Figure 3.8). This successfully tests the theory that particles with critical Stokes numbers accumulate at eddy peripheries (Burgisser and Bergantz, 2002). After the first rotation of the largest coherent turbulent structures, the resulting successive pressure peaks are likely to exacerbate the destructiveness of dilute PDCs although they do successively weaken. Just how they do this is an area for further research.

Figure 6.1 Remaining flow parallel wall in Kaliadem. *The remains of a house in Kaliadem show almost complete destruction. Only a wall that stood parallel to the flow direction remains after the passage of a pyroclastic density current. Due to the orientation of the wall, the dusty gas pressure only acted on a small area. The wall still shows signs of pockmarks. Photo courtesy of Gert Lube.*

The **particle impacts** are discrete and are caused by those particles that decouple from the fluid phase and impact structures rather than follow the fluid flow around them. Due to the mechanism explained above of turbulence-induced clustering, these impacts occur in detectable clusters. The rate of change of momentum of these particles causes an impulse force that acts on the surface and so is reported as a particle impact pressure, P_{impact}. Chapter 3 showed the particle impact pressure exceeds the average pressures by two orders of magnitude, accounting for up to 75 % of the total time-integrated kinetic energy at mid-flow height. Unlike the dusty gas pressure ($P_{dusty\ gas}$), particle impacts are discrete events restricted to small surface areas. Through high forces on small areas, particle impacts generate significant piercing forces, which cause their own distinct damages; for example, Figure 3.9 and Supplementary Figure 3.5 highlight characteristic pockmarks into walls during the Merapi 2010 eruption, and Kieffer (1981) reports particles being driven into trees as projectiles. Furthermore, survivors of the Whakaari (White Island) eruption on the 19th of December 2019 in Aotearoa (New Zealand) reported repeated waves of dynamic pressure, during which they were hit by white-hot crystals and rocks (Browitt, 2020, Cozad, 2020, Urey, 2022).

These reports further highlight the importance of the findings in Chapter 3 and the applicability of the experimental results to natural eruptions. The fluid pressure and discrete particle impacts occurring in destruction-causing waves must be considered for hazard forecasting. Projectile-like particle impacts pose a significant hazard and need to be considered as potential contributors to the injuries and lethality caused by dilute PDCs and included in hazard mitigation tactics. Detailed analysis of pockmarks could give information on the magnitude of particle impacts in nature. It is to be noted that brittle particles that break

upon impact with a concrete wall can still lead to significant injuries. Therefore, the material properties of particles and targets must be considered in such studies.

6.2.2 Vertical Stratification and Turbulence Structure in Dilute Pyroclastic Density Currents

To address the research question (ii), Chapter 4 investigated the vertical structure of experimental dilute PDCs through three large-scale experiments, varying the bed roughness and the lower boundary condition of the generated flows. For natural $100 - 500$ m thick dilute PDCs, the largest deployed roughness of $4 - 8$ mm scales to boulders of $0.2 - 2.2$ m, the intermediate roughness ($\sim$201 µm) to $1.1 - 5.5$ cm, and the smoothest roughness ($\sim$10 µm) to $0.56 - 2.8$ mm. Therefore, this variation in bed roughness presents terrains from bouldery down to sandy substrates. The tested substrate changes did not significantly influence the propagation of the generated dilute PDCs. This can be explained by sedimentation quickly overwriting the initial roughness and generating its own roughness. Alternatively, the deployed roughness variations may not produce detectable differences or even present hydraulically smooth substrates. Kashefipour *et al.* (2017) studied experimental turbidity currents with significantly larger roughness variations and found significant changes in velocity profiles. However, the magnitude of roughness change used by Koshefiqour et al. (2017) is not realistic for the substrate around volcanoes but scales to natural obstacles such as hills, which was studied in another PhD, that by Corna (2023), which conducted an experimental series investigating the influence of hill-like obstacles with heights smaller, similar, and larger than the wall region on the dilute PDC's propagation. He found that the flow detachment downstream of the obstacle leads to particle re-suspension and modifies the flow and turbulence structure of the dilute PDCs. This indicates that

modulations of the flow profile might be more dominant once the roughness is large enough to resuspend solid particles.

Significantly, this research shows that the vertical structure of dilute PDCs, for both the concentration and the downstream velocity, collapses onto a single curve in non-dimensional form. It is, therefore, self-similar throughout the flow runout. This has previously only been shown for turbidity currents (Altinakar *et al.*, 1996, Cantero-Chinchilla *et al.*, 2015). The self-similarity of the velocity magnitude and the concentration distributions implies that the dynamic pressure is also self-similar (Chapter 4 EQN. 13). The self-similar shape of the dynamic pressure shows the maximum average pressure to be c. 2.5 times higher than the integral-averaged pressure, indicating further potential shortfalls in the use of integral-averaged values. The maximum time-averaged dynamic pressure can be calculated following EQN. 14 in Chapter 4, using bulk densities and velocities. In this way, the maximum dynamic pressure occurs at c. 7% of the height of the density current body region, which is significantly lower than the height of the velocity maximum (at c. 24 % of the flow height). For the dilute PDC generated during the eruption of Whakaari (White Island), New Zealand, (9th of December 2019) with an average height of c. 26 m (Brosch *et al.*, 2021), this research suggests the maximum (time-integrated) dynamic pressures would occur at 1.8 m, i.e., the height of a standing person. For large PDCs with $100 - 500$ m height, the maximum dynamic pressure is predicted at c. $7 - 35$ m, therefore at heights of building infrastructure.

Figure 6.2 summarizes the structure of dilute PDCs schematically, including the new Power-Gaussian description of the vertical velocity component and the self-similar shape of the dynamic pressure distribution. The results from Chapter 4 show that the zonation into the wall and jet region has significance for the velocity magnitude, the concentrations, and

downstream and vertical velocities. This suggests that the wall-jet boundary is significant for the downstream dynamic and the mass and momentum transfer between different parts of the flow. The wake is not described well by the time-averaged flow profiles. Current multilayered PDC models focus on two layers: the dilute part and the dense underflow (Kelfoun, 2017, Shimizu *et al.*, 2019, Shimizu *et al.*, 2021). This research instead suggests a depth-averaged 3-layer model based on the empirical fits suggested in Chapter 4. A 3-layer depth-averaged model could be composed of a dense basal layer overridden by the wall and jet region. As defined in this thesis, the wake is a point of divergence and is not described well by the vertical concentration and velocity distributions. Therefore, I suggest first testing if models ignoring the wake produce meaningful results.

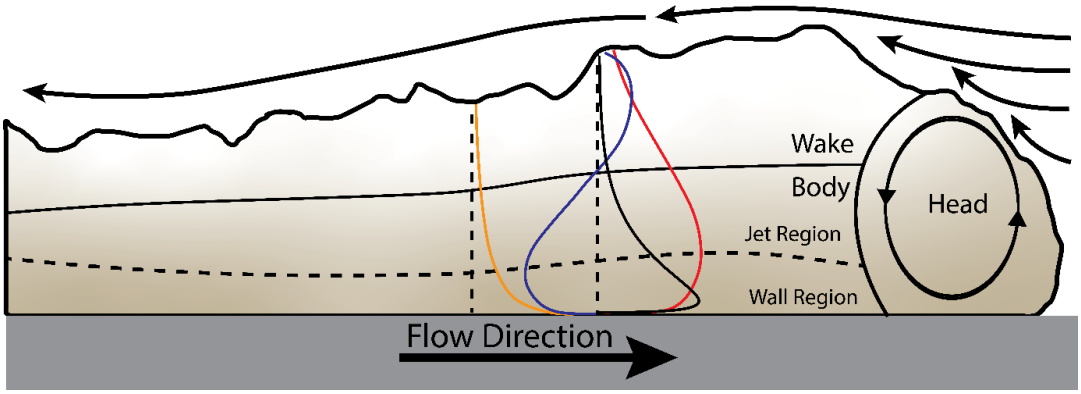

Figure 6.2 Schematic figure visualizing the structure of dilute PDCs. *The PDC begins with the upstream rotating head vortex, driven by the ambient shear. Vertically, the dilute upper part of the PDC comprises the wall and jet region overlain by the turbulent wake. Profiles show the downstream velocity (red), the vertical velocity (blue), concentration (yellow), and dynamic pressure (black).*

The presence of a dense granular bedload and erosional and depositional regimes (Brosch and Lube, 2020) suggest the presence of a basal slip condition. Current models either assume a zero slip boundary condition (Brosch *et al.*, 2021, Cerminara *et al.*, 2021) or do not describe the basal contact (Dellino *et al.*, 2008). The boundary conditions of the Power-Gaussian velocity profile were reevaluated by including a slip condition in the form of a Navier-

Maxwell slip length. The experimental data are well fit using a velocity profile with and without a slip condition. Due to the overall objectives and the resulting experimental setup, velocity data was recorded with a spatial resolution of c. 1 cm. The results suggest that both scenarios are possible, though the presence of a dense bedload and erosional phases (Brosch and Lube, 2020) making a slip condition more likely. Including a basal slip did not generate a significant difference in the overall velocity fits; only the basal boundary was modulated slightly. Data with higher spatial resolution, smaller than the expected viscous sublayer ($<$ 3 mm), is needed to further investigate the presence of a basal slip. Also, the influence on depositional and erosional processes needs to be tested.

6.2.3 Turbulence Field in Dilute Pyroclastic Density Currents

Chapters 4 and Chapter 5 investigated the turbulence structure of dilute PDCs, expanding on previous studies of Brosch *et al.* (2021) and Cerminara *et al.* (2021). The turbulence fields were investigated by studying the turbulence fluctuations, here extracted via Reynolds decomposition, following $U = \overline{U} + U'$ with the full flow field U, mean flow $\overline{U}$, and turbulence field U'. For most settings where turbulence fields are extracted, the mean flow field is constant in time and only a function of spatial coordinates ($\overline{U}(x, y, z)$). In contrast, mean flow fields for transient flows are highly time-dependent ($\overline{U}(x, y, z, t)$). Brosch et al. (2021) and Cerminara et al. (2021) fit temporal polynomials to the fit parameters of empirical functions. They apply assumptions that may influence calculated mean fields and the resulting turbulence fields. This research used temporal Savazki-Golay filters (Savitzky and Golay, 1964) with varying filter lengths to calculate the mean flow fields. The detail contained in the mean flow can be adjusted by changing the filter length (time), and so turbulence flow fields for different time scales can be extracted. Short time-windows will extract higher frequency turbulence flow fields by including more detail in the mean flow

fields. Long window lengths include less detail in the mean flow field, and so extract also lower frequency turbulence flow field.

In Chapter 4, turbulence generation and the influence of turbulence on the vertical structure of PDCs were investigated. The results show that turbulence is mostly generated at the top flow boundary, where concentrations and density stratification are low. On the other hand, turbulence generation at the base is hindered by high-density gradients inhibiting turbulence generation. Turbulence intensities increase with height and also towards the lower solid boundary. The turbulence kinetic energy does not increase significantly towards the base. For the wake and upper parts of the body, turbulence is dominant over the mean flow, generating an actively mixing layer. This also leads to deviations from the vertical distributions of velocity and concentration, even in time-averaged data.

Chapter 5 shows the spatial and temporal evolution of the turbulence structure of dilute gravity currents reaching Reynolds numbers up to 1.5×10^6. Temporal Savitzki-Golay filters with window lengths of 2 s and 250 ms were used to extract these turbulence patterns. During the initial flow propagation, distinct turbulence patterns are developed consisting of large, low frequency (c. 1.22 Hz) vortices, which are superimposed by smaller sub-vertical structures with c. 10 Hz, most pronounced in the vertical velocity. The largest turbulence structures encompass the upstream rotating head vortex and shear-induced Kelvin-Helmholtz instabilities spanning the entire flow height. The head vortex, which can be identified visually, shows how particles accumulate at the vortex margins, leading to a low concentration and low-pressure zone in its center (Figure 5.2). Consistent with the constant Strouhal number of 0.3 in PDCs (Brosch *et al.*, 2021), the period of the largest structures increases during flow propagation. The increasing period shows the spatial extent of these structures to be constant.

A separation of turbulence regions into wall and jet regions, as shown in Salinas *et al.* (2021), occurring in experimental turbidity currents with Reynolds numbers up to $1.8 \times 10^4 - 2 \times 10^4$, was not observed. The experimental flows analyzed in this thesis with Reynolds numbers of 1.5×10^6, resulted in less stratification (i.e., better mixing) and higher degrees of turbulence. Salinas *et al.* (2021) further show that by lowering the Reynolds number of the experimental flows to $6 \times 10^3 - 9 \times 10^3$, an intermediate zone forms, similar to that observed by Brosch *et al.* (2021), who found that turbulence features separate into wall and jet regions. As a note of caution, this difference potentially stems from an artifact of the algorithm used to perform the Reynolds decomposition or the different dynamic behavior of the experiment presented in Brosch *et al.* (2021) to the experimental data presented in this thesis. With respect to the Reynolds decomposition, using a Power-Gaussian definition of the mean velocity field, the occurrence of the velocity maximum at the wall jet boundary could force minima in turbulence fluctuations and thus explain the observed separation into the wall and jet region. Lagrangian algorithms need to be used to extract Lagrangian coherent structures to show the coherence of turbulence structures (Peacock and Haller, 2013, Haller, 2015). The extraction of Lagrangian coherent structures, such as Lagrangian-averaged vorticity deviation (LAVD) (Farazmand and Haller, 2016) and finite-time Lyapunov exponents (Haller and Yuan, 2000, Haller, 2002), was tested in this PhD research, but remained unsuccessful due to violations of smoothness conditions of the used velocity fields (Brandt and Coletti, 2022). This can be explained by the high levels of polydispersity resulting in a range of coupling regimes and noise from the measurement and PIV algorithm.

6.2.4 Gas Particle Feedback in Dilute Pyroclastic Density Currents

In Chapter 3 and Chapter 5, the turbulence structure and gas-particle feedbacks inside PDCs were investigated, focusing on research question (iii). The particle coupling was described

considering only the particle Stokes number, as opposed to previous research by Burgisser and Bergantz (2002) and Breard and Lube (2017), who also considered the Stability number (particle settling and turbulent fluid motion time scales) to describe the influence of gravity. Setting the Stokes number to a critical value of one identifies for which eddy frequencies a particle migrates to the margins. Smaller particles will be coupled to the eddy, and bigger particles decouple. This allowed linking eddy sizes (Figure 3.5) and frequencies with particle grain-size distributions (Figure 3.6 and Figure 5.8). In turbulent flows such as dilute PDCs, the energy is transferred from large to smaller structures along a turbulent energy cascade. The Kolmogorov cascade has a $-5/3$ slope in a log-log space, and is often assumed to be a constant in fully turbulent flows. Along this energy cascade, large eddies start a sequence of exciting ever-smaller eddies until the energy is dissipated in heat (Figure 6.3 a, b, and c). The largest eddies lie in the so-called energy-containing range where turbulence is generated; in the case of PDCs, this is primarily through shear with the ambient air. The shear-induced head vortex is the most prominent example of these large turbulence structures. The largest eddies with frequencies of ca. 1.3 Hz are the start of the inertial subrange, where the energy is passed down from larger to smaller structures. Based on the Stokes number, these largest eddies can theoretically support particles up to c. 2 mm in diameter. The dissipation range begins at the Kolmogorov scale at the end of the inertial subrange, where energy is viscously dissipated. For the large-scale experiments, reaching Reynolds numbers up to $1.5 \cdot 10^6$, the Kolmogorov scale was estimated to be $1.33 - 42$ µm much smaller than the initial d_{50} median grain size of 241 µm and the largest particles with 16 mm diameter (shown in Chapter 5). Along the inertial subrange, the particle sizes that are supported decrease with eddy size and eddy period, predominantly clustering the particles with $St = \mathcal{O}(1)$ for a given eddy (Figure 6.3 b) (Wang and Maxey, 1993, Fessler *et al.*, 1994, Aliseda *et al.*, 2002).

The analysis only studying the Stokes Number differs from analyses by Burgisser and Bergantz (2002) and Breard and Lube (2017), who also considered the Stability number. The Stability number describes the importance of gravitational forcing. These studies find a variety of coupling regimes. In other turbulence studies, the Gallileo Number is used to determine the influence of gravitational forces compared to viscous forces. For the presented experiments, Galileo numbers range from $5.9 \times 10^{-8} - 3.4 \times 10^{4}$. This indicates that large particles are influenced by gravitational forcing, while small and intermediate particles are largely unaffected. Therefore, the proposed model, ignoring gravitational effects by only considering the Stokes number, describes the sedimentation and gas-particle coupling of small to intermediate-sized particles well. However, for the largest particles, gravitational forcing becomes dominant.

Through the analog case of the cyclone separation in the industrial engineering case, the forces acting on one particle can be expressed as

$$F_{total} = F_E + F_G + F_B + F_D \qquad \textit{EQN. 6-1}$$

F_E the centrifugal force, F_G gravitational forces, F_B buoyancy forces, F_D drag force (see Figure 6.3 d). In this force balance and in Figure 6.3 d, only inward and outward-directed force components are considered, as the tangential force components do not determine the coupling of particles to turbulent vortices.

At the base of a circular vortex, the outward forces ($F_E + F_G$) are maximum. For a particle to be suspended in the vortex, the outward and inwards acting forces have to be equal. From this follows

$$F_E + F_G = F_B + F_D \rightarrow \frac{F_E + F_G}{F_B + F_D} = 1 = \theta \qquad \text{EQN. 6-2}$$

The fraction of outward and inward forces can be written as a coupling number θ. For $\theta > 1$, particles would uncouple, and $\theta < 1$, particles would be sufficiently coupled with the vortex. For calculations of the coupling number, the forces acting on one particle need to be investigated systematically.

Figure 6.3 e conceptually shows how particles may decouple from one vortex and either be coupled by a secondary vortex or fall through smaller secondary vortices. Turbulence fluctuations with different timescales for different runout distances were extracted. This revealed the shear-induced generation of the largest turbulence structures along the initial runout, generating vortices with constant spatial extend. These largest structures are superimposed by more frequent sub-vertical structures with frequencies of $\sim$10 Hz. These sub-vertical structures are presented as a signature in all measurements. A constant phase shift between vertical and downstream velocity is not observed. Therefore, sub-vertical structures are unlikely rotational eddies. I hypothesize that the sub-vertical velocity structures identified in Chapter 5 generate sedimentation pathways and are the origin of selective sedimentation. Figure 6.3 f suggests a mechanism for the generation of mesoscale clusters. At first t_1 particles with $St = \mathcal{O}(1)$ accumulate at the eddy margins. Through gravitational forcing particles slowly settle to the base of the eddies (t_2). Once a sufficient cluster is formed (t_3), the cluster's terminal fall velocity increases, and the cluster is decoupled from the vortex. After detachment, the cluster is in the fall regime (Burgisser and Bergantz, 2002) and collects more particles through collisional clustering and wake-induced clustering. In the experiments, the sedimentation pathways for rapid sedimentation of

clusters are visible as long as sufficient mass loading of specific grain sizes is present. $t_{4,5}$ schematically sets the whole mechanism into the context of a PDC.

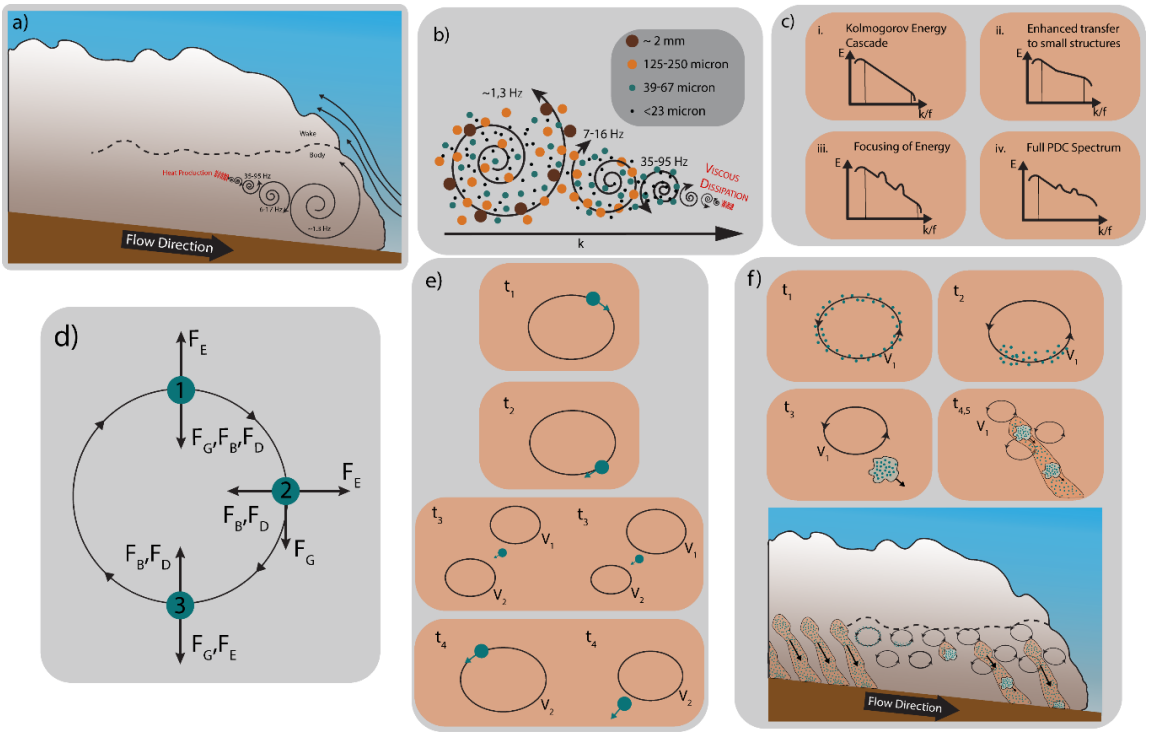

Figure 6.3 Conceptual figure summarizing the turbulent energy cascade and gas-particle feedbacks described in this thesis. a) conceptual sketch visualizing the energy cascade in PDCs. The largest eddies, such as the head vortex, are driven by shear and start a sequence of energy transfer from larger to smaller eddies until the energy is viscously dissipated. b) Schematic energy cascade as a function of the wave number k and frequency (marked above). Particles are distributed according to their Stokes number. Larger eddies can support a wider range of particles. With Stokes numbers of 1 accumulate at eddy margins, smaller particles are evenly distributed, and particles with Stokes numbers larger than 1 decouple from the vortex. c) i. The initial Kolmogorov cascade split into the energy-containing range, inertial subrange, and the dissipation range. ii) Energy cascade, including a change in slope induced through the presence of particles. iii) Energy cascade, including cluster-induced energy focusing for discrete frequency spectra. d) Schematic sketch of the forces acting on a particle inside a circular vortex with F_E the centrifugal force, F_G the gravitational forces, F_B the buoyancy forces, and F_D the drag force. Arrows indicate the direction of the forces; for simplicity, only force components parallel or orthogonal to the propagation direction are shown. e) Conceptual trajectory of a particle decoupling at the vortex's base. t_1: The particle is at the top of the eddie and well coupled. t_2: the particle

travels toward the base of the vortex where it is decoupled. t_3: the particle is decoupled from the first vortex V_1 and approaches another vortex V_2. V_2 can be either the same size larger (left), or smaller than the initial vortex (right). t_4: The particle is coupled again (left) for the equally or larger-sized vortex. If the secondary vortex is smaller, the particle falls through and is not coupled. f) Conceptual figure of the hypothesized generation mechanism of mesoscale clusters. t_1: Particles with Stokes numbers around 1 accumulate at eddie margins. t_2: Particles accumulate at the base of the vortex through gravitational forcing. t_3: If the concentration of the particle cluster is large enough, the particle cluster decouples from the vortex. t_4: After the cluster is decoupled, it falls through other vortices. During the fall the cluster generates a low-pressure wake, and with it, a sedimentation pathway. At the base of (f) this mechanism is schematically put in the context of PDCs.

6.2.5 Limitations of the Research

Conducting large-scale experiments is challenging and time-consuming, both in the experimental preparation and the data collection and processing stages. Through these challenges, two main limitations arise:

- **Repeatability:** Due to the large scale of the experiments and partially not controllable conditions such as the weather, repeatability is only given to a certain degree. Therefore, experiments with even the same starting conditions can have slightly different flow behavior. This makes very detailed experimental series such as those presented in this PhD difficult, and only clear results can be interpreted with confidence. Not consistent results may stem from the measurement accuracy/repeatability of the large-scale experiments.
- **Number of Feasible Experiments:** Each large-scale experiment is very time-consuming and complex to plan. In this PhD, five preliminary test experiments and an experimental series of three systematic experiments were conducted. The preliminary experiments were used to develop and test new sensors. Thus, reduced sensor setups were used, and the data collection was kept at a minimum. The

experimental series consisting of three experiments varying the bed roughness was conducted, assuring as much repeatability as possible. The experimental series conditions were matched as well as possible down to the ambient temperature, wind, and other weather conditions. This resulted in a data set investigating the influence of the roughness on the flow behavior. While the investigation of new physical mechanisms often only needs one experiment for detailed analysis and additional experiments for validation, detailed parameter studies need very accurate data sets. Our research from Chapter 4 suggests that the influence of the bed roughness in the scales tested does not affect the flow behavior significantly. A large-experimental series with large numbers of experimental runs for each condition could, though, show a systematic that is not presented in the presented small data set. Such an experimental series would also quantify the degree of repeatability. Large experimental series like this are not possible with large-scale experiments.

6.3 Future Perspectives

The outlined limitations of research necessitate further research, and preliminary data opens up new research opportunities. The suggested future research is outlined in the following.

6.3.1 Wider Range of Roughness

Testing bed roughness scales from the roughness deployed in this PhD to roughness deployed in Kashefipour *et al.* (2017) are suggested to investigate at which scales the roughness starts to affect the flow propagation of dilute PDCs.

6.3.2 Different Substrate Structures

In coastal protection, mangroves mitigate damage caused by tsunamis and storm surges by attenuating the energy flow (Marois and Mitsch, 2015). Walker *et al.* (1995) hypothesized PDCs to propagate as transient waves, suggesting similarity to Tsunamis and storm surges. Testing if different types of roughness and porous media dissipate significant flow energy, could inform environmental and infrastructure planning to minimize the risk posed by PDCs.

6.3.3 Different Grain-Size Distributions

Detailed studies using different grain-size distributions would inform on the influence of the grain-size distribution on the turbulence fields. Using less complex grain-size distributions with differently colored particles could give valuable insights comparable to results from numerical modeling in Chapter 3 (see Figure 3.7).

6.3.4 More Detailed Measurements

This thesis has demonstrated that deploying more detailed measurements provides valuable insights into the multiphase physics of PDCs. Measurements with higher spatial and temporal resolution will inform on smaller turbulence structures and and interactions of the PDC with the substrate.

6.3.5 Large Experimental Dataset

A larger experimental series is needed to investigate the influence of bed roughness on the propagation of dilute PDCs. The experimental series would need multiple repetition runs for each roughness to examine the reproducibility of the results. Due to time constraints and limitations in material availability, such a study is not feasible with large-scale experiments.

Here, benchtop experiments, where multiple experiments a day can be run instead of one or two experiments a month, have a strong advantage. Such benchtop experiments would lead to less scaling similarity but would still provide the valuable data, due to the possibility of creating large datasets.

6.3.6 Air Pulse and its Implications for Seismo-Acoustic Volcano Monitoring

The dynamic pressure measurements using Piezoelectric pressure sensors also reveal a pre-arrival signal caused by air displacement by the collapsing ash column. The signal is visible at distances from 1.8 to 9.6 m (see Figure 6.4). Further from impact outside the industrial building, the ambient noise becomes too high to detect this signal. The pressure signal propagates at sonic velocity ($\sim 340\ \mathrm{m \cdot s^{-1}}$) and is presented as a wind gust (Supplementary Video 2). The initial pressure pulse is followed by a continuous pressure signal caused by air displacement of the propagating flow front. The continuous signal can be compared as an analog to the air displacement that can be felt at train stations when a train approaches the platform. For the observer location at 9.6 m, the initial pressure pulse and the following continuous pressure signal are no longer differentiable.

A pressure signature preceding the PDC was also reported by Yamasato (1997), who detected a pressure wave in infrasound data and correlated it with seismic signals caused by rocks collapsing onto the mountain slope. Pre-arrival signals can be used to develop remote detection and early warning systems for pyroclastic currents. More focused interdisciplinary research investigating the physics of material collapse and generation of air displacement is needed to link it to the PDC's source conditions. For this, numerical models, as presented by Sweeney and Valentine (2017) and Valentine and Sweeney (2018) could be used. With a detailed understanding of the generation of the airwave, seismo-acoustic measurements

could be used to investigate the source mechanism of pyroclastic density currents. Infrasound is an emerging tool for volcano monitoring (Johnson and Ripepe, 2011, Watson *et al.*, 2022) and has been a standard tool for monitoring nuclear explosions (Christie and Campus, 2009). Furthermore, frequency spectra of infrasound data could potentially inform on the turbulent energy cascades inside PDCs. Understanding infrasound's information would open the opportunity to analyze more real-world data and validate concepts developed theoretically and experimentally. A detailed experimental series is currently being carried out to achieve this.

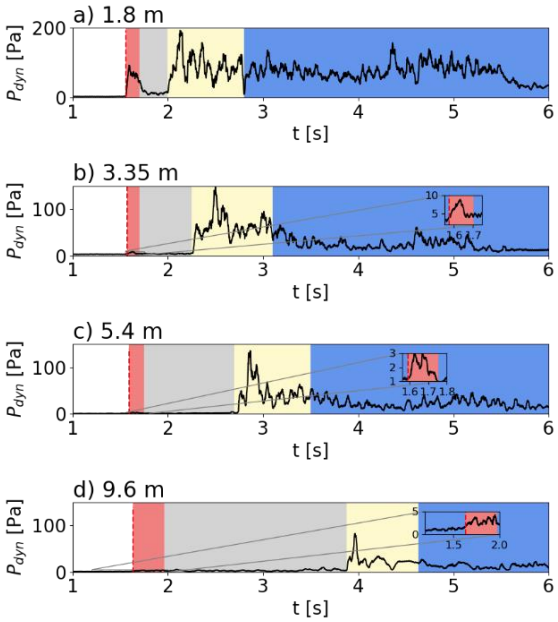

Figure 6.4Tracking the pre-arrival pressure signature along the runout. *a-d) Time series of the filtered dusty-gas Pressure along the runout (*1.8, 3.35, 5.4, *and* 9.6 *m) are shown, with the time-axis showing the time after the experiment-trigger experiment. The time series is color-coded with the pre-arrival airwave marked in red, the pre-arrival wind in grey, the flow head yellow, and the body and the tail. The expected arrival times, assuming the sonic velocity of* $340\ m \cdot s^{-1}$ *are marked by vertical red dashed lines.*

In addition to the large potential to forward seismo-acoustic volcano monitoring, the pre-arrival airwave also poses a significant hazard potential. For proximal locations, the

amplitude of the airwave reaches up to 94 Pa, a quarter of the dilute PDCs maximum dusty gas pressure (~390 Pa), and three times the often-used average pressure (32 Pa).

Due to the channeling of the air shock, real-world observations have to be considered to estimate the hazard in volcanic settings. The channeling in PELE could lead to an overestimation of hazard potential. Different generation mechanisms might generate air displacements and hazard impacts with different magnitudes.

6.4 References

Aliseda, A., Cartellier, A., Hainaux, F. & Lasheras, J.C., 2002. Effect of preferential concentration on the settling velocity of heavy particles in homogeneous isotropic turbulence. *Journal of Fluid Mechanics,* 468**,** 77-105.

Altinakar, M.S., Graf, W.H. & Hopfinger, E.J., 1996. Flow structure in turbidity currents. *Journal of Hydraulic Research,* 34**,** 713-718.

Auker, M.R., Sparks, R.S.J., Siebert, L., Crosweller, H.S. & Ewert, J., 2013. A statistical analysis of the global historical volcanic fatalities record. *Journal of Applied Volcanology,* 2**,** 2.

Brand, B.D., Pollock, N., Vallance, J.W., Ongaro, T.E., Roche, O., Trolese, M., Giordano, G., Marshall, A.A. & Criswell, C.W., 2023. Advances in our understanding of pyroclastic current behavior from the 1980 eruption sequence of Mount St. Helens volcano (Washington), USA. *Bulletin of Volcanology,* 85**,** 24.

Brandt, L. & Coletti, F., 2022. Particle-Laden Turbulence: Progress and Perspectives. *Annual Review of Fluid Mechanics,* 54**,** 159-189.

Breard, E.C.P. & Lube, G., 2017. Inside pyroclastic density currents – uncovering the enigmatic flow structure and transport behaviour in large-scale experiments. *Earth and Planetary Science Letters,* 458**,** 22-36.

Brosch, E. & Lube, G., 2020. Spatiotemporal sediment transport and deposition processes in experimental dilute pyroclastic density currents. *Journal of Volcanology and Geothermal Research,* 401**,** 106946.

Brosch, E., Lube, G., Cerminara, M., Esposti-Ongaro, T., Breard, E.C.P., Dufek, J., Sovilla, B. & Fullard, L., 2021. Destructiveness of pyroclastic surges controlled by turbulent fluctuations. *Nature Communications,* 12**,** 7306.

Browitt, S., 2020. Survivors of White Island Disaster say they felt abandoned after eruption | 60 Minutes Australia. Youtube: 60 Minutes Australia.

Burgisser, A. & Bergantz, G.W., 2002. Reconciling pyroclastic flow and surge: the multiphase physics of pyroclastic density currents. *Earth and Planetary Science Letters,* 202**,** 405-418.

Burgisser, A., Bergantz, G.W. & Breidenthal, R.E., 2005. Addressing complexity in laboratory experiments: the scaling of dilute multiphase flows in magmatic systems. *Journal of Volcanology and Geothermal Research,* 141**,** 245-265.

Cantero-Chinchilla, F.N., Dey, S., Castro-Orgaz, O. & Ali, S.Z., 2015. Hydrodynamic analysis of fully developed turbidity currents over plane beds based on self-preserving velocity and concentration distributions. *Journal of Geophysical Research-Earth Surface,* 120**,** 2176-2199.

Cerminara, M., Brosch, E. & Lube, G., 2021. A theoretical framework and the experimental dataset for benchmarking numerical models of dilute pyroclastic density currents. *arXiv preprint arXiv:2106.14057*.

Christie, D. & Campus, P., 2009. The IMS infrasound network: Design and establishment of infrasound stations. *Infrasound monitoring for atmospheric studies***,** 29-75.

Corna, L., 2023. The interactions of pyroclastic density currents with obstacles : a large-scale experimental study : a thesis presented in partial fulfilment of the requirements for the degree of Doctor of Philosophy in Earth Sciences at Massey University, Manawatū, Palmerston North, New Zealand. Doctoral. Massey University.

Cozad, J., 2020. Survivors of White Island Disaster say they felt abandoned after eruption | 60 Minutes Australia. Youtube: 02.11.2020.

Dellino, P., Mele, D., Sulpizio, R., La Volpe, L. & Braia, G., 2008. A method for the calculation of the impact parameters of dilute pyroclastic density currents based on deposit particle characteristics. *Journal of Geophysical Research-Solid Earth,* 113**,** B07206.

Dioguardi, F. & Mele, D., 2018. PYFLOW_2.0: a computer program for calculating flow properties and impact parameters of past dilute pyroclastic density currents based on field data. *Bulletin of Volcanology,* 80**,** 28.

Esposti Ongaro, T., Clarke, A.B., Voight, B., Neri, A. & Widiwijayanti, C., 2012. Multiphase flow dynamics of pyroclastic density currents during the May 18, 1980 lateral blast of Mount St. Helens. *Journal of Geophysical Research: Solid Earth,* 117**,** B06208.

Farazmand, M. & Haller, G., 2016. Polar rotation angle identifies elliptic islands in unsteady dynamical systems. *Physica D: Nonlinear Phenomena,* 315**,** 1-12.

Fessler, J.R., Kulick, J.D. & Eaton, J.K., 1994. Preferential concentration of heavy particles in a turbulent channel flow. *Physics of Fluids,* 6**,** 3742-3749.

Haller, G., 2002. Lagrangian coherent structures from approximate velocity data. *Physics of fluids,* 14**,** 1851-1861.

Haller, G., 2015. Lagrangian coherent structures. *Annual review of fluid mechanics,* 47**,** 137-162.

Haller, G. & Yuan, G., 2000. Lagrangian coherent structures and mixing in two-dimensional turbulence. *Physica D: Nonlinear Phenomena,* 147**,** 352-370.

Johnson, J.B. & Ripepe, M., 2011. Volcano infrasound: A review. *Journal of Volcanology and Geothermal Research,* 206**,** 61-69.

Kashefipour, S.M., Daryaee, M. & Ghomeshi, M., 2017. Effect of bed roughness on velocity profile and water entrainment in a sedimentary density current. *Canadian Journal of Civil Engineering,* 45**,** 9-17.

Kelfoun, K., 2017. A two-layer depth-averaged model for both the dilute and the concentrated parts of pyroclastic currents. *Journal of Geophysical Research: Solid Earth,* 122**,** 4293-4311.

Kieffer, S.W., 1981. Fluid dynamics of the May 18 blast at Mount St. Helens. *US Geol. Surv. Prof. Pap,* 1250**,** 379-400.

Lube, G., Breard, E.C.P., Esposti-Ongaro, T., Dufek, J. & Brand, B., 2020. Multiphase flow behaviour and hazard prediction of pyroclastic density currents. *Nature Reviews Earth & Environment,* 1**,** 348-365.

Marois, D.E. & Mitsch, W.J., 2015. Coastal protection from tsunamis and cyclones provided by mangrove wetlands–a review. *International Journal of Biodiversity Science, Ecosystem Services & Management,* 11**,** 71-83.

Peacock, T. & Haller, G., 2013. Lagrangian coherent structures: The hidden skeleton of fluid flows. *Physics Today,* 66**,** 41-47.

Salinas, J.S., Balachandar, S., Shringarpure, M., Fedele, J., Hoyal, D., Zuñiga, S. & Cantero, M.I., 2021. Anatomy of subcritical submarine flows with a lutocline and an intermediate destruction layer. *Nature Communications,* 12**,** 1649.

Savitzky, A. & Golay, M.J., 1964. Smoothing and differentiation of data by simplified least squares procedures. *Analytical chemistry,* 36**,** 1627-1639.

Shimizu, H.A., Koyaguchi, T. & Suzuki, Y.J., 2019. The run-out distance of large-scale pyroclastic density currents: A two-layer depth-averaged model. *Journal of Volcanology and Geothermal Research.*

Shimizu, H.A., Koyaguchi, T., Suzuki, Y.J., Brosch, E., Lube, G. & Cerminara, M., 2021. Validation of a two-layer depth-averaged model by comparison with an experimental dilute stratified pyroclastic density current. *Bulletin of Volcanology,* 83**,** 73.

Sweeney, M.R. & Valentine, G.A., 2017. Impact zone dynamics of dilute mono- and polydisperse jets and their implications for the initial conditions of pyroclastic density currents. *Physics of Fluids,* 29**,** 093304.

Urey, M., 2022. The Volcano: Rescue from Whakaari. Netflix.

Valentine, G.A. & Sweeney, M.R., 2018. Compressible Flow Phenomena at Inception of Lateral Density Currents Fed by Collapsing Gas-Particle Mixtures. *Journal of Geophysical Research: Solid Earth,* 123**,** 1286-1302.

Voight, B., 1981. Time scale for the first moments of the May 18 eruption. *US Geol. Surv. Prof. Pap,* 1250**,** 69-86.

Walker, G.P.L., Hayashi, J.N. & Self, S., 1995. Travel of Pyroclastic Flows as Transient Waves - Implications for the Energy Line Concept and Particle-Concentration Assessment. *Journal of Volcanology and Geothermal Research,* 66**,** 265-282.

Wang, L.-P. & Maxey, M.R., 1993. Settling velocity and concentration distribution of heavy particles in homogeneous isotropic turbulence. *Journal of fluid mechanics,* 256**,** 27-68.

Watson, L.M., Iezzi, A.M., Toney, L., Maher, S.P., Fee, D., Mckee, K., Ortiz, H.D., Matoza, R.S., Gestrich, J.E., Bishop, J.W., Witsil, A.J.C., Anderson, J.F. & Johnson, J.B., 2022. Volcano infrasound: progress and future directions. *Bulletin of Volcanology,* 84**,** 44.

Yamasato, H., 1997. Quantitative analysis of pyroclastic flows using infrasonic and seismic data at Unzen volcano, Japan. *Journal of Physics of the Earth,* 45**,** 397-416.

Appendix

The Following describes the supplementary codes and data. The supplementary data saved under: D Uhle Digital Appendix *DOI 10.5281/zenodo.10648325*

The Appendix is subdivided as follows.

Appendix A: General

All codes run in a free Python environment. To ensure reproducibility and avoid issues with versions of Python and single packages, Appendix A contains the Anaconda environment 'Anaconda_Environment.yaml'.

Appendix B: Supplementary Videos

The Appendix B contains the supplementary videos for Chapter 3.

Appendix C: Codes and Data: Deadly coupling – hazard impacts of pyroclastic density currents exacerbated by mesoscale particle clusters

Appendix C contains all data and codes to reproduce the figures shown in Chapter 3, except Figure 8 showing results of numerical simulations. The results of the numerical modeling where provided by Eric C.P. Breard (Eric.Breard@ed.ac.uk). For access to this data please contact Eric C.P. Breard.

Appendix D: Codes and Data: Characterizing the Flow and Turbulence Structure of Dilute Pyroclastic Density Currents Through Large-Scale Experiments

Appendix D contains all data and codes to reproduce the figures shown in Chapter 4.

Appendix E Codes and Data: Turbulence Structures in Dilute Pyroclastic Density Currents and their Implications on Turbulent Gas Particle Coupling

Appendix E contains all data and codes to reproduce the figures shown in Chapter 5.

Statements of contribution Doctorate with publications/manuscripts for Chapters 3-5.

Note for Examiners of Doctoral Theses - Explanation of Covid-19 Impacts

MASSEY UNIVERSITY
UNIVERSITY OF NEW ZEALAND

GRADUATE RESEARCH SCHOOL

STATEMENT OF CONTRIBUTION DOCTORATE WITH PUBLICATIONS/MANUSCRIPTS

We, the student and the student's main supervisor, certify that all co-authors have consented to their work being included in the thesis and they have accepted the student's contribution as indicated below in the Statement of Originality.

Student name:	Daniel Holger Uhle
Name and title of main supervisor:	Prof. Dr. Gert Lube
In which chapter is the manuscript/published work?	Chapter 3
What percentage of the manuscript/published work was contributed by the student?	80%

Describe the contribution that the student has made to the manuscript/published work:

The candidate designed and lead the experimental series, analyzed the data, conceptualized the figures, wrote the first manuscript draft, and iterated the manuscript based on supervisor and co-author comments.

Please select one of the following three options:

○ **The manuscript/published work is published or in press**

Please provide the full reference of the research output:

○ **The manuscript is currently under review for publication**

Please provide the name of the journal:

◉ **It is intended that the manuscript will be published, but it has not yet been submitted to a journal**

Student's signature:	Daniel Uhle Digitally signed by Daniel Uhle Date: 2023.09.20 13:24:10 +12'00'	Main supervisor's signature:	Gert Lube Digitally signed by Gert Lube Date: 2023.09.22 10:16:15 +12'00'

This form should be placed at the beginning of each relevant thesis chapter.

MASSEY UNIVERSITY
UNIVERSITY OF NEW ZEALAND

GRADUATE RESEARCH SCHOOL

STATEMENT OF CONTRIBUTION
DOCTORATE WITH PUBLICATIONS/MANUSCRIPTS

We, the student and the student's main supervisor, certify that all co-authors have consented to their work being included in the thesis and they have accepted the student's contribution as indicated below in the Statement of Originality.

Student name:	Daniel Holger Uhle
Name and title of main supervisor:	Prof. Dr. Gert Lube
In which chapter is the manuscript/published work?	Chapter 4
What percentage of the manuscript/published work was contributed by the student?	80%

Describe the contribution that the student has made to the manuscript/published work:

The candidate designed and lead the experimental series, analyzed the data, conceptualized the figures, wrote the first manuscript draft, and iterated the manuscript based on supervisor and co-author comments.

Please select one of the following three options:

○	**The manuscript/published work is published or in press** Please provide the full reference of the research output:
○	**The manuscript is currently under review for publication** Please provide the name of the journal:
◉	**It is intended that the manuscript will be published, but it has not yet been submitted to a journal**

Student's signature:	Daniel Uhle Digitally signed by Daniel Uhle Date: 2023.09.20 13:24:27 +12'00'	Main supervisor's signature:	Gert Lube Digitally signed by Gert Lube Date: 2023.09.22 10:17:28 +12'00'

This form should be placed at the beginning of each relevant thesis chapter.

MASSEY UNIVERSITY
UNIVERSITY OF NEW ZEALAND

GRADUATE RESEARCH SCHOOL

STATEMENT OF CONTRIBUTION
DOCTORATE WITH PUBLICATIONS/MANUSCRIPTS

We, the student and the student's main supervisor, certify that all co-authors have consented to their work being included in the thesis and they have accepted the student's contribution as indicated below in the Statement of Originality.

Student name:	Daniel Holger Uhle
Name and title of main supervisor:	Prof. Dr. Gert Lube
In which chapter is the manuscript/published work?	Chapter 5
What percentage of the manuscript/published work was contributed by the student?	80%

Describe the contribution that the student has made to the manuscript/published work:

The candidate designed and lead the experimental series, analyzed the data, conceptualized the figures, wrote the first manuscript draft, and iterated the manuscript based on supervisor and co-author comments.

Please select one of the following three options:

○ **The manuscript/published work is published or in press**

Please provide the full reference of the research output:

○ **The manuscript is currently under review for publication**

Please provide the name of the journal:

◉ **It is intended that the manuscript will be published, but it has not yet been submitted to a journal**

Student's signature:	Daniel Uhle Digitally signed by Daniel Uhle Date: 2023.09.20 13:24:43 +12'00'	Main supervisor's signature:	Gert Lube Digitally signed by Gert Lube Date: 2023.09.22 10:18:50 +12'00'

This form should be placed at the beginning of each relevant thesis chapter.

MASSEY UNIVERSITY
TE KUNENGA KI PŪREHUROA
UNIVERSITY OF NEW ZEALAND

GRADUATE RESEARCH SCHOOL

Note for Examiners of Doctoral Theses
Explanation of COVID-19 Impacts

The Doctoral Research Committee recognises the impacts of Covid-19 on research, particularly for doctoral candidates, and we appreciate the efforts made by supervisors and candidates to ensure timely completion of the doctoral thesis. We know that in some cases this has meant the project has needed to be changed in some way, including its final presentation. For students whose work has been impacted, we invite supervisors to provide a note for examiners explaining the circumstances.

Instructions for Supervisors:

The note is designed to enable you to communicate to examiners your desire for them to take account of certain factors in their assessment of a thesis to address delays and disruptions experienced by a thesis student as a result of the Covid-19 pandemic.

The attached form should be used to provide an explanation to the examiners on what to consider in their evaluation. It should detail how the project was altered or how the final product of the thesis has been affected as a result of the disruption. Statements should be clear and succinct for the benefit of the examiners and in fairness to the student and others in the student cohort.

The form should be signed by the student, the supervisor and the Head of Academic Unit, or nominee, and included in the information that is sent out with the thesis.

For doctoral candidates, the completed form should be inserted into the front of the thesis before the abstract by the candidate when submitting their digital thesis for examination in the Student Portal. At the completion of the examination, the amended form which excludes any confidential comments to the examiners, should be included in the appendices.

Please be sure to indicate whether a student has received a suspension of studies due to Covid-19 and/or an extension, as it is important to note if students have already had some special consideration.

Approved by DRC 10/Feb/2021
DRC 21/02/03

MASSEY UNIVERSITY
TE KUNENGA KI PŪREHUROA
UNIVERSITY OF NEW ZEALAND

GRADUATE RESEARCH SCHOOL

Note for Examiners
Explanation of COVID-19 Impacts

Thank you for taking the time to examine this thesis, which has been undertaken during the Covid-19 pandemic. The New Zealand Government's response to Covid-19 includes a system of Alert Levels which have impacted upon researchers. Our University's pandemic plan applied the Government's expectations to our research environment to ensure the health and safety of our researchers, however, research was impacted by restrictions and disruptions, as outlined below.

For a six-week period from March 26 to April 27 2020, New Zealand was placed under very strict lockdown conditions (Level 4 – Lockdown), with students and staff unable to physically access University facilities, unless they were involved in essential research related to Covid-19. All field work ceased and data collection with humans was restricted to online methods, if appropriate. The restrictions were partially lifted on April 27, but students and staff were not generally allowed back into University facilities until May 13.

Ongoing disruptions have also been encountered for some students due to uncertainties over the potential for future Covid-19-related restrictions on activities, and a Covid-19 cluster outbreak based in Auckland in New Zealand on 12 August 2020 led to the imposition of rolling Level 2 (Reduce) and Level 3 (Restrict) conditions until 23 September 2020. Auckland campus based students remained on Level 2 until 7 October 2020. This Alert Level system continues to be utilised throughout 2021.

These changing Alert Levels have meant that some research students had experimental, clinical, laboratory, field work, and/or data collection or analysis interrupted, and consequently may have had to adjust their research plans. For some students, the impacts of Covid-19 stretched far beyond the lockdown period in April/May 2020, as they may have had to significantly revise their research plans.

Overseas travel is not permitted by the University and restrictions have been placed on the New Zealand borders which are closed to non-New Zealand citizens and permanent residents. This meant that international students who were based offshore at the time of lockdown, were unable to return to New Zealand. A small number of offshore students were provided permission to return to New Zealand in early 2021. Many students have also suffered from anxiety and stress-related issues, and have had financial impacts, meaning their research progress has been significantly delayed.

This form, as completed by the supervisor and student, outlines the extent that the research has been affected by Covid-19 conditions.

Approved by DRC 10/Feb/2021
DRC 21/02/03

Please consider the factors listed below in your assessment of the work.

This statement has been prepared by the candidate's supervisor in consultation with the student and has been endorsed by the relevant Head of Academic Unit.

Student Name:	Daniel Holger Uhle	**ID Number:**	[redacted]
Supervisor Name:	Prof. Dr. Gert Lube	**Date:**	21-Sep-23

Thesis title:

Effects of Multiphase Turbulence on the Flow and Hazard Behavior of Dilute Pyroclast

Considerations to be taken into account. **Note: This statement will remain in the final copy of the thesis which will be available from the Massey University Library following the examination process.**
[Enter key considerations here for the examiners. This can include but is not limited to change of scope, scale, topic, focus; limitations in relation to data collection, access to necessary literature or archival materials, laboratories, field sites; disruptions as a result of lockdown and various alert levels, medical or health considerations etc]

In 2020, 2021, and 2022, national lockdowns and restrictions associated with the global COVID-19 pandemic led to delays and restrictions in access to lab and office facilities. These restrictions impacted the ability to conduct lab work and prepare and conduct experiments.

During Level 4 and Level 3, access to facilities on Massey University Palmerston North campus was denied.
At Level 2, restricted access was permitted with, at times, limited numbers of people able to work within one lab.
At all Levels, people with COVID-19 and household contacts were required to isolate at home. These restrictions heavily impacted the ability to perform lab work and conduct experiments for long periods of time.

Also, the first lockdown impacted the testing and production of sensors, as indicated in the thesis. Alert Levels took place for the indicated time frames.

LEVEL 4:
26 Mar 2020 - 27 Apr 2020;
18 Aug 2021 - 31 Aug 2021

LEVEL 3:
28 Apr 2020 - 13 May 2020;
01 Sept 2021 - 07 Sept 2021

LEVEL 2:
14 May 2020 - 08 Jun 2020;
12 Aug 2020 - 21 Sept 2020;
15 Feb 2021 - 17 Feb 2021;
28 Feb 2021 - 06 Mar 2021;
08 Sept 2021 - 02 Dec 2021

Level 1 occurred at all other times.

Approved by DRC 10/Feb/2021
DRC 21/02/03